Molecular Simulations in Zeolites for Industrial Applications

Julio E. Pérez Carbajo

Molecular Simulations in Zeolites for Industrial Applications

By

Julio E. Pérez Carbajo

Telecommunication Engineer

Department of Physical, Chemical, and Natural Systems

University Pablo de Olavide

Supervisors

Sofía Calero

Prof. Dr. University Pablo de Olavide

Patrick J. Merkling

Prof. Dr. University Pablo de Olavide

Dissertation submitted to obtain the degree of Doctor with international mention.

Seville, June 2019

ISBN: 978-84-09-11348-4

 https://orcid.org/0000-0003-0176-3643

Doctoral Supervisors

Prof. Dr. Sofía Calero
University Pablo de Olavide, Dept. of Physical, Chemical and Natural Systems

Prof. Dr. Patrick J. Merkling
University Pablo de Olavide, Dept. of Physical, Chemical and Natural Systems

Dissertation Committe

Dr. A. Özgür Yazaydın
University College London, Dept. of Chemical Engineering

Prof. Dr. José Manuel Martínez Fernández
University of Seville, Dept. of Physical Chemistry

Dr. MSc. Silvia V. Gaastra-Nedea
Eindhoven University of Technology, Dept. of Mechanical Engineering, Energy Technology

External Committe

Dr. Peyman Moghadam
University of Sheffield, Dept. of Chemical and Biological Engineering

Dr. Naseem A. Ramsahye
Institut Charles Gerhardt Montpellier, Dept. of Physical Chemistry

The research reported in this thesis was carried out at the Dept. of Physical, Chemical and Natural Systems, University Pablo de Olavide (Seville, Spain), with financial support from the European Research Council (ERC Consolidator Grant) and from the Spanish "Ministerio de Economía y Competitividad" (MINECO)

Contents

CHAPTER 1

INTRODUCTION

PREFACE

As far as I can remember, I have always tried to understand the mechanisms behind any kind of *system* and seek the keys to improve or optimize them. That natural trend was reinforced through my training as an engineer. A few years later, I encountered the world of nanoporous materials and realized that I had a chance of having an effect on macroscopic phenomena by making what seemed at first sight subtle decisions on microscopic details.

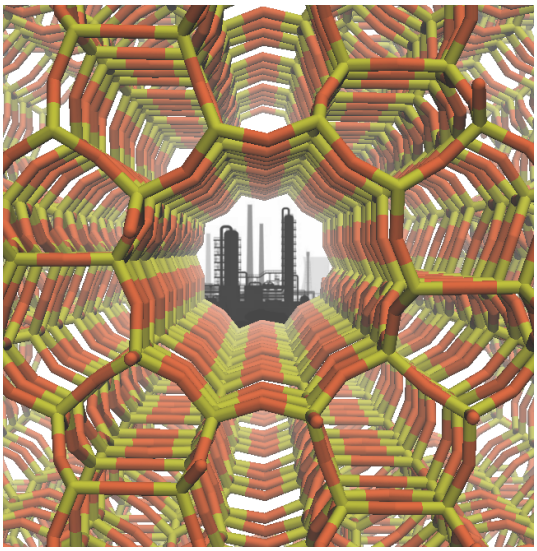

Crystalline nanoporous materials, those that show cavities sized in the range of tens to hundreds of nanometers within their ordered structures, are widely used both in industrial and technological processes, as well as representing a lively field of research and study. Zeolites, metal- and covalent-organic frameworks (MOF and COF, respectively) or zeolitic imidazolate frameworks (ZIF) are representative members of this family of nanostructured materials. Of these, zeolites are probably the most employed since they were the first to be studied and are solidly settled in industry as molecular sieves, gas traps, ion-exchangers, adsorbents or catalysts. In fact, they have a long-time journey behind: It was as early as the mid 18th century when A. F. Cronstedt coined the term *zeolite* (literally "*stone that boils*") a material that released water steam when heated and could adsorb water again when temperature lowered. [1] That *stone* is thought to have been stilbite, one of the more than 40 natural zeolites known today, which are part of the 245 topologies identified to date. [2] And

much more hypothetical zeolites are yet waiting to be synthesized. [3]

All of these topologies, with a complete bunch of variations based on their lattice composition, offer huge opportunities to tackle some of the physico-chemical issues existing in industrial processes involving mixture separations or gas capture. Undoubtedly, this context is ideal for molecular simulation: It provides the opportunity of performing computational experiments with an exhaustive control of simulation conditions, getting molecular level insight, and allowing to calculate macroscopic properties. Given that simulation validity relies on accuracy of the obtained results, filling the gap between the *real* system behavior and the predictions of the *simulated* one is a critical challenge. Therefore, the selection of the system models and their adaptation to the contour variables are crucial to reproduce the behavior of the real system.

With the previous in mind, this doctoral dissertation is threaded by two complementary ideas: On the one hand, to contribute to the enhancement of current industrial processes by proposing improved or new solutions, making an effort in their viability and applicability, and, on the other hand, to gain a deep knowledge on molecular mechanisms that usually take part in industrial processes when using zeolites.

1.1 Industrial Processes

1.1.1 Fischer-Tropsch process

Fischer-Tropsch (F-T) technology was proposed in 1925 by chemists Franz Fischer and Hans Tropsch to generate liquids fuels from coal.[4,5] The development of this technology was motivated by the scarcity of petroleum in Germany at the same time as having plenty of coal reserves, and its interest was reinforced some years later, during World War II, due to the main crude oil reserves located in territories controlled by the Allies. Since then, attention has been paid to F-T chemistry in an intermitent way, mostly linked to geopolitical reasons.[6] Nowadays, F-T processes are a mature technology which has demonstrated to be competitive in terms of fuel barrel price with respect to petroleum.[7–11] Even if associated costs of setting up a F-T production facility slows down new implementations, several production plants are operative all around the world and others are under construction,[6,12–14] and F-T processes are firmly considered as the future alternative to petroleum for hydrocarbon-based fuels.[8]

F-T processes refer today to several catalytic chemical reactions (equation 1) that generate liquid hydrocarbon fuels not only from coal but also from natural gas or biomass.

$$n\mathrm{CO} + m\mathrm{H_2} \rightarrow \left\{ \begin{array}{l} \mathrm{C_1 - C_{40+}\ alkanes} \\ \mathrm{C_1 - C_{40+}\ alkenes} \end{array} \right\} + \left\{ \begin{array}{l} \mathrm{H_2O} \\ \mathrm{CO_2} \end{array} \right\} \tag{1}$$

In this work, gas to liquid (GTL) conversion is considered starting from *syngas*, a mixture of gases (synthesis gas) resulting from a previous step of reforming natural gas.[15] This mixture of CO and H_2 is then polymerized to long-chain molecules (preferably in the C_5 to C_{10} range)[16,17] in the F-T hydrocarbon synthesis step according to $(2n+1)\mathrm{H_2} + n\mathrm{CO} \rightarrow \mathrm{C}_n\mathrm{H}_{2n+2} + n\mathrm{H_2O}$.[6,18] Finally, a phase of cracking works up the product to its near commercial form by means of conventional refinery processes, obtaining diesel, naphta, and kerosene.

1.1.2 CO_2 plasmolysis

Carbon dioxide emissions are identified as one of the main concerns relative to climate change, and fossil fuel consumption and industrial processes are the principal pollutant contributors.[19–22] In this context, CO_2 dissociation processes have arisen as an alternative to reintroduce CO_2 in the energy chain.[23,24] They have a twofold objective: mitigate its emission to the atmosphere and reuse it as feedstock to obtain CO and O_2. These gases are of industrial interest, but specially CO is highly demanded

for syngas generation (as noted in the previous section). Currently, coal gasification and natural gas reforming are the most used technologies to obtain syngas, but recent studies [25–28] have demonstrated that plasmolysis of CO_2 could became a feasible path for generating CO_2 -neutral hydrocarbon fuels.

CO_2 dissociation is described by the following expression: [29]

$$CO_2 \rightarrow CO + \frac{1}{2}O_2 \quad (\Delta H > 0) \tag{2}$$

In addition to its endothermic character, it should be noted that for traditional CO_2 plasmolysis, high power supply is necessary to reach and maintain high temperatures and ionization degrees required, with a maximum energy efficiency of 43%. [25] However, based on previous experimental results [30–33] pointing to an energy efficiency of 80%, Van Rooij et al. show that energy efficiency could be improved by using vibrational excitation in nonequilibrium plasmas, [28] which also implies lower temperatures. In turn, low gas temperatures make a thermal quenching process unnecessary because due to the diminishing, but not avoidance, of CO and O_2 recombination back to CO_2 .

1.1.3 Hydrogen isotope separation

Industrial applications of stable hydrogen isotopes, i.e. H_2 , D_2 , and T_2 , is beyond all discussion. H_2 is considered to be the most sustainable and non-pollutant energy carrier for the near future. [34–37] D_2 , among other applications in medical, pharmacological and physics research contexts, is key in neutron moderation of heavy water and as raw material in nuclear fusion reactors. [38–44] T_2 is well known for its use in nuclear power and armamentistic industry. [44–47] Obtaining pure H_2 is relatively affordable by its availability in nature but, despite increasing demand for it, D_2 is quite scarce (its natural abundance in oceans is estimated at 156 ppm) and T_2 is even rarer. [48,49] Therefore, separation of hydrogen isotopes has attracted great attention for such operations as recycling the fuel or the exhaust gases in tokamak-type fusion reactors, where the consumption of heavy isotopes of hydrogen is under 10%. [50]

Although there are several methods to separate hydrogen isotopes, including electrolysis, centrifugation, chromatography, thermal diffusion, metal hydride absorption, exchange processes, or cryogenic distillation, [51–61] all of them suffer from low separation factors, poor efficiency or high power consumption. [50,62] Even so, the most used industrial techniques for separating hydrogen isotopes are cryogenic distillation and chemical exchange. [63] The first one operates at extremely low temperature and high pressure and, although it is quite expensive in terms of energy consumption and

processing costs, it only achieves low separation factors.[52,58,63] Chemical exchange, trough the Girdler sulfide dual-temperature process, shows remarkable separation factors, but needs extremely costly catalyst and subsequent electrolysis processes, both of them diminishing the efficacy-cost ratio.[50,63]

As an alternative, membrane gas separation is in general an effective, efficient and affordable method, but conventional separation depends on differences in size, shape or thermodynamic properties. In this case, dealing with hydrogen isotopes that have almost identical properties, membrane separation seemed unsuitable. However, Beenakker *et al.*[64] proposed in the mid-nineties that the phenomenon of quantum sieving could enable separation. Quantum sieving is an effect promoting the access to the adsorption sites for the heavier isotope when the difference between the diameter of the molecules and the entrance of the pore become comparable to the de Broglie wavelength. Since then, an intensive effort has been made to find a highly selective nanoporous material to perform hydrogen isotope separation, including carbon nanotubes and sieves,[65–71] zeolites,[65,70,72–80] or MOFs.[76,81–89]

1.2 System Description and Modeling

1.2.1 Molecular Simulations

Simulated systems consist of host adsorbents, integrated by the framework atoms themselves and extra-framework cations –if present–, and guest molecules. The interaction energy between these particles is defined by a set of rules. Therefore, the systems studied could be described as thermodynamic systems composed of N particles. These particles have a microscopic behavior which must be translated to the macroscopic properties that can be measured. The techniques of statistical mechanics[90,91] provide this translation from microscopic to macroscopic world. This branch of physics is based on probability theory to perform accurate predictions on macroscopic thermodynamic properties from the analysis of position ($\boldsymbol{q}$) and momentum ($\boldsymbol{p}$) of all the N particles in the system.[92,93]

Thus, our N-particle system is described by $3N$ spatial coordinates and $3N$ velocities, which lead to a $6N$-dimensional system denominated phase space. Among all of the possible states of the phase space, so called *microstates*, a collection of them called an *ensemble* describe a particular thermodynamic state (*macrostate*). This macrostate could be characterized by several variables (Λ) whose average values remain constant (λ). The probability density of an ensemble, ρ, may be understood as the product of the probabilities allowed by the C constraints expressed by a generic conservation law

$\delta(\Lambda(\boldsymbol{q},\boldsymbol{p})-\lambda)$:

$$\rho(\boldsymbol{q},\boldsymbol{p}) = \prod_{n=1}^{C} \delta(\Lambda_n(\boldsymbol{q},\boldsymbol{p}) - \lambda_n) \tag{3}$$

Going back to phase space, changes in position–momentum pairs of all the N particles let the system evolve from an initial point $(\boldsymbol{q},\boldsymbol{p})|_0$ to a point $(\boldsymbol{q},\boldsymbol{p})|_t$. Applying Liouville's theorem

$$\int d(\boldsymbol{q},\boldsymbol{p}) = \int dp_1 dq_1 \cdots dp_N dq_N \quad , \tag{4}$$

and considering that a Hamiltonian can be built for our system and the volume of the phase space is conserved, $d(\boldsymbol{q},\boldsymbol{p})|_0 = d(\boldsymbol{q},\boldsymbol{p})|_t$, derive in Liouville's equation

$$\frac{d\rho(\boldsymbol{q},\boldsymbol{p})}{dt} = 0 \quad , \tag{5}$$

whose solution produces the probability density $\rho(\boldsymbol{q},\boldsymbol{p})|_t$, independent of time. Then, the *partition function* is defined as the number of microstates compatible with a determined macrostate:

$$Z = \int d(\boldsymbol{q},\boldsymbol{p})|_0 \, \rho(\boldsymbol{q},\boldsymbol{p})|_0 = \int d(\boldsymbol{q},\boldsymbol{p})|_t \, \rho(\boldsymbol{q},\boldsymbol{p})|_t \tag{6}$$

Although the partition function Z cannot be computed itself, the average value of a thermodynamic variable A which can also be measured experimentally, can be calculated for a statistical ensemble by

$$\langle A \rangle = \frac{1}{Z} \int d(\boldsymbol{q},\boldsymbol{p}) A(\boldsymbol{q},\boldsymbol{p}) \rho(\boldsymbol{q},\boldsymbol{p}) \quad , \tag{7}$$

which is also independent of time.

Depending on the constraints, several ensembles are defined, each one with their own statistical characteristics. The ones used in this thesis are the following:

- Canonical ensemble (NVT): It describes a closed system with only a weak exchange of heat with the surroundings. Number of particles (N), volume (V) and temperature (T) are kept constant. The probability density function and the partition function are given by

$$\begin{aligned} Z = Q(N,V,T) &= \frac{V^N}{\Lambda^{3N} N!} \int d(\boldsymbol{q},\boldsymbol{p}) e^{-\beta U(\boldsymbol{q},\boldsymbol{p})} \\ \rho(\boldsymbol{q},\boldsymbol{p}) &\propto e^{-\beta U(\boldsymbol{q},\boldsymbol{p})} \end{aligned} \tag{8}$$

being $\Lambda = \sqrt{h^2/2\pi m k_B T}$ the thermal de Broglie wavelength, k_B the Boltzmann constant, $\beta = 1/k_B T$, and $U(\boldsymbol{q},\boldsymbol{p})$ the total energy of the system.

- Grand Canonical ensemble (μVT): It describes a system in which both heat and mass could be exchanged with the surroundings, being in equilibrium with a reservoir of particles. Chemical potential (μ), volume (V) and temperature (T) are kept constant. The probability density function and the partition function are given by

$$\begin{aligned} Z = \Xi(\mu,V,T) &= \sum_{N=0}^{\infty} \frac{V^N e^{\beta\mu N}}{\Lambda^{3N} N!} \int d(\boldsymbol{q},\boldsymbol{p}) e^{-\beta U(\boldsymbol{q},\boldsymbol{p})} \\ \rho(\boldsymbol{q},\boldsymbol{p},N) &\propto \frac{V^N e^{\beta\mu N}}{\Lambda^{3N} N!} e^{-\beta U(\boldsymbol{q},\boldsymbol{p})} \end{aligned} \tag{9}$$

- Isothermal-isobaric ensemble (NPT): It describes a closed system with a variable volume. Number of particles (N), pressure (P) and temperature (T) are kept constant.

  In this ensemble, the volume of phase space does not remain fixed, so now $e^{-w(\boldsymbol{q},\boldsymbol{p})} d(\boldsymbol{q},\boldsymbol{p})|_0 = e^{-w(\boldsymbol{q},\boldsymbol{p})} d(\boldsymbol{q},\boldsymbol{p})|_t$. Consequently, calculation of partition function Z and averaged variable A is obtained in a more generic way,[94] and Equations 6 and 7 result in

$$Z = \int d(\boldsymbol{q}',\boldsymbol{p}') \sqrt{g(\boldsymbol{q}',\boldsymbol{p}')} \prod_{n=1}^{C} \delta(\Delta_n(\boldsymbol{q}',\boldsymbol{p}') - d_n) \quad , \quad \sqrt{g(\boldsymbol{q},\boldsymbol{p})} = e^{-w(\boldsymbol{q},\boldsymbol{p},t)} \tag{10}$$

$$\langle A \rangle = \frac{1}{Z} \int d(\boldsymbol{q},\boldsymbol{p}) \sqrt{g(\boldsymbol{q},\boldsymbol{p})} A(\boldsymbol{q},\boldsymbol{p}) \rho(\boldsymbol{q},\boldsymbol{p}) \tag{11}$$

  And, in the particular case of the isothermal-isobaric ensemble:

$$\begin{aligned} Z = \Delta(N,P,T) &= \frac{\beta P}{\Lambda^{3N} N!} \int dV V^{N+1} e^{-\beta P V} \left(\int d(\boldsymbol{q},\boldsymbol{p}) e^{-\beta U(\boldsymbol{q},\boldsymbol{p})} \right) \\ \rho(\boldsymbol{q},\boldsymbol{p},V) &\propto V^{N+1} e^{-\beta P V} e^{-\beta U(\boldsymbol{q},\boldsymbol{p})} \end{aligned} \tag{12}$$

Before starting to develop the details about the components and their relations, in the next subsections, a first assumption has to be made when talking about simulations:

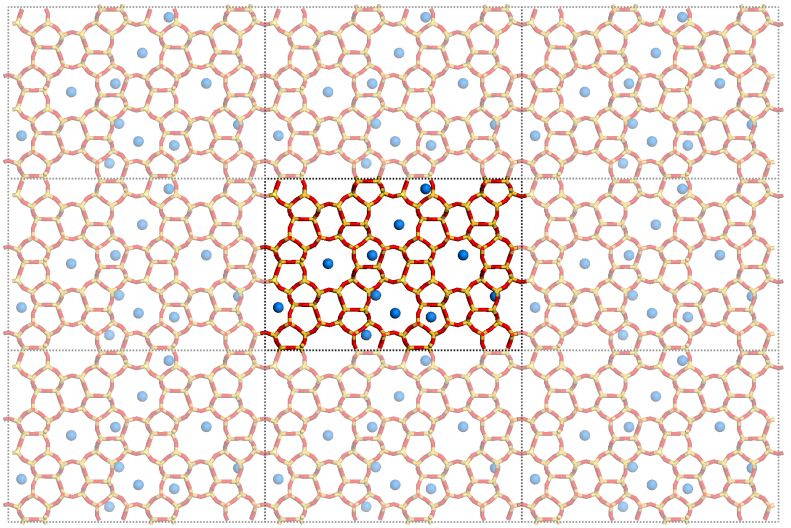

Figure 1: Schematic representation of the periodical boundary conditions. All the atoms of lattices and adsorbates interact not only with the components of the simulation box but also with their replicas (shadowed). In the example, methane molecules in MFI zeolite.

Computational resources, although incessantly increasing, are limited and it is impossible to simulate a complete (and therefore infinite) thermodynamic system. It is not even possible to get close to the thermodynamic limit, for example of the order of a mole of molecules in a large zeolite lattice. Therefore, in order to avoid surface effects on the systems and to model ideal crystal structures, periodic boundary conditions [91,95] are applied to replicate the simulation box along all the directions (Figure 1).

1.2.2 Force fields

The term *force field* summarizes the aforementioned rules used to describe and parametrize the interactions among all the parts of the modeled system. These interactions are expressed in terms of potential energy in Equation 13.

$$U(r_{ij}) = \sum_{\text{non-bonded}} U_{n-b} + \sum_{\text{bonded}} U_b \tag{13}$$

Intermolecular interactions

The non-bonded potential energies of Equation 13 account for the interactions between atoms of different guest molecules, interactions between atoms of guest

molecules and atoms of the host framework or the extra-framework cations, and for those connected atoms with three bonds of separation, at least. They can be divided in two terms: The first one corresponds to coulombic interactions and the second one to the short-range interactions composed by van der Waals interactions (Equation 14).

$$\sum_{\text{non}-\text{bonded}} U_{n-b}(r_{ij}) = U_{\text{coulombic}}(r_{ij}) + U_{\text{vdW}}(r_{ij}) \tag{14}$$

The coulombic potential is known to be a long-range interaction, only decaying with the inverse of the distance r^{-1}, where each charge interacts with all the rest of the charges. The coulombic potential energy in a periodical system, with N point charges in the fundamental simulation box (cubic with side length L), could be described by Equation 15:

$$U_{\text{coulombic}}(r_{ij}) = \frac{1}{2}\sum_{i=1}^{N} q_i \sum_{j,\boldsymbol{n}} \frac{q_j}{|r_{ij}+\boldsymbol{n}L|} \qquad , i \neq j \text{ if } \boldsymbol{n} = \mathbf{0}, \tag{15}$$

where $\boldsymbol{n}L$ calls for the replicas of the simulation box, so charge point i is also interacting with its replicas when $\boldsymbol{n} > \mathbf{0}$. This sum is hardly handled in computational systems and it is only conditionally convergent. This issue is solved by using the Ewald summation method,[96,97] which decomposes the main sum in several convergent sums in both real and Fourier transformed space.

Regarding the short-range interactions $U_{\text{vdW}}(r_{ij})$, they decay proportionally with r^{-d} $d \geq 6$, so only neighboring interacting particles contribute to the calculation of energy. The key is to correctly consider the definition of *neighbor*, since that distance is material-dependent. In zeolites, this radial distance r, known as *cutoff* distance, is usually considered to be $r = 12$ Å, from which on the van der Waals interactions are assumed to be negligible and the potential is shifted to zero.

The van der Waals interactions are here described through a Lennard-Jones potential:

$$U_{\text{vdW}}(r_{ij}) = 4\epsilon_{ij}\left[\left(\frac{\sigma_{ij}}{r_{ij}}\right)^{12} - \left(\frac{\sigma_{ij}}{r_{ij}}\right)^{6}\right] = A_{ij}r_{ij}^{-12} - B_{ij}r_{ij}^{-6} \ , \tag{16}$$

where ϵ_{ij} is the depth of the Lennard-Jones potential well, i.e. the minimum energy, σ_{ij} is the distance where attractive and repulsive forces are equal and $U_{\text{vdW}}(r_{ij}) = 0$, and r_{ij} is the distance between particles i and j.

Generic force fields usually define ϵ_{ij} and σ_{ij} for self-interactions ($i = j$), and rely on mixing rules to describe cross-interactions. Here, Lorentz-Berthelot mixing rules are used:[98]

$$\epsilon_{ij} = \sqrt{\epsilon_{ii} \cdot \epsilon_{jj}} \qquad \sigma_{ij} = \frac{\sigma_{ii} + \sigma_{jj}}{2} \tag{17}$$

Intramolecular interactions

The last term of Equation 13 refers to those interactions between 2, 3 or 4 consecutively connected atoms, and could be split up as shown in Equation 18.

$$\sum_{bonded} U_b = \sum_{bonds} U_r(r_{ij}) + \sum_{bends} U_\theta(\theta_{ijk}) + \sum_{dihedral} U_\phi(\phi_{ijkl}) \tag{18}$$

The first term corresponds to bond stretching, the energy variation produced when the distance r_{ij} between two atoms increases or diminishes. It is often described through an harmonic potential, parametrized by the bond constant, $k_{r_{ij}}$, and the equilibrium distance of atoms i and j, r^0_{ij} :

$$U_r(r_{ij}) = \frac{1}{2} k_{r_{ij}} (r_{ij} - r^0_{ij})^2 \tag{19}$$

The second term refers to bend energy to consider the energy fluctuation when the angle formed by three consecutive atoms varies. Angle bending can also be describde by using an harmonic potential,

$$U_\theta(\theta_{ijk}) = \frac{1}{2} k_{\theta_{ijk}} (\theta_{ijk} - \theta^0_{ijk})^2 \ , \tag{20}$$

where $k_{\theta_{ijk}}$ is the bend constant for the atoms i, j, and k, and θ^0_{ijk} is the equilibrium angle of these atoms.

The last term is for accounting the energy variation originated by torsional movements involving four consecutively linked atoms (i,j,k,l). The dihedral is defined by the two planes formed by (i,j,k) and (j,k,l) atoms, respectively. It is commonly expressed as:

$$U_\phi(\phi_{ijkl}) = k_{\phi_{ijkl}} [1 + \cos(n_{ijkl}\phi_{ijkl} + \delta_{ijkl})] \ , \tag{21}$$

where $k_{\phi_{ijkl}}$ is the torsion barrier, n_{ijkl} is the number of existent minimums in the range of the torsional angle, and δ_{ijkl} is a phase factor.

1.2.3 Adsorbents

Zeolites are porous crystals composed of covalently bonded TO_4 tetrahedra. Oxygen atoms occupy the vertices around a central T atom, which usually is either a silicon or an aluminum atom. These tetrahedra (Primary Building Units, PBUs) link others forming simple blocks (Secondary Building Units, SBUs) with a maximum of 16 SBUs. In turn, combined and arranged collections of SBUs define three-dimensional zeolite

topologies. Zeolite frameworks are characterized by having huge void space percentage (20% to 50%) and large superficial areas accessible to molecules. [99]

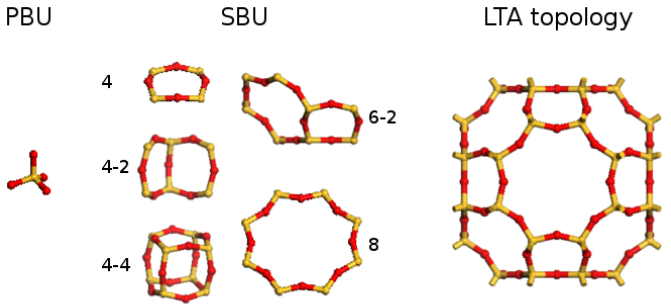

Figure 2: Schematic representation of the formation of LTA topology starting from a PBU and through its SBUs.

Although there are other options for the central T atom of the PBU (e.g. B^{3+}, Ga^{3+}, Ge^{4+}), zeolites considered in this thesis are aluminosilicates; that is, T atoms are only Si^{4+} or Al^{3+} ions. If the zeolite has a pure siliceous framework (of overall composition SiO_2), the charge of silicon and oxygen ions compensate, and the SiO_2 unit remains neutral. However, when an aluminum atom replaces a silicon atom, a negative charge is introduced in the system, which has to be counterbalanced by an extra-framework cation. This leads to the general expression to chemically define each of the zeolites in this thesis, assuming they are dehydrated,

$$\mathrm{Me}_{x/n}^{n+}[(\mathrm{AlO_2})_x(\mathrm{SiO_2})_{1-x}] \quad ,$$

where Me is the cation species, n its valence, and x the number of aluminum atoms within the framework.

Pure silica zeolites show a noticeable hydrophobic character and high thermal stability. A Si:Al ratio decreasing (Al^{3+} atoms and Me^{n+} are introduced in the system) make zeolites more hydrophilic, but at the expense of lowering the strong thermal structural resistance. These silicon by aluminum atom substitutions have to observe two well-known rules that regulate their quantity and distribution: Löwenstein's rule states that there can not be two AlO_4 consecutive tetrahedra (i.e. Al–O–Al atom chains are not allowed) while Dempsey's rule declares that the number of Al–O–Si–O–Al atom chains must be minimized. [100,101]

The properties of zeolites (high surface area, thermal stability, possibility of tailoring hydrophilic/-phobic character) enable these porous systems, formed by cavities,

channels and windows, to perform selective molecular sieving, molecular trapping, ion exchange or catalysis tasks.

To model these solids, lattices are considered rigid, i.e. atoms of the framework keep their crystallographic positions fixed during the whole simulation. This is due to the nature of zeolites, which usually show small structural deformations and, when so, flexibility of zeolite lattices are reported to have minor or negligible effects on either adsorption or diffusion when molecules are smaller than the diameter of the windows.[102–104] Therefore, except for some simulations in Chapter 6, intramolecular forces between framework atoms are neglected. On the other hand, electrostatic interactions are modeled by considering the atoms of the frameworks as point partial charges.[105] This has special relevance when Al atoms are present in the lattice because of the different charge of oxygen atoms when bridging two silicon atoms or when bridging one silicon and one aluminum atom, according to the approximation of Jaramillo and Auerbach.[106] Van der Waals interactions with adsorbates or extra-framework cations are defined by specific Lennard-Jones cross-interaction parameters. Extra-framework cations are modeled as point charges allowed to move through the framework ruled by the defined potentials. Due to their strong electrostatic interactions, no van der Waals interactions are taken into account between cations, but, like framework atoms, specific Lennard-Jones cross-interaction parameters are used to model cation-adsorbate relations.

1.2.4 Adsorbates

All the molecules with a relevant role in this thesis have a marked industrial interest. Whether their availability for industrial applications could be enhanced by a selective separation or, on the contrary, to trap and mitigate them. A complete list of the molecules considered follows, specifying their main characteristics of their model.

- CO_2 : Rigid three-sites model with partial charges and Lennard-Jones interacting centers on each one of the pseudoatoms.[105]

- CH_4 : United atom model with a single uncharged Lennard-Jones interaction center.[107,108]

- CO: Rigid three-sites model (carbon–*dummy*–oxygen). Carbon and oxygen pseudoatoms have partial negative charges and Lennard-Jones interaction centers, while the *dummy* interaction center only has a positive charge.[109]

- N_2 : Rigid and linear three-sites model with negative partial charges on nitrogen atoms and a positive charge on the central *dummy* interaction center. Only nitrogen pseudoatoms have Lennard-Jones interaction centers. [110]
- H_2 : United atom model with a single uncharged Lennard-Jones interaction center. [111]
- D_2 : United atom model with a single uncharged Lennard-Jones interaction center. Model derived from H_2 [111], as reported in Chapter 4.
- T_2 : United atom model with a single uncharged Lennard-Jones interaction center. Model derived from H_2 [111], as reported in Chapter 4.
- H_2O : Rigid five-sites model in a tetrahedral configuration (TIP5P/Ew). [112] A single Lennard-Jones interaction center is located at the oxygen pseudoatom, while its charge is distributed in two *dummy* pseudoatoms. Hydrogen pseudoatoms are only point charges.

All the Lennard-Jones interactions, both self- and cross-, are described by Equation 16, except for H_2 , D_2 , and T_2 molecules. Due to their nature and the conditions of the simulations in which they take part, quantum corrections, via the Feynman-Hibbs correction, [113] has been added to their intermolecular short-range interactions, as is detailed in Chapter 4.

1.3 Simulation Methods

1.3.1 Monte Carlo

This numerical statistical method is used to test all the microstates to obtain an estimation of a thermodynamic variable (Equations 7 and 11). To achieve it, Monte Carlo (MC) method has to face the existence of an enormous number of microstates. Additionally, due to the microstates have to meet the macroscopic conservation laws imposed, the most of them have no or negligible probability. [91] In order to deal with these problems, MC method makes use of random numbers and probability theory to explore the phase space by an statistical weighted sampling. In particular, the Markov Chain Monte Carlo (MCMC) method, based on previous Metropolis algorithm, [114] generates compatible configurations with an *a priori* weight proportional to the Boltzmann constant.

The MCMC method consist in purpose random trial moves from the current state (o) to a new one (n). Then, an evaluation on the acceptance or rejection of the transition

to the new state is done on the basis of their energies and the inclusion of a random number. Lets define the following probabilities: $\pi_{eq}(o)$ and $\pi_{eq}(n)$ are those of being the system in the states o or n, respectively; $\alpha(o \rightarrow n)$ and $\alpha(n \rightarrow o)$ are the conditional probabilities of performing the move $o \rightarrow n$ or $n \rightarrow o$, respectively; and $\pi_{acc}(o \rightarrow n)$ and $\pi_{acc}(n \rightarrow o)$ the probabilities of acceptance of the respective trial movements. To keep the underlying system equilibrium, the detailed balance condition is applied: [91,115]

$$\pi(o)\,\alpha(o \rightarrow n)\,\pi_{acc}(o \rightarrow n) = \pi(n)\,\alpha(n \rightarrow o)\,\pi_{acc}(n \rightarrow o) \tag{22}$$

Metropolis *et al.* [114] assumed that reciprocal state changes ($o \rightarrow n$ and $n \rightarrow o$) are equally *a priori* probable to happen

$$\alpha(o \rightarrow n) = \alpha(n \rightarrow o) \tag{23}$$

so the acceptance rule results in

$$\pi_{acc}(o \rightarrow n) = min\left(1, \frac{\pi(n)}{\pi(o)}\right) \tag{24}$$

where it is worth to remember that each statistical ensemble have a particular ρ probability distribution (Equations 8 , 9, 12). These probability distributions can be generically described as function of the energy of the state weighted by the Boltzmann factor $\rho(s) = f[U(s)]exp[-\beta U(s)]$ $s \in [o,n]$, and then the acceptance criteria is given by

$$\pi_{acc}(o \rightarrow n) = min\left(1, \frac{f[U(n)]}{f[U(o)]} e^{-\beta[U(n)-U(o)]}\right) = min\left(1, \frac{f[U(n)]}{f[U(o)]} e^{-\beta \Delta U}\right) \tag{25}$$

The following basic trial movements that give origin to the change of state $o \rightarrow n$ according to their acceptance probability:

- Translation

  The molecule is displaced in a random direction with an acceptance probability given by

  $$\pi_{acc}\left(\vec{r}^{\,N}_{o} \rightarrow \vec{r}^{\,N}_{n}\right) = min\left(1, e^{-\beta[(\vec{r}^{\,N}_{n}) - U(\vec{r}^{\,N}_{o})]}\right) \tag{26}$$

- Rotation

  The molecule is rotated randomly around its center of mass with probability given by the same expression than for translation movement (Equation 26).

- Insertion

  A molecule is introduced in the system at a random position with a probability of acceptance

$$\pi_{acc}(N \rightarrow N+1) = min\left(1, \frac{W^{N+1}\beta V}{N+1}\frac{\phi_p}{\langle W^{ig}\rangle}\right) \tag{27}$$

where W is the Rosenbluth factor of the molecule, a weight factor based on the conformational energy due to the shape of the molecule,[116–118] being W^{N+1} and W^{ig} those of the molecule to be inserted and of the ideal gas molecule, respectively. ϕ_p is the fugacity coefficient related and p refers to the pressure of the reservoir from which the molecule is inserted.

- Deletion

  The selected molecule is removed with a probability

$$\pi_{acc}(N \rightarrow N-1) = min\left(1, \frac{N}{W^{N-1}\beta V}\frac{\langle W^{ig}\rangle}{\phi_p}\right) \tag{28}$$

From the previous basic trial movements, other more complexes moves can be defined as a combination of those, like swapping one molecule by other of the same species, in order to improve the computational efficiency on evaluating the acceptance probability and enhance the velocity of calculus. Likewise, there are specific trial moves for mixtures of different kind of molecules, as interchanging the position of two molecules of different species, so called *identity change*.[91,95,119]

1.3.2 Molecular Dynamics

Molecular Dynamics (MD) simulations rely on the simultaneous application of Newton's laws of motion to all the particles of the system and their evaluation at increasing time. Particles with mass are initially described by their positions and velocities. Then, a field of forces is calculated for each particle from the rest of particles. Due to the effect of these forces, velocity is recalculated for any particle in the system and their positions updated. This cycle is iteratively repeated at time-increasing slots, describing the trajectories of the particles. From the succession of states, dynamical properties can be extracted, whereas equilibrium properties are obtained by averaging over the states.

To describe the evolution of the system, the velocity-Verlet algorithm is used to integrate the equations of motion according to the following expressions:[91]

$$\vec{r}_i(t+\Delta t) = \vec{r}_i(t) + \vec{v}_i(t)\Delta t + \frac{\vec{f}_i(t)}{2m_i}\Delta t^2 + O(\Delta t^4) \tag{29}$$

$$\vec{v}_i(t+\Delta t) = \vec{v}_i(t) + \frac{\vec{f}_i(t) + \vec{f}_i(t+\Delta t)}{2m_i}\Delta t + O(\Delta t^2) \tag{30}$$

where $\vec{r}_i(t)$, $\vec{v}_i(t)$ and $\vec{f}_i(t)$ are the position, velocity and force vectors of particle i at time t, m_i its mass, and Δt is the time step between samples.

This method has relevant advantages in terms of simplicity of implementation, producing rather small errors in position calculus and being time-reversible (as Newton's laws). However, these equations are numerically integrated, so there could be an unphysical energy drift produced by integrating a large number of steps or by choosing a large time step. It is possible to check if this drift is happening after M steps and a maximum deviation condition (δ) is usually required to accept the integration results

$$\frac{1}{M}\sum_{i=1}^{M}\left|\frac{E(0)-E(i\Delta t)}{E(0)}\right| < \delta \tag{31}$$

When a MD simulation starts, positions of particles are assigned by an MC simulation to get plausible starting conditions. Then, velocities are assigned to the particles from the Maxwell-Boltzmann distribution, which makes mandatory to allow the system to relax, setting the total momentum of the system to zero and considering that there is no external force acting on the system. During the equilibration of the system, ensemble averages are not computed. After that, the ergodicity hypothesis postulates that phase state averages, which could be obtained from time averages following Equation 32, is equal to ensemble averages (Equations 7 or 11).

$$\langle A \rangle = \lim_{t\to\infty}\int A\left(\vec{r}^{\,N}, t\right)dt \tag{32}$$

In this thesis, MD simulations have been performed in the Canonical ensemble, so the Nosé-Hoover chain method [120–123] was employed to keep the temperature stable and maintain the simulation within this ensemble.

1.3.3 Ideal Adsorbed Solution Theory

The Ideal Adsorbed Solution Theory (IAST) [124] is a not a simulation method but a thermodynamic approach to predict gas mixture adsorption behavior from pure-component adsorption isotherms, overcoming their implemented models for physical adsorption.This theory was formulated assuming three main requirements: All adsorbates in the mixture can access equally the whole area of the adsorbent; the adsorbent is homogeneous; and the interactions on the adsorbed phase have equivalent strengths. However, first two conditions have actually found to be not so restrictive. [125,126]

If an adsorbed phase is considered, with a constant temperature, the spreading pressures of the component must be the same and could be calculated by

$$\pi = \frac{RT}{A}\int_0^{p_i^0}\frac{n_i}{P_i}dP_i \tag{33}$$

where π is the spreading pressure, n_i the pure component i equilibrium adsorbed amount, P_i the partial pressure , $p_i^0(\pi)$ the partial pressure of the pure component calculated at (π, T) conditions of the mixture, and A is the surface area of the adsorbent. Partial pressure of components are calculated by applying the analogue of Raoult's law

$$P_i = y_i P = p_i^0(\pi)x_i\Big|_{T,\pi const} \ , \tag{34}$$

being x_i the mole fraction of component i of the mixture in the adsorbed phase.

Then, the total adsorbed amount n_T is calculated from the component loadings stated in the pure-component adsorption isotherms

$$\frac{1}{n_T} = \sum_{i=1}^{K}\frac{x_i}{n_i^0} \tag{35}$$

where K is the number of components of the mixture and n_i^0 the standard amount of component i at constant (π, T) calculated with no other components presence.

Usually, IAST cannot be solved analytically and numerical solutions are required. [127,128] Pure component adsorption isotherms used by IAST should be fitted previously, existing several models proposed. Choosing one or another depends on the type or shape of the pure component isotherm. The following models have been tested or used in this thesis: Langmuir, [129] Toth, [130] Jensen, [131] and Langmuir-Freundlich dual site. [132]

1.4 Computed Properties

Adsorption Loading

The amount of adsorbed molecules is computed through MC simulations in the grand canonical ensemble, so the chemical potential μ, volume of the system V, and temperature T are kept fixed (see section 1.2.1), but the number of molecules may vary in the course of the simulation. The addition or removal of molecules should be done without perturbing the equilibrium conditions of the simulated system so the reservoir has to have the same chemical potential and temperature as the simulated system.

Pressure (p) is related to fugacity (f) through the fugacity coefficient (ϕ), $f = \phi p$, and fugacity is used, in turn, to calculate the chemical potential μ

$$\mu(T,p) = \mu^0 + RT\ln(f/p^0) \tag{36}$$

where μ^0 and p^0 is the standard chemical potential and pressure, respectively, and R the ideal gas constant. Therefore, adsorption loading could be easily expressed versus the pressure to draw an adsorption isotherm.

Henry coefficients and isosteric heat of adsorption

The Widom test-particle method[133,134] is a MC method in which a unique *ghost* molecule is inserted and removed time after time during the simulation in the canonical ensemble. It is for this reason that this particular case is also known as $(N-1,V,T)$ ensemble. While the molecule is inside the framework, its interactions with the structure are measured and its Rosenbluth factor calculated, before being removed again. Therefore, the collected information refers to the way that an adsorbed molecule interacts with an adsorbent.

In particular, Henry coefficients (K_H) are directly related with the excess free energy of the adsorbed molecule (ΔF),[91] being possible to calculate from the Rosenbluth factors

$$K_H = \frac{1}{RT\rho}\frac{\langle W\rangle}{\langle W^{ig}\rangle} \tag{37}$$

where R is the ideal gas constant, ρ is the density of the framework, T is the temperature, and $\langle W\rangle$ and $\langle W^{ig}\rangle$ the average Rosenbluth factors of the molecule in the host and in the ideal gas, respectively.

The isosteric heat of adsorption (Q_{st}), or alternately the enthalpy of adsorption (ΔH), also provides information about how a molecule is adsorbed at infinite dilution. It is obtained from the average energies of the system, accounting for the potential energies of the host-guest system (U_{hg}), the host (U_h), and the guest (U_g)

$$-Q_{st} = \Delta H = \Delta U - RT = \langle U_{hg}\rangle - \langle U_h\rangle - \langle U_g\rangle - RT \tag{38}$$

To obtain $\langle U_g\rangle$, an independent simulation is needed in order to calculate the potential energy of the molecule in the reservoir.

Self-diffusion coefficients

Self-diffusion coefficients D provide a measure of the mobility of molecules through the structures. Note that D does not refer to collective diffusion and, therefore, neither to mass transport. From now on, self-diffusion coefficients will be named diffusion coefficients for short. To obtain the dynamical behavior of particles MD simulations

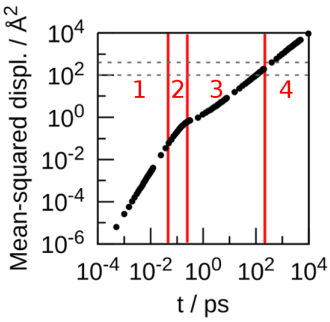

Figure 3: Mean-squared displacement of methane in MFI zeolite. Diffusive regimes are delimited by red lines.

---

are carried out in the canonical ensemble (see section 1.3.2 and 1.2.1). Diffusion coefficients in the direction $\alpha = x, y, z$ can be calculated from the slope of the mean-squared displacement at long times

$$D_\alpha = \frac{1}{2N} \lim_{t\to\infty} \frac{d}{dt} \left\langle \sum_{i=1}^{N} (r_{i\alpha}(t) - r_{i\alpha}(0))^2 \right\rangle \tag{39}$$

where N is the number of molecules, t is the time, and $r_{i\alpha}$ the α-component of the center-of-mass of the molecule i.

From the directional components, the directionally averaged diffusion coefficient is given by

$$D = \frac{D^x + D^y + D^z}{3} \tag{40}$$

The aforementioned requirement that D must be calculated at long times originates from the nature of the molecular diffusion in a confined system, simulated in a cage of side λ, in which it is possible to distinguish four regimes (Figure 3):[135]

1. For very short times (shorter than the typical time between collisions), the motion of molecules is ballistic and the mean-squared displacement proportional to t^2.

2. A time interval follows where some of the particles bounce back or towards other directions as collisions get increasingly probable. It ends when molecules suffer multiple collisions.

3. Then a confinement regime is reached, when the molecules, on average, have not yet hopped to the next cavity or pore. Mean-squared displacement of molecules is below the square of the half cell length.

4. At longer times, molecules are diffusing on average through the pores of the structure, and interacting with those molecules of other cages which are, in turn, also moving through the structure. This is the diffusive regime, where mean-squared displacement behaves linearly and the diffusion coefficients are calculated.

Energy profiles

A free energy profile is defined as a mapping of the free energy of a molecule from one adsorption point to a second one. It has traditionally been defined for reaction coordinates q, which is a function of Cartesian coordinates, in a chemical reaction, but can be applied to a route through the lattice. In other words, it provides an idea of how much it would take to move a molecule between these points, following a determined path, in terms of Helmholtz free energy (Figure 4). This is done by carrying out a MC simulation in the canonical ensemble (see section 1.2.1), using the Widom test-particle method,[133] and computing the probability of finding the molecule at a particular point of the reaction coordinate q.[135–137] The volume to sample could be restrained by a parallelepiped or cylinder whose longitudinal axis coincides with the reaction coordinate q. To achieve an accurate profile, the mapping should meet the following criteria:[135,138]

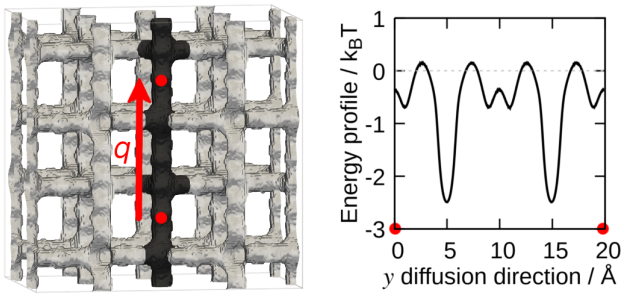

Figure 4: Left: Surface energy of MFI zeolite. A straight channel is shadowed and the red arrow indicates the sampled route characterized by a coordinate q. Right: Energy profile of one molecule of methane in zeolite MFI along the diffusion direction y (coincident with q). Deepest energy wells coincide with straight and zigzag channel intersections.

- Every coordinate sampled in the defined volume must correspond to a unique position in the simulation cage.
- Cartesian space should be divided into equivalent regions to obtain a correct entropic contribution.
- The mapping should go through a saddle point, the transition state.

1.5 Outline of the Thesis

Zeolites are known for their suitability as molecular sieves. Actually, they are already firmly settled in industry to selectively separate gases or capture them. In this thesis, the processes selected share the objective of contributing to make more competitive or enhance alternative processes to those based on carbon technology. These processes have been approached from a computational point of view. Molecular simulations have been carried out to gain molecular insight on gas mixtures separation processes at the same time as obtaining valuable information to suggest operational schemes to perform these separations. Additionally, some specific underlying molecular phenomena have been tackled to study supplementary aspects, not centered on particular industrial processes but relevant to understand the behavior of adsorbed molecules in separation procedures. Therefore, two blocks can be differentiated in this thesis:

Gas mixture separations for industrial processes

- *Chapter 2*
  An operating procedure is proposed to separate the components of a tail gas expelled from a Fischer-Tropsch process. The quinary gas mixture is composed of light gases, *i.e.* CO_2 , CO, CH_4 , N_2 , and H_2 in a typical, described composition. The Fischer-Tropsch process is a key step in a global gas-to-liquid process to synthesize hydrocarbons. The separation procedure has a twofold goal: upstream reintroduction of the captured CH_4 and CO and trapping of CO_2 to avoid its emission.

  To that end, the performance in the described separation is assessed for four zeolites of high industrial impact (DDR, FAU, MFI, and MOR), with main focus on the effect of location and amount of aluminum atoms in the zeolite lattices. The decision on the final scheme is based on the combination of computed adsorption isotherms, selectivity and diffusion coefficients. In addition, applicability and accuracy of IAST is studied in these adsorbate–adsobent systems.

- *Chapter 3*
  A large multi-scale computational study is performed to achieve a selective separation of a mixture of CO_2 , CO, and O_2 gases. The separation takes place in the context of the nonthermal plasma-assisted CO_2 dissociation process, involved in a process scheme aiming at the production of fuels with neutral carbon footprint. The proposed route requires an additional step to obtain pure CO from the mixture and avoid a high CO_2 recombination.

  A widespread screening on 174 zeolites, evaluating selectivity at low coverage and successive adsorption simulations at molecular level for specific structures, combined with IAST, provides a scheme to perform the separation under mild operation conditions. Then PSA simulations are carried out to find the optimal parameters to achieve the desired separation at a pilot-plant scale.

- *Chapter 4*
  Deuterium and tritium from hydrogen separations are studied over a wide range of pressures and low and cryogenic temperatures. Due to the nature of the adsorbates and operation conditions, quantum corrections are considered. Models for the deuterium and tritium molecules are proposed, derived from the hydrogen model previously reported. Experimental adsorption isotherms for H_2 and D_2 respectively check and validate the models for such molecules in pure silica zeolites. Then, a study on the adsorption selectivity at infinite dilution is done on 210 pure silica zeolites, and subsequent diffusion and adsorption simulations are performed over a range of pressures and temperatures for the most promising zeolites. Three zeolites, BCT, AVL, and MVY, are identified as the best candidates to perform a separation of a 1:1 D_2/H_2 mixture. One of them, BCT topology, is found to show, at low temperature, the highest adsorption selectivity reported to the best of our knowledge. The same structure is also found to obtain an extremely high selectivity for a 1:1 T_2/H_2 mixture.

Molecular insights on additional aspects for molecular separation

- *Chapter 5*
  A study on the effect of cations on diffusion of CO_2 and CH_4 molecules in MFI zeolite is carried out. The industrial relevance of both molecules and of the zeolite framework is beyond all discussion. Theoretical aluminum distributions are generated considering the 12 T crystallographic positions of framework MFI. Monovalent and divalent counterbalancing cations are considered to neutralize the negative charge introduced in the system by the aluminum atoms.

Probability density of cations and energy profiles for the adsorbates, both depending on aluminum distributions, are evaluated together to produce a prediction on the behavior of adsorbates and cations, which is found to be consistent with subsequent diffusion simulations. All the results shed light on why zeolites with the same chemical composition have different dynamical behaviors.

- *Chapter 6*
  Understanding the role of water in LTA zeolite is key due to the use of this topology in water removal and dehydration processes. The wide range of aluminum substitutions available experimentally for this topology, from the pure siliceous lattice up to the theoretical maximum of Si:Al=1, means the degree of hydrophobicity or hydrophilicity of the zeolite can be tailored. In the theoretical study, besides considering different Si:Al ratios, two lattices are examined for each one, keeping the crystallographic positions fixed after substitutions and allowing the lattice to relax. Adsorption isotherms in fixed and energy-minimized lattices and a thorough analysis of the location of water molecules reveals that: adsorption sites are determined by the hydrophilicity of the lattice. The more hydrophilic, the bigger the lattice, which reinforces the ability of the structure to adsorb in the narrow pores. The pressure is found to affect strongly the preference for large or narrow pores. A case is identified, in which at increasing pressures or loading narrow pores are first populated, then emptied as the large pores fill, and then finally populated again.

Bibliography

[1] Cronstedt, A. *Svenska Vetenskaps Akademiens Handlingar Stockholm* **1756**, *17*, 120.
[2] Baerlocher, C.; McCusker, L. Database of Zeolite Structures. `http://www.iza-structure.org/databases/`.
[3] Kuznetsova, E. D.; Blatova, O. A.; Blatov, V. A. *Chemistry of Materials* **2018**, *30*, 2829–2837.
[4] Fischer, F.; Tropsch, H. *Brennstoff-Chemie* **1923**, 276–285.
[5] Fischer, F.; Tropsch, H. *German patent 484337* **1925**,
[6] Wang, X.; Economides, M. In *Advanced Natural Gas Engineering*; Wang, X., Economides, M., Eds.; Gulf Publishing Company, 2009; pp 243 – 287.
[7] Suppes, G. J., Storvick, T. S., Eds. *Sustainable Nuclear Power*; Sustainable World; Academic Press: Burlington, 2007; pp 75 – 117.
[8] Naik, S.; Goud, V. V.; Rout, P. K.; Dalai, A. K. *Renewable and Sustainable Energy Reviews* **2010**, *14*, 578 – 597.
[9] Basu, P. In *Biomass Gasification and Pyrolysis*; Basu, P., Ed.; Academic Press: Boston, 2010; pp 301 – 323.
[10] Beneroso, D.; Bermúdez, J.; Montes-Morán, M.; Arenillas, A.; Menéndez, J. *Bioresource technology* **2016**, *218*, 687–691.
[11] Suppes, G. J.; Storvick, T. S. In *Sustainable Power Technologies and Infrastructure*; Suppes, G. J., Storvick, T. S., Eds.; Academic Press: Boston, 2016; pp 75 – 119.
[12] Sie, S.; Senden, M.; Van Wechem, H. *Catalysis Today* **1991**, *8*, 371–394.
[13] Watts, P.; Fabricius, N. 2003; `http://www.shell.com/static/qatar/downloads/nfabricius_speech.pdf`.
[14] Böhringer, W.; Kotsiopoulos, A.; de Boer, M.; Knottenbelt, C.; Fletcher, J. In *Fischer-Tropsch Synthesis, Catalyst and Catalysis*; Davis, B., Occelli, M., Eds.; Studies in Surface Science and Catalysis; Elsevier, 2007; Vol. 163; pp 345 – 365.

[15] van Steen, E.; Claeys, M. *Chemical Engineering & Technology: Industrial Chemistry-Plant Equipment-Process Engineering-Biotechnology* **2008**, *31*, 655–666.
[16] Probstein, R. F.; Hicks, R. E. *Synthetic fuels*; Courier Corporation, 2006.
[17] Choudhury, H. A.; Chakma, S.; Moholkar, V. S. *Recent advances in thermo-chemical conversion of biomass*; Elsevier, 2015; pp 383–435.
[18] Wood, D. A.; Nwaoha, C.; Towler, B. F. *Journal of Natural Gas Science and Engineering* **2012**, *9*, 196 – 208.
[19] U.S. Environmental Protection Agency, Global Greenhouse Gas Emissions. `https://www.epa.gov/ghgemissions/global-greenhouse-gas-emissions-data`.
[20] Le Quéré, C. et al. *Earth System Science Data* **2016**, *8*, 605–649.
[21] Jackson, R. B.; Canadell, J. G.; Le Quere, C.; Andrew, R. M.; Korsbakken, J. I.; Peters, G. P.; Nakicenovic, N. *Nature Climate Change* **2016**, *6*, 7–10.
[22] Edenhofer, O. *Climate change 2014: mitigation of climate change*; Cambridge University Press, 2015; Vol. 3.
[23] Olah, G. A.; Goeppert, A.; Prakash, G. S. *The Journal of organic chemistry* **2008**, *74*, 487–498.
[24] Centi, G.; Quadrelli, E. A.; Perathoner, S. *Energy & Environmental Science* **2013**, *6*, 1711–1731.
[25] Lebouvier, A.; Iwarere, S. A.; d'Argenlieu, P.; Ramjugernath, D.; Fulcheri, L. *Energy & Fuels* **2013**, *27*, 2712–2722.
[26] Brehmer, F.; Welzel, S.; van de Sanden, M. C. M.; Engeln, R. *Journal of Applied Physics* **2014**, *116*, 123303.
[27] Goede, Adelbert P.H.,; Bongers, Waldo A.,; Graswinckel, Martijn F.,; van de Sanden, Richard M.C.M,; Leins, Martina,; Kopecki, Jochen,; Schulz, Andreas,; Walker, Mathias, *EPJ Web of Conferences* **2014**, *79*, 01005.
[28] Van Rooij, G.; van den Bekerom, D.; den Harder, N.; Minea, T.; Berden, G.; Bongers, W.; Engeln, R.; Graswinckel, M.; Zoethout, E.; van de Sanden, M. *Faraday discussions* **2015**, *183*, 233–248.
[29] Fridman, A. *Plasma chemistry*; Cambridge university press, 2008.
[30] Capezzuto, P.; Cramarossa, F.; D'Agostino, R.; Molinari, E. *The Journal of Physical Chemistry* **1976**, *80*, 882–888.
[31] Rusanov, V.; Fridman, A.; Sholin, G. *Soviet Physics Uspekhi* **1981**, *24*, 447.
[32] Eletskii, A.; Smirnov, B. *Pure and Applied Chemistry* **1985**, *57*, 1235–1244.
[33] Fridman, A. A.; Rusanov, V. D. *Pure Appl Chem* **1994**, *66*, 1267–1278.
[34] Li, J.-R.; Kuppler, R. J.; Zhou, H.-C. *Chem. Soc. Rev.* **2009**, *38*, 1477–1504.
[35] Demirocak, D. E. *Hydrogen storage technologies*; Nanostructured Materials for Next-Generation Energy Storage and Conversion: Hydrogen Production, Storage, and Utilization; 2017; pp 117–142.
[36] Abdalla, A. M.; Hossain, S.; Nisfindy, O. B.; Azad, A. T.; Dawood, M.; Azad, A. K. *Energy Conversion and Management* **2018**, *165*, 602–627.
[37] Aasadnia, M.; Mehrpooya, M. *Applied Energy* **2018**, *212*, 57–83.
[38] others„ et al. *science* **2002**, *298*, 981–987.
[39] Armaroli, N.; Balzani, V. *Angewandte Chemie International Edition* **2007**, *46*, 52–66.
[40] Keppler, F.; Hamilton, J. T.; McRoberts, W. C.; Vigano, I.; Braß, M.; Röckmann, T. *New Phytologist* **2008**, *178*, 808–814.
[41] others„ et al. *Journal of environmental radioactivity* **2008**, *99*, 1596–1610.
[42] Daillant, J. *Soft Matter at Aqueous Interfaces*; Springer, 2016; pp 413–444.
[43] Pozzi, S. A.; Pázsit, I. *Nuclear science and engineering* **2006**, *154*, 367–373.
[44] Stacey, W. M. *Nuclear reactor physics*; Wiley Online Library, 2007; Vol. 2.
[45] Bergeron, K. D. Tritium on ice: The dangerous new alliance of nuclear weapons and nuclear power. 2003.
[46] Okada, S.; Momoshima, N. *Health physics* **1993**, *65*, 595–609.
[47] Voss, D. *Physics World* **1990**, *3*, 10.
[48] Greenwood, N.; Earnshaw, A. *Chemistry of the Elements 2nd Edition*; Butterworth-Heinemann, 1997.
[49] Meija, J.; Coplen, T. B.; Berglund, M.; Brand, W. A.; De Bièvre, P.; Gröning, M.; Holden, N. E.; Irrgeher, J.; Loss, R. D.; Walczyk, T.; Prohaska, T. *Pure Appl. Chem.* **2016**, *88*, 293–306.
[50] Cai, J.; Xing, Y.; Zhao, X. *RSC Advances* **2012**, *2*, 8579–8586.
[51] Bernhardt, A. F. *Applied physics* **1976**, *9*, 19–34.
[52] Rae, H. K. *Separation of hydrogen isotopes*; 1978.
[53] Alekseev, I.; Bondarenko, S.; Fedorchenko, O.; Vasyanina, T.; Konoplev, K.; Arkhipov, E.; Voronina, T.; Grushko, A.; Tchijov, A.; Uborsky, V. *Fusion engineering and design* **2003**, *69*, 33–37.
[54] Degtyareva, O.; Bondareva, L. *Journal of Analytical Chemistry* **2004**, *59*, 442–446.
[55] Lueders, T.; Manefield, M.; Friedrich, M. W. *Environmental Microbiology* **2004**, *6*, 73–78.
[56] Lis, G.; Wassenaar, L.; Hendry, M. *Analytical chemistry* **2008**, *80*, 287–293.
[57] Richter, F. M.; Watson, E. B.; Mendybaev, R.; Dauphas, N.; Georg, B.; Watkins, J.; Valley, J. *Geochimica et Cosmochimica Acta* **2009**, *73*, 4250–4263.

[58] Kowalczyk, P.; Gauden, P. A.; Terzyk, A. P.; Furmaniak, S. *Journal of Physics: Condensed Matter* **2009**, *21*, 144210.
[59] Leardini, F.; Ares, J.; Fernández, J.; Bodega, J.; Sánchez, C. *International Journal of Hydrogen Energy* **2011**, *36*, 8351–8357.
[60] Hu, S.; Hou, J.; Xiong, L.; Weng, K.; Yang, T.; Luo, Y. *Separation and purification technology* **2011**, *77*, 214–219.
[61] James, S. C.; Hamilton, J.; Wolfer, W. G. *Chemical engineering science* **2012**, *68*, 250–257.
[62] Wang, Y.; Zhao, D. *Crystal Growth & Design* **2017**, *17*, 2291–2308.
[63] Oh, H.; Hirscher, M. *European Journal of Inorganic Chemistry* **2016**, *2016*, 4278–4289.
[64] Beenakker, J.; Borman, V.; Krylov, S. Y. *Chem. Phys. Lett.* **1995**, *232*, 379–382.
[65] Wang, Q.; Challa, S. R.; Sholl, D. S.; Johnson, J. K. *Phys. Rev. Lett.* **1999**, *82*, 956–959.
[66] Dresselhaus, M.; Williams, K.; Eklund, P. *MRS Bull.* **1999**, *24*, 45–50.
[67] Challa, S. R.; Sholl, D. S.; Johnson, J. K. *J. Chem. Phys.* **2002**, *116*, 814–824.
[68] Tanaka, H.; Kanoh, H.; Yudasaka, M.; Iijima, S.; Kaneko, K. *J. Am. Chem. Soc.* **2005**, *127*, 7511–7516.
[69] Kowalczyk, P.; Gauden, P. A.; Terzyk, A. P. *J Phys Chem B* **2008**, *112*, 8275–8284.
[70] Niimura, S.; Fujimori, T.; Minami, D.; Hattori, Y.; Abrams, L.; Corbin, D.; Hata, K.; Kaneko, K. *J. Am. Chem. Soc.* **2012**, *134*, 18483–18486.
[71] Xing, Y.; Cai, J.; Li, L.; Yang, M.; Zhao, X. *Physical Chemistry Chemical Physics* **2014**, *16*, 15800–15805.
[72] Kumar, A. A.; Jobic, H.; Bhatia, S. K. *J. Phys. Chem. B* **2006**, *110*, 16666–16671.
[73] Pantatosaki, E.; Papadopoulos, G. K.; Jobic, H.; Theodorou, D. N. *The Journal of Physical Chemistry B* **2008**, *112*, 11708–11715.
[74] Chu, X.-Z.; Cheng, Z.-P.; Xiang, X.-X.; Xu, J.-M.; Zhao, Y.-J.; Zhang, W.-G.; Lv, J.-S.; Zhou, Y.-P.; Zhou, L.; Moon, D.-K.; Lee, C.-H. *Int. J. Hydrogen Energy* **2014**, *39*, 4437–4446.
[75] Kowalczyk, P.; Terzyk, A. P.; Gauden, P. A.; Furmaniak, S.; Pantatosaki, E.; Papadopoulos, G. K. *J. Phys. Chem. C* **2015**, *119*, 15373–15380.
[76] Friebe, S.; Wang, N.; Diestel, L.; Liu, Y.; Schulz, A.; Mundstock, A.; Caro, J. *Microporous Mesoporous Mater.* **2015**, *216*, 127–132.
[77] Physick, A. J.; Wales, D. J.; Owens, S. H.; Shang, J.; Webley, P. A.; Mays, T. J.; Ting, V. P. *Chem. Eng. J.* **2016**, *288*, 161–168.
[78] Salazar, J.; Lectez, S.; Gauvin, C.; Macaud, M.; Bellat, J.; Weber, G.; Bezverkhyy, I.; Simon, J. *Int. J. Hydrogen Energy* **2017**, *42*, 13099–13110.
[79] Xiong, R.; Xicohténcatl, R. B.; Zhang, L.; Li, P.; Yao, Y.; Sang, G.; Chen, C.; Tang, T.; Luo, D.; Hirscher, M. *Microporous and Mesoporous Materials* **2018**, *264*, 22–27.
[80] Giraudet, M.; Bezverkhyy, I.; Weber, G.; Dirand, C.; Macaud, M.; Bellat, J.-P. *Microporous and Mesoporous Materials* **2018**, *270*, 211–219.
[81] Pantatosaki, E.; Jobic, H.; Kolokolov, D. I.; Karmakar, S.; Biniwale, R.; Papadopoulos, G. K. *J. Chem. Phys.* **2013**, *138*, 034706.
[82] FitzGerald, S. A.; Pierce, C. J.; Rowsell, J. L.; Bloch, E. D.; Mason, J. A. *J. Am. Chem. Soc.* **2013**, *135*, 9458–9464.
[83] Teufel, J.; Oh, H.; Hirscher, M.; Wahiduzzaman, M.; Zhechkov, L.; Kuc, A.; Heine, T.; Denysenko, D.; Volkmer, D. *Advanced Materials* **2013**, *25*, 635–639.
[84] Oh, H.; Savchenko, I.; Mavrandonakis, A.; Heine, T.; Hirscher, M. *ACS Nano* **2014**, *8*, 761–770.
[85] Weinrauch, I.; Savchenko, I.; Denysenko, D.; Souliou, S.; Kim, H.; Le Tacon, M.; Daemen, L. L.; Cheng, Y.; Mavrandonakis, A.; Ramirez-Cuesta, A.; Volkmer, D.; Schütz, G.; Hirscher, M.; Heine, T. *Nat. Commun.* **2017**, *8*, 14496.
[86] Kim, J. Y.; Balderas-Xicohténcatl, R.; Zhang, L.; Kang, S. G.; Hirscher, M.; Oh, H.; Moon, H. R. *J. Am. Chem. Soc.* **2017**, *139*, 15135–15141.
[87] Kim, J. Y.; Zhang, L.; Balderas-XicohtèĄncatl, R.; Park, J.; Hirscher, M.; Moon, H. R.; Oh, H. *Journal of the American Chemical Society* **2017**, *139*, 17743–17746.
[88] Cao, D.; Huang, H.; Lan, Y.; Chen, X.; Yang, Q.; Liu, D.; Gong, Y.; Xiao, C.; Zhong, C.; Peng, S. *Journal of Materials Chemistry A* **2018**, *6*, 19954–19959.
[89] Han, G.; Gong, Y.; Huang, H.; Cao, D.; Chen, X.; Liu, D.; Zhong, C. *ACS applied materials & interfaces* **2018**, *10*, 32128–32132.
[90] Allen, M.; Tildesley, D. *Computer Simulation of Liquids*; Oxford University Press, 1987.
[91] Frenkel, D.; Smit, B. *Understanding Molecular Simulation: From Algorithms to Applications*; Academic Press: London, 2002.
[92] Chandler, D. *Introduction to modern statistical mechanics*; 1987; p 288.
[93] Tuckerman, M. *Statistical mechanics: theory and molecular simulation*; Oxford university press, 2010.
[94] Tuckerman, M. E.; Liu, Y.; Ciccotti, G.; Martyna, G. J. *The Journal of Chemical Physics* **2001**, *115*, 1678–1702.

[95] Dubbeldam, D.; Torres-Knoop, A.; Walton, K. S. *Mol. Simul.* **2013**, *39*, 1253–1292.
[96] Ewald, P. P. *Annalen der physik* **1921**, *369*, 253–287.
[97] Adams, D. *The Journal of Chemical Physics* **1983**, *78*, 2585–2590.
[98] Lorentz, H. A. *Ann. Phys.* **1881**, *248*, 127–136.
[99] Foster, M.; Rivin, I.; Treacy, M.; Friedrichs, O. D. *Microporous and mesoporous materials* **2006**, *90*, 32–38.
[100] Löwenstein, W.; Lowenstein, M. *American Mineralogist* **1954**, *39*, 92–96.
[101] Dempsey, E. *J. Soc. Chem. Ind., London* **1968**, *293*.
[102] Garcia-Sanchez, A.; Dubbeldam, D.; Calero, S. *J. Phys. Chem. C* **2010**, *114*, 15068–15074.
[103] Demontis, P.; Fois, E. S.; Suffritti, G. B.; Quartieri, S. *J. Phys. Chem.* **1990**, *94*, 4329–4334.
[104] Fritzsche, S.; Haberlandt, R.; Kärger, J.; Pfeifer, H.; Wolfsberg, M. *Chem. Phys. Lett.* **1990**, *171*, 109–113.
[105] Garcia-Sanchez, A.; Ania, C. O.; Parra, J. B.; Dubbeldam, D.; Vlugt, T. J. H.; Krishna, R.; Calero, S. *J. Phys. Chem. C* **2009**, *113*, 8814–8820, and references therein.
[106] Jaramillo, E.; Auerbach, S. M. *J. Phys. Chem. B* **1999**, *103*, 9589–9594.
[107] Dubbeldam, D.; Calero, S.; Vlugt, T. J. H.; Krishna, R.; Maesen, T. L. M.; Smit, B. *J. Phys. Chem. B* **2004**, *108*, 12301–12313.
[108] Ryckaert, J.-P.; Bellemans, A. *Faraday Discuss. Chem. Soc.* **1978**, *66*, 95–106.
[109] Martin-Calvo, A.; Lahoz-Martin, F. D.; Calero, S. *J. Phys. Chem. C* **2012**, *116*, 6655–6663.
[110] Murthy, C. S.; Singer, K.; Klein, M. L.; McDonald, I. R. *Mol. Phys.* **1980**, *41*, 1387–1399.
[111] Deeg, K. S.; Gutiérrez-Sevillano, J. J.; Bueno-Perez, R.; Parra, J. B.; Ania, C. O.; Doblaré, M.; Calero, S. *J. Phys. Chem. C* **2013**, *117*, 14374–14380.
[112] Rick, S. W. *J. Chem. Phys.* **2004**, *120*, 6085–6093.
[113] Feynman, R. P.; Hibbs, A. R. *Quantum Mechanics and Path Integrals*; McGraw-Hill, 1965.
[114] Metropolis, N.; Rosenbluth, A. W.; Rosenbluth, M. N.; Teller, A. H.; Teller, E. *The journal of chemical physics* **1953**, *21*, 1087–1092.
[115] Landau, D. P.; Binder, K. *A guide to Monte Carlo simulations in statistical physics*; Cambridge University Press: New York, 2002.
[116] Rosenbluth, M. N.; Rosenbluth, A. W. *J. Chem. Phys.* **1955**, *23*, 356–359.
[117] Harris, J.; Rice, S. A. *J Chem Phys* **1988**, *88*, 1298–1306.
[118] Siepmann, J. I. *Mol. Phys.* **1990**, *70*, 1145–1158.
[119] Dubbeldam, D.; Calero, S.; Ellis, D. E.; Snurr, R. Q. *Mol. Simul.* **2016**, *42*, 81–101.
[120] Nosè, S. *Mol Phys* **1984**, *52*, 255–268.
[121] Nosè, S. *J Chem Phys* **1984**, *81*, 511–519.
[122] Hoover, W. G. *Phys. Rev. A* **1986**, *34*, 2499–2500.
[123] Martyna, G. L.; Tobias, D. J.; Klein, M. L. *J. Chem. Phys.* **1994**, *101*, 4177–4189.
[124] Myers, A.; Prausnitz, J. M. *Aiche Journal* **1965**, *11*, 121–127.
[125] Talu, O. *The Journal of Physical Chemistry C* **2013**, *117*, 13059–13071.
[126] Myers, A. L.; Monson, P. A. *Adsorption* **2014**, *20*, 591–622.
[127] Cessford, N. F.; Seaton, N. A.; DuÌĹren, T. *Industrial & Engineering Chemistry Research* **2012**, *51*, 4911–4921.
[128] Walton, K. S.; Sholl, D. S. *AIChE Journal* **2015**, *61*, 2757–2762.
[129] Langmuir, I. *Journal of the American Chemical society* **1918**, *40*, 1361–1403.
[130] Toth, J. *Acta Chimica Academiae Scientarium Hungaricae* **1962**, *30*, 415.
[131] Jensen, C.; Seaton, N. *Langmuir* **1996**, *12*, 2866–2867.
[132] Sips, R. *The Journal of Chemical Physics* **1948**, *16*, 490–495.
[133] Widom, B. *J. Chem. Phys.* **1963**, *39*, 2808–2812.
[134] Vlugt, T. J. H.; Garcia-Perez, E.; Dubbeldam, D.; Ban, S.; Calero, S. *J. Chem. Theory Comput.* **2008**, *4*, 1107–1118.
[135] Dubbeldam, D.; Beerdsen, E.; Vlugt, T. J. H.; Smit, B. *J. Chem. Phys.* **2005**, *122*, –.
[136] Beerdsen, E.; Smit, B.; Dubbeldam, D. *Phys. Rev. Lett.* **2004**, *93*, 248301.
[137] Beerdsen, E.; Dubbeldam, D.; Smit, B. *Phys. Rev. Lett.* **2005**, *95*, 164505.
[138] Dubbeldam, D. Computer-simulation of adsorption and diffusion of hydrocarbons in zeolites. Ph.D. thesis, Universiteit van Amsterdam, 2005.

Optimisation of the Fischer-Tropsch process using zeolites for tail gas separation

Chapter 2

J. Perez-Carbajo, P. Gómez-Álvarez, R. Bueno-Perez, P. J. Merkling, and S. Calero

This work is aimed at optimizing a Fischer-Tropsch Gas To Liquid (GTL) process by recycling compounds of the expelled gas mixture using zeolites for the separation. To that end, we have performed a computational study on four structures widely used in industry. A range of Si/Al ratios have been explored and the effects of their distribution assessed. The ability of the considered force fields and molecular models to reproduce experimental results has been widely proved in previously reported studies. Since this tail gas is formed by a five-component mixture, namely carbon dioxide, methane, carbon monoxide, nitrogen and hydrogen, molecular simulations present clear advantages over experiments. In addition, the viability of the Ideal Adsorption Solution Theory (IAST) has been evaluated to easily handle further separation steps. On the basis of the obtained results, we provide a separation scheme to perform sequentially the separation of CO_2 , CH_4 , CO, N_2 , and H_2 .

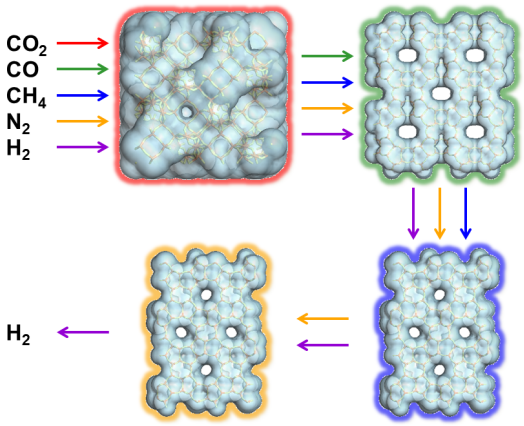

2.1 INTRODUCTION

Hydrocarbons have been the main source of power for the last three centuries. From the late 19th century, coal consumption shifted to the background, exceeded by petroleum exploitation. While known reserves are decreasing unceasingly, new exploratory drillings try to find new oil fields. Unfortunately, the demand for crude oil and its derivatives rises faster than the extraction of such a desired resource. In this scenario it becomes increasingly important to explore those alternatives that target other ways of generating energy.

Although green energies are being promoted as viable and sustainable alternatives, they are not yet ready for replacing the worldwide hydrocarbon consumption. Therefore, the possibility of obtaining refined fuels from a raw material different from petroleum has to be firmly considered. Especially in light of the ongoing shale gas revolution, the importance of producing synthetic liquid fuels is increasing. This is indeed what the Fischer-Tropsch (F-T) process [1,2] provides: liquid hydrocarbons as kerosene, petrol or diesel oil obtained from coal, biomass or natural gas. In a simplified way, the F-T process consists traditionally of a chemical reaction of carbon monoxide and hydrogen gas (syngas) to form a combination of low molecular weight alkanes, according to expression 1.

$$(2n+1)H_2 + nCO \rightarrow C_nH_{2n+2} + nH_2O \quad (1)$$

In addition to avoiding crude oil dependence, the F-T process has the advantage of generating low sulphur content products, resulting in less pollutant emissions when burned. Nevertheless, it bears an elevated economic and environmental cost: it requires expensive industrial plants and large quantities of carbon dioxide are emitted; besides, the GTL overall yield does not exceed fifty per cent. [3]

Table 1: Classical tail gas composition of a Fischer-Tropsch process

H_2	N_2	CO	CH_4	CO_2	C_{2+}
15–30%	20%	10–20%	20–30%	10–15%	5%

Therefore, on the basis of the great importance of the F-T process, it would be interesting to explore new options to improve its efficiency, apart from reducing carbon dioxide emissions. This work is focused on this task in the context of a Gas To Liquid (GTL) process, which involves several sub-processes. The first is the synthesis gas or syngas production, in which carbon-based feedstock (natural gas, coal, biomass) is converted into a mixture of hydrogen and carbon monoxide; particularly, syngas generation based on natural gas is the lowest cost route. It is followed by the Fischer-Tropsch synthesis of liquid hydrocarbons from the syngas; finally, it is usual to include a hydrocracking phase to upgrade the product. In the F-T step, a mixture of CO_2, CO, CH_4, N_2, H_2, and larger hydrocarbons (C_{2+}) is expelled as a tail gas, whose classical

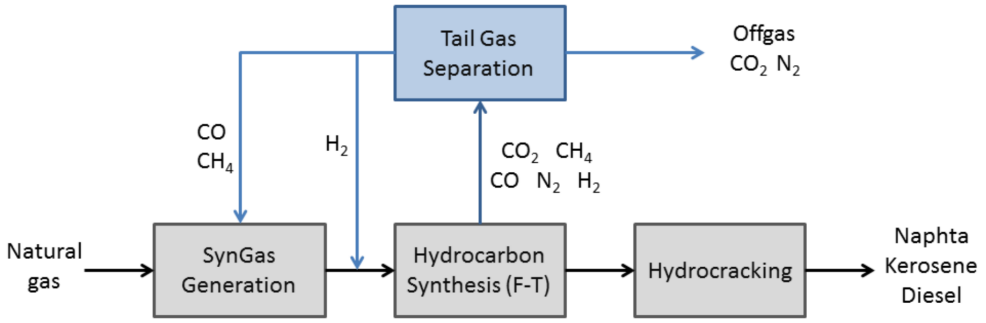

Figure 1: Classical GTL process with Fischer-Tropsch synthesis (grey) and the improvement proposed (blue).

composition is given in Table 1. In order to reduce both the hydrocarbon matter consumption according to Green Chemistry principles and pollutant emissions, an increase of the overall yield of the process [4] is sought through upstream recirculation of some of its compounds. Particularly, whereas nitrogen and carbon dioxide have no commercial value (offgas), a selective recycling of CH_4 and CO (as part of the upstream of the hydrocarbon synthesis) and of H_2 (as part of the syngas generation) is of importance. A schematic illustration of the process is sketched in Figure 1.

Due to the nature of the molecules inside the tail gas, the adsorption on highly selective zeolites is particularly suitable for the proposed separation. These molecular sieves are nanoporous crystalline structures formed by covalently bonded TO_4 tetrahedra, where the T central atoms are usually silicon or aluminium atoms. These primary units join to form secondary building units, groups of simple polyhedra, which merge in turn to form a three-dimensional system of cavities of molecular dimensions, which can be classified as windows, cages, and channels according to their spatial distribution. Pure silica zeolites are charge neutral but the introduction of AlO_4 units induces a negative net charge in the structure that has to be balanced by nonframework cations present during zeolite synthesis, the number of which depends on their valence. Whereas the amount of aluminium present in the zeolite structure is usually known and expressed as the Si/Al ratio, the positions of the aluminium atoms and cations in these materials are not very clear; the influence of both factors on the adsorption performance at the molecular level is yet not completely understood.

With all the previous information in mind, this work is focused on evaluat-

ing the influence of aluminium contents and distributions on various zeolites of high industrial impact, namely faujasite (FAU), mordenite (MOR), MFI, and DDR for their ability to separate the tail gas mixture of the F-T process. As is well-known, FAU presents large cages forming a three-dimensional (3D) network connected through 7.4 Å diameter windows; MOR is a 1D zeolite whose parallel channels of 6.5–7 Å have small cavities called side-pockets,[5] all along them; MFI is formed by a 3D pore system with straight parallel channels intersected by zigzag channels of around 5.5 Å in diameter; finally, DDR is a 2D structure with a window of 3.7× 4.4 Å . These selected zeolites are particularly suitable since in FAU all T atoms are equivalent and so the change in Al concentration in this zeolite allows one to observe clearly this effect; and the quite different exposed topologies of the remaining structures enable us to focus on other factors such as the influence of the specific position. On the whole, these structures offer a wide variety of properties that will enable us to select the most suitable for separation purposes.

To achieve the aforementioned goal, we have used molecular simulation (MS) techniques. Although this kind of calculations is highly time and resource consuming, the advances of hardware technology, simulation algorithms, and force fields have made these challenges affordable in the last decade. Likewise, it provides advantages over experiments since it affords a perfect control of the variables defining the system, as well as obtaining detailed information at the molecular level. Specifically, the MS technique represents a step forward in this study since data measurements of multicomponent mixtures are very difficult. Besides, we used the Ideal Adsorbed Solution Theory (IAST)[6] to obtain information on the mixture of the single-component adsorption isotherms in order to compare with results obtained by simulation and hence evaluate the suitability of this method for the proposed analysis.

The remainder of the paper is organized as follows. In Section 2, details of our simulation methodology, including descriptions of the zeolites, adsorbates and force fields, are presented. In Section 3, computed adsorption behaviour and selectivities are exposed and comprehensively discussed. Finally, some concluding remarks are given in Section 4.

2.2 METHODS

2.2.1 Frameworks and adsorbates: models and force fields

The zeolite lattices (Figure 2) were assumed to be rigid in the simulations, *i.e.*, the framework atoms are fixed at their crystallographic positions.[7–10] The aluminium-containing structures were obtained from silica ones by randomly replacing silicon by aluminium atoms satis-

fying the generally accepted Löwenstein rule, which states that Al–O–Al linkages are energetically forbidden.[11] These Al containing structures were generated for several numbers of random Al substitutions per unit cell and crystallographic positions at which the replacements were performed. The negative charge was counterbalanced by non-framework sodium cations in the zeolite pores, which can move freely, adjusting their position depending on their interactions with the framework atoms, other sodium cations, and the guest molecules. Depending on their framework aluminium density, FAU-type zeolites are labelled either X or Y; specifically, zeolite X has a framework aluminium density between 96 and 77 aluminium atoms per unit cell (Al per uc), whereas zeolite Y contains fewer than 77 Al per uc.[12] It has been proved[13,14] that the adsorption of CO_2 in the zeolites with high Al densities is accompanied by the formation of carbonates; thus, only the NaY up to 54 Al per uc is considered in this work. On the other hand, four and twelve distinct crystallographic T-sites (T can be Si or Al) can be identified for MOR and MFI, respectively, and each of these accepts up to 8 possible aluminium atoms per unit cell. It is worth noting that certain sites admit just up to 4 Al per uc, specifically, T_7, T_9, T_{10},and T_{12} for MFI, and T_3 and T_4 in the case of MOR. The numbering of the crystallographic sites follows the IZA-SC Database convention.[15] For all of this work, we will label a substitution of y Al per uc at crystallographic site x as $T_{x,y}$. Finally, DDR has seven T sites and accepts up to 5 Al per uc.

According to the classical tail gas composition we considered the following five-component mixture in our simulations: CO_2 (15%), CO (20%), CH_4 (30%), N_2 (20%) and H_2 (15%). We assume that C_{2+} products are previously removed from the mixture. They could easily be removed from the tail gas using zeolites such as MFI[16]: because of their larger sizes, they would be adsorbed in the structures at lower pressures.

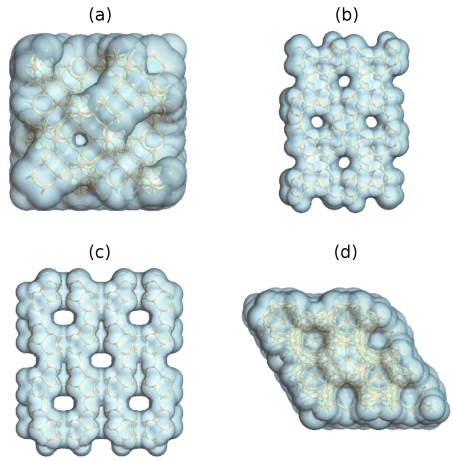

Figure 2: Accessible solvent surfaces for (a) FAU, (b) MFI, (c) MOR, and (d) DDR. The underlying atomic structure is shown.

The models used representing each gas molecule consider one atom (or set of atoms) as an interacting centre with an effective Lennard-Jones potential (L–J) and

point charges. The L–J parameters for the adsorbate–adsorbate interactions are collected in Table 2. The specific values of charges, as well as the molecular geometries, follow. The CO_2 molecule has been defined as a rigid three-site model with partial point charges on each one. The L-J interaction parameters were taken from Garcia-Sanchez *et al.* [17] as they had been shown to reproduce the adsorption properties in zeolites. The values of the point charges are $+0.6512\,e^-$ and $-0.3256\,e^-$ for carbon and oxygen atoms, respectively, and the bond length is $d_{OC} = 1.149$ Å.

Table 2: Adsorbate–adsorbate Lennard-Jones interactions

	ϵ/k_B[K]	σ[Å]
C_{CO_2} [17]	29.993	2.745
O_{CO_2} [17]	85.671	3.017
C_{CO} [18]	16.141	3.658
O_{CO} [18]	98.014	2.979
CH_4 [19]	158.5	3.72
N_{N_2} [20]	36.4	3.32
H_2 [21]	36.733	2.958

CO has also been represented by a rigid three-site model,[17] two of them corresponding to carbon and oxygen atoms, and a third site located between these two is defined as a dummy atom. The point charges of carbon and oxygen atoms, which are separated by a distance of 1.128Å, are $-0.2424\,e^-$ and $-0.2744\,e^-$, respectively. Balancing this negative charge, a $+0.5168\,e^-$ charge is located at 0.6643Å from the C atom. It is worth noting that a new set of L–J parameters from Martin-Calvo *et al.* [18] has been adopted. A united atom model has been used for CH_4, which was considered as a single and chargeless interaction centre with the potential parameters described in Dubbeldam *et al.* [19] As for the diatomic N_2 molecule, a linear, three-site model [20] was used with partial charges of $-0.405\,e^-$ on the N atoms, separated by a distance of 1.1 Å and $+0.810\,e^-$ on the centre of mass that reproduces the molecular quadrupole moment. Similarly to methane, H_2 was modelled as a single uncharged L–J centre. [21]

As the atomic positions of the structures are fixed, there is no need to consider interactions between framework atoms, and only those with adsorbates and non-framework atoms must be considered. The interactions are defined through both Coulombic and Lennard-Jones potentials. Since dispersive forces are dominated by oxygen atoms, interactions of Si atoms were not taken into account, except for hydrogen due to its small size; the corresponding L–J parameters considered are $\epsilon_{Si-H_2} = 28.256$ K and $\sigma_{Si-H_2} = 1.854$ Å. Likewise, dispersive interactions for cations between each other were neglected due to the strong electrostatic interactions. A summary of the considered Lennard-Jones parameters for cross interactions used in this work is given in Table 2. The remaining unspecified cross interactions were determined by Lorentz–Berthelot mixing rules. The Coulombic interactions in the system

Table 3: Cross-interaction Lennard-Jones parameters. Top-left corner ϵ/k_B [K]; bottom-right corner σ [Å]

	O_{zeo}/O_a		Na	
C_{CO_2} [17]	37.595	3.511	362.292	3.32
O_{CO_2} [17]	78.98	3.237	200.831	2.758
C_{CO} [22]	34.282	3.557	87.172	3.079
O_{CO} [22]	84.478	3.218	214.812	2.739
CH_4 [19]	115.0	3.47	582.0	2.72
N_{N_2} [20]	58.25	3.062	130.907	2.91
H_{H_2} [21,23]	66.055	2.890	280.18	2.339
Na [17]	23.0	3.4	—	—

were calculated using the Ewald summation [24] by assigning partial charges to every atom of the zeolite and extraframework cations. For silicon and aluminium atoms, $+0.786\,e^-$ and $+0.4859\,e^-$ values were considered, respectively; as regards the oxygen atoms, different charges for oxygen atoms bridging two silicon atoms ($q_O = -0.393\,e^-$) and bridging one silicon and one aluminium atom ($q_{O_a} = -0.4138\,e^-$) were applied. [17] The charge assigned to sodium is $+0.3834\,e^-$. [17]

2.2.2 Simulation details

The Grand Canonical Monte Carlo (GCMC) ensemble allows one to compute the adsorption isotherms of a certain set of guest molecules on the host framework, [24] as well as the following interesting properties. On the one hand, in order to analyse the preferential adsorption of a molecule over another, the adsorption selectivity is defined from the molar fraction in the adsorbed phase x and from the molar fraction in the bulk phase y according to the following expression:

$$S_{ij} = \frac{x_i \cdot y_j}{y_i \cdot x_j} \tag{2}$$

On the other hand, Henry coefficients (K_H) and heats of adsorption (Q_{st}) account for the adsorption properties at low coverage; Henry coefficients are related to the excess free energy of the adsorbed molecules and can be calculated attending to the following expression:

$$K_H = \frac{1}{RT\rho_f}\frac{\langle W\rangle}{\langle W^{ig}\rangle} \tag{3}$$

where T is the temperature, R the gas constant, ρ_f the density of the framework,

$\langle W \rangle$ the Rosenbluth factor of the single chain molecule and $\langle W^{ig} \rangle$ the Rosenbluth factor of the molecule in the ideal gas. From the ratio of the Henry coefficients of two components, the selectivity at zero loading can be estimated:

$$S_{z-l} = \frac{K_H^i}{K_H^j} \tag{4}$$

The heat of adsorption can be obtained by derivation of the Henry coefficient from the Clausius–Clapeyron equation. However, it is more efficient to calculate it directly from the energies of the system.

$$\begin{aligned} Q_{st} &= \Delta U - RT = \ldots \\ &= \left(\langle U_{hg} \rangle - \langle U_h \rangle - \langle U_g \rangle\right) - RT \end{aligned} \tag{5}$$

where $\langle U_{hg} \rangle$ denotes the average potential energy of the host–guest system; $\langle U_g \rangle$, the energy of the isolated guest molecule in the ideal gas; and $\langle U_h \rangle$, the average host energy. The Widom test-particle method has been proved to be an accurate and efficient technique to that end. [25]

Thus, using the above described models and force fields, Monte Carlo (MC) simulations in the Grand Canonical ensemble (μVT) were performed in this work to compute the adsorption behaviour of the tail mixture on the selected adsorbents using RASPA molecular simulation software. [26,27] Both pure components and the mixture isotherms were computed in a pressure range of 10^3–10^7 Pa, and 10^2–3×10^6 Pa, respectively, at 303.15 K for the four pure silica zeolites considered and for different aluminium concentrations and locations. Specifically, Si/Al ratios of 2.55 (54 Al per uc), 3 (48 Al per uc), 5.2 (32 Al per uc), 7 (24 Al per uc), and 15.2 (12 Al per uc) were considered for FAU, and 11 (8 Al per uc) in the case of MFI, 11 and 5 (4 and 8 Al per uc) for MOR, and 23 (5 Al per uc) for DDR; [28] the aluminium atoms were distributed over all possible T positions for pure components and over selected ones in the case of the mixture. Likewise, Henry coefficients and heats of adsorption were computed using the Widom test-particle method in the canonical ensemble (NVT) in order to complete the adsorption information. From these data, selectivities of the compounds of interest were determined. The number of unit cells for each structure was chosen in order to get a simulation box larger than twice the Lennard–Jones *cutoff* radius, which was fixed at 12 Å. Simulations were arranged in cycles of trial moves including molecular translation, rotation, regrowth at a random position, and insertion or deletion of a molecule in the case of simulations in the Grand Canonical ensemble. As regards the mixture isotherms, identity-changes of adsorbed molecules were also probed. It is worth noting that hydrogen was not taken into account to that end due to its small size. In fact, it was the only gas molecule allowed to enter the sodalite cages in the FAU zeolite. To ensure that the remaining molecules are not spuriously generated and adsorbed in these cages during the simulations, they were

blocked. A large number of cycles were needed both for equilibrating the system and for the production run.

2.3 Results and Discussion

The following analysis focuses on studying how adsorption properties of the considered gas mixture on FAU, MFI, MOR and DDR-type zeolites are affected by the amount and position of sodium cations on the structure of the pores.

Firstly, low-coverage properties of the different gas molecules for structures with all T-sites occupied with Si atoms andfor those with a considerable range of aluminium densities and locations are presented. Afterwards, selected adsorption isotherms and selectivities determined from the latter will be discussed, as well as the corresponding IAST predictions. Finally, calculations of the diffusion coefficients for structures of interest according to adsorption results and the average occupation profiles of some adsorbates on the considered structures are provided.

2.3.1 Adsorption in the low-coverage regime

Results concerning the heat of adsorption, which have been determined according to expression (5), are shown in Figure 3 for all pure silica zeolites (T_{Si}) and multiple cation containing structures, namely: FAU-type zeolite with varying Al atoms per unit cell (from 0 to 54), MFI, MOR and DDR with 8, both 4 and 8, and 5 cations per unit cell, respectively, at different T positions. Since this property is directly related to the interaction of molecules with the surface of the adsorbent, the higher its value, the stronger the affinity of the adsorbate–adsorbent pair. As can be observed, regardless of the type of structure, carbon dioxide exhibits remarkably the highest heat of adsorption, especially in the case of cation containing zeolites. This fact may be attributed to the adsorbate's molecular multipole moment and polarizability. Even though CO has a small permanent dipole moment, the higher quadrupole moment and polarizability of CO_2 (this is also expressed in the CO and CO_2 models, where the partial charges in carbon dioxide are higher) could make the affinity of the latter towards any adsorbent stronger than the affinities of the remaining guest molecules of this study. More specifically, heats of adsorption for the considered set of gas molecules decreases in the trend $CO_2 > CH_4 > CO > N_2 > H_2$ on all the zeolites; according to this result, the molecular size seems to be also a significant influencing factor on the adsorption at low coverage. In the following, the influence of aluminium density and location is discussed. As can be seen, this effect is basically negligible for H_2 and even N_2 regardless of the type of structure, whereas considerable differences can be appreciated for the remaining molecules. The presence and mobility of cations in FAU-type structures

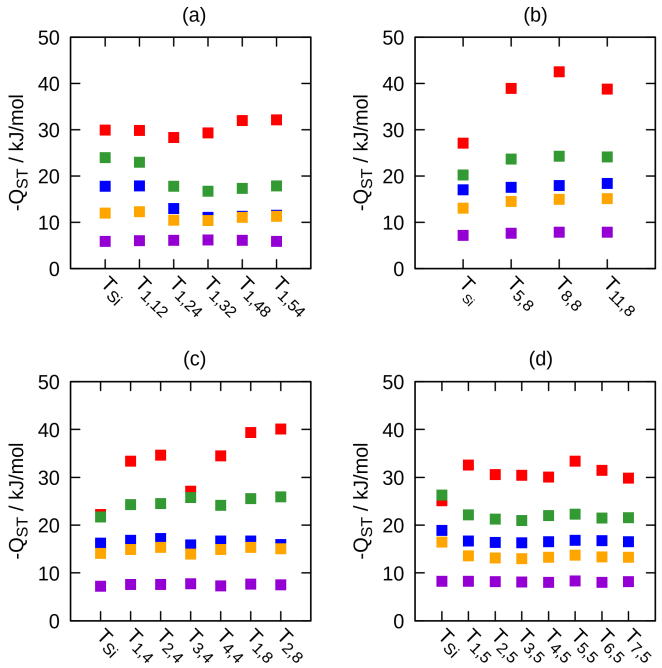

Figure 3: Computed heats of adsorption of CO_2 (red), CO (blue), CH_4 (green), N_2 (orange), and H_2 (violet) for various Al densities and positions ($T_{i,j}$, i being the crystallographic position and j the number of Al per uc; T_{Si} is the pure silica structure) in (a) FAU-type zeolite, (b) MFI-type zeolite, (c) MOR-type zeolite, and (d) DDR-type zeolite.

hinder the adsorption of CH_4 and CO in this regime, since their respective heats of adsorption notably decrease over the pure silica ones. However, CO_2 exhibits higher values for the structures with the lowest considered Si/Al ratios: 48Na-FAU and 54Na-FAU; the high quadrupole of this molecule probably leads the sodium cations to act as adsorption sites. A similar behaviour is observed for DDR-type zeolite. Unlike these cage-like structures, the presence of cations in zeolites MFI and MOR, which are channel-like structures, implies an increase in heat of adsorption for these three gas molecules, especially for CO_2 . As for the effect of the position of the aluminium atoms in the latter frameworks, non-negligible variations can be observed, especially for carbon dioxide and MOR-type zeolite.

Apart from the heats of adsorption, Henry coefficients were also computed according to equation (3), and presented in the Appendix A (Tables A1–A4). As expected, both magnitudes are in complete agreement exhibiting the same qualita-

tive behaviour. Likewise, selectivities at zero loading of one component over the other were obtained through eqn (4). It allows one to qualitatively observe the separation efficiency of each structure in this regime. According to the values of heats of adsorption and to the goal of this work, this property was examined for the following adsorbate couples: $CO_2 - CH_4$, $CH_4 - CO$, $CO - H_2$, and $N_2 - H_2$. Results are shown in Figure A1 in the Appendix A. As regards pure silica structures, MFI appears to be the most selective adsorbent in this regime, except for $CH_4 - CO$. On the other side, the presence of aluminium, and thus sodium cations, makes the adsorbents more selective for the removal of primarily CO_2 and then CH_4, whereas it makes the structure less suitable for separating the remaining compounds. Overall, the best separation at zero loading is given, both from the point of view of absolute Henry coefficients and selectivities, by MFI $T_{8,8}$ for $CO_2 - CH_4$, MOR $T_{2,8}$ for $CH_4 - CO$, and pure silica DDR for $CO - H_2$ and $N_2 - H_2$. In addition, unlike DDR-type zeolite, notable variations due to the Al location are appreciated in MFI and MOR for $CO_2 - CH_4$ and $CH_4 - CO$, respectively. As for these latter structures, only certain T sites for the Al locations will be henceforth considered in order to make figures simpler and clearer.

2.3.2 Adsorption isotherms

Adsorption isotherms in the four considered zeolites at different aluminium contents and distributions were evaluated at 303.15 K for both pure components and the mixture. They allow one to analyse the adsorption performance not only at zero loading but also in the intermediate and high-coverage regime. In the following discussion, attention is paid to the results concerning the five-component mixture. Figures corresponding to the computed adsorption isotherms of pure components can be found in the Appendix

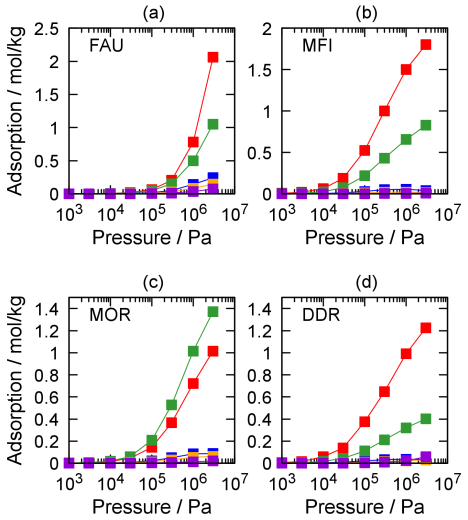

Figure 4: Computed adsorption isotherms of a five-component mixture in pure silica zeolites: (a) FAU, (b) MFI, (c) MOR, and (d) DDR-type zeolite. CO_2 in red circles, CO in blue squares, CH_4 in green diamonds, N_2 in orange up-pointing triangles, and H_2 in violet down-pointing triangles.

A (Figures A2–A5).

Results for pure silica structures are shown in Figure 4. As can be observed in it, the adsorption capacity of a given adsorbent follows the order CO_2 > CH_4 > CO, N_2 and H_2, which is the same trend observed for the low-coverage properties. Apart from the effect of the molecular size, CO_2 is most strongly adsorbed due to its high polarizability, resulting in a stronger interaction by dispersion forces, and to its permanent quadrupole moment, which interacts with the polar surface of the zeolite. In spite of its lack of electric moments, CH_4 is more strongly adsorbed than the remaining molecules, whose loading is virtually zero, because of its higher polarizability. An exception in the exposed trend was found in zeolite MOR, which exhibits higher adsorption affinity for CH_4 than CO_2 at intermediate or high pressures. This 'inversion' can be attributed to the side-pockets of this zeolite. It is more difficult for CO_2 molecules to access the side-pockets, and therefore they occupy basically the main channels, as can be observed in Figure 5.

Overall, the aluminium density and distribution in these zeolites strongly affect the adsorption behaviour of CO_2 and CH_4, whereas that of H_2, N_2, and CO was found roughly to be insensitive to the presence of cations, as can be observed from Figures A6–A9 in the Appendix A. Thus, due to the considerable difference between the low loading of the latter molecules (CO, N_2, and H_2) and the most adsorbed ones (CO_2 and CH_4), their isotherms were omitted in Figure 6 (FAU, MFI, and DDR) and 7 (MOR), where continuous and dotted lines represent the calculations for CO_2 and CH_4, respectively, by IAST. As is clearly apparent from Fig. 6a, the loading of CO_2 in FAU increases with an increasing number of Al atoms per unit cell, since it implies a higher cation density and so the existence of a higher number of preferential adsorption sites. As for CH_4, whose adsorption only becomes significant at high pressures as previously commented, the volume occupied by cations and CO_2 prevails over the sodium–adsorbate interactions. Thus,

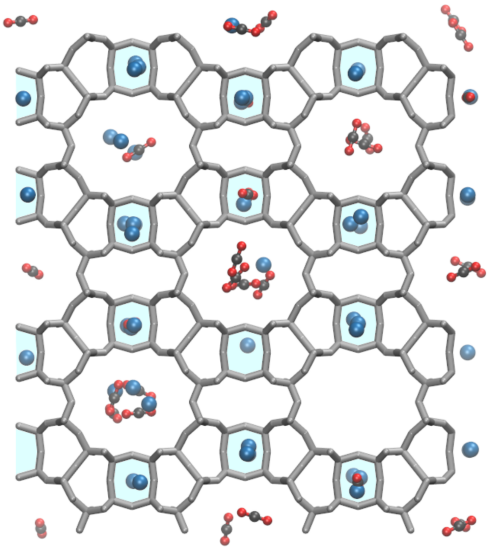

Figure 5: Mixture adsorption snapshot in pure silica MOR at 303.15 K and 10^6 Pa. Only CO_2 (red-grey) and CH_4 (blue) molecules are shown for clarity. Side-pockets are shaded light blue.

it exhibits a lower maximum loading for the Al containing structures than that obtained for pure silica. Thus, the presence of cations complicates the separation of CH_4 from the smaller molecules at high pressures, but favours that from CO_2 . Carbon dioxide adsorption starts at lower pressures than methane, but the largest adsorption difference between both components is observed at the highest pressures. This fact becomes more noticeable as the Al density increases, which has a twofold cause: on the one hand, the lower the Si/Al ratio, the more polar the zeolite, which favours CO_2 adsorption over CH_4 , on the other hand, the previously commented effect of the excluded volume on CH_4 . Therefore, the use of 54 Al per uc FAU ($T_{1,54}$) at high pressures appears to be the best option to separate CO_2 from CH_4 (or from any other component of the mixture).

As for MFI (Figure 6b), adsorption isotherms were performed for a given cation density, 8 Al per uc at selected T sites on the basis of the obtained heats of adsorption. The presence of cations in this zeolite clearly favours the adsorption of CO_2 and decreases the loading of CH_4 , improving considerably the separation of both adsorbates. However, virtually no variations in the loading are appreciated as a consequence of the Al position. This is also found when probing other sites in MFI: adsorption isotherms of pure components (Figure A10, Appendix A) and the five-component mixture (Figure A11,

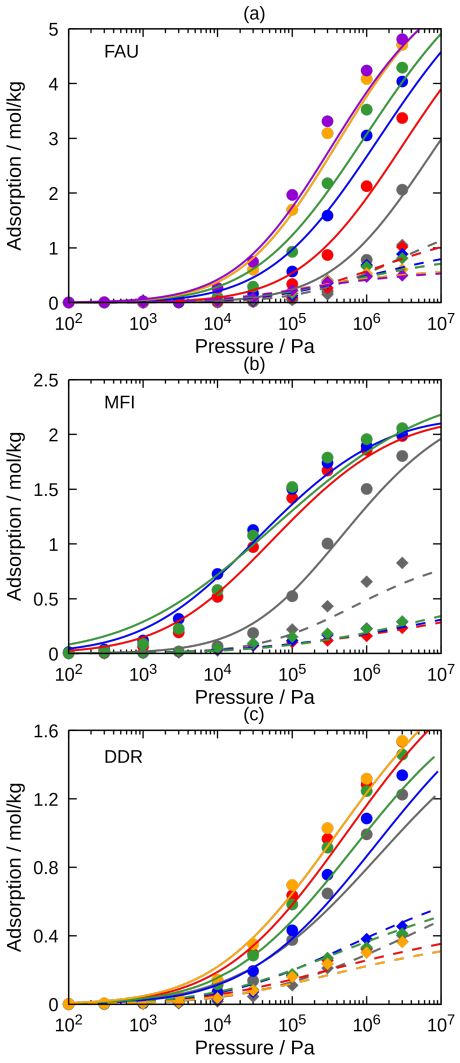

Figure 6: Adsorption isotherms from MC simulations (circles for CO_2 and diamonds for CH_4) of a five-component mixture and IAST calculations (continuous lines for CO_2 , dashed lines for CH_4) in various zeolite types. FAU-type (a) variants T_{Si} (grey), $T_{1,12}$ (red), $T_{1,24}$ (blue), $T_{1,32}$ (green), $T_{1,48}$ (orange), and $T_{1,54}$ (violet) are shown. MFI-type (b) variants T_{Si} (grey), $T_{5,8}$ (red), $T_{8,8}$ (blue), and $T_{11,8}$ (green) are shown. DDR-type (c) variants T_{Si} (grey), $T_{1,5}$ (red), $T_{2,5}$ (blue), $T_{4,5}$ (green), and $T_{5,5}$ (orange) are shown.

Appendix A) were computed for those MFI sites which only accept up to 4 Al per uc ($T_{7,4}$, $T_{9,4}$, $T_{10,4}$, and $T_{12,4}$). As can be observed, the curves follow similar trends to those for MFI with 8 Al per uc, although the CO_2 and CH_4 loadings are lower at low and intermediate pressures and slightly larger, respectively, as a consequence of a lower density of Al–Na^+ pairs. As is apparent from Figure 6c, on the whole the presence of cations increases slightly the adsorption of CO_2 in DDR-type zeolite and hardly affects that of CH_4 . We note pronounced changes as a function of the Al location in the case of CO_2 , T_5 being the optimal position for the CO_2 – CH_4 separation.

Finally, the adsorption performance of MOR-type zeolites with 4 and 8 Al per uc at the T_1 and T_2 Al locations is presented, as well as the pure silica structure in Figures 7a and b, respectively. Unlike the MFI structure, the adsorption performance is improved in relation to pure silica for both components. On the one hand, the effect of the Al density is noticeable, especially in the case of CO_2 ; the higher the number of sodium cations per unit cell, the higher the loading of the adsorbates. On the other hand, a slight dependence on the Al location can be also appreciated. In this respect, it must be emphasized that, as in pure silica, CH_4 exhibits higher maximum loading than CO_2 for structures with Al atoms at the T_1 site, whereas this fact is not observed in the case of T_2. Thus, both sodium density and distribution are essential factors during adsorption of molecules in MOR zeolite.

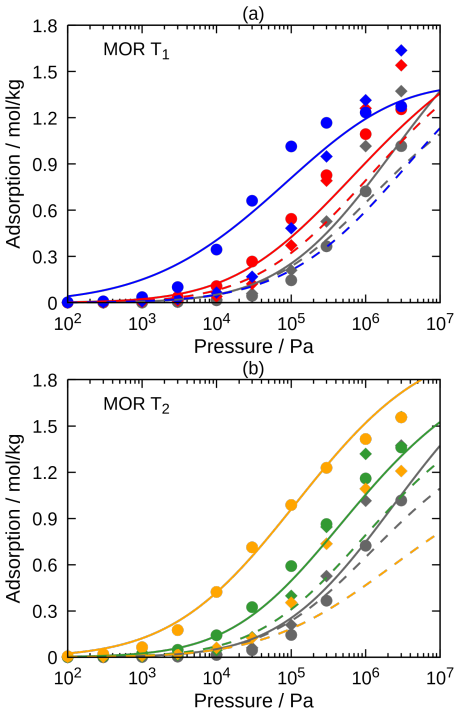

Figure 7: Adsorption isotherms from MC simulations (circles for CO_2 and diamonds for CH_4) of a five-component mixture and IAST calculations (continuous lines for CO_2 and dashed lines for CH_4) in MOR-type zeolites. Al substituted in T_1 (a) are shown $T_{1,4}$ (red) and $T_{1,8}$ (blue). Al substituted in T_2 (b) are shown $T_{2,4}$ (green) and $T_{2,8}$ (orange). In both, grey symbols are T_{Si}.

The Ideal Adsorption Solution Theory (IAST) [6] of Myers and Prausnitz is a popular approach to make reliable predictions of adsorption isotherms for fluid mixtures on the basis of the pure-component data, which are simpler to

collect. The approach has been widely used to describe adsorption from multicomponent mixtures in zeolites and other adsorbents, including mixtures of alkanes, CO_2, CH_4, and N_2, among others, and found to deliver accurate predictions. However, although it has been shown to provide good predictions for a wide variety of fluid–adsorbent systems, there are numerous cases where its predictions are inaccurate. It assumes ideal behaviour of the adsorbed phase and that all components have access to the same uniform surface; therefore, it works very well at low pressures and for materials with homogeneous adsorption sites but is known to fail in predicting mixture adsorption data if strong heterogeneity exists for adsorbed mixtures. In order to evaluate the suitability of this model for the targeted mixture and structures, we used it to obtain the isotherms of the five-component mixture using the pure component isotherm fit as data input. As is apparent from Figures 6 and 7, IAST predictions are generally good. They tend to underestimate slightly the adsorptions found by MC simulation in all structures except for MOR-type ones. This can be rationalised by the fact that the inner structure of MOR is characterised by side-pockets. If these side-pockets are made unavailable by introducing artificial blockers, the adsorption isotherms reproduce very well the IAST predictions, as can be unequivocally deduced from Figure A12 in the Appendix A, in which results for 8 Al per uc at T_2 are shown.

Adsorptions are normally not very sensitive to the technique used to determine the coordinates, so that crystallographic positions, minimizations with classical or quantum mechanical force fields generally yield very similar results. This has been checked in this work, in which selected structures were minimized using Vienna Ab initio Simulation Package (VASP):[29] negligible variations in adsorption properties were observed between both structures for each considered zeolitic topology.

2.3.3 Adsorption selectivities

In order to evaluate the performance of an adsorbent for separation, adsorption selectivities are extremely important. The selectivity is a pairwise property controlled by the ratio of adsorptions of two adsorbents. According to the five-component mixture adsorption isotherms, we focus on the $CO_2 - CH_4$ and $CH_4 -$ CO selectivities because they involve the strongest adsorbed species. They were calculated according to equation 2 taking into account the corresponding molar fraction of the targeted components in the mixture; the respective results are shown in Figures 8 and 9. We note that the values at low pressures are quite consistent with those determined from Henry coefficients and previously discussed. Overall, the presence of cations increases the selectivity and so improves the separation

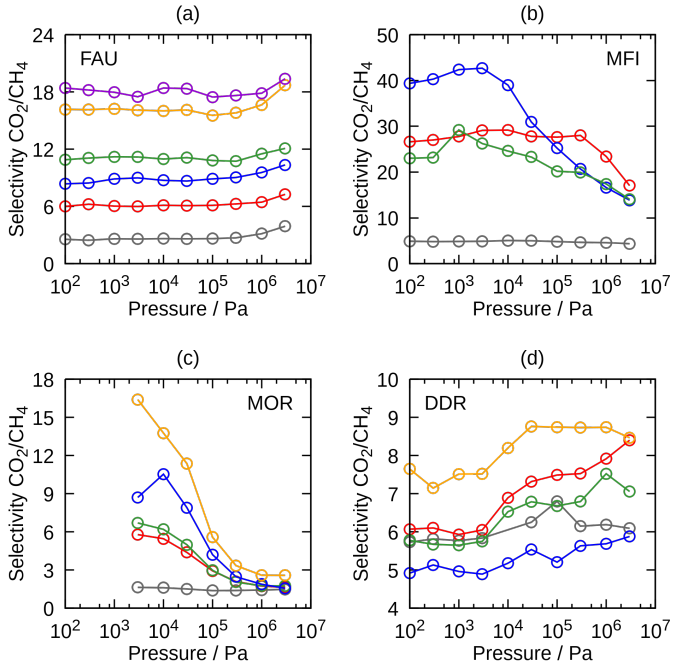

Figure 8: Computed $CO_2 - CH_4$ adsorption selectivity as a function of: (a) Al density in FAU [T_{Si} (grey), $T_{1,12}$ (red), $T_{1,24}$ (blue), $T_{1,32}$ (green), $T_{1,48}$ (orange), and $T_{1,54}$ (violet)]; (b) Al location in MFI [T_{Si} (grey), $T_{5,8}$ (red), $T_{8,8}$ (blue), and $T_{11,8}$ (green)]; (c) Al density and location in MOR [T_{Si} (grey), $T_{1,4}$ (red), $T_{2,4}$ (green) $T_{1,8}$ (blue), and $T_{2,8}$ (orange)]; and (d) Al location in DDR [T_{Si} (grey), $T_{1,5}$ (red), $T_{2,5}$ (blue), $T_{4,5}$ (green), and $T_{5,5}$ (orange)].

process in relation to pure silica frameworks. This is most clearly demonstrated in the case of the FAU-type zeolite series given the systematic decrease of Si/Al ratios probed, but is also apparent in the other structures of the study. A subtler influence is exerted by the Al position and depends on the structure and the selectivity considered (whether $CO_2 - CH_4$ or $CH_4 - CO$); whereas in MFI the precise position of 8 Al per uc affects basically only the $CO_2 - CH_4$ selectivity, differences as a function of the T position on both selectivities can be observed in 8 Al per uc MOR and 5 Al per uc DDR, although to a lesser extent.

The following comments are focused on the variation with pressure of selectivities. Regarding FAU, the results corresponding to $CO_2 - CH_4$ are virtually insensitive to pressure whereas the separation of CH_4 from CO is considerably favoured as pressure is raised. As for the remaining cation containing zeolites,

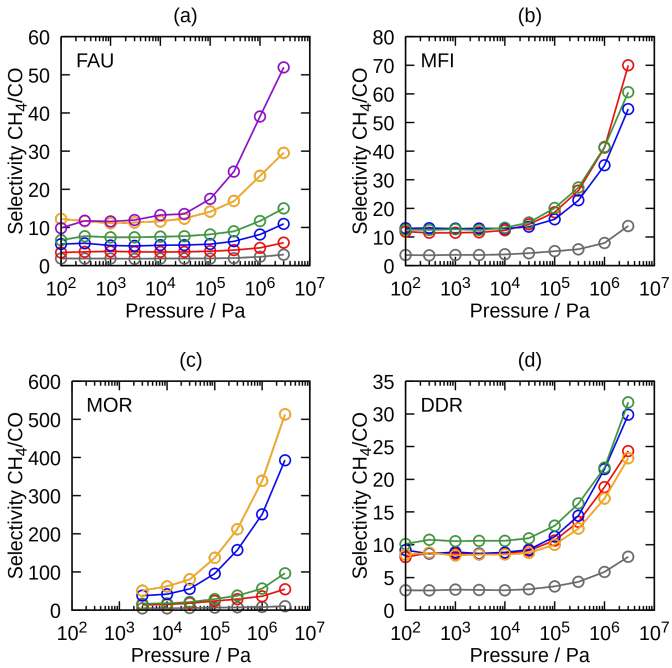

Figure 9: Computed CH_4-CO adsorption selectivity as a function of: (a) Al density in FAU [T_{Si} (grey), $T_{1,12}$ (red), $T_{1,24}$ (blue), $T_{1,32}$ (green), $T_{1,48}$ (orange), and $T_{1,54}$ (violet)]; (b) Al location in MFI [T_{Si} (grey), $T_{5,8}$ (red), $T_{8,8}$ (blue), and $T_{11,8}$ (green)]; (c) Al density and location in MOR [T_{Si} (grey), $T_{1,4}$ (red), $T_{2,4}$ (green) $T_{1,8}$ (blue), and $T_{2,8}$ (orange)]; and (d) Al location in DDR [T_{Si} (grey), $T_{1,5}$ (red), $T_{2,5}$ (blue), $T_{4,5}$ (green), and $T_{5,5}$ (orange)].

the behaviour as a function of pressure in the other cage-like structure, DDR, is coincident with the one found in FAU. With respect to the channel-like structures MFI and MOR, CH_4-CO selectivity behaves similarly as well, although CO_2-CH_4 selectivity is worsened by pressure increases. For these structures, that property exhibits the highest values at low pressures followed by a decreasing trend with increasing pressure, even down to the values corresponding to pure silica in the case of MOR, either with 4 or 8 aluminium atoms per unit cell. Thus, these structures appear not to be efficient for a simultaneous separation at a given operating pressure. Besides, it must be noted that the variations in this property due to the considered T site for Al locations are especially significant at low pressures. As shown in Figure A13 of the Appendix A, results of the selectivities for CO_2-CH_4 and CH_4-CO in MFI with 4 Al per uc are negatively affected and only

slightly improved, respectively, in relation to those of MFI with 8 Al per uc.

Finally, it is worth commenting that, taking into account all the structures, $T_{8,8}$ MFI at low pressures and $T_{2,8}$ MOR at high loadings were found to exhibit the highest selectivities for CO_2-CH_4 and CH_4-CO, respectively. At intermediate pressures (1–10 bar), CO_2-CH_4 selectivities in high cation ratio FAU zeolites and in the various cation-containing MFI are around 20. Note that our study is based only on the selectivity of the adsorption cycles. This provides an idea of which adsorbent material is more efficient for a given separation. However for practical applications this might require further validation as energy-efficient recovery of gases should take into account the complete adsorption–desorption cycles.

2.3.4 Diffusion coefficients

We have used Molecular Dynamics (MD) simulations to study the diffusion of the adsorbates in the mixture in those structures with highest CO_2-CH_4 selectivity at a pressure of one bar, namely: MFI with 8 Al at T_5 ($T_{5,8}$) and FAU with 48 and 54 Al per uc ($T_{1,48}$ and $T_{1,54}$, respectively), according to our previous results. In these simulations the velocity-Verlet algorithm was used to integrate Newton's law of motion. Previous MC simulations provided initial positions of the molecules. After 10^5 equilibration cycles, we performed MD simulation runs of 6×10^6 cycles in the NVT ensemble (Nosé-Hoover chain thermostat[30]) at 303.15 K using a time step of 0.5 fs and keeping the atoms of the framework fixed.

Self-diffusion coefficients were obtained by calculating the slope of the mean-squared displacement (MSD)[31] (Figure A14, Appendix A) at long times. While the self-diffusion in FAU-type zeolites is isotropic, the value of this magnitude for MFI depends on the orientation given the anisotropy of the channel-like pores. Self-diffusion values of $3.6\pm0.3\times10^{-9}$ m^2s^{-1} and $2.1\pm0.2\times10^{-9}$ m^2s^{-1} were obtained for $T_{1,48}$ FAU and $T_{1,54}$ FAU, respectively. The corresponding value for $T_{5,8}$ MFI is $6.4\pm0.8\times10^{-11}$ m^2s^-1, divided into $D_x = 2.9\times10^{-11}$, $D_y = 1.5\times10^{-10}$, and $D_z = 8.9\times10^{-12}$. This low diffusion result for MFI rules it out as a candidate for the proposed task, since it is important that the guests diffuse sufficiently fast into the structure. Therefore, considering the superior self-diffusion coefficients of $T_{1,48}$ FAU (Si/Al ratio 3), competitive, though slightly lower (roughly 10%) CO_2-CH_4 selectivities than $T_{1,54}$ FAU, and loadings (also roughly 10% at pressures of 1 bar), this zeolite offers the best trade-off. This structure is also less close to the Si/Al ratio where carbonatation has been observed,[13,14] which is likely to ensure a higher long-term stability.

2.3.5 Average occupation profiles

The distribution of CO_2 and CH_4 molecules at the different sites of the considered zeolites was analysed for various aluminium densities and positions. As expected, cations were observed to locate close to oxygen-bridging aluminium atoms to counter balance the negative charge (not shown). Regarding the FAU-type structure, an almost uniform distribution is found in the cages for both components in pure silica; the sodium cations are located mostly near the windows and act as preferential adsorption sites for CO_2 whereas their effect on CH_4 is negligible. In DDR, the average occupancy profile of both adsorbates is basically insensitive to the presence of cations, which is in complete consistency with the previously exposed results of the adsorption isotherms discussed in Figure 6c and supported by Figure A5 (Appendix A). Results for MOR and MFI offer a more interesting picture and are therefore shown in Figure 10 and Figures A15–A17 (Appendix A), respectively, both for a pure silica composition and for 8 Al atoms per unit cell at various T positions. The average values of MOR-type zeolites are presented in the $x-y$ plane, in which differences are easily noticeable. As expected from Figure 5, the side-pockets in pure silica appear as preferential adsorption sites for CH_4, whereas the distribution of CO_2 is more homogeneous. As the aluminium and

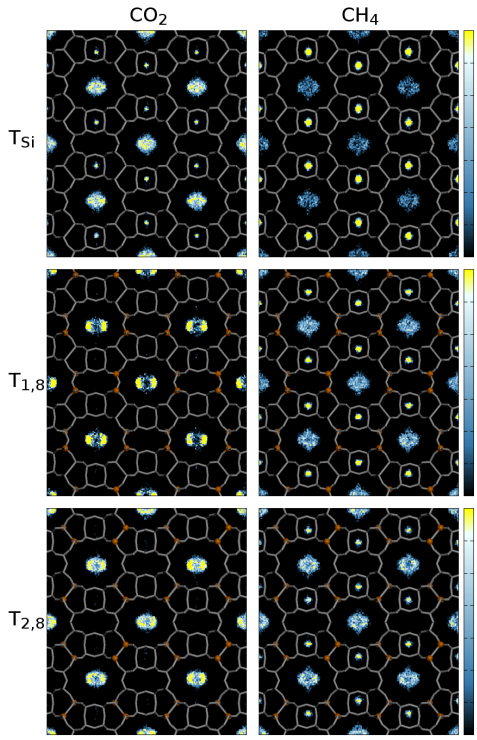

Figure 10: Average occupation profiles of CO_2 (left) and CH_4 (right) on pure silica mordenite (top), $T_{1,8}$ MOR (centre), and $T_{2,8}$ (bottom). The atomic structure has been included for reference, where aluminium atoms are highlighted in orange. The relation between colour and probability density (from black to yellow) is shown in the colour ramp on the right side of the figure. The average values are presented in the XY plane.

sodium content in the zeolite increases, population density in the side pockets decreases sharply: carbon dioxide is not found anymore in the side pockets even at moderate aluminium contents and the decrease in methane is marked. This is likely due to the location of the cations

at the windows giving access to the side-pockets. In Figures A15–A17 (Appendix A), three views of MFI are shown in order to obtain a thorough image of the locations of the adsorbates in this structure. It can be concluded from these that in pure silica, CO_2 tends to be located at the channel intersections whereas CH_4 exhibits a more homogeneous distribution. This is seen most clearly from the $z-x$ view and confirmed by the other views. The presence of cations in the structure favours the occupancy of the intersections, both for CO_2 and CH_4 , so these adsorbates end up competing for the same region within the guest. Different cation locations block or make available different regions within the structure, but these regions are the same for CO_2 and CH_4 .

2.3.6 Consequences for the optimization of the Fischer-Tropsch process

According to the results discussed, the presence of cations on structures increases their polarity, improving considerably the removal of carbon dioxide and methane at working pressures up to 10 MPa. In particular, although CO_2 is the most adsorbed molecule in all zeolites studied, $T_{1,48}$ FAU was identified the best option for its capture. Then, in the absence of CO_2 , the separation of CH_4 from the remaining tail gases can be efficiently achieved on an aluminium-containing zeolite at high pressures, especially on $T_{2,8}$ MOR. Although it is not usually possible to actively choose the aluminium site in experimental structures, a random mixture of sites is still performing better than any other random mixture considered in this study.

After these preliminary separation steps, a ternary mixture of CO (36%), N_2 (36%), and H_2 (28%) remains. In this study, the validity of IAST for the five-component mixture has been established

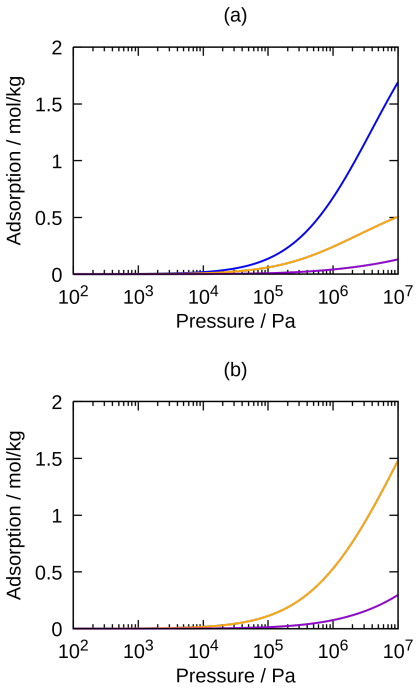

Figure 11: IAST predictions in pure silica MFI of: (a) ternary mixture of CO (blue), N_2 (orange), and H_2 (violet) in percentages of 36, 36, and 28, respectively. (b) Binary mixture of N_2 (orange) and H_2 (violet) in percentages of 57 and 43, respectively.

for all structures except MOR. This can now be used to determine the separations of our ternary and binary mixtures. In this case, the presence of cations in the structures was found detrimental. The most suitable structure for the selective removal of gases is MFI. Results are shown in Figure 11, in which pure silica MFI allows the removal of both CO, in a first step, and N_2 in the remaining $N_2 - H_2$ (57 : 43) mixture.

2.4 CONCLUSIONS

This computational analysis, whose major objective was the evaluation of the cation effect on the adsorption performance of various zeolitic adsorbents for the separation of the Fischer-Tropsch tail gas mixture and the proposal of a separation scheme for all the components of the quinary mixture, has led to the following conclusions.

As regards the fundamental study of the effect of the amount and position of aluminium in these four completely different topologies, the following general statements can be made. The amount of Al–Na^+ pairs sensitively affects the adsorption behaviour; in particular CO_2 adsorption is enhanced. The T site location for a given aluminium density was found to be an important influencing factor in MOR at higher pressures (above 10^5 Pa), even leading in some cases to a preferential adsorption of methane over carbon dioxide. It is also an important factor in DDR, although to a lesser extent than MOR, but is negligible in MFI. Besides, the effect of cations depends not only on the adsorbent but also on the adsorbate. Indeed, whereas the loading of carbon dioxide increases with increasing Al density regardless of the structure and pressure, the adsorption of methane has been proved to be dependent on those factors, and virtually no influence is observed for the remaining gas molecules, which are hardly adsorbed. All in all, the structure with the best CO_2 over CH_4 (the generally next best adsorbed species) separation performance is $T_{1,48}$ FAU. The structure that most readily adsorbs methane is a cation-containing MOR, especially in a CO_2 -depleted mixture. Between these, $T_{2,8}$ MOR has an edge over $T_{1,8}$ MOR.

On the basis of separation performance in terms of total adsorption, selectivity and diffusion coefficients, the following operating procedure is therefore proposed to achieve a complete five-component separation, and so improve the targeted industrial process: a gradual removal of gas molecules in the order of CO_2 , CH_4 , CO, and N_2 using successively the $T_{1,48}$ FAU, $T_{2,8}$ MOR, and two steps with pure silica MFI.

Bibliography

[1] Fischer, F.; Tropsch, H. *Brennstoff-Chemie* **1923**, 276–285.
[2] Fischer, F.; Tropsch, H. *German patent 484337* **1925**,
[3] Unruh, D.; Pabst, K.; Schaub, G. *Energy Fuels* **2010**, *24*, 2634–2641.

[4] Heymans, N.; Alban, B.; Moreau, S.; De Weireld, G. *Chem. Eng. Sci.* **2011**, *66*, 3850–3858.

[5] Garcia-Perez, E.; Parra, J. B.; Ania, C. O.; Garcia-Sanchez, A.; Van Baten, J. M.; Krishna, R.; Dubbeldam, D.; Calero, S. *Adsorption-Journal of the International Adsorption Society* **2007**, *13*, 469–476.

[6] Myers, A.; Prausnitz, J. M. *Aiche Journal* **1965**, *11*, 121–127.

[7] Hriljac, J. A.; Eddy, M. M.; Cheetham, A. K.; Donohue, J. A.; Ray, G. J. *J. Solid State Chem.* **1993**, *106*, 66–72.

[8] van Koningsveld, H.; van Bekkum, H.; Jansen, J. C. *Acta Crystallogr., Sect. B* **1987**, *43*, 127–132.

[9] Meier, W. *Z. Kristallogr.* **1961**, *115*, 439–450.

[10] Gies, H. *Z. Kristallogr.* **1986**, *175*, 93–104.

[11] Löwenstein, W.; Lowenstein, M. *American Mineralogist* **1954**, *39*, 92–96.

[12] Szostak, R. *Molecular Sieves: Principles of Synthesis and Identification.*; Springer, 1997.

[13] Jacobs, P. A.; Vancauwe.Fh,; Vansatn, E. F. *J. Chem. Soc.,Faraday Trans. I* **1973**, *69*, 2130–2139.

[14] Martra, G.; Coluccia, S.; Davit, P.; Gianotti, E.; Marchese, L.; Tsuji, H.; Hattori, H. *Res. Chem. Intermed.* **1999**, *25*, 77–93.

[15] Baerlocher, C.; McCusker, L. Database of Zeolite Structures. `http://www.iza-structure.org/databases/`.

[16] Krishna, R.; Calero, S.; Smit, B. *Chemical Engineering Journal* **2002**, *88*, 81–94.

[17] Garcia-Sanchez, A.; Ania, C. O.; Parra, J. B.; Dubbeldam, D.; Vlugt, T. J. H.; Krishna, R.; Calero, S. *J. Phys. Chem. C* **2009**, *113*, 8814–8820, and references therein.

[18] Martin-Calvo, A.; Lahoz-Martin, F. D.; Calero, S. *J. Phys. Chem. C* **2012**, *116*, 6655–6663.

[19] Dubbeldam, D.; Calero, S.; Vlugt, T. J. H.; Krishna, R.; Maesen, T. L. M.; Smit, B. *J. Phys. Chem. B* **2004**, *108*, 12301–12313.

[20] Murthy, C. S.; Singer, K.; Klein, M. L.; McDonald, I. R. *Mol. Phys.* **1980**, *41*, 1387–1399.

[21] Deeg, K. S.; Gutiérrez-Sevillano, J. J.; Bueno-Perez, R.; Parra, J. B.; Ania, C. O.; Doblaré, M.; Calero, S. *J. Phys. Chem. C* **2013**, *117*, 14374–14380.

[22] Martin-Calvo, A.; Lama, C.; Parra, J. B.; Ania, C. O.; Calero, S. *Private communication*

[23] Deeg, K. S.; Jose Gutierrez-Sevillano, J.; Bueno-Perez, R.; Parra, J. B.; Ania, C. O.; Doblare, M.; Calero, S. *Private communication*

[24] Frenkel, D.; Smit, B. *Understanding Molecular Simulation: From Algorithms to Applications*; Academic Press: London, 2002.

[25] Vlugt, T. J. H.; Garcia-Perez, E.; Dubbeldam, D.; Ban, S.; Calero, S. *J. Chem. Theory Comput.* **2008**, *4*, 1107–1118.

[26] Dubbeldam, D.; Calero, S.; Ellis, D. E.; Snurr, R. Q. *RASPA 1.0: Molecular Software Package for Adsorption and Diffusion in Flexible Nanoporous Materials* **2013**,

[27] Dubbeldam, D.; Torres-Knoop, A.; Walton, K. S. *Mol. Simul.* **2013**, *39*, 1253–1292.

[28] Valyocsik, E. *U.S. Patent 4698217* **1987**,

[29] Kresse, G.; Hafner, J. *Physical Review B* **1993**, *47*, 558.

[30] Hoover, W. G. *Phys. Rev. A* **1986**, *34*, 2499–2500.

[31] Dubbeldam, D.; Ford, D. C.; Ellis, D. E.; Snurr, R. Q. *Mol. Simul.* **2009**, *35*, 1084–1097.

CHAPTER 3

ZEOLITES FOR CO_2 -CO -O_2 SEPARATION TO OBTAIN CO_2 -NEUTRAL FUELS

J. Perez-Carbajo, I. Matito-Martos, S. R. G. Balestra, M. N. Tsampas, M. C. M. van de Sanden, J. A. Delgado, V. I. Águeda, P. J. Merkling, and S. Calero

Carbon dioxide release has become an important global issue due to the significant and continuous rise in atmospheric CO_2 concentrations and the depletion of carbon-based energy resources. Plasmolysis is a very energy-efficient process for reintroducing CO_2 into energy and chemical cycles by converting CO_2 into CO and O_2 utilizing renewable electricity. The bottleneck of the process is that CO remains mixed with O_2 and residual CO_2 . Therefore, efficient gas separation and recuperation are essential for obtaining pure CO, which, via water gas shift and Fischer-Tropsch reactions, can lead to the production of CO_2 -neutral fuels. The idea behind this work is to provide a separation mechanism based on zeolites to optimize the separation of carbon dioxide, carbon monoxide, and oxygen under mild operational conditions. To achieve this goal, we performed a thorough screening of available zeolites based on topology and adsorptive properties using molecular simulation and ideal adsorption solution theory. FAU, BRE, and MTW are identified as suitable topologies for these separation processes. FAU can be used for the separation of carbon dioxide from carbon monoxide and oxygen and BRE or MTW for the separation of carbon monoxide from oxygen. These results are reinforced by pressure swing adsorption simulations at room temperature combining adsorption columns with pure silica FAU zeolite and zeolite BRE at a Si/Al ratio of 3. These zeolites have the added advantage of being commercially available.

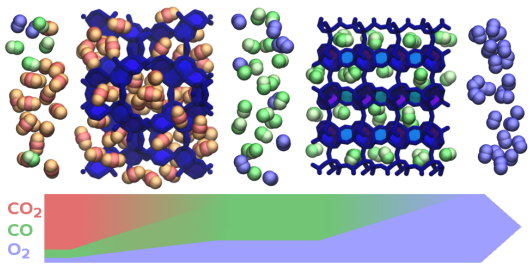

3.1 INTRODUCTION

Reducing greenhouse gas (GHG) emissions has been identified as one of the principal keys to mitigate climate change. It was already pointed out two decades back in the Kyoto Protocol (1997) and reinforced by the Copenhagen Accord (2009) and the 21st Conference of the Parties agreements, also known as the Paris Climate Change Conference (2015). Although the increasing rate of pollutant emissions has been slowed down over the last couple of years, total carbon emissions keep rising, as well as carbon-based fuel demand. [1,2] Thus, finding alternatives to overcome the fossil fuel dependence while at the same time decreasing the GHG emissions is a goal behind both research and industrial efforts. The search for new clean-energy technologies is driven by the challenge of reducing these gas emissions and the desire to make industrial processes environmentally sustainable.

A promising solution is the large-scale replacement of fossil fuel by renewable energy sources. [3–6] Wind or photovoltaics integration into energy-intensive industries is presently hampered by their intermittency in conjunction with the absence of useful storage solutions. Additionally, the direct introduction of sustainable energy into, for example, the value chain of chemical industry remains challenging: heat is the desired form of energy, whereas renewables are frequently harvested in the form of electricity. Therefore, technologies that can convert renewable electricity into storable chemical fuels have attracted tremendous interest. [3–6]

Carbon dioxide is often considered as the key molecule in many strategies to replace conventional energy sources by renewable ones. Although the dissociation of CO_2 is a strongly endothermic process, a sustainable production of CO or syngas, $CO + H_2$ (via the water gas shift reaction: $CO + H_2O \rightarrow CO_2 + H_2$), would be an elegant route to implement renewable energy into the chemical production chain while adding value to the waste gas, CO_2. Synthesis gas is used in the petroleum industry for long-chain liquid hydrocarbons via the Fischer-Tropsch process. [3]

Carbon dioxide splitting mechanisms are energy-costly processes per se; however, nonthermal plasma-assisted dissociation has been proved to be able to reach energy efficiency of 80%. [4–6] These electrical discharges are characterized by nonequilibrium conditions under which electrons, ions, and neutral species have different translational and —in the case of molecules— internal energies. The corresponding energy distribution functions may be described by separate temperatures. Therefore, nonthermal plasmas with unequal electron, gas, and vibrational temperatures provide an entirely different environment for chemical reactions than known from conventional processing under thermal equilibrium. In

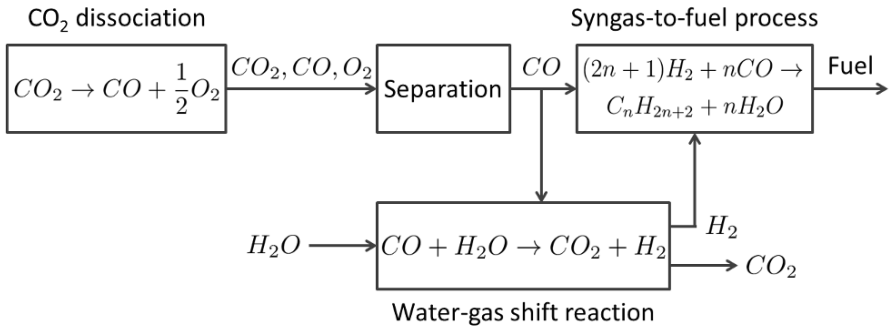

Figure 1: Diagram of the CO_2 -neutral production of fuel.

the case of CO_2 dissociation (to CO and O_2) or CO_2 plasmolysis under nonthermal conditions, the vibrational excitation of CO_2 molecules in a plasma process provides the highest energy-efficient route for its dissociation. To maintain high efficiencies for CO_2 plasmolysis, low CO_2 conversion should be implemented, which results in the production of a CO_2 , CO, and O_2 mixture. Therefore, an extra separation step for obtaining pure CO is necessary before the utilization for both water gas shift and syngas-to-fuel processes, as depicted in the diagram of Figure 1.

Nanoporous materials are commonly used for gas flow sieving. In particular, zeolites have been previously proposed as materials that can perform highly selective separations. This is one of the reasons for their wide use in the industry. Zeolites are well-known porous crystalline structures made of TO_4 tetrahedra, where the tetravalent central atom T is usually a silicon atom. These basic blocks form different building units, which allow zeolites to adopt a large number of topologies, with a wide range of molecular-sized pores and high surface areas.

Molecular simulation is a useful tool for finding suitable materials for gas separation, considering many factors and conditions. Despite the fact that multicomponent simulations in complex systems require significant amounts of time and resources, the evolution of computational algorithms, theoretical approaches, and hardware technology make them affordable nowadays. Additionally, molecular simulations offer some advantages over experiments, providing complete control over the system, producing information at a molecular level, and allowing screenings, which would be unfeasible using other approaches. In this sense, several works of the literature validate simulation procedures in zeolite screenings.[7–13] Essentially, screening can be tackled in one of two ways. The first one is dealing with reduced, preselected sets of porous mate-

rials (up to typically 20) and performing a specific study on the separation of a particular mixture based on sorption and/or diffusion criteria.[7–9] The second one is to perform coarse-grained characterizations of large structure databases to aid further aimed research, but limiting the study to calculations derived from heat of adsorption results.[10,11] Although some recent works have started overcoming these computational restrictions,[12,13] widespread detailed studies remain challenging.

This work focuses on finding an effective separation scheme to capture carbon dioxide and recover carbon monoxide from a gas mixture made of CO_2 (85%), CO (10%), and O_2 (5%). This composition is typical of carbon dioxide splitting, as reported in Fridman,[6] Van Rooij *et al.*,[4] and Bongers *et al.*[14] Pure component adsorption isotherms were calculated for the three gases in most of the zeolite topologies reported in the IZA database.[15] A first approximation to adsorption isotherms for the mixture was obtained applying the ideal adsorption solution theory (IAST).[16] We also simulated adsorption isotherms of binary and ternary mixtures in selected zeolites. Simulations of pressure swing adsorption (PSA) processes were performed to confirm the feasibility of the separation scheme suggested.

3.2 METHODS

Adsorption isotherms were obtained using Monte Carlo simulation in the Grand Canonical ensemble (μVT). This ensemble fixes the average value of the chemical potential, volume, and temperature. Owing to the nature of our systems, the chemical potential of a gas can be directly related to the fugacity, and thereby to the pressure through the fugacity coefficient, using the Peng-Robinson equation of state. RASPA software[17] was used to carry out all simulations. Temperature was set to 298 K, and the pressure values used for the adsorption isotherms were selected in the range of 10^0–10^{12} Pa, depending on the zeolite.

The gas molecules are described by rigid three-site models. Each site is considered as an interacting center with a point charge and effective Lennard-Jones potentials. The parameters used are compiled in Table 1.

Table 1: Lennard-Jones parameters and point charges used for the adsorbates

	ϵ/k_B[K]	σ[Å]	q[e$^-$]
C_{CO_2}	29.993	2.745	+0.6512
O_{CO_2}	85.671	3.017	−0.3256
C_{CO}	16.141	3.658	−0.2424
O_{CO}	98.014	2.979	−0.2744
D_{CO}			+0.5168
O_{O_2}	53.023	3.045	−0.112
D_{O_2}			+0.224

Whereas each site of the carbon dioxide molecule corresponds to an atom

center, for carbon monoxide and oxygen, a central dummy pseudo-atom (D_{CO} and D_{O_2}, respectively) is defined to reproduce their first nonzero electrostatic moment. These dummies are therefore interacting centers with nonzero point charges, but their Lennard-Jones parameters and mass are set to zero. The point charges and Lennard-Jones parameters for carbon dioxide are taken from Garcia-Sanchez *et al.* [18] and those for carbon monoxide and oxygen from Martin-Calvo *et al.* [19,20]

Zeolites are considered rigid, and, for the initial screening, we focused only on pure silica structures. Among all of the zeolite topologies contained in the IZA database, [15] we selected a subset of 174 structures, avoiding the structures defined as zero-dimensional and also the structures containing OH groups. The point charges for the atoms of the framework (q_{Si} = +0.786 e^- and q_O = −0.393 e^-) are also taken from Garcia-Sanchez *et al.* [18] Further simulations in selected zeolites were performed considering not only silicon atoms in their structures, but also aluminum atoms in the lattices. Given that Al atoms and oxygen atoms bridging silicon and aluminum atoms (q_{Al} = +0.4859 e^-, q_{O_a} = −0.4138 e^-) [18] differ from Si atoms and oxygen atoms linking two Si atoms, nonframework cations have to be introduced to compensate the net charge. One sodium cation, with charge q_{Na} = +0.3834 e^-, [18] is introduced for each T central silicon atom replaced by an aluminum atom.

Adsorbate–adsorbate and adsorbate–adsorbent atomic interactions are described by Lennard-Jones and Coulombic potentials. Lennard-Jones potentials are cut and shifted to zero at a cutoff radius of 12 Å. Coulombic interactions were calculated using Ewald summation. Interactions between framework atoms are not taken into account because their positions are kept fixed. Lennard-Jones interactions of guest molecules with framework silicon atoms are neglected because their dispersive forces with the oxygen atoms prevail. Cross-interactions are collected in Table 2. They imply that the carbon monoxide model leads to strong interactions with sodium cations to account for the significant quadrupole moment of this molecule. Other interactions not specified in the table are calculated using Lorentz-Berthelot rules. Additional Lennard-Jones parameters for cross-terms between adsorbate molecules and sodium cations are also summarized in Table 2. In terms of dispersion forces, O_a atoms are assumed

Table 2: Cross-interactions Lennard-Jones parameters

	ϵ/k_B[K]	σ[Å]
C_{CO_2}–O_{zeo} [18]	37.595	3.511
O_{CO_2}–O_{zeo} [18]	78.98	3.237
C_{CO}–O_{zeo} [21]	40.109	3.379
O_{CO}–O_{zeo} [21]	98.014	2.979
C_{CO}–Na [21]	369.343	2.332
O_{CO}–Na [21]	579.793	2.212
O_{O_2}–Na [21]	241.284	2.06

to behave identically to Si–O–Si oxygen atoms. All of the forcefields used in this work are parameterized to reproduce adsorption properties in zeolites and have been extensively validated.[19–21] The ideal adsorption solution theory (IAST)[16] is used to predict the mixture behavior from modeling pure compound adsorption using the Dual-Site Langmuir equation[22] in Gaiast software.[23] We calculated the adsorption for the $CO_2/CO/O_2$ ternary mixture and for the remaining CO/O_2 binary mixture once the molecules of carbon dioxide are removed. The preferential adsorption of one gas over the others is identified by adsorption selectivity. This property (S_{ij}) is defined as the ratio between the adsorbed amount (x_i) and the molar fraction (y_i) of component i over the adsorbed amount (x_j) and the molar fraction (y_j) of component j.

Pressure swing adsorption (PSA) simulations have been carried out with PSASIM software[24] in those structures selected to perform the desired separations. It has been assumed that the PSA processes are adiabatic to resemble the usual conditions of industrial PSA cycles. It is also assumed that the adsorbent crystals are agglomerated in pellets and that mass transfer between the gas and the adsorbent is controlled by macropore diffusion, neglecting intracrystalline resistance.[25]

3.3 Results and Discussion

To design the separation process for the mixture composed of carbon dioxide (85%), carbon monoxide (10%), and oxygen (5%), we performed two independent screenings. The first screening was meant to identify the optimal structure for the separation of carbon dioxide from carbon monoxide and oxygen, as carbon dioxide is more strongly adsorbed in all structures, and a second screening was meant to separate the two remaining gases. Figure 2 shows the adsorption selectivity of carbon dioxide over the second most adsorbed species, either carbon monoxide or oxygen, as a function of the specific surface area of the zeolites and as a function of the effective pore diameter. A table listing the numerical values is also provided in the Appendix B (Table B1). The adsorption selectivity is obtained from the adsorption isotherms of the ternary mixture, at operating conditions of 25 °C (298 K) and 1–10 atmospheres (10^5–10^6 Pa). The surface area of the zeolites is calculated with the RASPA code by rolling an atom over the surface of the structure. The fraction of overlap with the structure is calculated from the points that are generated on a sphere around each atom of the framework. This fraction is multiplied by the area of the sphere, and the summation over all framework atoms provides the geometric surface area. The optimal structure for the separation sought should provide a large surface area and at the same

time high selectivity for carbon dioxide over the other two components of the mixture. As seen in Figure 2, these two properties tend to be inversely related because physisorption for small gases usually involves confinement. [26] A few structures stand out because they combine high selectivity, reasonable surface areas, and additionally big pore diameters, which favor the mobility of the guest molecules: MRE and ATN zeolites have the largest selectivities for carbon dioxide but low specific surface area and moderate and very low pore diameter, respectively. Both them are one-dimensional zeolites with non-interpenetrating pores of 10-membered ring (10-MR) 5.6×5.6 $Å^2$ for MRE and 8-MR 4.0×4.0 $Å^2$ for ATN. Therefore, the windows in these structures are far narrower compared with the opening in the FAU-type framework, which is almost 7.4 Å wide. The pores of FAU are also defined by 12-MR, leading into larger cavities of 12 ao in diameter. These cavities are surrounded by 10 sodalite cages (truncated octahedra), which are connected on their hexagonal faces. The sodalite cages are inaccessible to the molecules of carbon dioxide, carbon monoxide, and oxygen. On the contrary, RWY (also formed by 12-MR channels) is the zeolite with the largest pore diameter and high surface area, and therefore high storage capacity for carbon dioxide, but it has relatively low separation selectivity. The structures of MRE, ATN, FAU, and RWY are depicted in Figure B1 of the Appendix B.

On the basis of Figure 2, we mentioned the importance of effective pore diameters because they strongly affect molecular diffusion. The effective pore diameter is obtained from the analysis of the pore size distribution (PSD) that we have calculated for each empty framework. It is defined as the smallest pore able to host a molecule of adsorbate having a kinetic radius larger than 2.298 Å if the PSD peak associated with that pore represents at least 15% of the frequency of the most common pore. It should be large enough to enable diffusion but small enough for carbon dioxide adsorption. We also considered the selectivity related to the capacity of zeolites for capturing carbon dioxide. Figure B2 in the Appendix B shows selectivity curves for the adsorbed loading of carbon dioxide corresponding to the range of pressures between 1 and 10 atm. The choice of high selectivity together with the relevant carbon dioxide uptake is necessary given that carbon dioxide is present in large excess in the considered mixtures. Otherwise, it would still be present in substantial amounts after the carbon dioxide removal step. Therefore, on the basis of Figures 2 and B2b, zeolite FAU represents a compromise for this separation between selectivity for carbon dioxide of 17–18 with uptakes up to 5.2 mol/kg at the operating conditions (Figure B3 of the Appendix B) and the still relatively large specific surface area (1020.88 m^2g^{-1}) and effective pore diameter (10.14 Å).

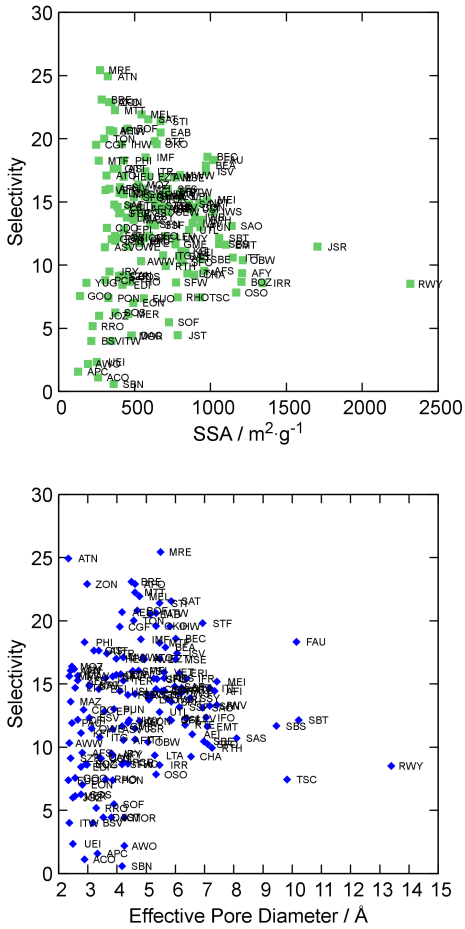

Figure 2: Maximum adsorption selectivity of carbon dioxide over the second most adsorbed species (carbon monoxide or oxygen) as a function of the specific surface area (top) and the effective pore diameter (bottom). Selectivity values were obtained at 10^5–10^6 Pa, from the adsorption isotherms of the ternary mixtures at 298 K obtained by applying IAST.

FAU can also be used to separate our ternary mixture at temperatures higher than 298 K. However, a temperature increase of 100 K also requires increasing the pressure by one order of magnitude to maintain the carbon dioxide capture but entails a notable decrease in selectivity toward carbon dioxide (see Figure B4 of the Appendix B). Similarly, a decrease in temperature of 100 K at constant pressure (10^5 and 10^6 Pa) increases the adsorption selectivity toward carbon dioxide by one order of magnitude (Figure 3).

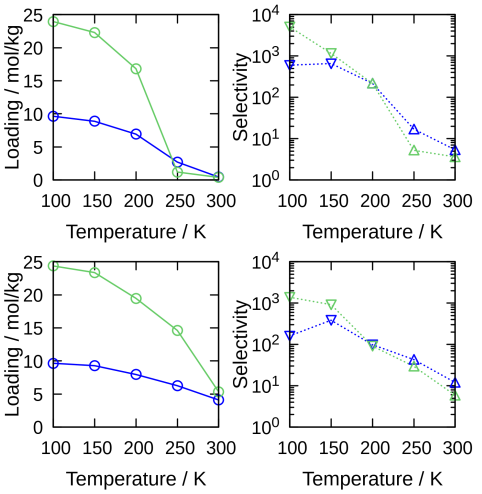

Figure 3: Adsorption of carbon dioxide (left) and adsorption selectivity in favor of carbon dioxide (right) in RWY (green) and FAU (blue) zeolites versus temperature. Both adsorption loading and adsorption selectivity are taken from adsorption isotherms resulting from molecular simulation of the ternary mixtures at values of pressure of 10^5 (up) and 10^6 Pa (down). In all cases, the adsorption selectivity depicted is the one obtained for the most unfavorable case between carbon dioxide over carbon monoxide (up-triangles) or oxygen (down-triangles).

The adsorption selectivity was also calculated for RWY under these operating conditions. We selected the zeolite with the largest effective pore to evaluate the trade-off between adsorption capacity and selectivity. It is interesting to note that this compromise is much lower at 10^6 Pa than at 10^5 Pa. Surprisingly enough, at 200 K and 10^6 Pa, the adsorption selectivity in both zeolites is almost the same, whereas RWY doubles FAU in adsorption capacity. Unfortunately, under operating conditions of 300 K and 10^5–10^6 Pa, the selectivity in RWY is always lower than that in FAU, thus capturing significant traces of carbon monoxide. Although, based on the combination of capacity, selectivity, specific surface area, and effective pore diameter, we rely upon FAU for this separation, other structures such as BEA, BEC, ISV, and GIS could also be candidates for it. Like FAU, the first three framework topologies have a three-dimensional large 12-MR pore system: both BEA and ISV are tetragonal structures with systems of 12-MR interconnected straight channels with cylindrical cavities,whereas BEC (tetragonal) and FAU (cubic) contain large cages connected by 12-MR windows. GIS also has a three-dimensional intersecting-channel pore system but connectedthrough 8-MR windows. The adsorption isotherms of the ternary mixture for these structures are collected in Figure B5 of the Appendix B.

The mixture, after complete removal of carbon dioxide, is formed by CO (67%) and O_2 (33%). As mentioned above, the separation of these two components of the mixture is tricky because of their similarity in size, shape, and polarity. We performed a screening based on the adsorption isotherms of the binary mixtures in all zeolites. The screening shows that none of these zeolites can separate completely the two components of the mixture at the operating conditions initially considered, that is, 300 K and 10^5–10^6 Pa. Although the selectivity is very low, we found that under these conditions of temperature and pressure, zeolites such as AEI preferentially adsorbed oxygen over carbon monoxide, whereas the adsorption selectivities for zeolites such as BRE, THO, and RTE are toward carbon monoxide (Figure B6 of the Appendix B). In zeolites such as MTW, the increase in pressure once adsorption gets significant leads to reasonable values of adsorption selectivity, always in favor of molecular oxygen (Figure 4, top). However, for other zeolites such as BRE, the increase in pressure at a given temperature leads to an inversion of the selectivity (Figure 4, bottom). Hence, contrary to most structures, selectivity toward carbon monoxide decreases when pressure increases, and at 10^8 Pa, the preferential adsorption of the structure switches from carbon monoxide to oxygen. This is probably due to size entropy effects because oxygen packs more efficiently than carbon dioxide in all structures at higher molecular loadings. The same effect is observed when decreasing

the temperature to 100 K in the pressure range 10^5–10^6 Pa.

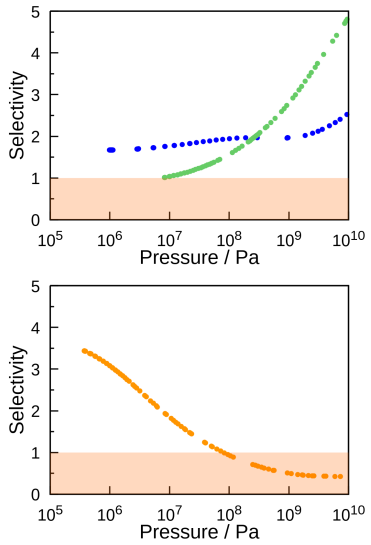

Figure 4: Top: Adsorption selectivity of oxygen over carbon monoxide as a function of pressure in MTW (green) and AEI (blue). Bottom: Adsorption selectivity of carbon monoxide over oxygen in BRE (orange). Note the inversion of preferential adsorption at 10^8 Pa. The adsorption selectivity is obtained from the binary adsorption isotherms of carbon monoxide (67%) and oxygen (33%) obtained by applying IAST.

In search of a structure with better separation performance under the initial operating conditions, we turned to aluminum containing MTW and BRE structures for which we performed additional simulations using sodium as nonframework cations. First, we generated low-energy structures with 2 and 4 aluminum atoms per unit cell. To this end, the first silicon by aluminum substitution is determined randomly. The following sequential silicon by aluminum substitution selects those atoms whose average distance to existing aluminum atoms is maximized, provided the substitution observes Löwenstein's and Dempsey's rules, which prevents Al–O–Al linkages and minimizes the number of Al–O–Si–O–Al elements, respectively. [27,28]

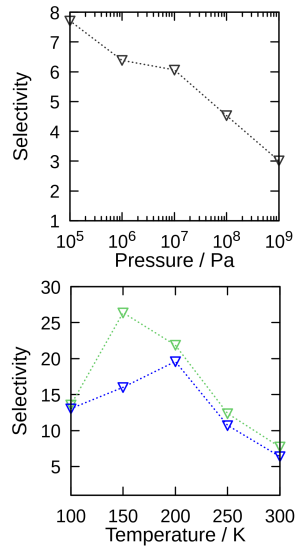

Figure 5: Adsorption selectivity of carbon monoxide over oxygen in BRE zeolite with 4 Na^+/Al pairs per unit cell as a function of pressure at 298 K (top) and as a function of temperature (bottom) at 10^5 Pa (green) and 10^6 Pa (blue). Isotherms to calculate selectivity come from molecular simulations.

The adsorption isotherms for the binary mixtures in the two MTW structures containing cations lead to smaller values of selectivity compared to those obtained in the pure silica structures, even favoring

Table 3: Model parameters and operating conditions in PSA simulations

PSA cycle	I	II
Adsorbent	FAU	BRE
Feed composition, CO_2 /CO/O_2 , %v/v	85/10/5	0/64.7/35.3
Temperature, K	300	300
P_{high}, P_{low}, bar	2, 0.1	2, 0.1
Bed length, m	1	1
Cycle time, min	8	8
Bed porosity	0.4	0.4
[a]Extracrystalline porosity	0.3	0.3
[b]Particle density, kg m^{-3}	940	1395
Particle radius, m	7×10^{-4}	7×10^{-4}
[c]Molecular diffusivity, 10^{-6} m^2 s^{-1}	8.4/8.5/8.6	-/10.1/10.1
Tortuosity	3	3
[c]μ, Pa s	1.5×10^{-5}	1.9×10^{-5}
[d]Adsorbent heat capacity, J kg^{-1} K^{-1}	1000	1000
[e]Isosteric heats, CO_2 /CO/O_2 , kJ mol^{-1}	17.3/9.99/9.31	–/28.8/21

[a] Taking a typical zeolitic pellet extracrystalline porosity from Tomita *et al.* [29]
[b] Calculated as crystal density ×(1 – xtracrystalline porosity).
[c] Calculated with AspenPlus.
[d] Jiang *et al.* 2017. [30]
[e] Average values calculated with the Van't Hoff equation between zero loading and the loading at feed conditions.

carbon monoxide below 10^{10} Pa. In other words, the presence of cations in this structure worsens the separation obtained in the pure silica structure. On the contrary, the presence of sodium cations in BRE-type structures improves the adsorption selectivity compared with those in the pure silica structure. As shown in Figure 5, in this case, the selectivity improves almost three times, and its absolute value increases even more at low temperatures. Therefore, the presence of sodium cations in BRE enhances the adsorption of carbon monoxide and worsens the adsorption of oxygen (Figure B7 of the Appendix B). Using both zeolite capacity and adsorption selectivity, we can provide different separation schemes that are depicted in Figure 6. Under operating conditions of 300 K and 10^5–10^6 Pa, the most efficient separation scheme using the screened zeolites consists in employing FAU for carbon dioxide removal, followed by using BRE for the separation of carbon monoxide from oxygen. BRE containing aluminum atoms and sodium cations preferentially adsorbs carbon monoxide, letting oxygen pass through. These results could be fur-

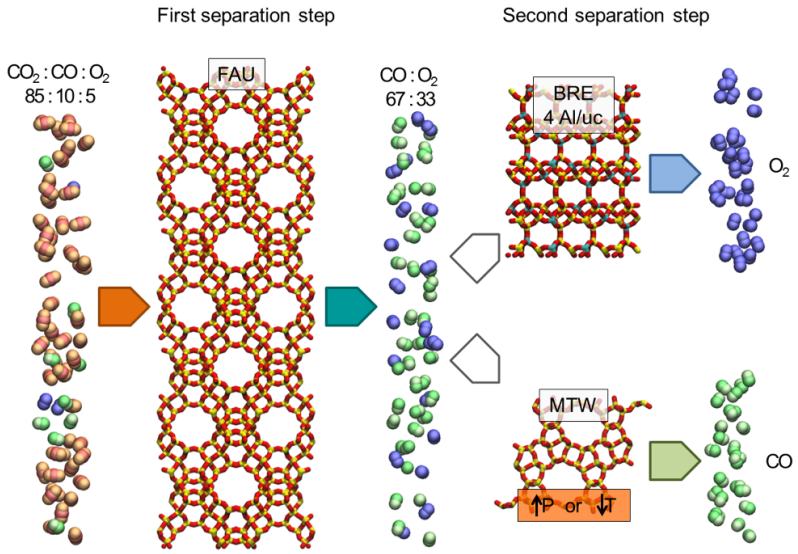

Figure 6: Separation scheme for the mixture of CO_2 (85%), CO (10%), and O_2 (5%) using zeolites. Two options are available for the second separation step.

ther improved by working at temperatures lower than 300 K. On the contrary, capturing oxygen while carbon monoxide flows through can be achieved by using pure silica MTW zeolite, but it would be necessary to relax the operating conditions by increasing pressure and/or decreasing temperatures.

To verify the capabilities of the selected adsorbents in the desired separations under operating conditions, PSA simulations were performed for the removal of CO_2 from a mixture of CO_2 (85%), CO (10%), and O_2 (5%) using FAU zeolite as the adsorbent and the concentration of CO in the resulting light product (containing CO and O_2) using BRE zeolite with 4 Al/uc. Model parameters and operating conditions used in the simulations are shown in Table 3. For the first separation, a typical PSA cycle for hydrogen purification is considered,[29] which is called PSA cycle I henceforth. For the second separation, a modification of the first cycle, including a rinse (RIN) step to increase the concentration of CO in the heavy product,[31] is considered, which is called PSA cycle II. Bed length and cycle time are also taken from Tomita et al.[29] A scheme, time schedule, and pressure history of these cycles are given in Figure B8 in the Appendix B. Details about the working of these cycles are available elsewhere.[31]

The multicomponent adsorption isotherms for the PSA simulations are

obtained by applying the IAST method to the pure component isotherms. A comparison between the pure component fitted isotherms and molecular simulation data is shown in Figure B9. The resulting Langmuir parameters are shown in Table B2.

PSA cycle I is designed to meet the two following specifications: (i) CO_2 concentration in the light product (L) below 0.5% v/v, and (ii) CO recovery in the light product above 85%. The feed gas velocity in the adsorption (ADS) step (u_F), the high pressure of the cycle (P_{high}), and the final pressure of the provide purge (P_{PP}) step are considered to carry out a parametric study to measure their influence on CO_2 concentration and CO recovery in the light product. CO_2 productivity in the heavy product (H) is also calculated to evaluate the process throughput. The results of the parametric study (listed in Table B3 in the Supporting Information) show that an increase in P_{high} from 1 to 2 bar allows reaching high purity of the light product and high CO recovery simultaneously. The separation performance improves if P_{PP} is increased from 0.9 to 1.0 bar. Increasing the feed gas velocity results, on the one hand, in lower product purity because the adsorption front of CO_2 advances more along the bed in the ADS step, but, on the other hand, in higher recovery because the bed has a higher loading of CO_2 during the regeneration and therefore a lower loss of light compounds in the heavy product. Designing the PSA cycle I with P_{high} = 2 bar, P_{PP} = 1 bar, and u_F = 0.0064 m s^{-1} leads to the highest CO_2 productivity (0.1 kg kg^{-1} h^{-1}) and CO recovery (87.6%) for the runs fulfilling the purity specification. The resulting heavy product has the following composition: CO_2 (98.1%), CO (1.4%), and O_2 (0.5%). This stream can be recycled to the plasma reactor to avoid CO losses in PSA cycle I and to reuse the CO_2 removed.

From Figure 7, it is clear that the concentration of CO_2 is very low in the final part of the column when ending the ADS step, and there is a high concentration of CO and O_2 in the light product. Concurrently, the concentration of CO_2 at the end of regeneration (end of RP step) is very high. The temperature profiles show that the bed heats up notably as the CO_2 adsorption front advances along the bed because of its high concentration in the feed, whereas it gets cooled during the regeneration due to desorption.

The light product of PSA cycle I is then introduced as a feed stream in PSA cycle II at the same pressure (2 bar). To simplify the design, the presence of CO_2 in this stream (below 0.5%) is neglected. On this basis, the composition of the feed mixture for PSA cycle II is CO (65.67%), and O_2 (34.33%). The design specifications for this cycle are CO purity and recovery in the heavy product above 98%. After performing the same parametric analysis as for the previous cycle, it was found that the design specifications can be achieved

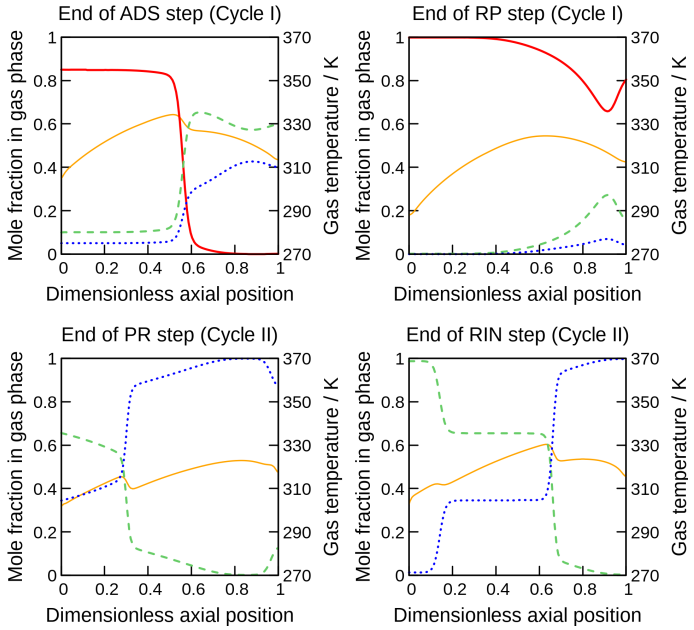

Figure 7: Top: spatial profiles of composition and temperature at the end of the ADS step (left) and at the end of the RP step (right) in PSA cycle I. Bottom: spatial profiles of composition and temperature at the end of the PR step (left) and at the end of the RIN step (right) in PSA cycle II. CO_2 plotted as a solid red line, CO as a dashed green line, O_2 as a dotted blue line, and temperature as a solid orange line.

with a P_{PP} = 0.8 bar, and a feed gas velocity of the ADS and rinse (RIN) steps of 0.022 m s^{-1}. Results at the onset of the light product production (end of the PR step) and at the end of the light product production (end of the RIN step) in PSA cycle II, shown in Figure 7, provide CO in the heavy product at a 98.73% purity with a 98.04% CO recovery, along with a productivity of 0.0575 kg CO kg^{-1} h^{-1}. Moreover, the O_2 purity in the light product is 96.3%, with an O_2 recovery of 97.6% and a productivity of 0.0342 kg O_2 kg^{-1} h^{-1}. The movement of the CO profile between the end of PR and RIN steps is indicative of the gradual loading of the bed with CO while releasing a light product with low CO concentration. The bed inlet reaches a very high concentration of CO due to the introduction of a heavy product in the RIN step. This loading is recovered as high-purity CO in the heavy product at the regeneration step. The good performance of this separation ultimately stems from the high selectivity of BRE zeolite toward CO in CO/O_2 mixtures, combined with the high linearity of the isotherms. Considering the whole industrial process,

our results show that the desired separations can be carried out efficiently by PSA using the adsorbents we propose.

3.4 Conclusions

Molecular simulation, in combination with the ideal adsorption solution theory, allows zeolite screening for the separation under mild operating conditions of a mixture of gases from carbon dioxide dissociation. On the basis of our screening, we suggest the use of FAU for removing CO_2 and BRE at 4 Al/uc to capture CO as the optimal zeolite framework combination for this separation. Conditions for a PSA process were optimized to enable an efficient separation. In the first PSA cycle (CO_2 removal), we recommend a high pressure of 2 bar, final pressure of the PP step of 1.0 bar and feed gas velocity of 0.0064 m s^{-1}. The composition of the heavy product extracted would thus be 98.1% CO_2 , 1.4% CO, and 0.5% O_2 . This stream could then be recycled to the plasma reactor to avoid CO losses and to reuse the CO_2 removed. The second PSA cycle coupled to the first should set the final pressure of the PP step to 0.8 bar, and feed gas velocities of the ADS and RIN steps to 0.022 m s^{-1}. This yields 98.04% CO recovery at 98.73% purity with a productivity of 0.0575 kg CO kg^{-1} h^{-1}. As for O_2 , a 97.6% recovery at 96.3% purity is calculated with a productivity of 0.0342 kg O_2 kg^{-1} h^{-1}.

It is worth noting that both FAU and BRE zeolites are already commercially available and the suggested process improvement could be straightforwardly implemented by the industry. The idea of separation mechanisms based on adsorption with zeolites is also transferable to other separations of industrial interest like olefin/paraffin separation in the European Petrochemical Industry. Market penetration of this technology in this area (ethane/ethylene, propane/propylene, etc.) would bring about substantial reductions in energy consumption, paving the way for the development of long-term research strategies.

Bibliography

[1] Jackson, R. B.; Canadell, J. G.; Le Quere, C.; Andrew, R. M.; Korsbakken, J. I.; Peters, G. P.; Nakicenovic, N. *Nature Climate Change* **2016**, *6*, 7–10.

[2] Le Quéré, C. et al. *Earth System Science Data* **2016**, *8*, 605–649.

[3] Lebouvier, A.; Iwarere, S. A.; d'Argenlieu, P.; Ramjugernath, D.; Fulcheri, L. *Energy & Fuels* **2013**, *27*, 2712–2722.

[4] Van Rooij, G.; van den Bekerom, D.; den Harder, N.; Minea, T.; Berden, G.; Bongers, W.; Engeln, R.; Graswinckel, M.; Zoethout, E.; van de Sanden, M. *Faraday discussions* **2015**, *183*, 233–248.

[5] Brehmer, F.; Welzel, S.; van de Sanden, M. C. M.; Engeln, R. *Journal of Applied Physics* **2014**, *116*, 123303.

[6] Fridman, A. *Plasma chemistry*; Cambridge university press, 2008.

[7] Krishna, R.; van Baten, J. M. *Journal of Membrane Science* **2010**, *360*, 323–333.

[8] Krishna, R.; van Baten, J. M. *Chemical Engineering Journal* **2007**, *133*, 121–131.

[9] Peng, X.; Cao, D. *Aiche Journal* **2013**, *59*, 2928–2942.

[10] Lin, L. C.; Berger, A. H.; Martin, R. L.; Kim, J.; Swisher, J. A.; Jariwala, K.; Rycroft, C. H.; Bhown, A. S.; Deem, M. W.; Haranczyk, M.; Smit, B. *Nature materials* **2012**, *11*, 633–641.

[11] Braun, E.; Zurhelle, A. F.; Thijssen, W.; Schnell, S. K.; Lin, L.-C.; Kim, J.; Thompson, J. A.; Smit, B. *Molecular Systems Design & Engineering* **2016**, *1*, 175–188.

[12] Matito-Martos, I.; Martin-Calvo, A.; Gutierrez-Sevillano, J. J.; Haranczyk, M.; Doblare, M.; Parra, J. B.; Ania, C. O.; Calero, S. *Phys. Chem. Chem. Phys.* **2014**, *16*, 19884–19893.

[13] Jeong, W.; Kim, J. *The Journal of Physical Chemistry C* **2016**, *120*, 23500–23510.

[14] Bongers, W.; Bouwmeester, H.; Wolf, B.; Peeters, F.; Welzel, S.; van den Bekerom, D.; den Harder, N.; Goede, A.; Graswinckel, M.; Groen, P. W. *Plasma processes and polymers* **2017**, *14*.

[15] Baerlocher, C.; McCusker, L. Database of Zeolite Structures. `http://www.iza-structure.org/databases/`.

[16] Myers, A.; Prausnitz, J. M. *Aiche Journal* **1965**, *11*, 121–127.

[17] Dubbeldam, D.; Calero, S.; Ellis, D. E.; Snurr, R. Q. *Mol. Simul.* **2016**, *42*, 81–101.

[18] Garcia-Sanchez, A.; Ania, C. O.; Parra, J. B.; Dubbeldam, D.; Vlugt, T. J. H.; Krishna, R.; Calero, S. *J. Phys. Chem. C* **2009**, *113*, 8814–8820, and references therein.

[19] Martin-Calvo, A.; Lahoz-Martin, F. D.; Calero, S. *J. Phys. Chem. C* **2012**, *116*, 6655–6663.

[20] Martin-Calvo, A.; Garcia-Perez, E.; Garcia-Sanchez, A.; Bueno-Perez, R.; Hamad, S.; Calero, S. *Phys. Chem. Chem. Phys.* **2011**, *13*, 11165–11174.

[21] Martin-Calvo, A.; Gutierrez-Sevillano, J. J.; Parra, J. B.; Ania, C. O.; Calero, S. *Phys. Chem. Chem. Phys.* **2015**, *17*, 24048–24055.

[22] Myers, A. *Aiche Journal* **1983**, *29*, 691–693.

[23] Rodríguez-Gómez Balestra, S.; Bueno-Perez, R.; Calero, S. GAIAST. 2016.

[24] Delgado, J. A.; Águeda, V. I.; Uguina, M. A.; Brea, P.; Grande, C. A. *Chemical Engineering Journal* **2017**, *326*, 117–129.

[25] Vemula, R. R.; Sircar, S. *Aiche Journal* **2017**, *63*, 4066–4078.

[26] Krishna, R.; Smit, B.; Calero, S. *Chemical Society Reviews* **2002**, *31*, 185–194.

[27] Löwenstein, W.; Lowenstein, M. *American Mineralogist* **1954**, *39*, 92–96.

[28] Dempsey, E. *J. Soc. Chem. Ind., London* **1968**, *293*.

[29] Tomita, T.; Sakamoto, T.; Ohkamo, U.; Suzuki, M. The effects of variables in fourbed pressure swing adsorption for hydrogen purification. Proceedings of the Second Engineering Foundation Conference on Fundamentals of Adsorption, Liapis, AI (ed), Engineering Foundation, Nueva York.

[30] Jiang, Y.; Ling, J.; Xiao, P.; He, Y.; Zhao, Q.; Chu, Z.; Liu, Y.; Li, Z.; Webley, P. A. *Chemical Engineering Journal* **2017**, *334*, 2593–2602.

[31] Delgado, J. A.; Agueda, V. I.; Uguina, M. A.; Sotelo, J. L.; Brea, P. *Adsorption* **2015**, *21*, 107–123.

CHAPTER 4

MOLECULAR SIEVES FOR THE SEPARATION OF HYDROGEN ISOTOPES

J. Perez-Carbajo, J. B. Parra, C. O. Ania, P. J. Merkling, and S. Calero

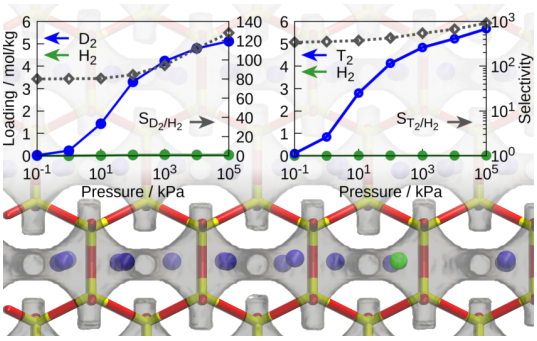

Stable molecular hydrogen isotopes, D_2 and T_2, are both scarce and essential in several energy, industrial and large-scale, fundamental research applications. Due to the chemical similarity of these isotopes, their extraction and purification from hydrogen has relied for decades on expensive and energy-demanding processes. However, factoring in the phenomenon of quantum sieving could provide a new route for these separations. In this work, we have explored how to separate hydrogen isotopes by adsorption taking these quantum effects into account. To this end, we have conducted adsorption measurements to test our deuterium model, and performed a widespread computational screening over 210 pure-silica zeolites for D_2:H_2 and T_2:H_2 separations. Based on low-coverage adsorption properties, a reduced set of zeolites have been singled out and their performance in terms of adsorption capacity, selectivity and dynamic behavior have been assessed. Overall, the BCT-type zeolite clearly stands out for highly selective separations of both D_2 and T_2 over H_2, achieving the highest reported selectivities at cryogenic temperatures. We also identified other interesting zeolites for the separation of hydrogen isotopes that offer an alternative way to tackle similar isotopic separations by an aimed selection or design of porous materials.

4.1 INTRODUCTION

Separation of hydrogen isotopes is one of the most challenging current research areas, especially from an industrial point of view. The natural abundances of non-synthetic hydrogen isotopes are about 156 ppm for deuterium (D) and only traces for tritium (T).[1,2] Despite their scarcity, they both turn out to be crucial in several technological and industrial fields. Deuterium is employed in isotopic tracing for medical treatment and detection, nuclear magnetic resonance and neutron scattering techniques, and in development of deuterated drugs. Tritium has uses in the armament industry and in analytical chemistry. They are both used as raw materials in tokamak-type nuclear fusion reactors, where deuterium is also a key component for moderating neutrons. In fact, the yield of hydrogen isotopes for nuclear feedstock is under 10%, so recovering them from waste is crucial to increase the efficiency and reduce nuclear residues. Additionally, even if hydrogen is the desired product, extraction of deuterium from hydrogen bulk might be economically attractive, while for the case of tritium its environmental impact may make this operation a mandatory requirement.

Chemical similarities between H_2, D_2, and T_2 have been traditionally considered a major obstacle for the separation by molecular sieving methods. Other methods have therefore been used to carry out that separation: Cryogenic distillation, proton exchange reactions, thermal diffusion, centrifugation, electrolysis, or chromatography, among others.[3,4] These techniques are quite energy consuming (the first three enumerated), and hence econonomically expensive, or have a low yield (the last three mentioned). Thus, a cost-effective method with a high separation throughput would be desirable. In the mid-nineties, Beenakker *et al.*[5] published a study on quantum sieving, an effect arising when the difference between diameters of the pore and of the molecule approaches the de Broglie wavelength. Under these conditions, similar molecules with different masses present different adsorption behaviors that can lead to heavier molecules in confined channels experiencing less repulsive interaction energies than lighter ones; this also affects diffusion properties in favor of the heavier isotope. That finding helped understanding the separation of isotopes in nanoporous materials. From then on, several works have explored hydrogen isotope separation in carbon nanotubes or sieves,[6–12] zeolites,[6,11,13–21] and metal-organic frameworks (MOFs).[17,22–27] Although single-walled carbon nanotubes and zeolites were the first materials to be investigated, main research efforts in the last years have been focused on MOFs, for which increasingly higher selectivities have been obtained: Teufel et al. reported a selectivity of 7.5 at 60 K;[24] Weinrauch *et*

al. obtained 36.9 at 80 K;[26] Kim *et al.* reported selectivities of 13.6 at 40 K[28] and ~26 at 77 K;[27] recently even higher selectivities have been announced at extremely low temperatures by Cao *et al.*, who reported selectivity of 41.4 at 20 K,[29] or Han *et al.*, who found a selectivity of 53.8 at 25 K.[30] Admittedly, flexibility and breathing effects in MOFs are achieving promising results, but zeolites, advantageously with respect to MOFs, are known for their thermal stability, economical production and scalability. In this sense, to the best of our knowledge, most studies on zeolites have only examined a few specific structures, obtaining moderate selectivy values (~6 by Giraudet *et al.*,[21] and 8.8 by Xiong *et al.*[20]), so a widespread screening is lacking.

This work performs a computational investigation on 210 zeolites to find the best candidates for the separation of D_2 or T_2 from H_2 at temperatures running from cryogenic up to 200 K, and in the $10^{-1} - 10^5$ kPa pressure range. To that end, we have validated and used a Lennard-Jones (L–J) potential with Feynman–Hibbs quantum corrections for H_2, and then derived the corresponding L–J parameters for the isotopes. D_2 interactions with pure silica zeolites have been validated with experimental adsorption isotherms at cryogenic temperatures. This study comprises an exhaustive comparison of hydrogen isotopes adsorption characteristics at low loading, and then both dynamic and static analysis for selected zeolites to recommend the structures and working conditions leading to a highly-selective hydrogen isotope separation.

4.2 Methods

4.2.1 Experimental procedures

Experimental gas adsorption isotherms on pure silica zeolites (MFI and ITQ-29) at cryogenic temperatures were performed in a volumetric analyzer provided with a turbomolecular vacuum pump and three pressure transducers (0.13, 1.33 and 133 kPa, uncertainty within 0.15% of each reading). The volumetric analyzer was coupled to a helium cryocooler (Gifford-McMahon) that allows a fine temperature control between 25–325 K with a stability of ±0.1 K. Isotherms were recorded in the pressure range between 10^{-2} and 120 kPa. Before the analysis, zeolites were outgassed under dynamic vacuum at 623 K (1K/min) overnight. All gases were supplied by Air Products at an ultrahigh purity (i.e., 99.995%). MFI and ITQ-29 (LTA topology) pure silica zeolites were supplied by the Institute of Chemical Technology (ITQ), being both structures nearly completely pure SiO_2 crystals.

4.2.2 Computational methods, models, and force field

Energies between adsorbates and of adsorbates with zeolites are dominated by electrostatic and van der Waals interactions. Electrostatic interactions are

$$U_{\mathrm{F-H}}(r_{ij}) = U_{\mathrm{L-J}}(r_{ij}) + \frac{\hbar^2}{24\mu_{ij}k_BT}\left[U''_{\mathrm{L-J}}(r_{ij}) + \frac{2U'_{\mathrm{L-J}}(r_{ij})}{r_{ij}}\right] \quad (1)$$

modeled by Coulombic potentials, using Ewald summation to compute the long-range terms. On the other hand, Lennard–Jones (L–J) potentials are used to describe the van der Waals interactions. Quantum corrections have been added to Lennard–Jones potentials via an effective potential based on the Feynman-Hibbs variational approach [31] to reproduce the quantum behavior of hydrogen isotopes at cryogenic temperatures. This approach has been repeatedly reported as an effective way to study the adsorption of quantum H_2, D_2, and T_2 in zeolites and other nanoporous materials. [9,13,16,19,32–37] Lennard–Jones potential with Feynman-Hibbs corrections is cut and shifted to zero at a cutoff radius of 12 Å.

Zeolite lattices are considered rigid and only formed by interconnected SiO_4 tetrahedra. Zeolites are known for their relatively high rigidity that leads to small temperature-induced [?] and/or adsorption-loading induced changes. [?] Thus, both from the point of view of the low temperatures used in this work and the tiny mass of the molecules adsorbed, the rigidity assumption appears justified. The coordinates of the framework atoms are taken from IZA database [38] except for ISW, ITE, ITW, LTA, and MWW whose pure silica atom coordinates have been provided by ITQ: ITQ-7, [39] ITQ-3, [40] ITQ-12, [41] ITQ-29, [42] and ITQ-1, [43] respectively. Static point charges for all of them (q_{Si} = +0.786 e^- and q_O = −0.393 e^-) stem from Garcia-Sanchez *et al.* [44] Lennard–Jones interactions between framework atoms need not be considered in a rigid framework.

Hydrogen is modeled as a single, uncharged Lennard–Jones center, taken from van den Berg *et al.*, [45] and modified by Deeg *et al.* [46] to make it a Feynman-Hibbs potential. The Feynman-Hibbs parameters defining the interaction with zeolites have also been developed by Deeg. *et al.* [46] Likewise, deuterium and tritium inherit the same model characteristics but updating their mass in relation to hydrogen molecule, so self– and cross–interaction Lennard–Jones parameters remain unaltered for them. Molecular weight of hydrogen isotopes are taken from NIST: M_{H_2} = 2.01588 u, M_{D_2} = 4.02820 u, and M_{T_2} = 6.03209 u. [47] These increases in mass directly affect the effective radius of the molecules as a consequence of the Feynman-Hibbs effective potential expression (Equation 1), where $U_{\mathrm{L-J}}$ is the classical Lennard-Jones po-

tential, prime and double prime symbols refer to first- and second-derivative, r_{ij} is the distance between two interacting particles, μ_{ij} is the reduced mass of i and j particles given by $\mu_{ij}^{-1} = M_i^{-1} + M_j^{-1}$ (being M the molecular mass), $\hbar$ is the reduced Planck constant, k_B is the Boltzmann constant, and T is the temperature.

Widom test-particle method,[48,49] through Monte Carlo simulations using the so called N-1 Canonical ensemble, was used to determine Henry coefficients (K_{H}) of adsorbates from 25 K to 200 K. K_{H} is related to the excess free energy of an adsorbed molecule by the following expression:

$$K_{\mathrm{H}} = \frac{1}{\mathrm{RT}\rho_{\mathrm{f}}} \frac{\langle W \rangle}{\langle W^{ig} \rangle} \tag{2}$$

where T is the temperature, R the gas constant, ρ_f the density of the framework, $\langle W \rangle$ the Rosenbluth factor of the single chain molecule and $\langle W^{ig} \rangle$ the Rosenbluth factor of the molecule in the ideal gas. Given that $\mathrm{K_H}$ provides information about adsorption at infinite dilution, selectivity at zero loading, $S_{ij}^0 = K_{\mathrm{H}}^i / K_{\mathrm{H}}^j$, establishes a measure of preferential adsorption of adsorbate i over j.

Adsorption isotherms were computed by Monte Carlo simulations in the Grand Canonical ensemble (μVT), in which the chemical potential μ is directly related to fugacity and thereby to the pressure through the fugacity coefficient. Constant values were set for temperature and pressure in simulations, spanning the ranges $\mathrm{T} \in [25 - 200]$ K and, at least, $\mathrm{P} \in [10^{-1} - 10^{5}]$ kPa. Both pure component and 1:1 mixture simulations were carried out for selected zeolites. Adsorption selectivity (S_{ij}) highlights the preferential adsorption of one component (i) over another (j) from their molar fractions in the adsorbed phase (θ) and in the bulk phase (x), according to:

$$S_{ij} = \frac{\theta_i \cdot x_j}{\theta_j \cdot x_i} \tag{3}$$

Molecular dynamics (MD) simulations were performed to obtain self-diffusion coefficients (D) of the adsorbates. They were determined from the slope of the mean-square displacements once the adsorbed species reached the diffusive regime inside the structure.[50] MD simulations were performed in the Canonical ensemble (NVT), integrating Newton's laws of motion using a velocity-Verlet algorithm with an integration time step of 0.5 fs and simulated times upwards of 325 ns. A Nosé–Hoover chain thermostat[51] was used to ensure the average temperature was constant. The number of adsorbates was set to 1.

All the aforementioned techniques were simulated using RASPA molecular simulation software.[52,53]

4.3 Results and Discussion

4.3.1 Deuterium/Hydrogen separation

To determine the operational properties and performance of 1:1 hydrogen isotope

separation using zeolites, we have carried out a thorough study on both equilibrium and time-dependent conditions. To that end, molecular simulations have proven to provide deep physical insights from which macroscopic behavior of adsorbates is inferred for these confined systems. Additionally, simulation methods allow to span the operation conditions further than experiments, which are restricted by economical considerations and number of trials. However, accurate models and force fields are completely necessary to obtain useful simulation results to target further experimental research. Therefore, we first validated the hydrogen model taken from literature [46] and also the derived model for deuterium used in this work by comparing the computed and experimental adsorption isotherms of two well-known pure silica zeolites (MFI and LTA) at 77.3 K and 90.2 K.

Both models reproduce precisely the experimental adsorption isotherms in LTA throughout the whole pressure range, as shown in Figure 1. Computed adsorption isotherms also reproduce the experimental data in MFI, although the loading of the two molecules is slightly underestimated at 77.3 K and 5–10 kPa. Nevertheless, deviations affect both hydrogen and deuterium in much the same way, meaning selectivity determinations are reliable, and differences are not substantial either.

We have computed and analyzed Henry coefficients for H_2 and D_2 as a function of temperature in the range of 25–200 K for 210 zeolites. As a general trend, $K_H^{D_2}$ and $K_H^{H_2}$ are found to decrease with temperature and the heavier D_2 is more strongly adsorbed than H_2, therefore $S^0_{D_2/H_2} > 1$. This trend is declining as temperature increases (figure 2). Figure 2 shows the five most selective zeolites at each temperature; as seen, zeolite BCT stands out by far as the best candidate (*i.e.*, highest $S^0_{D_2/H_2}$) to perform a separation at low loading over the whole temperature range. It is especially selective

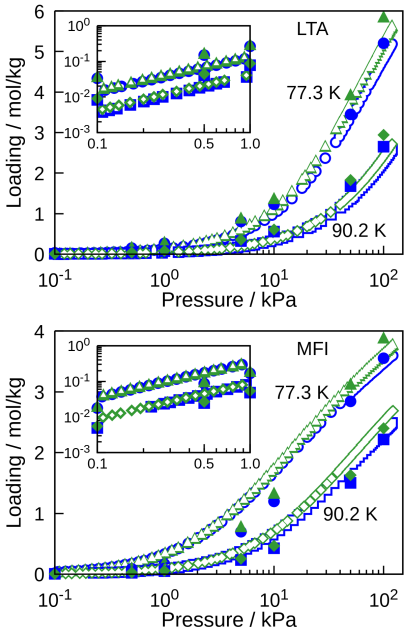

Figure 1: Experimental (open symbols) and simulated (filled symbols) adsorption isotherms of D_2 (green triangles and diamonds) and H_2 (blue circles and squares) in LTA (top) and MFI (bottom) at 77.3 K and 90.2 K. Insets to ease visualization in 0.1–1 kPa pressure range.

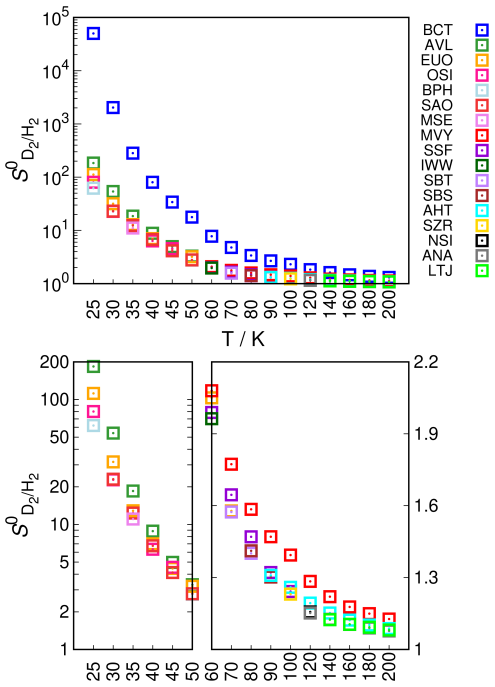

Figure 2: Selectivity at zero loading of deuterium over hydrogen as a function of temperature. Only the five highest selectivities are depicted for each temperature. Detailed graphics show close-up for the 25–50 K (bottom-left) and 60–200 K (bottom-right) temperature ranges, excluding BCT zeolite to ease the view.

up to 50–60 K. The second most selective zeolite depended on the temperature: AVL up to 50 K and MVY from 60 K to 200 K.

Other zeolite structures in the top five at some temperatures are: AHT, ANA, BPH, EUO, IWW, LTJ, MSE, NSI, OSI, SAO, SBS, SBT, SSF, and SZR. All the computed $S^0_{D_2/H_2}$ values are summarized in Table C1 in the Appendix C.

All pores of the frameworks were initially considered to be accessible due to the size of hydrogen isotope molecules and the quantum effects at cryogenic temperatures leading in some cases to an overestimation of the available adsorption volume and sites. Geometrical calculations and visual inspection were performed subsequently and repeatedly to block inaccessible pockets where necessary, to guarantee that molecules were not accessing unreachable pores in, at least, the ten zeolites with highest $S^0_{D_2/H_2}$ for each temperature.

Given the superior selectivity values of zeolites BCT, AVL, and MVY for the separation of deuterium from hydrogen, these zeolites were investigated in more detail. Zeolite BCT has a tetragonal structure with a one-dimensional pore system, formed by parallel 8-membered-ring channels along the z-axial direction with transversal side-pockets on alternating sides. The orthorhombic form of zeolite MVY also has a one-dimensional, sinusoidal channel system, comprised of 10-membered-ring cavities along the x-axial direction. On the other hand, zeolite AVL is a two-dimensional structure, with a trigonal crystalline system consisting of cylindrical-like cages connected by six 8-membered-ring windows (three on each end of the cylinder) and lentil-like cages with three 8-membered-ring windows (Figure 3).

Diffusion coefficients for single molecules have been evaluated with a twofold goal: determine the capacity of

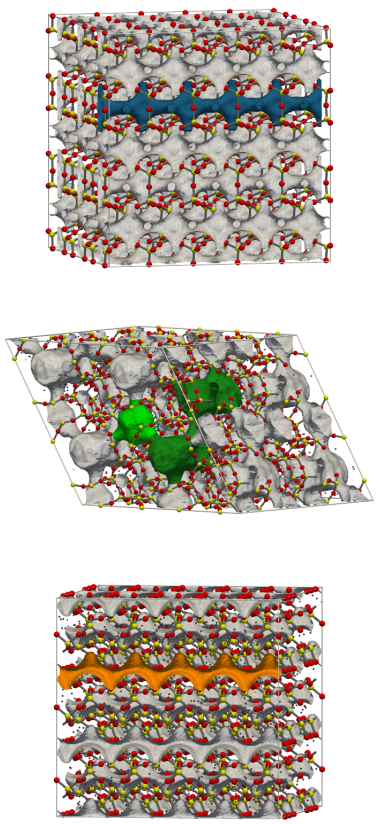

Figure 3: Energy surface areas and lattice atoms (yellow for Si and red for O) for BCT (top), AVL (bottom-left), and MVY (bottom-right) zeolites. Individual channels or pore systems are highlighted in blue, green, and orange, respectively, to ease the view. In AVL, bright-green is for lentil-like cages and dark-green for cylindrical cages.

adsorbates to access adsorption centers inside zeolites and search for conditions under which a noticeable difference between D_{D_2} and D_{H_2} is reached, which would open up the possibility of performing a quantum kinetic sieving of the isotopes. Results are presented in Figure 4. Diffusion was computed in the temperature ranges in which zero-loading selectivities stood out: The whole range for BCT, 25–50 K for AVL, and 60–200 K for MVY. However, it is worth noting that diffusion coefficients for zeolite MVY at 80, 70, and 60 K could not be accurately determined after simulating 500 ns molecular dynamics, and were of no practical use. For the same reason diffusion coefficients in BCT are not considered below 40 K. Regarding kinetic sieving, diffusion coefficients for D_2 and H_2 are quite similar in AVL and MVY, and also for the most of the analyzed temperatures in BCT. However, in principle a kinetic-based separation at 40–50 K is possible in BCT, although diffusion coefficients are quite low.

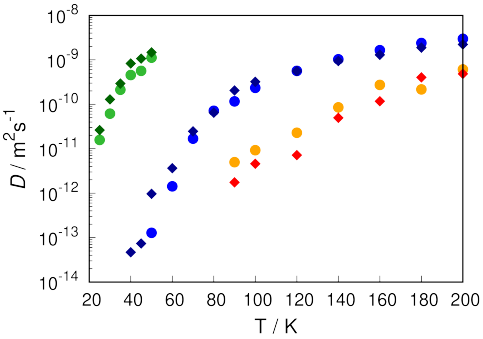

Figure 4: Self-diffusion coefficients of D_2 (diamonds) and H_2 (circles) in BCT (blue tones), AVL (green tones), and MVY (orangy-red tones) at the temperatures at which they have high selectivity (see text) at zero loading.

After considering diffusion results, acceptable operation ranges to perform the D_2/H_2 separation were restricted to 25-50 K in AVL, 40-200 K in BCT, and 90-200 K in MVY. Pure compound as well as 1:1 mixture adsorption isotherms were simulated at the temperatures of choice spanning a pressure range of at least $[10^{-1} - 10^4]$ kPa. For all three structures, in pure component adsorption isotherms (Figure C1, Appendix C), deuterium starts to be adsorbed at lower pressure than hydrogen, although this difference diminishes when temperature increases. Additionally, the location of the adsorption sites within the pores of the zeolites is shown for pure component adsorptions in Figures C2-C4 at Appendix Cfor BCT, AVL and MVY, respectively. Both deuterium and hydrogen adsorb at the same sites, and their loading dependency is also similar due to the competition for the same sites. Paradoxically, adsorbates' positions at high loading tend to be better defined as the adsorption sites are narrowed down by the steric interactions between adsorbates. The pure-component data suggest the separation capability of the zeolites but, rather than predicting mixture separation from pure compound isotherms as is common practice in many other works, [6,8,17,35,36] we simulated 1:1 D_2/H_2 mixture adsorption isotherms to calculate S_{D_2/H_2} selectivities.

Figures 5, C5, and C6 contain the adsorption isotherms of the components of the mixture and also the temperature-

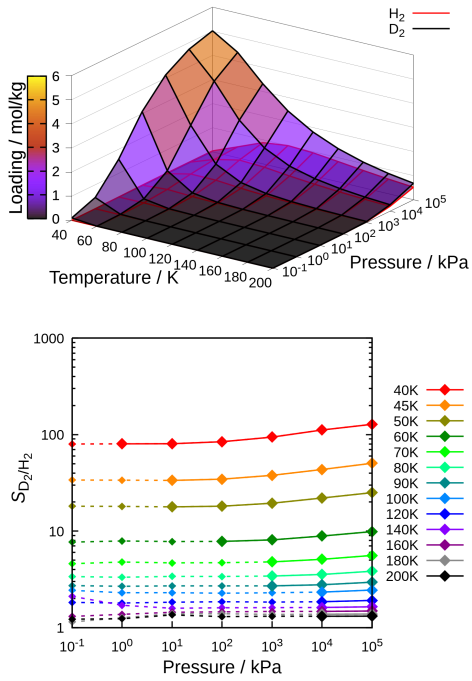

Figure 5: Adsorption loading (top) of deuterium (black lines grid) and hydrogen (red lines grid) from a 1:1 mixture as a function of pressure and temperature; grid cell colors match loading color-box. Adsorption selectivity (bottom) of deuterium over hydrogen as a function of pressure and temperature (color code assigned univocally for each temperature). Dashed lines and small symbols apply to selectivities at which the associated loading of D_2 is less than 0.1 mol/kg.

and pressure-dependent adsorption selectivities in zeolites BCT, AVL, and MVY, respectively. In view of the adsorption selectivities exhibited by BCT (Figure 5, bottom), it must be noted that they are nearly parallel (in the log-log scale) over the whole pressure range at different temper-

atures. Additionally, the pressure dependence is rather small, selectivities remain within 0.8–1.3 times the selectivity at 100 kPa, so that an increase in pressure to ensure a high loading is not detrimental to separation. Selectivities between 80 and 128 depending on pressure are reached at 40 K, which, to the best of our knowledge, are the highest reported in the literature. It is especially advisable to maintain the pressure at 100 kPa or more to obtain deuterium loadings of 3 mol/kg or more. Under these cryogenic conditions, temperature control is important: a 20 K increase leads to selectivity decreases by one order of magnitude. Still, BCT achieves relevant separation ratios of ~8-9 at 60 K. Further rises in temperature lead to more moderate decreases in selectivity, but then the absolute values are not very high.

Zeolite AVL also achieves high D_2/H_2 adsorption selectivities at low temperatures (Figure C5). As in zeolite BCT, selectivity decreases with temperature but, in this case, its increase with pressure is much larger, reaching a remarkable value of $S_{D_2/H_2} = 22$ at 25 K and 10^5 kPa while adsorbing 14 mol/kg of molecular deuterium vs. barely 0.6 mol/kg of molecular hydrogen. It is also worth noting that $S_{D_2/H_2} = 15$ at 25 K and atmospheric pressure, with 13 mol/kg deuterium adsorbed. Regarding zeolite MVY, selectivities remain poor, $S_{D_2/H_2} < 2$, remaining even under 1.5 for most of the operation conditions considered acceptable (Figure C6).

4.3.2 Tritium/Hydrogen separation

Following the same methodology used for D_2 and H_2, T_2/H_2 separation at low coverage has been screened. As is clear from Figure 6, BCT zeolite clearly stands out from the rest of zeolites, exhibiting the largest selectivity at all the temperatures simulated. Zeolites EUO, SAO, and OSI

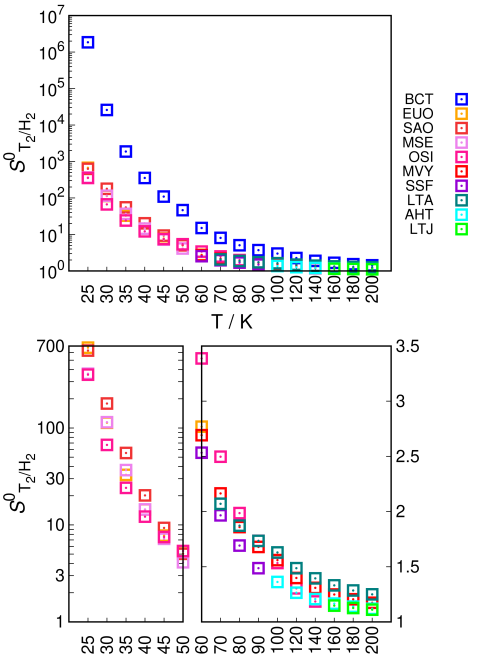

Figure 6: Selectivity at zero loading of tritium over hydrogen as a function of temperature. Only the five highest selectivities are depicted for each temperature. Detailed graphics show close-up for the 25–50 K (bottom-left) and 60–200 K (bottom-right) temperature ranges, excluding BCT zeolite to ease the view.

are second best at some temperature

within the 25–80 K temperature range, for which these adsorption selectivities remain greater or equal to two. All the computed $S^0_{T_2/H_2}$ values are summarized in Table C2 in the Appendix C.

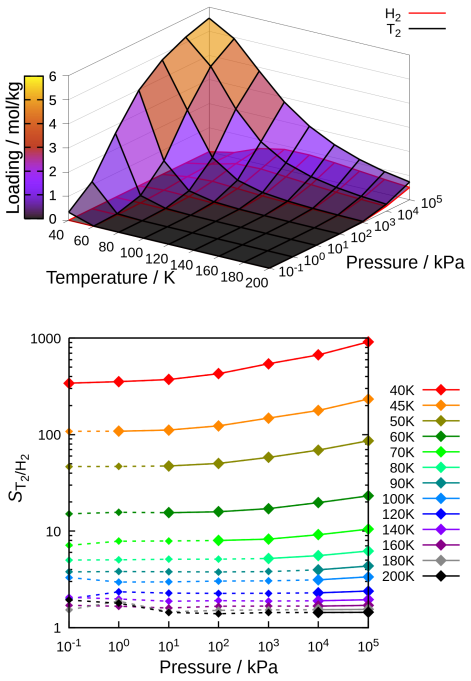

Figure 7: Adsorption loading (top) of tritium (black lines grid) and hydrogen (red lines grid) from a 1:1 mixture as a function of pressure and temperature; grid cell colors match loading color-box. Adsorption selectivity (bottom) of deuterium over hydrogen as a function of pressure and temperature (color code assigned univocally for each temperature). Dashed lines and small symbols apply to selectivities at which the associated loading of T_2 is less than 0.1 mol/kg.

Given the prevalence of BCT for the separation of hydrogen isotopes, this zeolite was selected to further simulate the selectivity and adsorption performance for an equimolar T_2/H_2 mixture.Based on the diffusion coefficients obtained for D_2 and H_2, the adsorption of the equimolar mixture adsorption was computed at temperatures above 40 K (Figure 7). Although a similar shape of adsorption isotherms/isobars is obtained compared with the deuterium case, it is worth noting that tritium loading is higher under the same (T,P) conditions while hydrogen is slightly less adsorbed, and therefore adsorption selectivity values rise up to $S_{T_2/H_2} = 915$ under optimal conditions (T=40 K and P=10^5 kPa).

4.4 Conclusions

We have screened various zeolite structures and operating conditions to select the best performing materials for the separation of hydrogen isotopes (D_2/H_2 and T_2/H_2 mixtures). To this end, we have proposed a deuterium model developed from an existing hydrogen model that incorporates quantum corrections. The model has been validated versus experimental hydrogen and deuterium adsorption isotherms in two pure silica zeolites (MFI and LTA). At low temperatures, these quantum corrections are responsible for the stronger adsorption of deuterium over hydrogen, as expressed by the adsorption selectivity. The adsorption selectivity at low loading was found to

be a good indicator for the adsorption selectivity at higher loadings, and much more temperature-sensitive than pressure-dependent. We have identified several zeolites to perform hydrogen isotope separation with a high selectivity. Notably, zeolite BCT exhibits the highest adsorption selectivity reported for D_2/H_2 separation at low temperature. For instance, at 40 K and high loadings deuterium is *ca.* 80 and 130 times more adsorbed than hydrogen, depending on pressure. This zeolite also presents a high deuterium selectivity (*ca.* S_{D_2/H_2} of 20) at 50 K and atmospheric pressure. We have also explored whether if in addition to the quantum sieving responsible for enhancing the adsorption of the heavier isotope, a quantum kinetic sieving effect –a diffusion-driven separation due to differences in the energy barriers– could be used advantageously in this system. Data showed that the quantum kinetic sieving effect was small at the temperatures of interest. In a few zeolites, this had already been reported. Alternatively to BCT, zeolite AVL has a high loading capacity at temperatures in the 25–45 K range and is able to separate deuterium from hydrogen reasonably well. With regard to T_2/H_2 separation, zeolite BCT has proven to have an extremely high selectivity, favoring the heavier isotope.

In sum, we have demonstrated that hydrogen isotope separation is feasible using zeolites at cryogenic temperatures and, especially, zeolite BCT stands out for this task. Besides, this study provides new perspectives to tackle other isotope mixture separations such as H_2/HD (hydrogen deuteride) or T_2/D_2, by selecting or designing highly selective and efficient porous materials.

Bibliography

[1] Greenwood, N.; Earnshaw, A. *Chemistry of the Elements 2nd Edition*; Butterworth-Heinemann, 1997.

[2] Meija, J.; Coplen, T. B.; Berglund, M.; Brand, W. A.; De Bièvre, P.; Gröning, M.; Holden, N. E.; Irrgeher, J.; Loss, R. D.; Walczyk, T.; Prohaska, T. *Pure Appl. Chem.* **2016**, *88*, 293–306.

[3] Cai, J.; Xing, Y.; Zhao, X. *RSC Advances* **2012**, *2*, 8579–8586.

[4] Wang, Y.; Zhao, D. *Crystal Growth & Design* **2017**, *17*, 2291–2308.

[5] Beenakker, J.; Borman, V.; Krylov, S. Y. *Chem. Phys. Lett.* **1995**, *232*, 379–382.

[6] Wang, Q.; Challa, S. R.; Sholl, D. S.; Johnson, J. K. *Phys. Rev. Lett.* **1999**, *82*, 956–959.

[7] Dresselhaus, M.; Williams, K.; Eklund, P. *MRS Bull.* **1999**, *24*, 45–50.

[8] Challa, S. R.; Sholl, D. S.; Johnson, J. K. *J. Chem. Phys.* **2002**, *116*, 814–824.

[9] Tanaka, H.; Kanoh, H.; Yudasaka, M.; Iijima, S.; Kaneko, K. *J. Am. Chem. Soc.* **2005**, *127*, 7511–7516.

[10] Kowalczyk, P.; Gauden, P. A.; Terzyk, A. P. *J Phys Chem B* **2008**, *112*, 8275–8284.

[11] Niimura, S.; Fujimori, T.; Minami, D.; Hattori, Y.; Abrams, L.; Corbin, D.; Hata, K.; Kaneko, K. *J. Am. Chem. Soc.* **2012**, *134*, 18483–18486.

[12] Xing, Y.; Cai, J.; Li, L.; Yang, M.; Zhao, X. *Physical Chemistry Chemical Physics* **2014**, *16*, 15800–15805.

[13] Kumar, A. A.; Jobic, H.; Bhatia, S. K. *J. Phys. Chem. B* **2006**, *110*, 16666–16671.

[14] Pantatosaki, E.; Papadopoulos, G. K.; Jobic, H.; Theodorou, D. N. *The Journal of Physical Chemistry B* **2008**, *112*, 11708–11715.

[15] Chu, X.-Z.; Cheng, Z.-P.; Xiang, X.-X.; Xu, J.-M.; Zhao, Y.-J.; Zhang, W.-G.; Lv, J.-S.; Zhou, Y.-P.; Zhou, L.; Moon, D.-K.; Lee, C.-H. *Int. J. Hydrogen Energy* **2014**, *39*, 4437–4446.

[16] Kowalczyk, P.; Terzyk, A. P.; Gauden, P. A.; Furmaniak, S.; Pantatosaki, E.; Papadopoulos, G. K. *J. Phys. Chem. C* **2015**, *119*, 15373–15380.

[17] Friebe, S.; Wang, N.; Diestel, L.; Liu, Y.; Schulz, A.; Mundstock, A.; Caro, J. *Microporous Mesoporous Mater.* **2015**, *216*, 127–132.

[18] Physick, A. J.; Wales, D. J.; Owens, S. H.; Shang, J.;

Webley, P. A.; Mays, T. J.; Ting, V. P. *Chem. Eng. J.* **2016**, *288*, 161–168.

[19] Salazar, J.; Lectez, S.; Gauvin, C.; Macaud, M.; Bellat, J.; Weber, G.; Bezverkhyy, I.; Simon, J. *Int. J. Hydrogen Energy* **2017**, *42*, 13099–13110.

[20] Xiong, R.; Xicohténcatl, R. B.; Zhang, L.; Li, P.; Yao, Y.; Sang, G.; Chen, C.; Tang, T.; Luo, D.; Hirscher, M. *Microporous and Mesoporous Materials* **2018**, *264*, 22–27.

[21] Giraudet, M.; Bezverkhyy, I.; Weber, G.; Dirand, C.; Macaud, M.; Bellat, J.-P. *Microporous and Mesoporous Materials* **2018**, *270*, 211–219.

[22] Pantatosaki, E.; Jobic, H.; Kolokolov, D. I.; Karmakar, S.; Biniwale, R.; Papadopoulos, G. K. *J. Chem. Phys.* **2013**, *138*, 034706.

[23] FitzGerald, S. A.; Pierce, C. J.; Rowsell, J. L.; Bloch, E. D.; Mason, J. A. *J. Am. Chem. Soc.* **2013**, *135*, 9458–9464.

[24] Teufel, J.; Oh, H.; Hirscher, M.; Wahiduzzaman, M.; Zhechkov, L.; Kuc, A.; Heine, T.; Denysenko, D.; Volkmer, D. *Advanced Materials* **2013**, *25*, 635–639.

[25] Oh, H.; Savchenko, I.; Mavrandonakis, A.; Heine, T.; Hirscher, M. *ACS Nano* **2014**, *8*, 761–770.

[26] Weinrauch, I.; Savchenko, I.; Denysenko, D.; Souliou, S.; Kim, H.; Le Tacon, M.; Daemen, L. L.; Cheng, Y.; Mavrandonakis, A.; Ramirez-Cuesta, A.; Volkmer, D.; Schütz, G.; Hirscher, M.; Heine, T. *Nat. Commun.* **2017**, *8*, 14496.

[27] Kim, J. Y.; Balderas-Xicohténcatl, R.; Zhang, L.; Kang, S. G.; Hirscher, M.; Oh, H.; Moon, H. R. *J. Am. Chem. Soc.* **2017**, *139*, 15135–15141.

[28] Kim, J. Y.; Zhang, L.; Balderas-XicohtèĄncatl, R.; Park, J.; Hirscher, M.; Moon, H. R.; Oh, H. *Journal of the American Chemical Society* **2017**, *139*, 17743–17746.

[29] Cao, D.; Huang, H.; Lan, Y.; Chen, X.; Yang, Q.; Liu, D.; Gong, Y.; Xiao, C.; Zhong, C.; Peng, S. *Journal of Materials Chemistry A* **2018**, *6*, 19954–19959.

[30] Han, G.; Gong, Y.; Huang, H.; Cao, D.; Chen, X.; Liu, D.; Zhong, C. *ACS applied materials & interfaces* **2018**, *10*, 32128–32132.

[31] Feynman, R. P.; Hibbs, A. R. *Quantum Mechanics and Path Integrals*; McGraw-Hill, 1965.

[32] Sesé, L. M. *Mol. Phys.* **1994**, *81*, 1297–1312.

[33] Sesé, L. M. *Mol. Phys.* **1995**, *85*, 931–947.

[34] Darkrim, F.; Aoufi, A.; Levesque, D. *Mol. Simul.* **2000**, *24*, 51–61.

[35] Noguchi, D.; Tanaka, H.; Kondo, A.; Kajiro, H.; Noguchi, H.; Ohba, T.; Kanoh, H.; Kaneko, K. *J. Am. Chem. Soc.* **2008**, *130*, 6367–6372.

[36] Tanaka, H.; Noguchi, D.; Yuzawa, A.; Kodaira, T.; Kanoh, H.; Kaneko, K. *J. Low Temp. Phys.* **2009**, *157*, 352–373.

[37] Noguchi, D.; Tanaka, H.; Fujimori, T.; Kagita, H.; Hattori, Y.; Honda, H.; Urita, K.; Utsumi, S.; Wang, Z.-M.; Ohba, T.; Kanoh, H.; Hata, K.; Kaneko, K. *J. Phys.: Condens. Matter* **2010**, *22*, 334207.

[38] Baerlocher, C.; McCusker, L.; Olson, D. *Atlas of Zeolite Framework Types*, 6th ed.; 2007.

[39] Villaescusa, L. A.; Barrett, P. A.; Camblor, M. A. *Angew. Chem. Int. Ed.* **1999**, *38*, 1997–2000.

[40] Camblor, M. A.; Corma, A.; Lightfoot, P.; Villaescusa, L. A.; Wright, P. A. *Angew. Chem. Int. Ed.* **1997**, *36*, 2659–2661.

[41] Barrett, P. A.; Boix, T.; Puche, M.; Olson, D. H.; Jordan, E.; Koller, H.; Camblor, M. A. *Chem. Commun.* **2003**, 2114–2115.

[42] Corma, A.; Rey, F.; Rius, J.; Sabater, M. J.; Valencia, S. *Nature* **2004**, *431*, 287–290.

[43] Camblor, M. A.; Corma, A.; Díaz-Cabañas, M.-J.; Baerlocher, C. *J. Phys. Chem. B* **1998**, *102*, 44–51.

[44] Garcia-Sanchez, A.; Ania, C. O.; Parra, J. B.; Dubbeldam, D.; Vlugt, T. J. H.; Krishna, R.; Calero, S. *J. Phys. Chem. C* **2009**, *113*, 8814–8820, and references therein.

[45] van den Berg, A. W.; Bromley, S. T.; Wojdel, J. C.; Jansen, J. C. *Microporous Mesoporous Mater* **2006**, *87*, 235–242.

[46] Deeg, K. S.; Gutiérrez-Sevillano, J. J.; Bueno-Perez, R.; Parra, J. B.; Ania, C. O.; Doblaré, M.; Calero, S. *J. Phys. Chem. C* **2013**, *117*, 14374–14380.

[47] Stein, S. NIST Chemistry WebBook, NIST Standard Reference Database Number 69, Eds. PJ Linstrom and WG Mallard.

[48] Widom, B. *J. Chem. Phys.* **1963**, *39*, 2808–2812.

[49] Vlugt, T. J. H.; Garcia-Perez, E.; Dubbeldam, D.; Ban, S.; Calero, S. *J. Chem. Theory Comput.* **2008**, *4*, 1107–1118.

[50] Dubbeldam, D.; Beerdsen, E.; Vlugt, T. J. H.; Smit, B. *J. Chem. Phys.* **2005**, *122*, –.

[51] Hoover, W. G. *Phys. Rev. A* **1986**, *34*, 2499–2500.

[52] Dubbeldam, D.; Calero, S.; Ellis, D. E.; Snurr, R. Q. *Mol. Simul.* **2016**, *42*, 81–101.

[53] Dubbeldam, D.; Torres-Knoop, A.; Walton, K. S. *Mol. Simul.* **2013**, *39*, 1253–1292.

CHAPTER 5

DIFFUSION PATTERNS IN ZEOLITE MFI: THE CATION EFFECT

J. Perez-Carbajo, D. Dubbeldam, P. J. Merkling, and S. Calero

Zeolite MFI is one of the most important, stable porous materials used in catalysis and separation processes. However, some fundamental properties remain in the dark, such as the effect of different aluminum distributions on diffusion. This work, through calculations on cation probability densities, guest energy profiles and diffusion coefficients, provides a consistent picture of accessibility and mobility for two representative adsorbates, the nonpolar methane and the quadrupolar carbon dioxide and helps to explain the stark differences in diffusion behavior among varying aluminum distributions. A distribution was identified close to the practical limit of maximum aluminum substitution and sodium cation content that actually leads to a collapse in diffusion. For all aluminum distributions studied, the diffusion properties are closely linked to the number of cations. Compensating aluminum negative charge with divalent calcium instead of monovalent sodium increases methane but decreases carbon dioxide diffusion. With respect to increasing adsorbate loading, it induces a monotonous decrease in self-diffusivities for all structures studied. This study highlights the desirability of controlling the aluminum substitution location and, more importantly, that two heavily substituted MFI zeolites with identical composition reported in the literature may have very different diffusion properties.

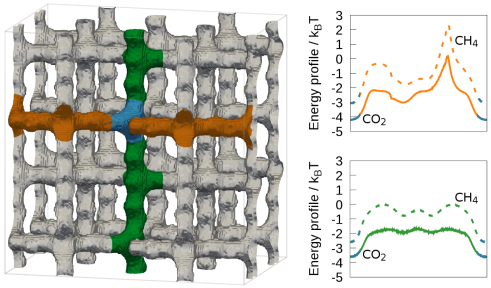

5.1 INTRODUCTION

Zeolites are regular crystalline porous materials that span a variety of topologies. As a consequence, overall large nanoporosity and quite different molecular-sized pores throughout the whole range of zeolites are achieved that make them very attractive for industrial purposes. They are therefore widely used in adsorption and separation processes, molecular sieving, catalysis, and ion exchange processes. One of the zeolites with most applications in industry is the MFI-type, and it has thus been the focus of many studies. This type of zeolite present a framework with many different local environments and are defined by 12 T crystallographic sites, which form a three-dimensional interconnected channel and pore system, in which the straight channels, parallel to [010], are intersected by zigzag channels.[1] They can be synthesized in a pure silica form (silicalite-1)[2] or with aluminum replacing some of the silicon atoms, up to a Si/Al limit of 11/1.[3] Although it is almost impossible by synthesis to direct the aluminum atoms to a specific crystallographic site, the aluminum environment of prepared samples can be characterized. While X-ray diffraction is not suitable in this case given that Si^{4+} and Al^{3+} are isoelectronic, MAS NMR for example is capable of gathering information on the local environment of ^{27}Al.[4–6] Additionally, the presence of trivalent Al atoms instead of tetravalent Si atoms induces a net negative charge in the system which has to be compensated by including cations as extra-framework ions that are potentially free to move within the structure. It has been reported that the position of the Al atoms has a strong effect on the location and stability of cations that tend to remain close.[7] Hence, the distribution of cations could be used as an indicator for the aluminum distribution in the structure. At the same time, the presence of cations influences the behavior of the adsorbates within the nanostructured material.

Experimental and computational works have reported both on the structural characteristics of MFI-type zeolites[8–13] and their equilibrium adsorption properties.[14–21] Concerning transport phenomena, these zeolites have been studied less and when so, mainly in pure silica MFI.[22–31] Even those works that consider the presence of cations do so just for a few particular cases,[32–35] so a complete understanding of their location and diffusion in aluminated MFI and their effects on adsorbates is missing. When tailoring an MFI zeolite for specific uses in separation or storage, the Si/Al ratio can be engineered, but this has profound implications both for the hydrophobic/hydrophilic nature of the framework and its diffusion properties. It would be desirable to identify structures that maintain the hydrophilicity of the framework but provide very efficient or very inefficient diffusion for chosen,

relevant guest molecules.

The present work has thus a twofold goal: on one hand, to establish the pattern of cation distributions in MFI-type zeolites depending on the crystallographic positions of the aluminum atoms and, on the other hand, to measure the effects of aluminum location and of cations on the industrially relevant molecules carbon dioxide and methane. For the first goal, we consider aluminum distributions restricted to a single crystallographic site. According to this and to Löwenstein's rule [36] that states that Al-O-Al linkages are energetically forbidden, the maximum aluminum content is 8 aluminum atoms per unit cell (Al/uc) at eight of the 12 crystallographic sites and 4 Al/uc at the other four sites. This means that, as is typical for MFI, the Si/Al ratio is of 11/1 or above throughout all of our study, and yet the aluminum and cation contents have profound effects on the diffusion of guest molecules. In this study, we will consider Na^+ or Ca^{2+} cations to balance the charges. Of special interest were the density distributions for the cations and their diffusion through the MFI channels in order to get a comprehensive picture. For the second goal, we have computed diffusion of guest molecules, CO_2 and CH_4, as a function of loading and number of Al/uc. We relate the diffusion behavior with adsorption free energy profiles for single molecules of the adsorbates along the diffusion paths.

5.2 METHODS

To assess the goals set in this study, we have performed both Monte Carlo (MC) and Molecular Dynamics (MD) simulations to calculate equilibrium and time-dependent features, respectively. Molecular simulations are often used to help understand the behavior of confined systems. They are able to provide a clear relation between the underlying microscopic interactions and the macroscopic properties of a host-guest system, and may yield accurate predictions where it is hard or expensive to get results from experiments. For this to happen, however, the selection of an appropriate force field is crucial for describing properly the interactions between the adsorbates and the structures, especially those that involve nonframework cations. Further, adsorbate models have been chosen that reproduce some key experimental data such as the vapour-liquid equilibrium curve.

5.2.1 Models and force field

Interactions between the atoms of the structure, extra-framework cations, and adsorbates are defined by electrostatic and van der Waals (vdW) interactions. Coulombic potential is used to model electrostatic interactions, using the Ewald summation to handle the periodicity of the system, whereas Lennard–Jones (L–J) potential is used to model vdW interactions.

We have defined the structures as rigid frameworks with static partial charges.[18] In pure silica MFI, oxygen and silicon atoms have charges of q_O = −0.3930 e^- and q_{Si} = +0.7860 e^-, respectively. Aluminum affects the partial charge on silicon, so that in aluminum-containing structures q_{Al} was set to +0.4860 e^-.[37,38] A consequence of this charge distribution is that cations tend to be near AlO_4 tetrahedra. According to the Auerbach approximation, to take into account the polarizing effects of cations on nearby oxygen atoms, the charge of oxygen atoms bridging two silicon atoms (q_O) differs from the one linking aluminum and silicon atoms (q_{O_a} = −0.4138 e^-). In relation to the assumed rigidity of the lattices, it is worth noting that this assumption has proved to reproduce satisfactorily experimental adsorption data when molecules such as carbon dioxide or methane are smaller than the size of the windows.[39] Additionally, it has also been reported that flexibility of zeolite lattices could be neglected for the diffusion of these species.[40,41]

The number of cations introduced in the structure depends on the number of aluminum atoms substituted. Sodium and calcium cations are considered as point charges whose values were taken from Garcia-Sanchez *et al.*[18] and Garcia-Perez *et al.*,[42] respectively. Both species are allowed to move within the zeolites constrained only by the interaction potentials defined previously.

The parameters for methane are taken from Dubbeldam *et al.*,[43] who used a united atom model with a single chargeless interaction center[44]. Carbon dioxide is defined as a rigid three-site model with partial point charges on each site ($q_{O_{CO_2}}$ = −0.3256 e^-, $q_{C_{CO_2}}$ = +0.6512 e^-) and two covalent bonds of d_{oc} = 1.149 Å.[18] Both molecules were modeled to reproduce the vapor-liquid equilibrium curve.

The vdW interactions of guest molecules with zeolite host frameworks are dominated by dispersive forces between molecules' pseudo-atoms and oxygen atoms of the framework,[45,46] so that the effect of silicon atoms can be incorporated into effective potentials on oxygen atoms. Most L–J parameters for host-guest and guest-guest interactions are taken as defined in the literature,[18,42,43] except for CO_2-Ca^{2+}, which has been assumed to be equal to those for CO_2-Na^+ on behalf of the close similarity of the ionic radii for both cation species. Lorentz–Berthelot (L–B) mixing rules[47,48] are considered for C_{CO_2}-O_{CO_2} cross interactions. Table 1 contains a summary of the L–J parameters used in this work.

5.2.2 Framework details

At the temperatures considered in this work, zeolite MFI adopts an orthorhombic[49] crystal structure. Atomic positions were taken from silicalite characterized by

Table 1: Lennard-Jones parameters. Top-left corner σ [Å]; bottom-right corner ϵ/k_B [K]. L-B means the Lorentz-Berthelot mixing rules apply.

	O/O_a	C_{CO_2}	O_{CO_2}	CH_4
C_{CO_2}	3.511 37.595	2.745 29.933	L-B	–
O_{CO_2}	3.237 78.98	L-B	3.017 85.671	–
CH_4	3.237 115.00	–	–	3.72 158.5
Na^+	3.4 23.0	3.320 362.292	2.758 200.831	2.72 582.00
Ca^{2+}	3.45 18.0	3.320 362.292	2.758 200.831	2.56 590.17

van Koningsveld *et al.* [10] Consequently, the unit cell dimensions are $20.022 \times 19.899 \times 13.383$ Å^3, and the inner space is subdivided in straight channels with 5.3×5.5 Å^2 elliptical section, [1] which are intersected by 5.1×5.6 Å^2 xz zigzag channels every 10 Å roughly. Given that it has been reported that Al substitution takes place at preferred sites, [11,12] we generated highly specific distributions in order to analyse the effect of crystallographic sites.

Given that MFI zeolite has 12 crystallographically different tetrahedrical sites consisting of eight T atoms (Al or Si) per unit cell (uc) each, site-specific substitutions of Si for Al were done in any one T crystallographic position at a time (Figure D1 in Appendix D). Throughout this work, a substitution for m Al/uc at crystallographic site n will be labeled as $T_{n,m}$. All Si atoms from any one T-site 1-6, 8 or 11 may be simultaneously substituted by Al atoms, yielding a Si/Al ratio of 11/1, and defining the $T_{1,8}$, $T_{2,8}$, $T_{3,8}$, $T_{4,8}$, $T_{5,8}$, $T_{6,8}$, $T_{8,8}$, or $T_{11,8}$ MFI-type structures. Additionally, we have generated several structures with only 4 Al/uc (Si/Al ratio of 23/1) in the previous T-sites, both in a random way and at certain set positions. Further, structures $T_{4,m}$ were generated with m covering the whole range from 1 to 8. In this case, the mean average distance between Al atoms was maximized and therefore low energy structures generated, but it should be clear that for m between 2 and 7 other nonequivalent $T_{4,m}$ structures exist that would yield slightly different results. T_7, T_9, T_{10}, and T_{12} positions are limited to 4 Al/uc by Löwenstein's rule, due to the adjacency of these atoms on the 10-membered rings of the xz channels, and each offers just two equivalent maximally substituted aluminum distributions. All of the aforementioned frameworks are charge-compensated by introducing cations: we consider Na^+ cations for all the structures, and Ca^{2+} for selected ones.

5.2.3 Simulation techniques

Simulation boxes of MFI are supercells made of $2 \times 2 \times 2$ unit cells, to satisfy that system size is at least twice the L-J potential cutoff, set to 12 Å throughout the development of the interaction potentials.

Monte Carlo simulations in the Grand Canonical ensemble (μVT) are used to compute adsorption isotherms of guest molecules in the host framework[50]. Fugacity of a gas f can be related to μ through the expression $\mu = \mu^0 + RT\ln(f/p^0)$, being μ^0 and p^0 the standard chemical potential and pressure, respectively. Cations are placed inside the structures using trial random insertions to bypass energy barriers[38] and moved by trial displacements.

Molecular Dynamics (MD) simulations are performed to calculate the mean-square displacement (MSD) of adsorbates and cations. On the timescale for the species to reach diffusive regime in a confined environment[51], self-diffusion coefficients D_S^α ($\alpha = x, y, z$) are calculated from the slope of their MSD. MD simulations are performed in the NVT ensemble, integrating Newton's laws of motion using a velocity-Verlet algorithm with an integration time step of 0.5 fs. A Nosé-Hoover chain thermostat[52] is set at 500 K. The maximum number of molecules in these simulations is determined in line with the adsorption loading at the highest pressure previously calculated at 298 K. Several N values below this maximum have been considered to assess the guest density effects.

Energy surface areas use the Widom test-particle method, with a helium atom as probing particle. Similarly, adsorption free energy profiles are computed during NVT-ensemble MC simulations, also using the Widom method,[53] but inserting CO_2 and CH_4 probe particles. To that end, taking into account the geometry of MFI zeolite, it is necessary to isolate the sampled section of the channel (whether the straight or the zigzag one) not to overlap contributions of other channels to the energy profile. Part of transverse channels are also sampled to considere the possibility of molecules moving from one to the other channel at intersections. All the simulations were performed using RASPA software.[54]

5.3 Results and Discussion

In this work we have studied the behavior of nonframework cations depending on the aluminum location in MFI-type zeolites and their effects on the diffusion of adsorbates. In the following sections we first focus on structures charge-compensated by sodium cations. Then, we discuss the effects on diffusion of high adsorbate loading and finally consider divalent calcium cations.

5.3.1 MFI-type structures with sodium cations

The adsorption capacity of MFI-type zeolites is known to be cation-dependent in aluminum-containing frameworks. In a previous study, we have shown for some T-sites that this dependence lies not in the sodium cation distribution but in their number [20]. In this study, we have expanded the scope to all T-sites. Adsorption loadings were found to be almost unaffected by the Na^+ distribution, a conclusion shown more thoroughly in Figures D2 and D3 (in Appendix D) of the present study, whereas especially CO_2 adsorption strongly depended on sodium cation numbers due to an increasing excluded volume. The lone exception is found in the T_{11} structure: at high pressures, the loading remains quite similar from the first aluminum in this crystallographic position on up to 8 aluminum atoms per unit cell. Here, the presence of Na^+ cations does not affect the dense packing. Unlike adsorption capacity, the onset of adsorption is favoured by the presence of cations because of the energetically beneficial Na^+-CO_2 interaction. The presence of Na^+ is thus providing new adsorption sites.

To determine the behavior of the cations as a function of the location of the substituted Si, we have computed the sodium probability density along the channels by using MD simulations. In this way, we are able to identify not only the preferential sites for cations but also the paths through which they diffuse. The more intense the blue tone in Figure 1, the more likely their presence, while transparency indicates transition regions or more generally lower presence areas. Although cations are located around their equilibrium positions, transitions from one to another equilibrium position are possible and performed by colective movements. [55?] These areas reveal that Na^+ cations can be found with significant probability along all of the y-channel whereas along the xz channels there are pockets of high density and regions of very low density. A complete range of sodium distribution patterns can be observed in the representations included in Figures D4

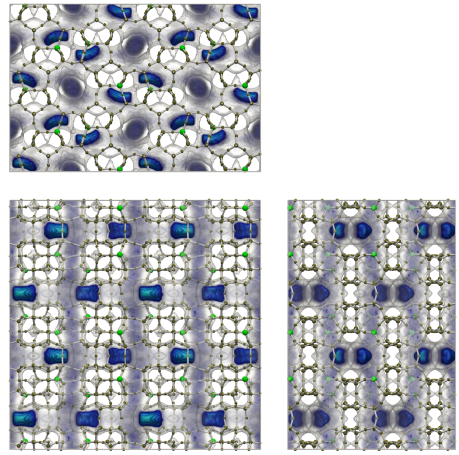

Figure 1: Probability density of Na^+ cations in $T_{4,8}$ MFI channels projected on xz plane (top), xy plane (bottom-left), and zy plane (bottom-right). For easier identification, Al atoms are oversized and colored green.

and D5 for all sites containing 8 Al/uc. At the lower end of mobility is the structure possessing 8 aluminum atoms in site 5 ($T_{5,8}$), in which the sodium cations are narrowly confined around their equilibrium positions. Wider distributions are found for $T_{4,8}$, $T_{8,8}$, and $T_{11,8}$ structures, for which sodium has well defined equilibrium regions, but can diffuse along the channels, and finally $T_{1,8}$, $T_{2,8}$, $T_{3,8}$, and $T_{6,8}$ structures, for which Na^+ cations occupy large areas.

The inclusion of aluminum atoms and sodium cations modifies the preferential sites of adsorption, identified by the free energy wells shown in Figure 2, with respect to those described by Beerdsen *et al.* [30] in pure silica MFI. Although the deepest wells correspond to the channel intersections on the energy surface representation, every 10 Å roughly as referred previously, being quite similar independently of the location of the Si substituted, the sites of adsorption located between intersections have relevant variations due to the Al location. Hence, while adsorption sites for the pure silica structure matches the broadenings of the channels, the same cannot be directly said in presence of cations. Note that the energy profile for molecules diffusing along zigzag channels is asymmetric between intersections, whereas consecutive sections have the same energy profile. The configuration of these energy barriers allows us to explain in a first aproximation the diffusion of the adsorbates through the

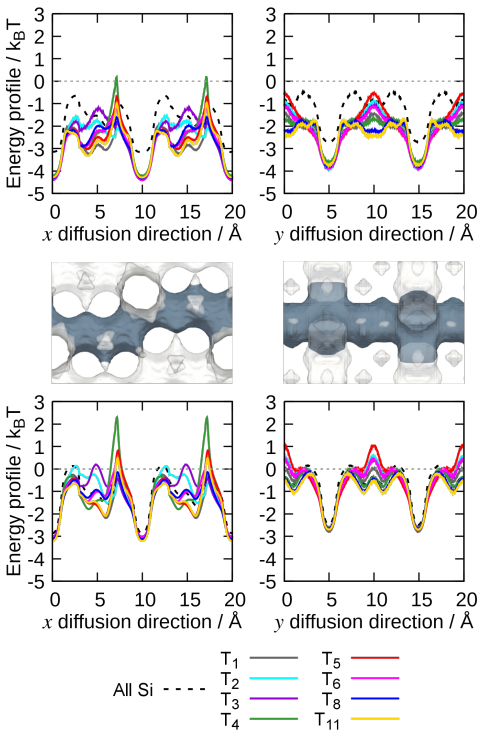

Figure 2: Energy profiles of a single molecule of CO_2 (top) and CH_4 (bottom) along the diffusion directions x (left) and y (right) in 8 Al/uc MFI structures with Na^+ cations; Energy surface of the channels (center).

zeolite: the lower the energy barriers from the wells to the peaks, the easier a molecule can get across them. Thus, adsorbate molecules diffuse better through the y-axis straight channels that have a flatter energy profile, and the asymmetric energy profiles for zigzag channels suggest that diffusion takes place preferentially in one direction through them. This is because several lower barriers allow

the molecule in some cases to regain momentum. Also, the role of intersections as molecular traps already observed in the pure silica structure is reinforced in aluminum-containing structures by the deepening of the wells for CO_2 molecules. Noticeable differences are observed in energy profiles depending on the aluminum substitution pattern. For instance, energy profiles along the y-direction are especially low in pure silica, T_1, T_4, T_8 and T_{11} and high in T_5. Along the less favoured zigzag channels, energy profiles are especially low in pure silica and T_8 whereas they are high in T_4 and T_5. We also observe that the energy profile of T_8 and T_{11} are remarkably similar along the whole of the y-direction, but markedly different along the zigzag channels. The previous observations are valid for both CO_2 and CH_4 probe molecules.

The energy profiles are consistent with the diffusion coefficients (D) obtained at low loading (Figure 3). The whole set of data at infinite dilution are also available in Table D1, in which diffusion data are broken down into x, y and z directions and data for Na^+ cations are additionally provided. As a general trend, we found that Na^+ diffusion is only mildly affected by the adsorbate type and led to slightly higher diffusion coefficients with the faster diffusing CH_4 than with CO_2, an unsurprising result given that there are 8 cations and only one guest molecule in our simulations. It was also found that D_{CH_4} is higher than D_{Na^+} or D_{CO_2} for all

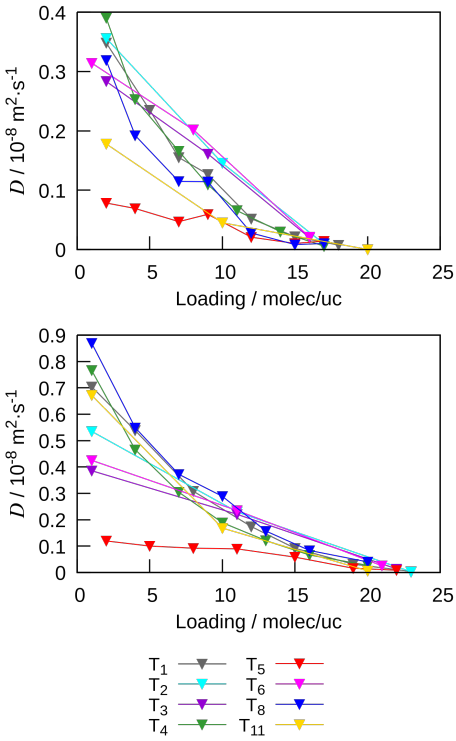

Figure 3: Diffusion coefficients of CO_2 (top) and CH_4 (bottom) as a function of loading in 8 Al/uc MFI structures with Na^+ cations.

the structures with 8 Al/uc: since CH_4 is a nonpolar molecule and the simulation model has no multipole, its interactions both with the framework and sodium cations are weaker. A detailed analysis of the directional components (D^x and D^y) of D_{CH_4} and D_{Na^+} led us to conclude that diffusion of methane is not heavily correlated with sodium diffusion. This is especially clear in $T_{8,8}$ and $T_{11,8}$, where $D_{CH_4} \gg D_{Na^+}$. At the lower end of diffusion in the $T_{5,8}$ structure, cations barely

move and are located in the channel intersections and in the middle of the straight channels (see Figure D5), almost impeding methane diffusion altogether. Regarding CO_2, its diffusion coefficients remain similar to D_{Na^+} for all the $T_{n,8}$ structures, not only for the overall diffusion terms but also for their x- and y-direction components. This noticeable coupling of diffusions must be down to electrostatic interactions between CO_2 and the cations. Similarly to CH_4 diffusion, carbon dioxide diffusion is severely restricted in $T_{5,8}$. Given that diffusion in z direction requires moving through different sections of straight and zigzag channels, the extremely low $D^z_{CO_2}$ for all structures denote that CO_2 hardly ever switches to a different channel, whereas the values of $D^x_{CO_2}$ and $D^y_{CO_2}$ indicate that CO_2 diffusion relies mainly on straight channels. The most favourable aluminum-containing configuration for diffusion of both CH_4 and CO_2 is $T_{4,8}$: although the cations prevent diffusion along the zigzag channel, diffusion along the straight channels is very effective. In fact, the loading-dependent D^y diffusion coefficients in this structure amount to 50-60 % of the ones in the pure silica case. Figure 3 further shows a decrease in self-diffusivities for both adsorbates in all the structures as a function of loading. This lowering in molecular diffusivity is steeper the higher the diffusion coefficient at low loading. This dependence is closer to the behavior of unidimensional zeolites than three-dimensional ones,[31] but it is found to be consistent with CO_2 and CH_4 molecules that diffuse mainly through the straight y-channels. The ranking by importance of the y-, x-, and z-contributions is generally unaffected by the increase in loading (and follows in general the same decreasing trend as the overall diffusion coefficient). Sodium cations also have a diffusion decreasing pace with loading, similar to the trends observed for adsorbates.

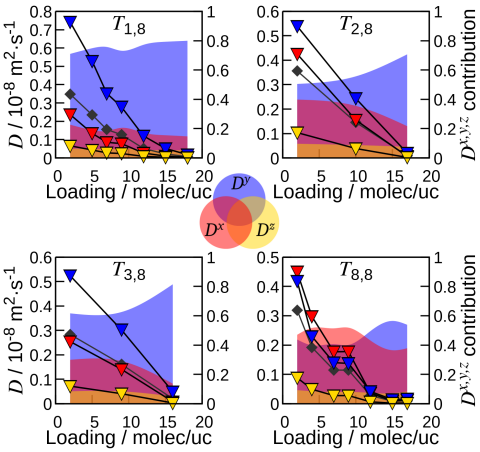

Figure 4: Diffusion coefficients (symbols, left vertical axis) of CO_2 and normalized contributions to total diffusion (colored areas, right vertical axis) of the directional components D^x, D^y, and D^z in $T_{1,8}$, $T_{2,8}$, $T_{3,8}$, and $T_{8,8}$ MFI structures with Na^+ cations. The total diffusion coefficient D is depicted in dark grey diamond symbols.

It is worth noting that for some of the structures ($T_{2,8}$, $T_{3,8}$, and $T_{8,8}$), the relative contribution of $D^y_{CO_2}$ to the overall diffusion increases with loading, as shown

Table 2: Self diffusion coefficient at zero loading D_0 and number of guest molecules $N_{1/2}$ for which diffusion is half the initial value

System	CO_2		CH_4	
	$D_0/10^{-8}$ m^2s^{-1}	$N_{1/2}$ molec/uc	$D_0/10^{-8}$ m^2s^{-1}	$N_{1/2}$ molec/uc
$T_{1,8}$	0.35	5.8 ± 0.1	0.70	7.2 ± 0.2
$T_{2,8}$	0.36	8.0 ± 0.2	0.54	9.6 ± 0.3
$T_{3,8}$	0.28	9.6 ± 0.1	0.39	12.5 ± 0.3
$T_{4,8}$	0.39	4.8 ± 0.1	0.77	5.4 ± 0.2
$T_{5,8}$	0.08	9.2 ± 0.8	0.12	14.5 ± 0.4
$T_{6,8}$	0.31	10.2 ± 0.3	0.43	12.1 ± 0.2
$T_{8,8}$	0.32	4.0 ± 0.2	0.87	5.7 ± 0.3
$T_{11,8}$	0.18	6.0 ± 0.7	0.67	6.3 ± 0.7

in Figure 4, meaning that it is less severely affected by the growing number of adsorbate molecules. This indicates that this channel has a lower tendency to clog, which is understandable given that it is straighter than the xz-channel. To the contrary, we observe that for methane, the relative contribution of D^x increases with loading in structure $T_{3,8}$ (not shown).

The correlation between high diffusion coefficient at low loading and rapid loss of diffusivity with increasing loading can be confirmed numerically by introducing the number of guest molecules at which diffusion halves with respect to its value at infinite dilution ($N_{1/2}$). Results are shown in Table 2.

As seen in Table 2, methane diffusion in sodium $T_{n,8}$ structures decreases rapidly with loading when silicon has been substituted in sites 1, 4, 8 and 11 (the sites with strongest diffusion at low loading), it decreases a little slower when substituted in site 2 ($N_{1/2}$ at around 10, that is almost half-maximum loading), but much more slowly when in sites 3, 5 and 6. A similar behavior pattern is also observed for the CO_2 diffusion. In this case, sites 1, 4, 8 and 11 maintain at least 50% diffusivity only if 6 or even less CO_2 molecules per uc are present, site 2 is of intermediate sensitivity to loading with 8 CO_2 molecules per uc whereas sites 3, 5 and 6 are less affected by loading ($N_{1/2} \geq 9.2$).

In accordance with Löwenstein's rule, the T crystallographical positions not considered so far (T = 7, 9, 10, and 12) only admit up to 4 Al/uc. For these maximally substituted cases, carbon dioxide and methane molecules diffuse noticeably slower than in the pure silica case. If compared to the structures with 8 Al/uc analysed previously (Figure D6 vs. Figure 3), the picture is more mixed: carbon dioxide molecules diffuse either similarly ($T_{9,4}$ and $T_{12,4}$) or substantially faster ($T_{7,4}$ and $T_{10,4}$) than in the 8 cations/uc cases, especially at low loading. On the other hand, methane molecules are not

affected by charges of cations and find the channels less populated by obstructive cations, therefore increasing their diffusivity throughout.

5.3.2 Effect of increasing aluminum substitution

To get a more detailed view of the effect of substitution, we have selected T_4 to perform a progressive substitution of silicon by aluminum atoms from pure silica MFI zeolite to $T_{4,8}$ MFI structure and have computed D_{CO_2} and D_{CH_4} as a function of loading (Figure 5). Although diffusion of both adsorbates decreases progressively with increasing number of sodium cations as can be seen for a single guest molecule from Figure D7 of the Appendix D, this decrease is stronger for CH_4. This seems to be related to the growing number of obstacles for a methane molecule to diffuse well. For CO_2, from $T_{4,5}$ on till $T_{4,8}$, diffusivities remain very similar. The adverse steric effect of the increasing number of cations is compensated at high substitution levels by the aluminum grid getting dense enough for cations to diffuse more strongly (Figure D7), and to the fact that the cation and CO_2 diffusions get coupled because of the strong interaction between cation and CO_2. In fact, above 6 Al/uc sodium cations diffuse even slightly more than CO_2. In methane, due to the lower cation-guest interactions, this tipping point is not reached even at maximum aluminum substitution.

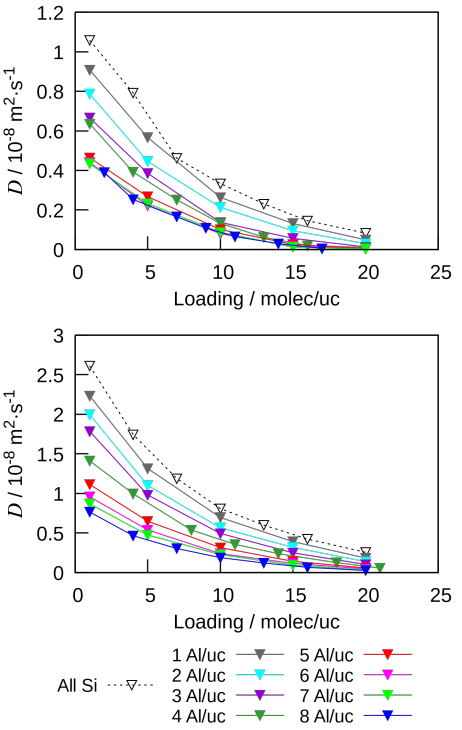

Figure 5: Diffusion coefficients of CO_2 (top) and CH_4 (bottom) for $T_{4,m}$ MFI structures with $m \in [1-8]$ Na^+ cations and for pure silica structure (dashed line).

In order to test the explanation in methane that diffusion is essentially determined by the number of particles ("obstacles"), diffusion of methane in pure silica MFI at infinite dilution has been taken as a reference. Numerically, at the temperature of the study (500K), this value is 2.612 $\times 10^{-8}$ m^2 s^{-1}. The sum of the number of cations per unit cell (m) plus the number of methane molecules necessary to achieve either 50% ($N_{50\%}$) or 30% ($N_{30\%}$) of the reference diffusion

have been plotted versus m in Figure 6. Fractional values of N are obtained due to interpolation of the loading-dependent diffusion data. For m greater or equal to 5, methane diffusion is always lower than 50% of the reference value, so no data are obtained in these cases. The interpretation of these data is that in a first approximation diffusion in methane is determined by the total number of particles in the system given that $m+N$ can be considered roughly constant. A value of around 10 particles per unit cell (roughly half maximum loading in pure silica) leaves the diffusion at 30% of its original value. In a slightly finer interpretation, one aluminum+sodium substitution accounts for roughly 1.2 methane molecules in their effect of reducing the diffusivity of methane molecules. We undertook a similar analysis for CO_2. In this case, the reference value in pure silica MFI is 1.058 $\times 10^{-8}$ m^2 s^{-1} and the sum of m and N is also roughly constant. As in the methane case, a value of around 10 particles per unit cell (roughly half maximum loading in pure silica) leaves the diffusion at 30% of its original value. But unlike for methane, a finer analysis yields a nonmonotonic behavior with increasing aluminum/sodium substitution. $m+N_{30\%}$ decreases to a minimum of 9 at m = 5 and then increases again. As was previously observed in Figure D7, this is due to diffusivity of CO_2 coupling with Na^+ diffusivity.

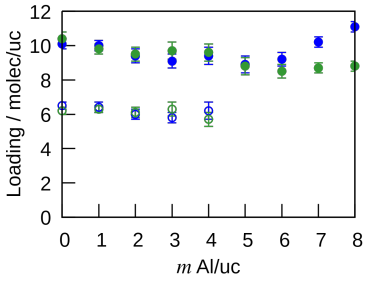

Figure 6: Number of cations + guest molecules/uc at which the guest self diffusion coefficient in $T_{4,m}$ is 50 ($m+N_{50\%}$) (open symbols) and 30 % ($m+N_{30\%}$) (full symbols) of the value of D_0 in pure silica. Carbon dioxide in blue and methane in green.

The validity of the previous analysis has been established for substitutions specifically in position T_4. But what about other substitutions? For methane diffusion, aluminum substitutions in all other positions except T_5 yield $m+N$ values similar to the T_4 case (not shown) over the whole m range (T_1, T_8) or at least up to m = 4 (T_{2-3}, T_6 and T_{11}). As for substitutions in site 5, already in $T_{5,4}$ increasing N from 1.7 (total particles per u.c. "$m+N$"=5.7) to just 4.3 ("$m+N$"=8.3) reduces diffusion from 50 to 30% of the reference value, indicating the sensitivity of this site to particles that clog the structure. For CO_2, essentially the behavior is site-specific: whereas diffusion for substitutions in sites T_2 and T_6 are similarly affected by loading to site T_4, in sites T_1 and T_8 it is much more severely affected at intermediate substitutions ("$4+N_{30\%}$"≈6). A still different behavior is observed in T_3, T_5 and T_{11}, in which diffusion at high sub-

stitution (m=8) is below 30% of the reference diffusion. In conclusion, the anomalous diffusion versus loading dependence in T_5 has been observed both in methane and carbon dioxide while diffusion for substitutions in other sites are dependent on the nature of the diffusing species.

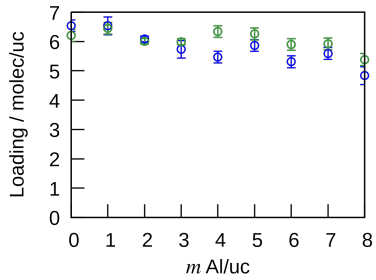

Figure 7: Number of CO_2 (blue) and CH_4 (green) guest molecules per unit cell that halve the self diffusion coefficient from its initial value at infinite dilution as a function of the number of aluminum substitutions per unit cell in position $T_{4,m}$. Systems are charge-compensated by sodium cations.

A slightly different way of interpreting the diffusion data is to use the $N_{1/2}$ values introduced in the previous section that take as a reference value the guest molecule diffusion at infinite dilution for each framework $T_{n,m}$ instead of the pure silica diffusion coefficient at infinite dilution. This reference frame enables us to test the loading dependence in all circumstances and to focus more clearly on the effect of the number of guest molecules rather than the total number of particles. In the study based on progressive substitution of Si for Al in site T_4, the data for the $T_{4,m}$ substitution are shown in Figure 7. From $T_{4,0}$ to $T_{4,8}$ the loading dependence shows consistently that the more cations, the steeper the decrease in self-diffusivities of guest molecules for whatever guest (methane or carbon dioxide), that is, the sooner the structure gets clogged and diffusion coefficients drop. Self-diffusivities of sodium cations also drop faster with increasing guest loading the more cations are present (not shown).

5.3.3 MFI-type structures with calcium cations

Instead of Na^+, the negative charge induced by aluminum atoms can be compensated by nonframework Ca^{2+} cations. In this case, the number of cations per unit cell is half the amount of aluminum atoms substituted and, consequently, for the same lattice the number of calcium cations is half the number of sodium cations. This has a direct influence on the carbon dioxide saturation loading, which is increased due to a lower excluded volume (Figure D9), while its adsorption loading at low pressure is enhanced with respect to the one obtained with sodium cations. This can be explained because Ca^{2+} interacts more strongly with CO_2 and promotes its adsorption at lower pressures. Additionally, differences in adsorption up to 17% were found depending on the location of aluminum atoms, specifically between $T_{11,8}$ and $T_{6,8}$ structures.

Regarding methane adsorption (Figure D10), it is almost unaffected either by the presence of calcium cations or by their and the aluminum location.

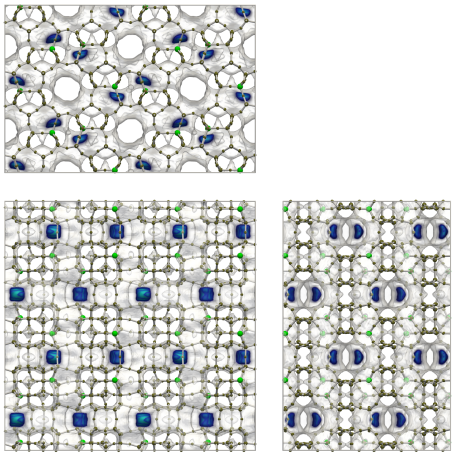

Figure 8: Probability density of Ca^{2+} cations in $T_{4,8}$ MFI channels projected on xz plane (top), xy plane (bottom-left), and zy plane (bottom-right). For easier identification, Al atoms are oversized and colored in green.

For the dynamic behavior analysis in the presence of calcium cations, we have selected some of the most salient structures according to the previous sections: in particular, $T_{4,8}$ and $T_{8,8}$ were chosen based on enabling high CO_2 and CH_4 diffusivities, respectively, $T_{5,8}$ because of almost blocking the diffusion of the adsorbates, and $T_{1,8}$ as a representative structure of an intermediate dynamic behavior. Given the divalent nature of calcium, it compensates for two aluminum atoms, and as can be seen in the representation of the density probability of calcium cations (e.g. $T_{4,8}$ in Figure 8, and $T_{1,8}$, $T_{5,8}$, and $T_{8,8}$ in Figure D11), the cations occupy a space within the zigzag channel between two adjacent aluminum atoms and remain within this region throughout the whole of the simulation. In most structures, this region adopts a finite, convex envolving shape. Therefore, and in contrast to the sodium case, calcium cations are not diffusing through the zeolite.

With respect to adsorbates, structures with calcium cations offer flatter energy profiles (Figure 9) for methane molecules along straight channels compared with those with sodium cations, but are quite similar to pure silica MFI, which lead us to anticipate an increase in methane diffusion. Concurrently, the low energy barrier for carbon dioxide found in $T_{5,8}$ can be explained based on the comparison of locations of sodium and calcium cations –at and away from the intersections– for that structure (Figures D5 and D11, respectively). This reinforces the relevance of the equilibrium positions of cations for the diffusion of the adsorbates. It is also worth pointing out that the introduction of calcium cations increases the energy barrier of $T_{8,8}$-substituted MFI for carbon dioxide with respect to the sodium case.

As was previously apparent from the probability densities, although calcium cations are moving around their equilibrium positions, they do not migrate

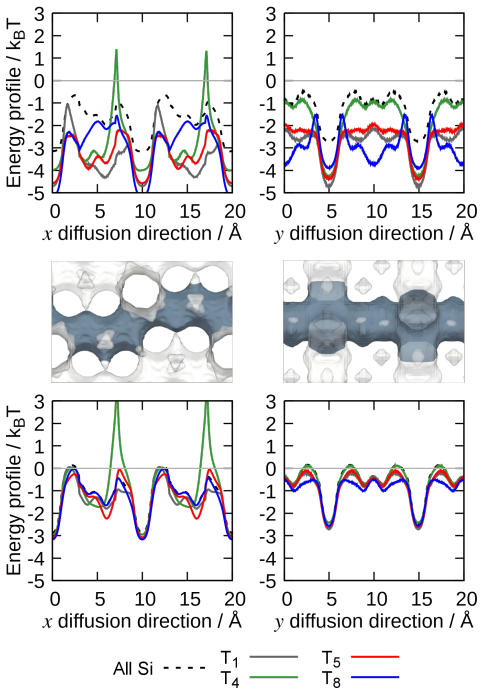

Figure 9: Energy profiles of a single molecule of CO_2 (top) and CH_4 (bottom) along the diffusion directions x (left) and y (right) in 8 Al/uc MFI structures with Ca^{2+} cations. Energy surface of the channels in the middle as reference. Continuous lines of different colors for each $T_{n,8}$. Dashed grey lines correspond to the pure silica MFI.

through the structure, meaning $D_{Ca^{2+}} = 0$ for all the structures studied. Nonetheless, since they are blocking neither channel intersections nor straight channels, diffusion of adsorbates is not significantly hindered. In fact, when considering only one methane molecule, D_{CH_4} doubles at least the values obtained for sodium cations, and in $T_{8,8}$-substituted MFI it almost equals the diffusion coefficient in pure silica MFI, as can be seen from the comparison of Figures 3 and 10: the highly localized calcium cations (Figure D11) in this case lead to flat energy profiles for methane in the x and y directions (Figure 9) and have therefore a very small impact on diffusion.

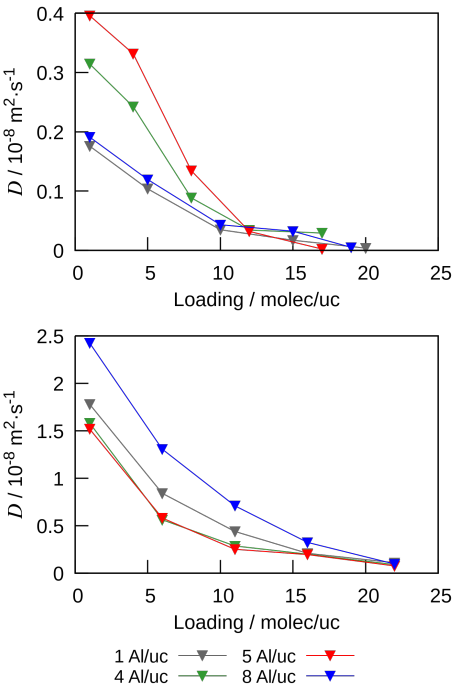

Figure 10: Diffusion coefficients of CO_2 (top) and CH_4 (bottom) as a function of loading in $T_{1,8}$, $T_{4,8}$, $T_{5,8}$, and $T_{8,8}$ MFI structures with Ca^{2+} cations.

For carbon dioxide, diffusion at low loading decreases for $T_{1,8}$, $T_{4,8}$, and $T_{8,8}$ structures up to a factor of two with respect to the sodium case, but in $T_{5,8}$ the blocking is removed and this structure shows the highest diffusion coefficient of

all site-specific Al-substitutions. Additionally, higher diffusion in $T_{4,8}$ and $T_{5,8}$ than in $T_{1,8}$ and $T_{8,8}$ because of Ca^{2+} cations occupy more invasive equilibrium positions into straight channels in the latters (Figure D11). Owing to the high diffusivities of methane in $T_{8,8}$ with calcium cations, the carbon dioxide diffusion is strikingly low and related to high energy barriers at the intersections (Figure 9). When considering directional components (not shown), a clear prevalence of diffusion through straight channels is found both for methane and carbon dioxide species in $T_{1,8}$, $T_{4,8}$, and $T_{5,8}$ structures, even when loading is increased to saturation.

It has been established previously that methane diffusion depends mostly on the crystallographic site and the sum of sodium cations and methane molecules per uc. How does a change from sodium to calcium cations affect diffusion? Figure 11 shows that at 4 cations per unit cell diffusion of methane is essentially the same in frameworks T_1, T_4 and T_5 compensated by sodium or by calcium, but different in T_8. On the whole, methane diffusion is affected by the number of cations, but not by their nature.

Figure 11 also shows that carbon dioxide diffusion from low to medium loading is always higher for sodium structures than for the corresponding calcium-containing structures. This is because calcium cations that do not diffuse due to the strong interactions with the framework

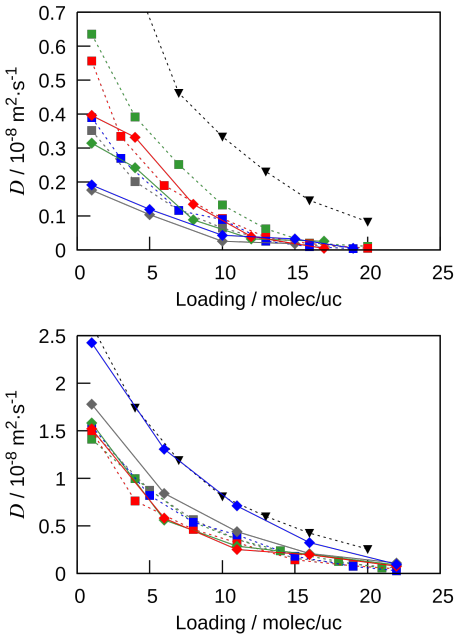

Figure 11: Diffusion coefficients of CO_2 (top) and CH_4 (bottom) as a function of loading in structures with 4 cations per unit cell: diamond symbols with continous lines for Ca^{2+} and square symbols with dashed lines for Na^+. Colors of the curves stand for the T crystallographical position of the Al substitutions: T_1 in grey, T_4 in green, T_5 in red, and T_8 in blue. Black triangle symbols with dotted lines are for pure silica MFI structure, included as a reference.

---

also interact strongly with carbon dioxide. However, diffusions vary quite a lot from framework to framework and, for instance, diffusion in $T_{5,8}$ compensated by 4 calcium cations is similar to diffusion in $T_{8,4}$ compensated by 4 sodium cations. The diffusion of carbon dioxide is strongly dependent on the valency of

the cation: at four calcium cations per uc, diffusion is noticeably lower than even at eight sodium cations per uc. Site T_5 is an exception because at 4 Ca^{2+} cations/uc it allows the diffusion of species while at 8 Na^+ cations/uc it blocks them physically. Sodium density distributions for $T_{1,4}$, $T_{4,4}$, $T_{5,4}$, and $T_{8,4}$ MFI structures are available in Figure D12.

5.4 Conclusions

We have studied MFI-type zeolites with different site-specific aluminum substitutions. As counterions, Na^+ and Ca^{2+} were considered. It is found that at 500 K, Na^+ ions are able to occupy the whole porous volume of the zeolite in most structures, whereas Ca^{2+} ions are always limited to a small volume between two aluminum atoms. In some site-specific substitutions, the calcium equilibrium site is at the intersections of straight and zigzag channels while in others it is away from the intersections. We assessed the effect of a wide range of Na and Al or Ca and Al substitutions on CO_2 and CH_4 adsorption and loading-dependent diffusion. Diffusion takes place mainly through the straight channels. From this study, a consistent picture of substantial differences in diffusion emerges, that can be explained by energy profiles that are ultimately caused by cation distributions. A noticeable fact about the energy profiles is that they are symmetrical along the straight channels but nonsymmetrical along zigzag channels, suggesting a preferred direction of diffusion.

Methane as a nonpolar species diffuses faster than CO_2 or the nonframework cations, but is limited by cations that may physically block it. Accordingly, at whatever loading, the more cations, the lower the diffusion. Another implication is that in structure $T_{5,8}$, 8 Na^+ cations block the diffusion almost completely, whereas 4 Ca^{2+} cations are localized at the centers of the channels and are constrained to a small region, leaving room for methane circulation. Therefore, compensating aluminum negative charge with calcium cations increases methane diffusion. In particular,methane diffusion in $T_{8,8}$ with Ca^{2+} cations almost equals that one obtained in pure silica MFI.

Unlike methane, carbon dioxide, owing to its charge distribution, diffuses slower the higher the charges of the cations and its diffusion coefficients remain similar to the ones of the cations. The only exception to this rule among the structures probed is T_5, in which diffusion is impaired with 8 Na atoms because they clog the channels. However, including 4 Ca^{2+} cations to compensate the charge in $T_{5,8}$ leads to high CO_2 diffusion coefficients, similar to those obtained in $T_{4,8}$ with sodium cations.

Finally, the adsorbate loading induces a monotonous decrease in self-diffusivities. For methane, the diffusion coefficient depends on the total number of particles (cations plus methane

molecules), for carbon dioxide the behavior is less straightforward, but generally at either low or high enough sodium cations per unit cell, diffusion is favoured.

Bibliography

[1] Baerlocher, C.; McCusker, L.; Olson, D. *Atlas of Zeolite Framework Types*, 6th ed.; 2007.

[2] Flanigen, E. M.; Bennett, J. M.; Grose, R. W.; Cohen, J. P.; Patton, R. L.; Kirchner, R. M.; Smith, J. V. *Nature* **1978**, *271*, 512–516.

[3] Kulprathipanja, S. *Zeolites in Industrial Separation and Catalysis*; John Wiley & Sons, 2010.

[4] Haouas, M.; Taulelle, F.; Martineau, C. *Prog. Nucl. Magn. Reson. Spectrosc.* **2016**, *94*, 11–36.

[5] Sartbaeva, A.; Rees, N. H.; Edwards, P. P.; Ramirez-Cuesta, A. J.; Barney, E. *J. Mater. Chem.A* **2013**, *1*, 7415–7421.

[6] Auerbach, S. M.; Carrado, K. A.; Dutta, P. K. *Handbook of Zeolite Science and Technology*; CRC press, 2003.

[7] Buttefey, S.; Boutin, A.; Mellot-Draznieks, C.; Fuchs, A. H. *J. Phys. Chem. B* **2001**, *105*, 9569–9575.

[8] Kokotailo, G. T.; Lawton, S. L.; Olson, D. H.; Meier, W. M. *Nature* **1978**, *272*, 437–438.

[9] Olson, D. H.; Kokotailo, G. T.; Lawton, S. L.; Meier, W. M. *J. Phys. Chem.* **1981**, *85*, 2238–2243.

[10] van Koningsveld, H.; van Bekkum, H.; Jansen, J. C. *Acta Crystallogr., Sect. B* **1987**, *43*, 127–132.

[11] Stave, M. S.; Nicholas, J. B. *J. Phys. Chem.* **1995**, *99*, 15046–15061.

[12] Alvarado-Swaisgood, A. E.; Barr, M. K.; Hay, P. J.; Redondo, A. *J. Phys. Chem.* **1991**, *95*, 10031–10036.

[13] Grau-Crespo, R.; Acuay, E.; Ruiz-Salvador, A. R. *Chem. Commun.* **2002**, 2544–2545.

[14] Sun, M. S.; Shah, D. B.; Xu, H. H.; Talu, O. *J. Phys. Chem. B* **1998**, *102*, 1466–1473.

[15] Beerdsen, E.; Smit, B.; Calero, S. *J. Phys. Chem. B* **2002**, *106*, 10659–10667.

[16] Beerdsen, E.; Dubbeldam, D.; Smit, B.; Vlugt, T. J.; Calero, S. *J. Phys. Chem. B* **2003**, *107*, 12088–12096.

[17] Wirawan, S. K.; Creaser, D. *Microporous Mesoporous Mater.* **2006**, *91*, 196–205.

[18] Garcia-Sanchez, A.; Ania, C. O.; Parra, J. B.; Dubbeldam, D.; Vlugt, T. J. H.; Krishna, R.; Calero, S. *J. Phys. Chem. C* **2009**, *113*, 8814–8820, and references therein.

[19] Caremans, T. P.; van Erp, T. S.; Dubbeldam, D.; Castillo, J. M.; Martens, J. A.; Calero, S. *Chem. Mater.* **2010**, *22*, 4591–4601.

[20] Perez-Carbajo, J.; Gomez-Alvarez, P.; Bueno-Perez, R.; Merkling, P. J.; Calero, S. *Phys. Chem. Chem. Phys.* **2014**, *16*, 5678–5688.

[21] Newsome, D.; Gunawan, S.; Baron, G.; Denayer, J.; Coppens, M.-O. *Adsorption* **2014**, *20*, 157–171.

[22] Caro, J.; Bülow, M.; Schirmer, W.; Kärger, J.; Heink, W.; Pfeifer, H.; Ždanov, S. P. *J. Chem. Soc., Faraday Trans. 1 F* **1985**, *81*, 2541–2550.

[23] Kärger, J.; Pfeifer, H. *Zeolites* **1987**, *7*, 90–107.

[24] Kärger, J. *J. Phys. Chem.* **1991**, *95*, 5558–5560.

[25] Kärger, J.; Pfeifer, H.; Stallmach, F.; Feoktistova, N.; Zhdanov, S. *Zeolites* **1993**, *13*, 50–55.

[26] Catlow, C.; Freeman, C.; Vessal, B.; Tomlinson, S.; Leslie, M. *J. Chem. Soc., Faraday Trans.* **1991**, *87*, 1947–1950.

[27] Xiao, J.; Wei, J. *Chem. Eng. Sci* **1992**, *47*, 1123–1141.

[28] Jobic, H. *J. Mol. Catal. A: Chem.* **2000**, *158*, 135–142.

[29] Papadopoulos, G. K.; Jobic, H.; Theodorou, D. N. *J. Phys. Chem. B* **2004**, *108*, 12748–12756.

[30] Beerdsen, E.; Dubbeldam, D.; Smit, B. *Phys. Rev. Lett.* **2005**, *95*, 164505.

[31] Krishna, R.; Van Baten, J.; Garcia-Perez, E.; Calero, S. *Ind. Eng. Chem. Res.* **2007**, *46*, 2974–2986.

[32] Caro, J.; Hŏcevar, S.; Kärger, J.; Riekert, L. *Zeolites* **1986**, *6*, 213–216.

[33] Jobic, H.; Bée, M.; Caro, J.; Bülow, M.; Kärger, J. *J. Chem. Soc., Faraday Trans. 1 F* **1989**, *85*, 4201–4209.

[34] Masuda, T.; Fujikata, Y.; Nishida, T.; Hashimoto, K. *Microporous Mesoporous Mater.* **1998**, *23*, 157–167.

[35] Newsome, D.; Coppens, M.-O. *Chem. Eng. Sci.* **2015**, *121*, 300–312.

[36] Löwenstein, W.; Lowenstein, M. *American Mineralogist* **1954**, *39*, 92–96.

[37] Jaramillo, E.; Auerbach, S. M. *J. Phys. Chem. B* **1999**, *103*, 9589–9594.

[38] Calero, S.; Dubbeldam, D.; Krishna, R.; Smit, B.; Vlugt, T. J. H.; Denayer, J. F. M.; Martens, J. A.; Maesen, T. L. M. *J. Am. Chem. Soc.* **2004**, *126*, 11377–11386.

[39] Garcia-Sanchez, A.; Dubbeldam, D.; Calero, S. *J. Phys. Chem. C* **2010**, *114*, 15068–15074.

[40] Demontis, P.; Fois, E. S.; Suffritti, G. B.; Quartieri, S. *J. Phys. Chem.* **1990**, *94*, 4329–4334.

[41] Fritzsche, S.; Haberlandt, R.; Kärger, J.; Pfeifer, H.; Wolfsberg, M. *Chem. Phys. Lett.* **1990**, *171*, 109–113.

[42] Garcia-Perez, E.; Dubbeldam, D.; Maesen, T. L.; Calero, S. *J. Phys. Chem. B* **2006**, *110*, 23968–23976.

[43] Dubbeldam, D.; Calero, S.; Vlugt, T. J. H.; Krishna, R.; Maesen, T. L. M.; Smit, B. *J. Phys. Chem. B* **2004**, *108*, 12301–12313.

[44] Ryckaert, J.-P.; Bellemans, A. *Faraday Discuss. Chem. Soc.* **1978**, *66*, 95–106.

[45] Bezus, A. G.; Kiselev, A. V.; Lopatkin, A. A.; Du, P. Q. *J. Chem. Soc., Faraday Trans. 2* **1978**, *74*, 367–379.

[46] Kiselev, A. V.; Lopatkin, A. A.; Shulga, A. A. *Zeolites* **1985**, *5*, 261–267.

[47] Lorentz, H. A. *Ann. Phys.* **1881**, *248*, 127–136.

[48] Berthelot, D. *C.R. Hebd. Seances Acad. Sci.* **1898**, *126*,

1703–1855.
[49] Hay, D. G.; Jaeger, H. *J. Chem. Soc., Chem. Commun.* **1984**, 1433–1433.
[50] Frenkel, D.; Smit, B. *Understanding Molecular Simulation: From Algorithms to Applications*; Academic Press: London, 2002.
[51] Dubbeldam, D.; Beerdsen, E.; Vlugt, T. J. H.; Smit, B. *J. Chem. Phys.* **2005**, *122*, –.
[52] Hoover, W. G. *Phys. Rev. A* **1986**, *34*, 2499–2500.
[53] Beerdsen, E.; Smit, B.; Dubbeldam, D. *Phys. Rev. Lett.* **2004**, *93*, 248301.
[54] Dubbeldam, D.; Calero, S.; Ellis, D. E.; Snurr, R. Q. *Mol. Simul.* **2016**, *42*, 81–101.
[55] Tabourier, P.; Carru, J.-C.; Wacrenier, J.-M. *J. Chem. Soc., Faraday Trans. 1* **1983**, *79*, 779–783.

Effect of lattice shrinking on the migration of water within zeolite LTA

J. Perez-Carbajo, S. R. G. Balestra, P. J. Merkling, and S. Calero

Water adsorption within zeolites of the Linde Type A (LTA) structure plays an important role in processes of water removal from solvents. For this purpose, knowing in which adsorption sites water is preferably found is of interest. In this paper, the distribution of water within LTA is investigated in several aluminum-substituted frameworks ranging from a Si:Al ratio of 1 (maximum substitution, framework is hydrophilic) to a Si:Al ratio of 191 (almost pure siliceous framework, it is hydrophobic). The counterion is sodium. In the hydrophobic framework, water enters the large α-cages, whereas in the most hydrophilic frameworks, water enters preferably the small β-cages. For frameworks with moderate aluminum substitution, β-cages are populated first, but at intermediate pressures water favors α-cages instead. Framework composition and pressure therefore drive water molecules selectively towards α- or β-cages.

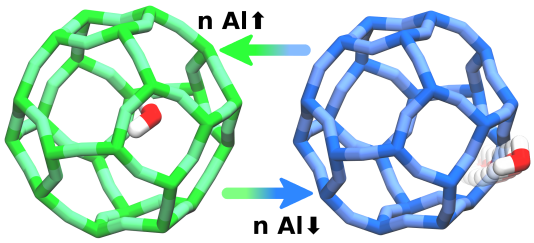

6.1 INTRODUCTION

Zeolites are natural or synthetic crystalline compounds containing most commonly only silicon, aluminum, oxygen, and exchangeable cations. Zeolites have important industrial applications due to their nanoporosity. The zeolite of interest in this work, Linde Type A (LTA) zeolite has a cubic unit cell. It possesses two types of roughly spherical cavities, lta cages (or α-cages) with an approximate diameter of 11.2 Å and sodalite (sod) cages (or β-cages) with an average diameter of 6.6 Å. α-cages are connected to another six α-cages through eight-membered windows (S8R) of about 4.2 Å and connected to eight β-cages through six-membered windows of about 2.2 Å openings. Although the idealized cell found in the pure silica version contains one α- and one β-cage, and has a chemical formula of $Si_{24}O_{48}$, for the sake of simplicity we will refer to the unit cell as the supercell found in aluminum-substituted versions of chemical formula $Na_x[Al_xSi_{192-x}O_{384}]$ which contains eight α- and eight β-cages. Its side length, depending on aluminum content, varies between 23.75–24.55 Å at room temperature.

Water molecules are able to enter α- and β-cages of zeolite LTA,[1–3] which can be made more hydrophilic by substituting some of the silicon atoms by aluminum. This has significant industrial consequences, as pervaporation processes for removal of water using LTA have been conducted both in the lab and in large-scale industrial plants.[4] Thus, Mitsui Engineering and Shipbuilding Co., Japan, built an industrial facility for ethanol dehydration using sodium-containing LTA zeolite membranes. Other applications include removal of water from other solvents, water desalination and water removal from esterification processes. It is therefore useful to get a more fundamental understanding of water in LTA. How water behaves within the LTA crystalline structure has been studied in a number of ways: by X-ray diffraction,[5] Fourier-transform infrared spectroscopy,[6,7] spin-echo nuclear magnetic resonance,[8] and several neutron scattering techniques.[8–11] Theoretical studies, with their very detailed insight into the microscopic world of the structure, contribute also significantly to the understanding of these systems. Adsorption isotherms,[12–14] hydrogen-bond statistics,[12,14–17] diffusion coefficients,[18,19] thermodynamic considerations[20] and some characterization of the bonding sites and behavior of water[15,16,21,22] have been obtained for specific compositions like pure silica LTA or the maximally aluminum-substituted LTA called LTA 4A, NaA or zeolite 4A. However, the composition-dependent location of water molecules has not been explored. Thus, it is the purpose of this work to study the distribution of water molecules in LTA across the whole range of sodium-compensated aluminum substi-

tutions, namely from almost pure silica LTA to $Na_{96}[Al_{96}Si_{96}O_{384}]$.

6.2 METHODS

Structures are defined as rigid frameworks with static partial charges,[23] where oxygen and silicon atoms have charges of $q_O = -0.3930\ e^-$ and $q_{Si} = +0.7860\ e^-$, respectively. Since introducing aluminum affects the partial charge on silicon, its charge is set to $q_{Al} = +0.4860\ e^-$.[24,25] This charge redistribution results in Na^+ cations tending to be located nearby Al atoms, affecting thereby the partial charge of these oxygen atoms forming the AlO_4 tetrahedra:[24] ($q_{O_a} = -0.4138\ e^-$). Na^+ extra-framework cations introduced in the structure are considered as point charges $q_{Na^+} = +0.3834\ e^-$[23] and are allowed to move trough the system. The water molecule is defined by the TIP5P/Ew model.[26] This model, formed by five sites arranged tetrahedrally, in which the oxygen atom transfers its negative charge to two *dummy* pseudo-atoms, has been previously reported to reproduce the adsorption behavior of water in zeolites.[12,14,17,27]

Interactions between the interaction sites of the system (lattice atoms, extra-framework cations, and adsorbates) are ruled by Coulombic potential for electrostatic interactions, using the Ewald summation to handle the periodicity of the system, and Lennard–Jones (L–J) potentials are used to model van der Waals (vdW) interactions. L–J interactions of adsorbates with zeolites are dominated by dispersive forces with the oxygen atoms (O and O_a) so the interactions with silicon and aluminum atoms are neglected.[28,29] vdW interactions are also not considered between sodium cations themselves due to their strong electrostatic interactions. The rest of L–J interactions are already parametrized in and taken from previous works.[12,27]

Different LTA-type lattices have been considered in this work, attending to their aluminum content. All of the frameworks are charge-compensated by introducing an equal number of Na^+ cations as aluminum atoms in the framework. LTA zeolites have been synthesized over a wide range of Si:Al ratios, from pure silica framework[30,31] up to LTA 4A[32,33] with the same amount of Si atoms as Al atoms. This latter structure meets the theoretical maximum substitution of Si by Al atoms allowed, according to Löwenstein's rule.[34] The Si:Al ratios of our structures span this range, from Si:Al=1 (96 Al/Na^+ pairs per supercell, henceforth called "LTA-96" for simplicity) down to almost pure silica LTA (Si:Al=191, 1 Al/Na^+ pair per supercell, "LTA-1"). The other ratios used in this study are 1.02 (95 Al/Na^+ per supercell, "LTA-95"), 1.91 (66 Al/Na^+ per supercell, "LTA-66"), 3.57 (42 Al/Na^+ per supercell, "LTA-42"), and 5 (32 Al/Na^+ per supercell, "LTA-32").

While atomistic positions for both alu-

minum atoms and sodium cations are described for LTA 4A[33] and were taken from the literature, the rest of LTA structures were generated computationally. To that end, starting from the lattice of LTA 4A, aluminum atoms were progressively substituted by silicon atoms. The first substitution was made randomly and subsequent substitutions were restrained by Dempsey's rule[35], to minimize the number of Al–O–Si–O–Al elements and in order to obtain a more uniform aluminum distribution in the lattice. This method generates frameworks with well-defined properties.

As was mentioned previously, frameworks were considered rigid throughout the simulation with the exception of the extra-framework cations but, for each Si:Al ratio, we considered two lattices. For the first one, atomistic positions of the LTA 4A lattice[33] were kept unchanged. For the second one, not only lattices, but also extra-framework cations, were allowed to relax their crystallographic positions to meet a minimum energy configuration. These minimizations were performed ten times independently and the lowest energy configuration was selected to avoid false minima and energy saddle points. This configuration was taken as the initial configuration of the simulations.

To compute adsorption isotherms of water and its average occupation profile in LTA-type zeolites, Monte Carlo simulations are run in the Grand Canonical ensemble (μVT).[36] Setting the chemical potential μ, the fugacity of a gas f and therefore the pressure are also set. Fugacity and chemical potential are related through the equation $\mu = \mu^0 + RT\ln(f/p^0)$, in which p^0 is the standard chemical pressure, R the gas constant and T the temperature, set to 298K in this study. Cations are placed inside the structures using random trial insertions to bypass energy barriers[25] and move by trial displacements. Since the L–J potential cutoff was set to 12 Å in the development of the interaction potentials, the same cutoff has been applied in our study. The sides of our simulation boxes were at least twice the L–J cutoff.

Structural relaxations have been carried out using the GULP code.[37] We have used the well-known shell-model potentials of Sanders *et al.*[38] for the structure and the potential of Jackson *et al.* for the cations.[39,40] Broyden–Fletcher–Goldfarb–Shanno (BFGS) and Rational Function Optimization (RFO) minimization methods were used to ensure convergence to true energy.[41,42] Although the BFGS algorithm is faster than RFO, RFO behaves better than BFGS in the vicinity of the minimum. So, we have used initially the BFGS algorithm, and when the gradient norm dropped below 0.03, we have switched to the RFO minimizer. This methodology has been validated in many previous works and provides cell parameters and realistic crystal structures.[43–45] Monte Carlo simulations of this work were performed using

RASPA software.[46] Average occupation profiles were obtained by using the software SITES-ANALYZER.[47]

6.3 Results and Discussion

Experimentally, from purely siliceous LTA to LTA 4A the crystal cell dimensions increase noticeably,[31,33] which translates into a 10% volume increase. This has important consequences for the pore volume of the nanoporous cavity. The force field used in our zeolite is able to reproduce the experimental volumes, as shown in Figure 1. We therefore expect it to predict reasonably well the volumes of structures with an intermediate aluminum content. All of the structures were optimized as dehydrated frameworks and then frozen. This is a valid approach because in test calculations we have found the effect of hydration on volume change to be negligible. A similar observation had been done previously for LTA 4A,[13] using a different force field from ours. The size of the unit cell, and especially the size of the openings in the sodalite cages is an important factor for the capacity of the zeolite for separating multicomponent mixtures. For the sake of naming the frameworks simply, they will be called LTA-x, with x the number of aluminum atoms in the 2×2×2 supercell, i.e. the cell that contains 8 α-cages and 8 β-cages. Thus, LTA-96 is LTA 4A.

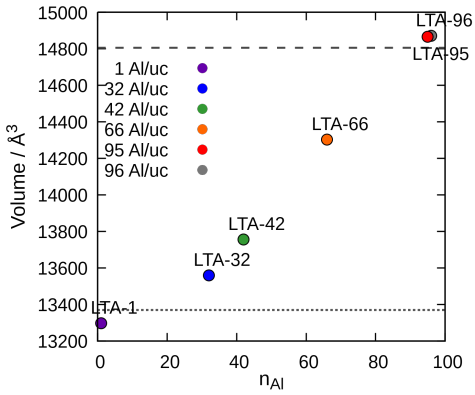

Figure 1: Minimized LTA cell volumes. Dashed line for experimental volume of LTA4A and of fixed-size frameworks. Dotted line for volume of pure silica LTA (ITQ-29). All volumes apply to 2 × 2 × 2 supercell.

The hydrophobicity of the zeolite has dramatic consequences on adsorption behavior. The almost pure siliceous zeolite LTA-1 requires pressures in excess of 10^5 Pa to adsorb water (Figure 2), and the adsorption curve is very steep. This is a consequence of the hydrophobic environment, but once water enters, it creates nucleation sites for other water molecules around it. Clusters of water are created. At LTA-32 already, nucleation sites exist (the sodium cations), which draw in water more gradually. Therefore, half-loading is achieved at around 10^4 Pa. This means that the framework at this level of aluminum-enrichment has already a marked hydrophilic character. Further aluminum enrichment of the framework to 66 aluminum atoms per supercell reduces

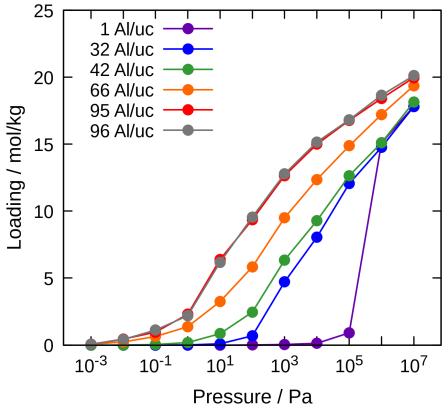

Figure 2: Full circle, solid line: Reversible water adsorption isotherms in minimized LTA frameworks

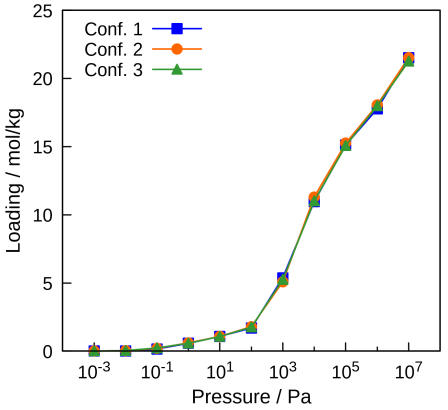

Figure 3: Water adsorption isotherms for three frameworks with the same overall composition $Na_{42}[Al_{42}Si_{150}O_{384}]$

the necessary pressure another order of magnitude, and for LTA 4A, half-loading is achieved at 10^2 Pa. In terms of the IUPAC classification of isotherms,[48] siliceous zeolite is a type V isotherm whereas the other isotherms are of type I.

Figure 3 shows the water adsorption isotherms at 298 K of three frameworks of composition LTA-42, but with a different distribution of aluminum atoms. All three distributions comply with Löwenstein's and Dempsey's rules. It can be appreciated that the three frameworks led to virtually the same adsorption curves.

An understanding of the site-dependent hydration can be drawn from a loading-dependent representation of the percentage of water present in the structural features of zeolite LTA, namely the small β-cages, the large α-cages and the window-area S8R. This is shown in Figure 4. At low aluminum-content, water is not contained in the β-cages until high loading, a conclusion in qualitative agreement with a study by Coudert *et al.*[15] At maximum loading however, we can assume water molecules to be distributed among the sites with no preference for any given site, which means that the distribution should reflect the volumes of the regions: α-cages account for roughly 78% of the available pore volume, β-cages for 15% and the S8R window area for 7%. According to this, at lower pressures and loading, water has a strong affinity for the window region. At increasing pressure, it populates much more strongly the α-cages, whereas β-cages are the last to be populated. Already in LTA-32, the behavior is radically different: β-cages are disproportionately populated at low pressures, even more so than

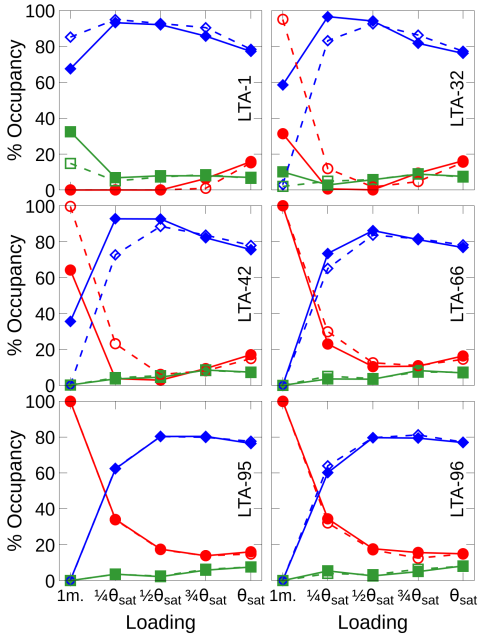

Figure 4: Distribution of water molecules by adsorption sites in percent: α-cage (blue diamonds), β-cage (red circles) and S8R windows (green squares) for fixed-size (empty symbols, dashed lines) and minimized (full symbols, solid lines) LTA as a function of the fraction of maximum loading

the window region. At high pressures, saturation is responsible for the filling of the pores and the volume-based distribution indicated earlier is reached. β-cages contain three to four water molecules each, α-cages 22 and three quarters of the windows one molecule. But the most striking part is the behavior at intermediate pressures, in this case 10^3-10^5 Pa, in which β-cages are statistically depopulated, on average one water molecule in the supercell, compared to of the order of 100 in the α-cages. LTA-42 and LTA-66 exhibit a similar phenomenon. If we relate this to the sodium positions, these striking results make sense: in LTA-1, the sodium cations are located in the S8R region at low pressures, but are forced into the α-cages at higher pressures. In LTA-32 at low pressure, sodium cations are located mainly in the window-region, and also disproportionately in the β-cages (16 and 7 Na^+ per window- and β-cage region of the supercell, respectively). Then, at 10^3 Pa, these numbers drop to 1 and 0.6 respectively, most cations and water molecules are then located in the α-cages. From 10^6 Pa on, a few cations (and water molecules) are back in the β-cages. This is a very interesting behavior, because it means that by choosing the Si:Al ratio and regulating the pressure, one can direct the water towards one or another type of site. Similar patterns are seen in LTA-42 and to a lesser extent in LTA-66, sodium populations in the β-cages decrease at the intermediate pressures at which water also is driven out of these cages and gets back in again at higher pressures. No such behavior is observed in LTA-95 and LTA-96, sodium cation populations are roughly constant throughout the pressure range and water molecules are located overwhelmingly (> 99%) in the β-cages at low pressure. At higher pressures, water molecules also populate α-cages, a finding already pointed out by Castillo *et al.* [13] The curves for LTA-96 (maximum aluminum substitution) and LTA-95 (one

aluminum short of maximum aluminum-substitution) are, not surprisingly, very similar, an indication for good sampling.

In the frameworks with intermediate aluminum substitution such as LTA-32, LTA-42 and LTA-66, at low pressures sodium-water interactions and interactions with the framework in the confined area of the β-cages have energetic advantages. Then, at higher loading, confinement turns into an obstacle, large clusters of water that can be formed only in the α-cages engage in many water-water hydrogen bonds, which is energetically favorable. In the frameworks LTA-95 and LTA-96, the high amount of sodium cations relative to water means that most water molecules are part of the hydration shell of sodium, which is a stronger interaction than that provided by hydrogen bonds.

So far, we have commented on the curves of the minimized structures in Figure 4. These structures describe the confined environment and its size accurately. We have identified a behavior of sodium and water distribution that is dependent on the Si:Al ratio. But, given that the preference of a water molecule for the confined region of β-cages or the larger α-cages is highly sensitive to the cell size, we would like to identify if the adsorption behavior at specific sites is due to the loss of charges and hydrophilicity brought about by decreasing the number of sodium and aluminum atoms, or if the shrinking of the cell with decreasing number of sodium and aluminum atoms is essential to the location of the adsorbates. To answer this question, GCMC simulations in a cell of the size of LTA 4A have been performed. The distribution of water molecules by adsorption sites is also represented in Figure 4. The curves for LTA-96 and LTA-95 are almost superimposable with the ones for the minimized structures because the cell size is identical or virtually identical. Differences are due to statistics because they were obtained in independent simulation runs. The less aluminum in the structure, the greater the difference in volume (Figure 1) between the fixed-size cell and the minimized cell. Some differences in water distribution show at low loading. The interpretation is that the shrinking of the cell brought about by lowering the aluminum content does not favor water population of the β-cages. The fact that water in the minimized structures LTA-32 and LTA-42 still populate disproportionately the β-cages is because the presence of cations in these cages is a powerful driver that offsets the shrinking. Qualitatively, the migration out of the β-cages and back in as pressure is increased (infinitely slowly) is also observed in the fixed-size cells. It is thus an effect of electrostatics, i.e. hydrophilicity/hydrophobicity, and not an effect of the size of the structure due to the Si:Al ratio.

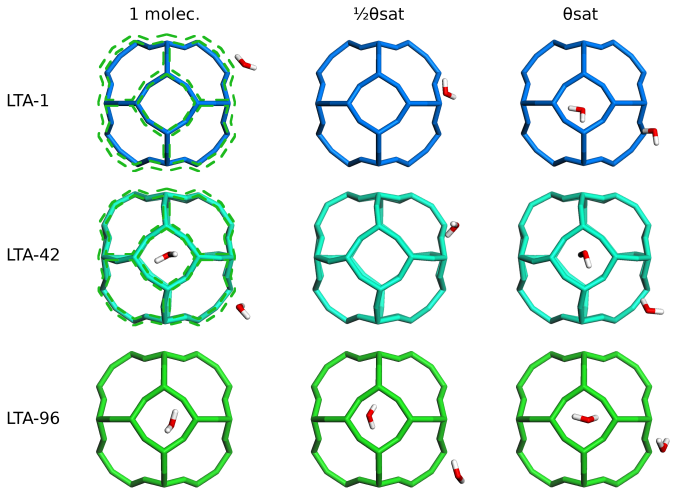

Figure 5: Schematic representation to illustrate the water migration in or out of β-cages observed in zeolite LTA depending on composition and loading. Green dashed lines in first column mark the contour of LTA-96, evidencing lattice shrinking when Si:Al ratio grows.

6.4 Conclusions

In nearly pure siliceous zeolite LTA, water is located in the α-cages and, as pressure or loading increase, it finally gets into the β-cages. On the contrary, for frameworks with significant aluminum content (Si:Al $\leq$ 5) such as LTA-42, β-cages are populated disproportionately at low pressure. For these systems, the percentage of water in β-cages drops as more and more water gets into the α-cages with increasing pressure. The most exciting situation arises in the systems with Si:Al ratios of 1.91-5: water molecules and sodium cations move out of the β-cages at intermediate pressures, and are forced back in at sufficiently high pressures (10^6 Pa), at which the whole of the available volume is occupied. These findings are summarized visually in Figure 5.

This is a very interesting behavior, because it means that by choosing the Si:Al ratio and regulating the pressure, one can direct the water towards one or another type of site. This could be used technologically, because it would allow separating multi-component mixtures by tuning the adsorption selectivity of water.

Bibliography

[1] Di Lella, A.; Desbiens, N.; Boutin, A.; Demachy, I.; Ungerer, P.; Bellat, J.-P.; Fuchs, A. H. *Physical Chemistry Chemical Physics* **2006**, *8*, 5396–5406.

[2] Boddenberg, B.; Rakhmatkariev, G. U.; Hufnagel, S.; Salimov, Z. *Phys. Chem. Chem. Phys.* **2002**, *4*, 4172–4180.

[3] Gedeon, A.; Ito, T.; Fraissard, J. *Zeolites* **1988**, *8*, 376–380.

[4] Wenten, I. G.; Dharmawijaya, P. T.; Aryanti, P. T. P.; Mukti, R. R.; Khoiruddin, *R. S. C. Adv.* **2017**, *7*, 29520–29539.
[5] Gramlich, V.; Meier, W. M. *Z. Kristallogr.* **1971**, *133*, 143–149.
[6] Crupi, V.; Majolino, D.; Migliardo, P.; Venuti, V.; Wanderlingh, U. *Eur. Phys. J. E* **2003**, *12*, S55–S58.
[7] Crupi, V.; Longo, F.; Majolino, D.; Venuti, V. *J. Chem. Phys.* **2005**, *123*, 154702.
[8] Paoli, H.; Méthivier, A.; Jobic, H.; Krause, C.; Pfeifer, H.; Stallmach, F.; Kärger, J. *Microporous Mesoporous Mater.* **2002**, *55*, 147–158.
[9] Corsaro, C.; Crupi, V.; Majolino, D.; Migliardo, P.; Venuti, V.; Wanderlingh, U.; Mizota, T.; Telling, M. *Mol. Phys.* **2006**, *104*, 587–598.
[10] Corsaro, C.; Crupi, V.; Longo, F.; Majolino, D.; Venuti, V.; Wanderlingh, U. *Phys. Rev. E* **2005**, *72*, 061504.
[11] Corsaro, C.; Crupi, V.; Longo, F.; Majolino, D.; Venuti, V.; Wanderlingh, U. *J. Phys.: Condens. Matter* **2005**, *17*, 7925–7934.
[12] Calero, S.; Gómez-Álvarez, P. *J. Phys. Chem. C* **2014**, *118*, 9056–9065.
[13] Castillo, J. M.; Silvestre-Albero, J.; Rodriguez-Reinoso, F.; Vlugt, T. J. H.; Calero, S. *PCCP* **2013**, *15*, 17374–17382.
[14] Gómez-Álvarez, P.; Calero, S. *Cryst. Eng. Comm.* **2015**, *17*, 412–421.
[15] Coudert, F.-X.; Vuilleumier, R.; Boutin, A. *Chem. Phys. Chem.* **2006**, *7*, 2464–2467.
[16] Coudert, F.-X.; Cailliez, F.; Vuilleumier, R.; Fuchs, A.; Boutin, A. *Faraday Discuss.* **2009**, *141*, 377–398.
[17] Gómez-Álvarez, P.; Perez-Carbajo, J.; Balestra, S. R. G.; Calero, S. *J. Phys. Chem. C* **2016**, *120*, 23254–23261.
[18] Demontis, P.; Gulín-González, J.; Jobic, H.; Suffritti, G. B. *J. Phys. Chem. C* **2010**, *114*, 18612–18621.
[19] Faux, D. A. *The Journal of Physical Chemistry B* **1999**, *103*, 7803–7808.
[20] Manon Higgins, F.; de Leeuw, N. H.; Parker, S. C. *J. Mater. Chem.* **2002**, *12*, 124–131.
[21] Demontis, P.; Gulín-González, J.; Jobic, H.; Masia, M.; Sale, R.; Suffritti, G. B. *ACS Nano* **2008**, *2*, 1603–1614.
[22] Faux, D. A.; Smith, W.; Forester, T. R. *J. Phys. Chem. B* **1997**, *101*, 1762–1768.
[23] Garcia-Sanchez, A.; Ania, C. O.; Parra, J. B.; Dubbeldam, D.; Vlugt, T. J. H.; Krishna, R.; Calero, S. *J. Phys. Chem. C* **2009**, *113*, 8814–8820, and references therein.
[24] Jaramillo, E.; Auerbach, S. M. *J. Phys. Chem. B* **1999**, *103*, 9589–9594.
[25] Calero, S.; Dubbeldam, D.; Krishna, R.; Smit, B.; Vlugt, T. J. H.; Denayer, J. F. M.; Martens, J. A.; Maesen, T. L. M. *J. Am. Chem. Soc.* **2004**, *126*, 11377–11386.
[26] Rick, S. W. *J. Chem. Phys.* **2004**, *120*, 6085–6093.
[27] Castillo, J. M.; Dubbeldam, D.; Vlugt, T.; Smit, B.; Calero, S. *Mol. Sim.* **2009**, *35*, 1067–1076.
[28] Bezus, A. G.; Kiselev, A. V.; Lopatkin, A. A.; Du, P. Q. *J. Chem. Soc., Faraday Trans. 2* **1978**, *74*, 367–379.
[29] Kiselev, A. V.; Lopatkin, A. A.; Shulga, A. A. *Zeolites* **1985**, *5*, 261–267.
[30] Fyfe, C. A.; Kennedy, G. J.; Kokotailo, G. T.; DeSchutter, C. T. *J. Chem. Soc. Chem. Comm.* **1984**, 1093–1094.
[31] Corma, A.; Rey, F.; Rius, J.; Sabater, M. J.; Valencia, S. *Nature* **2004**, *431*, 287–290.
[32] Reed, T. B.; Breck, D. *Journal of the American Chemical Society* **1956**, *78*, 5972–5977.
[33] Pluth, J. J.; Smith, J. V. *J. Am. Chem. Soc.* **1980**, *102*, 4704–4708.
[34] Löwenstein, W.; Lowenstein, M. *American Mineralogist* **1954**, *39*, 92–96.
[35] Dempsey, E. *J. Soc. Chem. Ind., London* **1968**, *293*.
[36] Frenkel, D.; Smit, B. *Understanding Molecular Simulation: From Algorithms to Applications*; Academic Press: London, 2002.
[37] Gale, J. D. *J. Chem. Soc., Faraday Trans.* **1997**, *93*, .
[38] Sanders, M. J.; Leslie, M.; Catlow, C. R. A. *J. Chem. Soc., Chem. Commun.* **1984**, 1271.
[39] Jackson, R.; Bell, R.; Catlow, C. In *Recent Advances in Zeolite Science Proceedings of the 1989 Meeting of the British Zeolite Association*; Klinowski, J., Barrie, P. J., Eds.; Studies in Surface Science and Catalysis; Elsevier, 1989; Vol. 52; pp 203 – 208.
[40] Jackson, R. A.; Catlow, C. R. A. *Mol. Simul.* **1988**, *1*, 207–224.
[41] Fletcher, R. *Practical methods of optimization*; Wiley: Chichester New York, 1987.
[42] Byrd, R. H.; Gilbert, J. C.; Nocedal, J. *Math. Program.* **2000**, *89*, 149–185.
[43] Almora-Barrios, N.; Ruiz-Salvador, A. R.; Gómez, A.; Mistry, M.; Lewis, D. W. *Chem. Comm.* **2001**, 531–532.
[44] Lewis, D. W.; Ruiz-Salvador, A. R.; Almora-Barrios, N.; Gómez, A.; Mistry, M. *Mol. Sim.* **2002**, *28*, 649–661.
[45] Balestra, S. R. G.; Hamad, S.; Ruiz-Salvador, A. R.; Domínguez-García, V.; Merkling, P. J.; Dubbeldam, D.; Calero, S. *Chem. Mat.* **2015**, *27*, 5657–5667.
[46] Dubbeldam, D.; Calero, S.; Ellis, D. E.; Snurr, R. Q. *Mol. Simul.* **2016**, *42*, 81–101.
[47] Vicent-Luna, J. M. SITES-ANALYZER. 2017; `https://github.com/jmviclun/SITES-ANALYZER`.
[48] Thommes, M.; Kaneko, K.; Neimark, A. V.; Olivier, J. P.; Rodriguez-Reinoso, F.; Rouquerol, J.; Sing, K. S. *Pure Appl. Chem.* **2015**, *87*, 1051–1069.

CHAPTER 7

CONCLUSIONS

The main conclusions from this Thesis on gas mixture separations for industrial processes are:

- Specific separation schemes are proposed to achieve highly-selective separations to enhance the performance of selected industrial processes (Fischer-Tropsch hydrocarbon synthesis (*Chapter 2*) and plasma-assisted CO_2-dissociation (*Chapter 3*)) and open doors for new perspectives on hydrogen isotope separation processes (*Chapter 4*) by tailoring the suite of adsorbent structures or by a rational selection.

- The effect of substituting silicon by aluminum atoms on CO_2 and CH_4 adsorption behavior is reported for four commercially-available topologies (DDR, FAU, MFI, and MOR). In these topologies, aluminum atom location, for a given aluminum density, have either significant impact or almost negligible effects on CO_2 and CH_4 adsorption. With respect to the density of Al/Na^+ pairs in the system, while CO_2 adsorption is systematically enhanced when density rises, for all the structures and pressures, CH_4 is found to be dependent in a non-trivial way on those factors. The rest of gases of the five-component mixture are neither significantly affected nor adsorbed. (*Chapter 2*).

- Adsorption selectivity at zero-loading, defined by the Henry coefficients ratio of different molecules, is proved to be a useful screening indicator to predict further loading-dependent adsorption selectivity. (*Chapters 3 and 4*).

- Molecular simulation predictions are found to be in line with large-scale PSA process simulation results, filling the gap between molecular and process simulation levels. In particular, a study on the separation of a ternary mixture separation, composed by CO_2 , CO, and O_2 , is endorsed by a two-cycles PSA process. (*Chapter 3*).

- New models for D_2 and T_2 molecules in pure silica zeolites are proposed. D_2 model is validated by experimental adsorption isotherms performed at cryogenic temperatures in two pure silica zeolites, MFI and LTA. Quantum corrections, incorporated into the model of molecules, are essential to reproduce experimental adsorption curves. (*Chapter 4*).

- BCT zeolite is found to be able of efficiently separating D_2/H_2 and T_2/H_2 equimolar mixtures. Actually, it shows the highest adsorption selectivity reported for nanoporous materials performing these hydrogen isotope sieving. This finding creates room for going further in hydrogen isotope enrichment processes. (*Chapter 4*).

The following conclusions about the molecular insights on relevant aspects of separation processes can be drawn:

- Effect of cations on diffusion of CO_2 and CH_4 in MFI is assessed. It is shown that, in a general way, structures with the same global composition lead to quite different diffusion behaviors of these guest molecules, depending on location and amount of aluminum atoms, and nature of cations. (*Chapter 5*).

- The computation of energy profiles is extended from pure silica structures reported in the literature to aluminosilicate frameworks counterbalanced by mono or divalent cations, namely Na^+ and Ca^{2+} ions. Energy profiles for polar and nonpolar reference molecules, *i. e.* CO_2 *and* CH_4 , are found to be a powerful tool to explain molecular diffusion through channels of Al-substituted MFI-type zeolites. Diffusion simulations and density profiles complement and validate the findings. (*Chapter 5*).

- A new mechanism is described to direct water adsorption towards one or another type of pore in LTA-type zeolites by choosing the Si:Al ratio and controlling the adsorption pressure. This would allow a technological application on separating multi-component mixtures by tuning the adsorption selectivity of water. (*Chapter 6*).

Overall, in this thesis molecular simulation is employed as a powerful, flexible and useful tool to help understand and improve some key steps of industrial processes. It has been proved to be able to provide both deep physical insights on molecular mechanisms and accurate predictions on separation processes, supported by a proper parametrization and modeling of the studied systems.

Resumen y conclusiones

Las zeolitas son materiales porosos nanoestructurados que se caracterizan por tener amplias áreas superficiales y poros de tamaño molecular, propiedades muy adecuadas para labores de tamizado molecular. Es por ello por lo que su utilización es habitual en procesos industriales de separación o captura de gases. Los procesos que se han considerado en la presente tesis comparten el objetivo común de facilitar o proponer mejoras a algunos procesos industriales que se presentan como alternativas a aquellos basados en el consumo de hidrocarburos. El enfoque computacional de la tesis, a través de la simulación molecular, permite tanto obtener información de los sistemas estudiados a nivel atómico como sugerir esquemas operacionales para conseguir realizar la separación de gases deseada de una forma eficaz y selectiva. De forma adicional, se han estudiado algunos aspectos suplementarios que, sin ser propiamente procesos industriales, *sí* tienen un papel relevante en los procedimientos de separación. Por lo tanto, se pueden diferenciar dos bloques en la presente tesis:

Separación de gases en procesos industriales

- *Capítulo 2*
  Se propone un procedimiento, basado en una eliminación gradual, para separar los componentes de una columna de gas resultante de un proceso Fischer-Tropsch. La mezcla está compuesta por cinco gases ligeros –CO_2 , CO, CH_4 , N_2 y H_2 – en una composición molar típica y previamente descrita. El proceso Fischer-Tropsch se incluye para sintetizar hidrocarburos en un proceso GTL (de sus siglas en inglés gas-to-liquid) global de obtención de combustibles a partir de gas natural. La separación propuesta tiene un objetivo doble: por un lado la recirculación del metano y el monóxido de carbono capturados, debido a que aún tienen interés energético, y, por otro lado, la captura del dióxido de carbono y así evitar su emisión contaminante a la atmósfera.

  Con estos propósitos, se ha evaluado la eficacia de cuatro zeolitas de alto impacto

industrial (DDR, FAU, MFI y MOR), analizando los efectos de la localización y la cantidad de átomos de aluminio incluidos en las estructuras de las zeolitas. La decisión sobre el esquema final sugerido para la separación está fundamentada en las isotermas de adsorción computadas, la selectividad de adsorción y los coeficientes de difusión para las distintas especies moleculares. Adicionalmente, se ha evaluado la aplicabilidad y la precisión de aplicar IAST como método predictivo de separación a este tipo de sistemas.

- *Capítulo 3*
  Se ha realizado un amplio estudio multiescala para conseguir una separación selectiva de una mezcla gaseosa de CO_2 , CO y O_2 . La separación se enmarca en el contexto de un proceso de disociación de CO_2 asistido por plasma a baja temperatura, a su vez incluido en un proceso de producción de combustible con una huella de carbono nula. La forma propuesta para su consecución requiere un paso adicional para obtener CO puro desde la mezcla y para evitar la recombinación del CO_2 sobrante, ya que la disociación de CO_2 no alcanza un rendimiento del 100%.

  Para proponer el esquema de separación sugerido, en condiciones operacionales fácilmente alcanzables, se ha realizado un extenso estudio sobre 174 zeolitas, evaluando inicialmente su selectividad en condiciones de dilución infinita (baja adsorción), para pasar a continuación al análisis de propiedades de adsorción mediante isotermas e IAST en las estructuras elegidas. Posteriormente, se han realizado simulaciones PSA (*Pressure Swing Adsorption*) para determinar los parámetros óptimos para conseguir la separación requerida a nivel de proceso.

- *Capítulo 4*
  En este capítulo se estudia la separación de molecular de deuterio y tritio de su isótopo más liviano, el hidrógeno, en un amplio rango de presiones y considerando temperaturas bajas y criogénicas. Debido a estas condiciones de trabajo y a la naturaleza de los adsorbatos, se han incorporado efectos cuánticos a las simulaciones. Así mismo, se han propuesto modelos para las moléculas de deuterio y tritio, que han sido derivados del modelo de hidrógeno, ya descrito previamente en la literatura. El modelo de hidrógeno se ha evaluado mediante comparación con isotermas de adsorción realizadas experimentalmente en dos zeolitas completamente silíceas bien conocidas y descritas, MFI y LTA. Igualmente, el modelo para el deuterio se ha validado mediante comparación con isotermas de adsorción experimentales en las mismas zeolitas. A partir de aquí, se ha evaluado la selectividad a dilución infinita en 210 zeolitas pura

sílice y, para las estructuras con mayor selectividad, se ha realizado un posterior estudio de sus propiedades de adsorción y difusión. Se han identificado tres zeolitas, BCT, AVL y MVY, como las mejores candidatas a realizar una separación de mezclas equimolares de D_2/H_2 y T_2/H_2, dependiendo de las condiciones de presión y temperatura impuestas. EN una de ellas, BCT, se ha determinado la mayor selectividad descrita hasta ahora para materiales nanoporosos. Esta misma estructura muestra también una selectividad extremadamente alta para la separación de la mezcla equimolar de tritio e hidrógeno.

Estudio de aspectos adicionales que afectan a la separación molecular

- *Capítulo 5*
  En este capítulo se aborda un estudio sistemático del efecto que tienen los cationes sobre la difusión de las moléculas de CO_2 y CH_4 en la zeolita MFI. Se hace una especial mención al hecho de que tanto la zeolita MFI como las moléculas consideradas tienen un indudable interés industrial. Para realizar el estudio, se ha generado distribuciones teóricas de los átomos de aluminio en la zeolita, considerando las 12 posiciones cristalográficas T que conforman la estructura de MFI. Dada la carga negativa que se deriva de la sustitución de los átomos de silicio por átomos de aluminio, se han considerado dos tipos de cationes, monovalente (sodio) y divalente (calcio), para neutralizar la carga neta del sistema. Se han tenido en cuenta conjuntamente las distribuciones de densidad de población de los cationes y los perfiles de energía de los adsorbatos, ambas dependietes de la distribución de los átomos de aluminio, para bosquejar una predicción sobre el comportamiento de los cationes y los adsorbatos, comprobándose su consistencia y coherencia con los posteriores resultados de la simulaciones de difusión. La suma de resultados arrojan luz sobre los distintos comportamientos dinámicos de los adsorbatos que se pueden dar en estos sistemas a pesar de que la composición química de los adsorbentes de idéntica.

- *Capítulo 6*
  Entender el comportamiento de las moléculas de agua en la zeolita LTA es crucial dado el amplio uso que se hace de esta zeolita en procesos de eliminación de agua y deshidratación. El amplio rango de sustitución de átomos de aluminio que permite esta estructura, desde la estructura pura sílice hasta el máximo teórico en el que el ratio Si:Al=1, hace que el comportamiento de la zeolita pueda ser moldeado como hidrofóbico o hidrofílico. Además de las distintas proporciones de Si:Al, dos estructuras atómicas se han considerado para cada ratio: la primera de ellas conservando las posiciones cristalográficas de los

silicios y, la segunda, permitiendo una relajación estructural tras la introducción de los átomos de aluminio. El estudio de las isotermas de adsorción de agua, tanto en las estructuras rígidas como en aquellas en las que se ha realizado la minimización energética, y un detallado análisis sobre la ubicación de las moléculas adsorbidas en las estructuras muestran que la sustitución de átomos de silicio por aluminio conlleva cambios en la estructura LTA, que a su vez producen una destacable migración de la adsorción de agua entre sitios de adsorción de diferente tipo.

Finalmente, el capítulo 7 contiene las principales **conclusiones** a las que han llevado los distinto estudios que componen esta tesis y que se exponen a continuación.

En referencia a las separaciones de gases para procesos industriales:

- Se han propuesto esquemas de separación específicos para conseguir separaciones altamente selectivas destinadas a la mejora de los procesos industriales escogidos (síntesis de hidrocarburos Fischer-Tropsch (*Capítulo 2*) y disociación de CO_2 asistido por plasma no termal (*Capítulo 3*)) y se han abierto las puertas a nuevas perspectivas para procesos de separación de isótopos de hidrógeno (*Capítulo 4*) modificando a medida los adsorbentes o realizando una selección racional de los mismos.

- Se reporta el efecto en la adsorción de CO_2 y CH_4 debido a la sustitución de átomos de silicio por aluminio en cuatro zeolitas comercialmente disponibles (DDR, FAU, MFI y MOR). La localización de los átomos de aluminio, para una determinada densidad, tiene efectos diversos en la adsorción de CO_2 y CH_4 en estas topologías, bien un impacto significativo o bien efectos despreciables. Respecto a la densidad de las duplas Al/Na^+ en el sistema, la adsorción de CO_2 aumenta sistemáticamente con la densidad, en todas las estructuras y a todas las presiones, mientras que el CH_4 muestra dependencias no triviales respecto a los mismos factores. El resto de los gases que componen la mezcla no se ven afectados o apenas son adsorbidos (*Capítulo 2*).

- Se ha probado que la selectividad a cero *loading*, o dilución infinita, definida por la división de los coeficientes de Henry de las distintas moléculas, es un indicador muy útil en *screenings* para la predicción de selectividad de adsorción, dependiente de las cantidad de moléculas adsorbidas (*Capítulos 3* y *4*).

- Las predicciones derivadas de las simulaciones moleculares han probado estar en concordancia con las simulaciones PSA de procesos a gran escala, conectando los distintos niveles entre simulación molecular y simulación de procesos. En particular,

el estudio por simulación de una separación de una mezcla ternaria de gases, compuesta por CO_2 , CO y O_2 , se ve respaldado por un proceso PSA de dos ciclos (*Capítulo 3*).

- Se han propuesto nuevos modelos para las moléculas de D_2 y T_2 en zeolitas pura sílice. El modelo de D_2 ha sido validado mediante isotermas de adsorción experimentales realizadas a temperaturas criogénicas en dos zeolitas compuestas únicamente por SiO_4, MFI y LTA. Las correcciones cuánticas, incorporadas en los modelos de las moléculas, son esenciales para reproducir las curvas experimentales de adsorción (*Capítulo 4*).

- La zeolita BCT ha demostrado ser capaz de separar eficientemente mezclas equimolares de D_2/H_2 y T_2/H_2 . De hecho, BCT muestra la selectividad de adsorción más alta reportada para materiales nanoporosos al realizar dichas separaciones isotópicas. Este hallazgo abre nuevas opciones para avanzar en los procesos de enriquecimiento de isótopos de hidrógeno (*Capítulo 4*).

Las siguientes conclusiones corresponden a la investigación de algunos aspectos adicionales, relevantes en los procesos de separación:

- El efecto de los cationes en la difusión de CO_2 y CH_4 en zeolitas tipo MFI es evaluado. Se demuestra que , en general, estructuras con una misma composición química pueden determinar diferentes comportamientos en estas moléculas, dependiendo de la localización y cantidad de átomos de aluminio y la naturaleza de los cationes (*Capítulo 5*).

- El cálculo de perfiles de energía es ampliado desde estructuras pura sílice a aluminosilicatos, cuya carga neta es compensada con cationes mono- o divalentes, en particular iones Na^+ Ca^{2+}. Se ha determinado que los perfiles de energía para moléculas polares y apolares, CO_2 y CH_4 , son una potente herramienta para dar explicación a la difusión molecular a través de los canales de las zeolitas tipo MFI que contengan aluminio en su estructura. Simulaciones de difusión y perfiles de densidad de ocupación complementan y validan lo descrito (*Capítulo 5*).

- Se describe un nuevo mecanismo para dirigir la adsorción de agua hacia uno u otro tipo de poro en zeolitas tipo LTA a través de la elección del ratio Si:Al y el control de la presión de adsorción. Esto permite su aplicación tecnológica para la separación de mezclas multicomponente de gases calibrando la selectividad de adsorción del agua (*Capítulo 6*).

En resumen, la simulación molecular es utilizada en la presente tesis como una poderosa, flexible y útil herramienta que permite entender y mejorar algunas etapas esenciales de los procesos industriales. Se ha demostrado su capacidad para ofrecer tanto conocimiento fundamental de los aspectos fisicoquímicos de los mecanismos moleculares como de realizar certeras predicciones en procesos de separación, basándose en una apropiada parametrización y modelado de los sistemas bajo estudio.

Associated content of *Optimisation of the Fischer-Tropsch process using zeolites for tail gas separation*

APPENDIX A

Table A1: Henry coefficients and isosteric heats of adsorption in FAU-type structures.

	CO_2		CO		CH_4		N_2		H_2	
	K_H [mol/bar/kg]	Q_{st} [kJ/mol]	K_H [mol/bar/kg]	Q_{st} [kJ/mol]	K_H [mol/bar/kg]	Q_{st} [kJ/mol]	K_H [mol/bar/kg]	Q_{st} [kJ/mol]	K_H [mol/bar/kg]	Q_{st} [kJ/mol]
T_{Si}	2.81	−29.90	0.24	−17.74	1.11	−23.96	0.10	−11.97	0.03	−5.82
$T_{1,12}$	4.85	−29.85	0.21	−17.82	1.16	−22.95	0.10	−12.26	0.03	−6.02
$T_{1,24}$	4.78	−28.34	0.10	−12.98	0.56	−17.78	0.07	−10.42	0.03	−6.06
$T_{1,32}$	6.77	−29.28	0.08	−11.06	0.62	−16.71	0.07	−10.38	0.03	−6.18
$T_{1,48}$	15.50	−31.97	0.08	−11.30	0.83	−17.33	0.07	−11.04	0.04	−6.05
$T_{1,54}$	19.00	−32.13	0.08	−11.46	0.91	−17.86	0.08	−11.28	0.04	−5.83

Table A2: Henry coefficients and isosteric heats of adsorption in MFI-type structures.

	CO_2		CO		CH_4		N_2		H_2	
	K_H [mol/bar/kg]	Q_{st} [kJ/mol]	K_H [mol/bar/kg]	Q_{st} [kJ/mol]	K_H [mol/bar/kg]	Q_{st} [kJ/mol]	K_H [mol/bar/kg]	Q_{st} [kJ/mol]	K_H [mol/bar/kg]	Q_{st} [kJ/mol]
T_{Si}	4.20	−27.07	0.22	−17.01	0.86	−20.19	0.09	−13.02	0.02	−7.16
$T_{5,8}$	46.59	−38.93	0.14	−17.51	1.68	−23.61	0.07	−14.49	0.02	−7.62
$T_{8,8}$	86.50	−42.51	0.15	−17.94	1.98	−24.29	0.08	−14.92	0.02	−7.86
$T_{11,8}$	51.47	−38.78	0.17	−18.34	2.21	−24.10	0.09	−15.11	0.02	−7.86

Table A3: Henry coefficients and isosteric heats of adsorption in MOR-type structures.

	CO_2		CO		CH_4		N_2		H_2	
	K_H [mol/bar/kg]	Q_{st} [kJ/mol]	K_H [mol/bar/kg]	Q_{st} [kJ/mol]	K_H [mol/bar/kg]	Q_{st} [kJ/mol]	K_H [mol/bar/kg]	Q_{st} [kJ/mol]	K_H [mol/bar/kg]	Q_{st} [kJ/mol]
T_{Si}	1.03	−22.17	0.13	−16.22	0.61	−21.66	0.08	−14.09	0.02	−7.23
$T_{1,4}$	6.42	−33.36	0.10	−16.80	1.31	−24.30	0.07	−14.87	0.02	−7.58
$T_{2,4}$	9.67	−34.61	0.10	−17.15	1.65	−24.53	0.08	−15.37	0.02	−7.56
$T_{3,4}$	2.39	−27.11	0.09	−15.88	1.20	−25.72	0.06	−13.91	0.02	−7.70
$T_{4,4}$	14.00	−34.48	0.10	−16.65	1.65	−24.11	0.08	−14.88	0.02	−7.29
$T_{1,8}$	28.30	−39.31	0.07	−16.69	2.39	−25.49	0.06	−15.32	0.03	−7.64
$T_{2,8}$	29.80	−40.08	0.05	−15.95	2.45	−25.90	0.04	−15.02	0.03	−7.53

Table A4: Henry coefficients and isosteric heats of adsorption in DDR-type structures.

	CO_2		CO		CH_4		N_2		H_2	
	K_H [mol/bar/kg]	Q_{st} [kJ/mol]	K_H [mol/bar/kg]	Q_{st} [kJ/mol]	K_H [mol/bar/kg]	Q_{st} [kJ/mol]	K_H [mol/bar/kg]	Q_{st} [kJ/mol]	K_H [mol/bar/kg]	Q_{st} [kJ/mol]
T_{Si}	3.50	−25.11	0.29	−18.88	2.08	−26.25	0.16	−16.42	0.02	−8.24
$T_{1,5}$	8.30	−32.58	0.14	−16.66	1.24	−22.09	0.06	−13.56	0.03	−8.26
$T_{2,5}$	5.94	−30.57	0.13	−16.35	0.93	−21.21	0.06	−13.11	0.02	−8.13
$T_{4,5}$	6.53	−30.04	0.15	−16.54	1.17	−21.94	0.06	−13.25	0.02	−8.03
$T_{5,5}$	14.90	−33.32	0.17	−16.85	1.44	−22.28	0.07	−13.70	0.03	−8.33

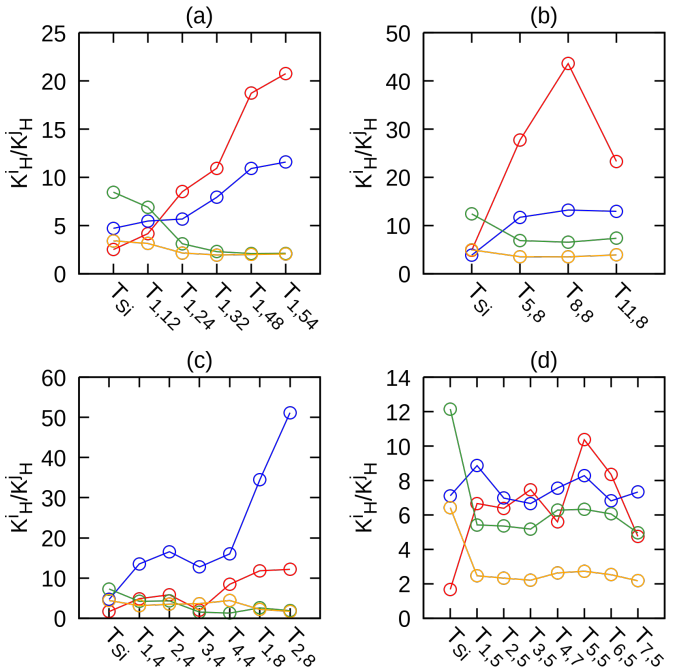

Figure A1: Selectivity at zero loading of CO_2/CH_4 (red), CH_4/CO (blue), CO/H_2 (green), and N_2/H_2 (orange) in: (a) FAU-type structures, (b) MFI-type structures, (c) MOR-type structures, and (d) DDR-type structures.

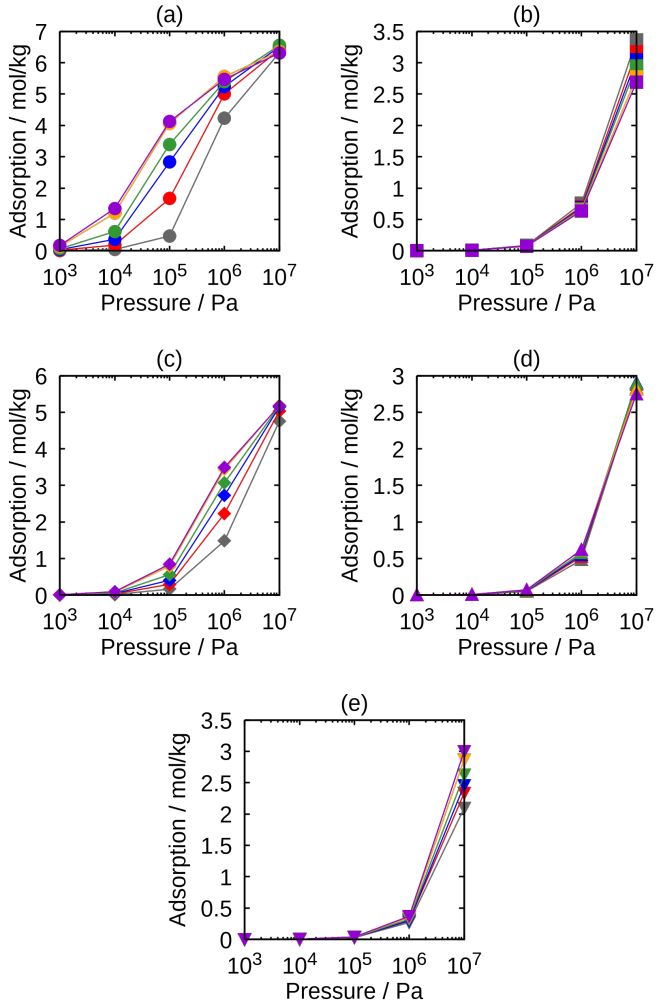

Figure A2: Pure component adsorption isotherms in FAU-type structures: T_{Si} (grey), $T_{1,12}$ (red), $T_{1,24}$ (blue), $T_{1,32}$ (green), $T_{1,48}$ (orange), and $T_{1,54}$ (violet). Circles at top left (a) are for CO_2 , squares at top right (b) are for CO, diamonds at centre left (c) are for CH_4 , up-pointing triangles at centre right (d) are for N_2 , and down-pointing triangles at bottom (e) are for H_2 .

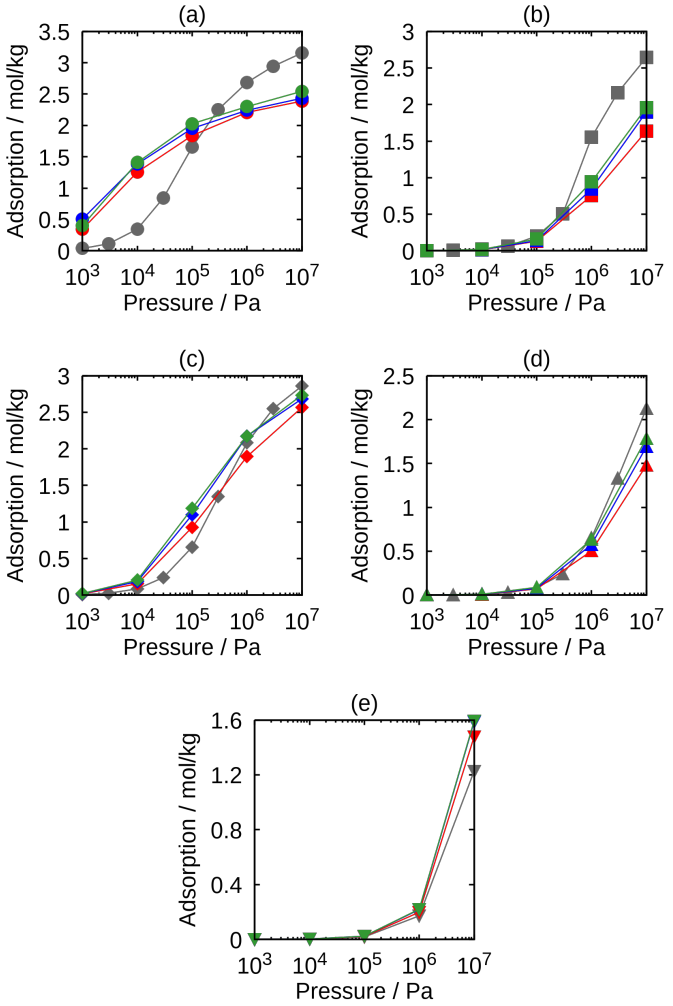

Figure A3: Pure component adsorption isotherms in MFI-type structures: T_{Si} (grey), $T_{5,8}$ (red), $T_{8,8}$ (blue), and $T_{11,8}$ (green). Circles at top left (a) are for CO_2, squares at top right (b) are for CO, diamonds at centre left (c) are for CH_4, up-pointing triangles at centre right (d) are for N_2, and down-pointing triangles at bottom (e) are for H_2.

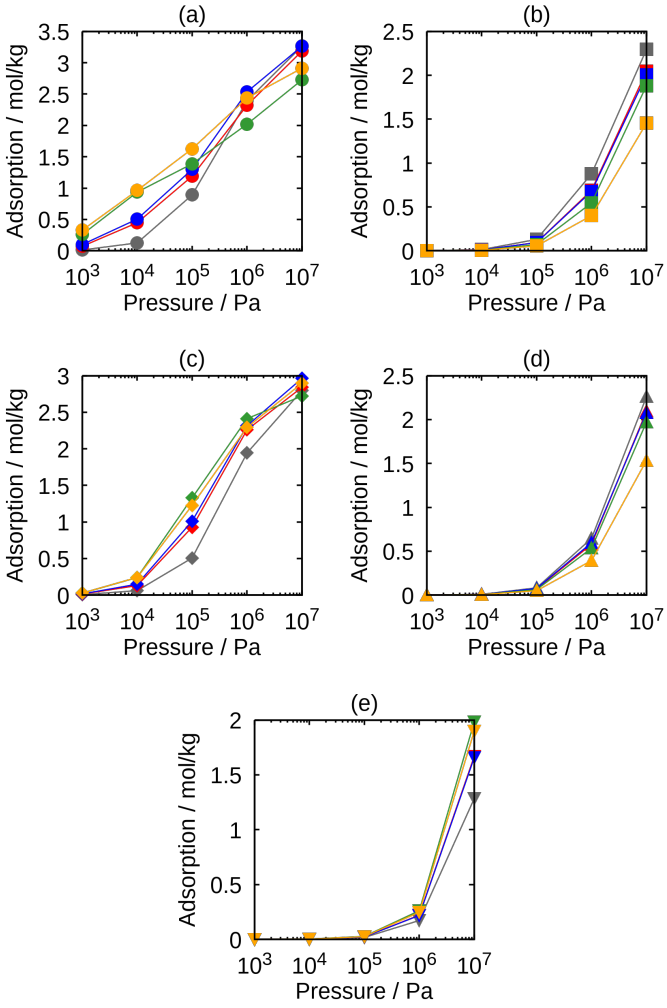

Figure A4: Pure component adsorption isotherms in MOR-type structures: T_{Si} (grey), $T_{1,4}$ (red), $T_{2,4}$ (blue), $T_{1,8}$ (green), and $T_{2,8}$ (orange). Circles at top left (a) are for CO_2, squares at top right (b) are for CO, diamonds at centre left (c) are for CH_4, up-pointing triangles at centre right (d) are for N_2, and down-pointing triangles at bottom (e) are for H_2.

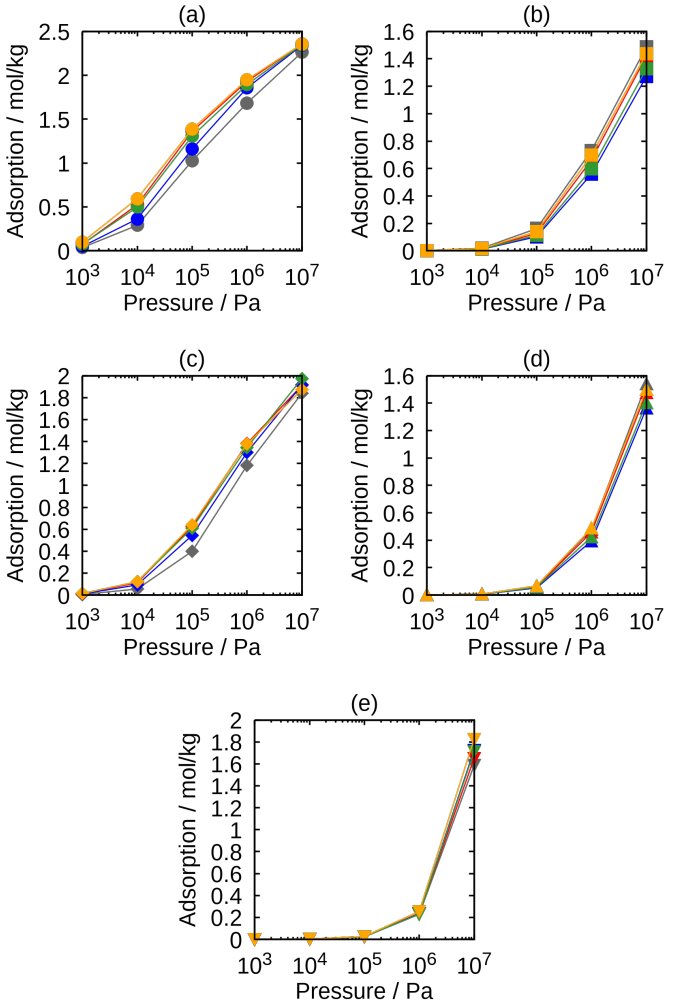

Figure A5: Pure component adsorption isotherms in DDR-type structures: T_{Si} (grey), $T_{1,5}$ (red), $T_{2,5}$ (blue), $T_{4,32}$ (green), and $T_{5,48}$ (orange). Circles at top left (a) are for CO_2, squares at top right (b) are for CO, diamonds at centre left (c) are for CH_4, up-pointing triangles at centre right (d) are for N_2, and down-pointing triangles at bottom (e) are for H_2.

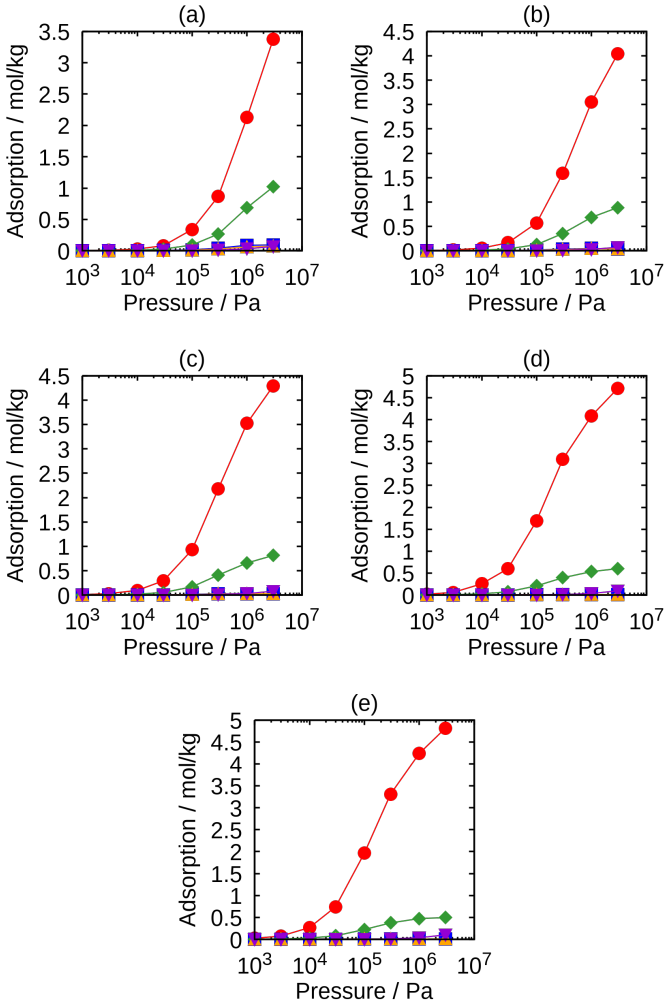

Figure A6: Computed adsorption isotherms of the five-component mixture (red circles for CO_2 , blue squares for CO, green diamonds for CH_4 , orange up-pointing triangles for N_2 , and violet down-pointing triangles for H_2) in FAU type structures: $T_{1,12}$ at top left (a), $T_{1,24}$ at top right (b), $T_{1,32}$ at centre left (c), $T_{1,48}$ at centre right (d), and $T_{1,54}$ at bottom (e).

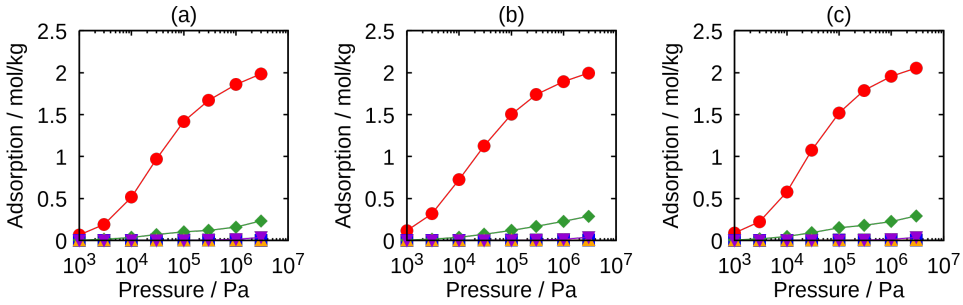

Figure A7: Computed adsorption isotherms of the five-component mixture (red circles for CO_2 , blue squares for CO, green diamonds for CH_4 , orange up-pointing triangles for N_2 , and violet down-pointing triangles for H_2) in MFI type structures: $T_{5,8}$ at left (a), $T_{8,8}$ at center (b), and $T_{11,8}$ at right (c).

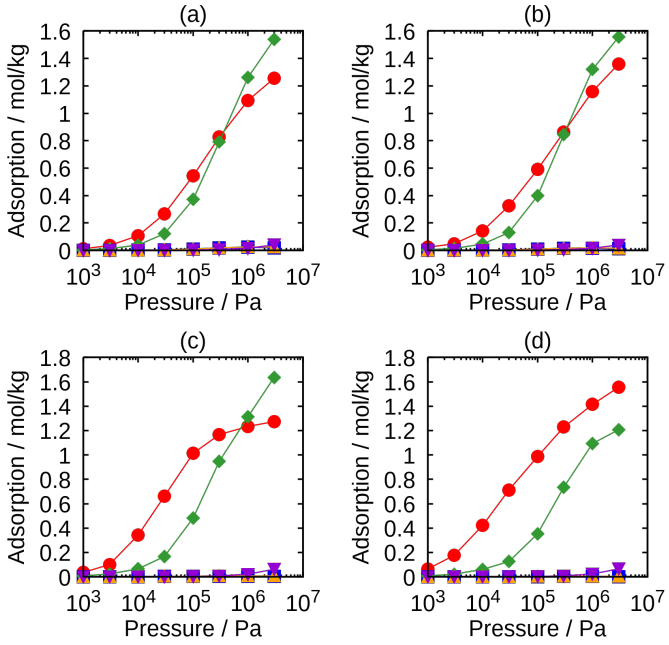

Figure A8: Computed adsorption isotherms of the five-component mixture (red circles for CO_2 , blue squares for CO, green diamonds for CH_4 , orange up-pointing triangles for N_2 , and violet down-pointing triangles for H_2) in MOR type structures: $T_{1,4}$ at top left (a), $T_{2,4}$ at top right (b), $T_{1,8}$ at bottom left (c), and $T_{2,8}$ at bottom right(d).

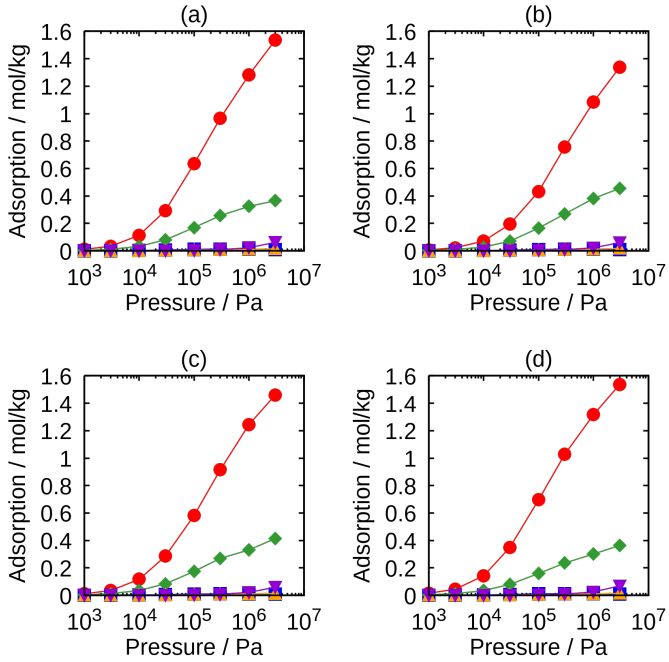

Figure A9: Computed adsorption isotherms of the five-component mixture (red circles for CO_2 , blue squares for CO, green diamonds for CH_4 , orange up-pointing triangles for N_2 , and violet down-pointing triangles for H_2) in DDR type structures: $T_{1,5}$ at top left (a), $T_{2,5}$ at top right (b), $T_{4,5}$ at bottom left (c), and $T_{5,5}$ at bottom right(d).

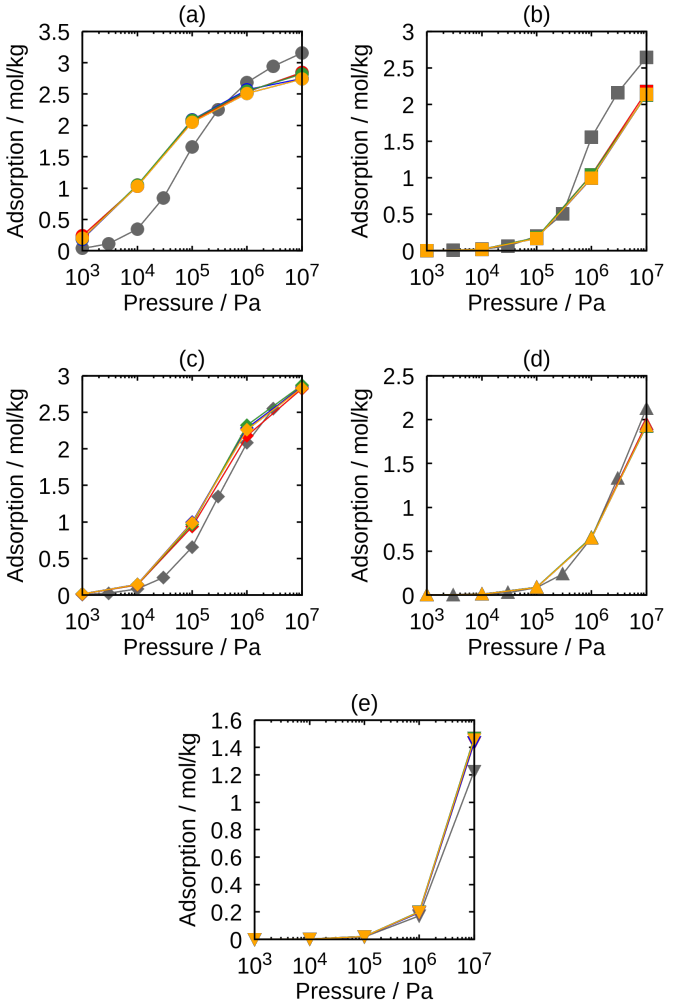

Figure A10: Pure component adsorption isotherms in MFI-type structures: T_{Si} (grey), $T_{7,4}$ (red), $T_{9,4}$ (blue), $T_{10,4}$ (green), and $T_{12,4}$ (orange). Circles at top left (a) are for CO_2, squares at top right (b) are for CO, diamonds at centre left (c) are for CH_4, up-pointing triangles at centre right (d) are for N_2, and down-pointing triangles at bottom (e) are for H_2.

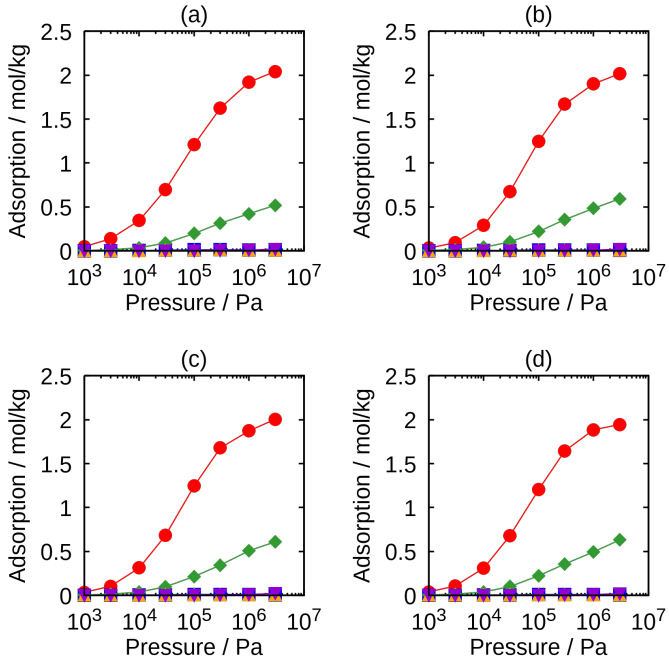

Figure A11: Computed adsorption isotherms of the five-component mixture (red circles for CO_2 , blue squares for CO, green diamonds for CH_4 , orange up-pointing triangles for N_2 , and violet down-pointing triangles for H_2) in DDR type structures: $T_{7,4}$ at top left (a), $T_{9,4}$ at top right (b), $T_{10,4}$ at bottom left (c), and $T_{12,4}$ at bottom right(d).

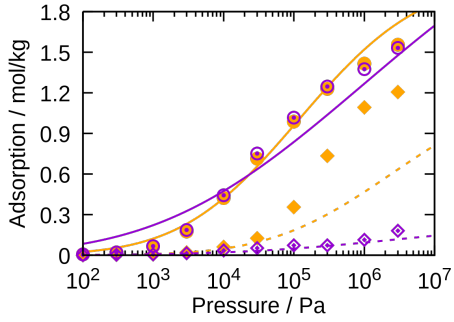

Figure A12: Computed adsorption isotherms (circles for CO_2 and diamonds for CH_4) of five-component mixture and IAST calculations (continuous lines for CO_2 and dashed lines for CH_4) in $T_{2,8}$ MOR (orange) and $T_{2,8}$ MOR with the *side pockets* artificially blocked (violet).

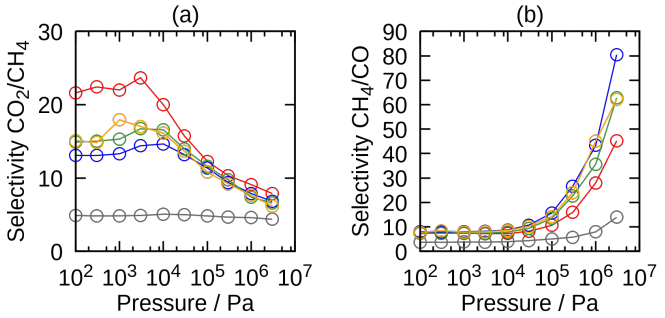

Figure A13: Computed CO_2/CH_4 (left) and CH_4/CO (right) adsorption selectivity in MFI structures: T_{Si} (grey), $T_{7,4}$ (red), $T_{9,4}$ (blue), $T_{10,4}$ (green), and $T_{12,4}$ (orange).

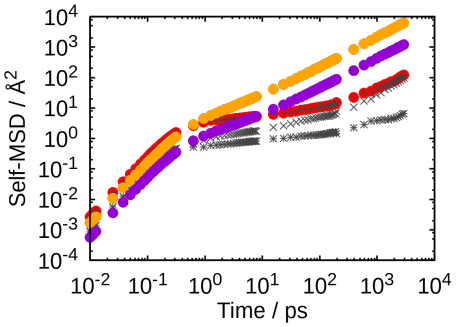

Figure A14: Mean square displacement for CO_2 in $T_{1,48}$ (orange) and $T_{1,54}$ (violet) FAU, and $T_{5,8}$ MFI (red). In grey, the MSD for $T_{5,8}$ MFI for each diffusion direction: x axe (x symbol), y axe (+ symbol), and z axe ($*$ symbol).

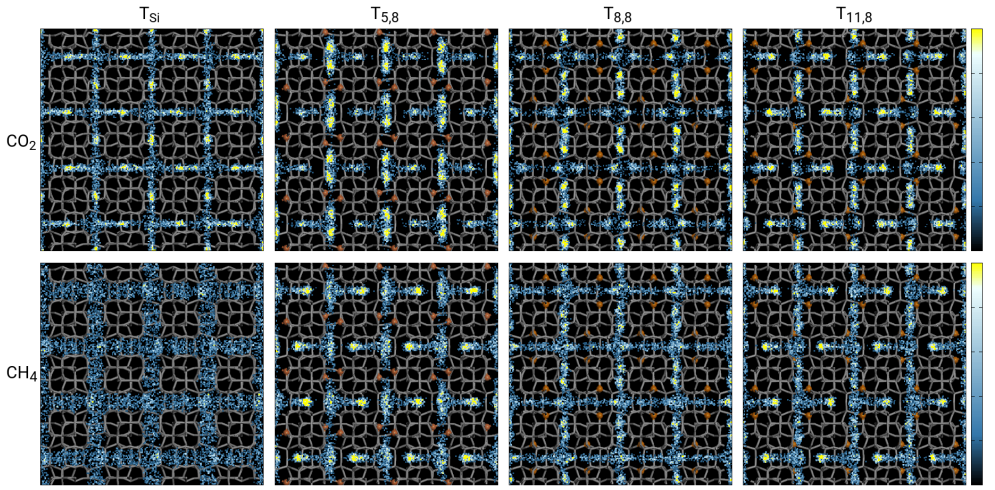

Figure A15: XY view of the average occupation profiles of CO 2 (up) and CH 4 (bottom) on pure silica MFI (left end), $T_{5,8}$ MFI (left), $T_{8,8}$ (right), and $T_{11,8}$ (right end). The atomic structure has been included for reference, where aluminium atoms are highlighted in orange. The relation between colour and probability density (from black to yellow) is shown in the colour ramp on the right side of the figure.

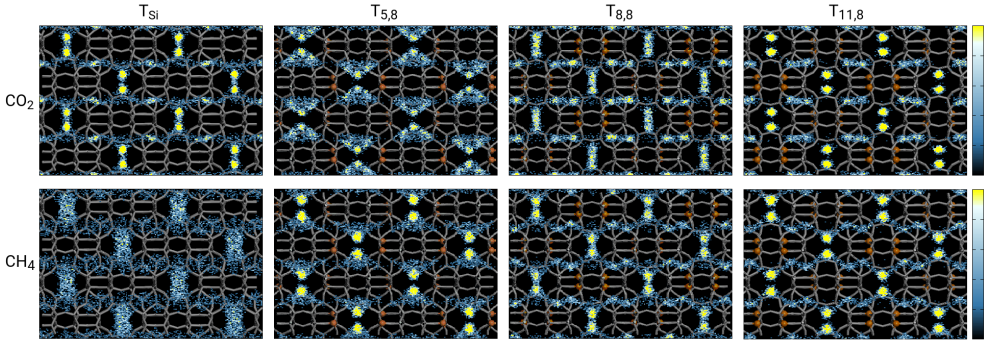

Figure A16: YZ view of the average occupation profiles of CO 2 (up) and CH 4 (bottom) on pure silica MFI (left end), $T_{5,8}$ MFI (left), $T_{8,8}$ (right), and $T_{11,8}$ (right end). The atomic structure has been included for reference, where aluminium atoms are highlighted in orange. The relation between colour and probability density (from black to yellow) is shown in the colour ramp on the right side of the figure.

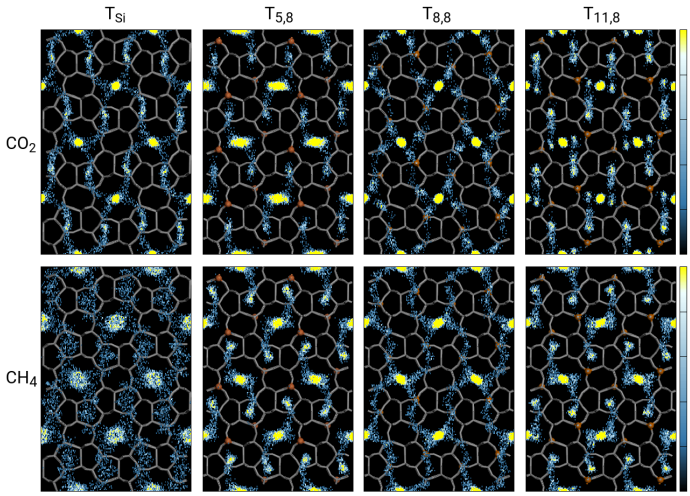

Figure A17: ZX view of the average occupation profiles of CO 2 (up) and CH 4 (bottom) on pure silica MFI (left end), $T_{5,8}$ MFI (left), $T_{8,8}$ (right), and $T_{11,8}$ (right end). The atomic structure has been included for reference, where aluminium atoms are highlighted in orange. The relation between colour and probability density (from black to yellow) is shown in the colour ramp on the right side of the figure.

Associated content of *Zeolites for CO_2-CO-O_2 separation to obtain CO_2-neutral fuels*

APPENDIX B

Table B1: Effective pore diameter, specific surface area and selectivity against second most adsorbed species for zeolites shown in Figure 2.

Zeolite	Effective Pore Diameter [Å]	Specific Surface Area [$m^2 \cdot g^{-1}$]	Selectivity	Zeolite	Effective Pore Diameter [Å]	Specific Surface Area [$m^2 \cdot g^{-1}$]	Selectivity
ACO	2.89	260.31	1.12±0.06	EEI	3.37	387.96	14.6±0.7
AEI	6.58	835.66	11.0±0.5	EMT	7.1	1101.73	11.6±0.5
AEL	4.17	336.18	20.7±1.1	EON	2.81	493.11	7.0±0.4
AFI	7.34	526.97	14.4±0.8	EPI	3.57	431.14	12.8±0.7
AFN	2.41	333.64	16.0±0.8	ERI	6.14	716.94	15.9±0.9
AFO	4.61	331.95	22.9±1.2	ESV	3.05	371.18	12.3±0.6
AFS	2.81	958.88	9.6±0.4	ETR	5.61	690.49	14.5±0.7
AFT	4.21	806.11	10.5±0.6	EUO	2.33	559.68	7.4±0.4
AFV	6.22	716.73	14.6±0.7	EZT	5.45	587.83	17.0±0.8
AFY	3.85	1208.05	9.4±0.4	FAU	10.14	1020.88	18.3±0.9
APC	3.33	127.9	1.58±0.07	FER	4.37	407.41	14.1±0.7
ASV	3.85	305.35	11.4±0.5	GIS	3.21	361.53	17.6±1.0
ATN	2.33	324.46	24.9±1.2	GME	4.17	770.47	11.6±0.6
ATO	4.89	315.21	17.1±0.9	GON	4.77	348.58	12.1±0.6
ATS	6.3	655.75	14.5±0.7	GOO	2.57	140.17	7.6±0.4
ATT	3.37	387.41	17.6±0.9	HEU	3.97	428.69	17.0±0.8
AVL	4.93	685.25	16.9±0.9	IFO	7.06	596.53	12.3±0.7
AWO	4.25	194.56	2.2±0.1	IFR	6.38	649.61	15.4±0.8
AWW	2.37	542.8	10.3±0.5	IHW	5.82	415.23	19.6±1.1
BEA	5.65	968.97	17.9±0.9	IMF	4.81	574.25	18.5±1.0
BEC	6.02	979.81	18.6±1.0	IRR	5.45	1342.38	8.6±0.4
BOF	4.69	453.2	20.8±1.1	ISV	6.06	970.27	17.4±0.7
BOZ	2.93	1204.7	8.7±0.5	ITE	7.18	693.71	14.7±0.7
BPH	5.86	939.8	13.6±0.7	ITG	3.41	689.4	10.8±0.6
BRE	4.49	282.78	23.1±1.3	ITH	3.61	566.78	15.5±0.8
BSV	3.17	216	4.0±0.2	ITR	3.65	572.14	17.4±0.8
CAN	3.41	413.37	9.2±0.5	ITT	4.61	1146.6	10.6±0.5
CDO	2.85	318.53	13.0±0.7	ITW	2.37	348.21	4.0±0.2
CFI	2.65	515.49	12.2±0.6	IWR	5.74	900.4	13.8±0.7
CGF	4.09	247.49	19.5±1.0	IWS	6.18	1013.75	14.2±0.7
CGS	5.05	509.44	14.2±0.7	IWV	7.42	883.29	13.3±0.7
CHA	6.54	893.84	9.2±0.5	IWW	2.65	698.37	15.6±0.7
CON	5.33	890.24	14.6±0.5	JOZ	2.49	265.88	6.0±0.3
DAC	3.53	480.87	4.4±0.2	JRY	3.81	333.56	9.5±0.5
DDR	3.97	400.5	15.7±0.8	JSN	4.37	371.95	11.9±0.7
EAB	5.13	672.16	20.5±1.2	JSR	4.61	1705.03	11.5±0.7
EDI	2.77	418.83	8.4±0.4	JST	3.81	785.16	4.5±0.2

Zeolite	Effective Pore Diameter [Å]	Specific Surface Area [$m^2 \cdot g^{-1}$]	Selectivity	Zeolite	Effective Pore Diameter [Å]	Specific Surface Area [$m^2 \cdot g^{-1}$]	Selectivity
KFI	2.77	806.87	11.1±0.5	MAZ	2.41	494.46	13.6±0.7
LAU	5.09	450.52	13.8±0.7	MEI	7.42	975.62	15.2±0.8
LEV	6.38	706.26	12.3±0.7	MEL	4.77	544.9	21.9±0.9
LTA	5.29	849.28	9.4±0.5	MER	2.57	458.01	6.1±0.3
LTF	2.57	457.16	14.7±0.7	MFI	4.73	547.67	16.1±1.0
MFS	2.37	429.49	15.6±0.8	SBT	10.22	1057.79	12.1±0.6
MOR	4.25	477.92	4.4±0.2	SEW	4.61	719.66	14.2±0.7
MOZ	2.45	524.38	16.4±0.8	SFE	5.86	563.61	12.1±0.6
MRE	5.49	273.3	25.4±1.3	SFG	5.37	494.73	15.4±0.8
MSE	6.02	759.1	16.9±0.9	SFH	2.65	601.75	15.3±0.8
MTF	5.45	263.69	18.3±1.0	SFN	7.18	602.16	13.3±0.7
MTT	4.61	370.58	22.2±0.9	SFO	7.1	815.83	10.2±0.4
MTW	5.33	360.08	13.6±0.7	SFS	4.53	718.05	16.0±0.8
MWW	4.21	801.18	17.1±0.8	SFV	3.85	587.77	15.6±0.9
NES	5.61	702.01	15.5±0.8	SFW	4.17	773.56	8.64±0.43
NPT	3.05	927.91	14.9±0.8	SIV	2.53	404.65	16.2±0.8
OBW	5.05	1212.74	10.4±0.5	SOF	3.89	725.74	5.49±0.25
OFF	5.53	685.54	14.4±0.7	SOS	2.77	372.84	6.3±0.3
OKO	5.33	646.12	19.6±1.0	SSF	6.14	634.33	13.2±0.7
OSI	5.82	399.07	12.2±0.7	SSY	6.5	564.34	13.9±0.7
OSO	5.33	1171.12	7.8±0.4	STF	6.94	633.6	19.8±1.0
OWE	3.13	456.02	11.5±0.7	STI	5.45	671.06	21.4±1.0
PAU	2.45	538.21	11.9±0.6	STO	5.21	397.62	14.1±0.7
PCR	4.21	306.7	8.8±0.4	STT	6.22	637.66	14.7±0.8
PHI	2.89	428.66	18.3±1.0	STW	4.13	804.79	15.8±0.9
PON	3.85	329.22	7.4±0.4	SZR	2.41	398.51	9.1±0.5
PUN	3.89	932.68	13.0±0.6	TER	4.21	647.26	15.3±0.8
RHO	3.61	783.41	7.5±0.4	THO	4.37	468.65	8.7±0.5
RRO	3.29	224.31	5.2±0.3	TON	4.57	301.41	20.0±1.0
RTE	6.34	533.27	11.8±0.6	TSC	9.82	931.08	7.4±0.3
RTH	7.26	704.7	9.9±0.5	UEI	2.49	251.6	2.3±0.1
RWY	13.39	2317.48	8.5±0.5	UFI	5.25	798.21	15.4±0.8
SAF	5.98	365.85	14.8±0.7	UOS	3.45	466.48	9.1±0.5
SAO	6.94	1140.04	13.1±0.7	USI	4.09	870.09	14.4±0.7
SAS	8.1	794.58	10.7±0.5	UTL	5.45	859.21	12.8±0.6
SAT	5.86	590.64	21.6±1.1	UWY	4.41	769.21	12.1±0.6
SAV	3.05	858.68	14.8±0.7	VET	5.61	308.18	15.9±0.8
SBE	6.98	938.12	10.5±0.5	YUG	2.97	182.34	8.6±0.4
SBS	9.46	1057.67	11.7±0.5	ZON	2.97	347.79	22.9±1.2

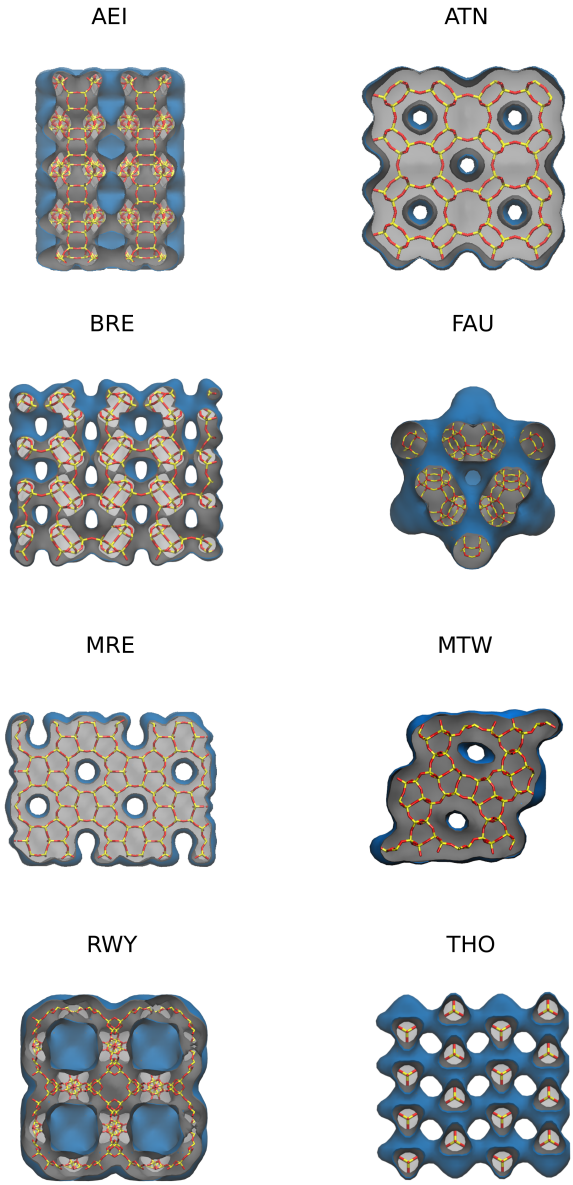

Figure B1: Structures of the main zeolites discussed in this work.

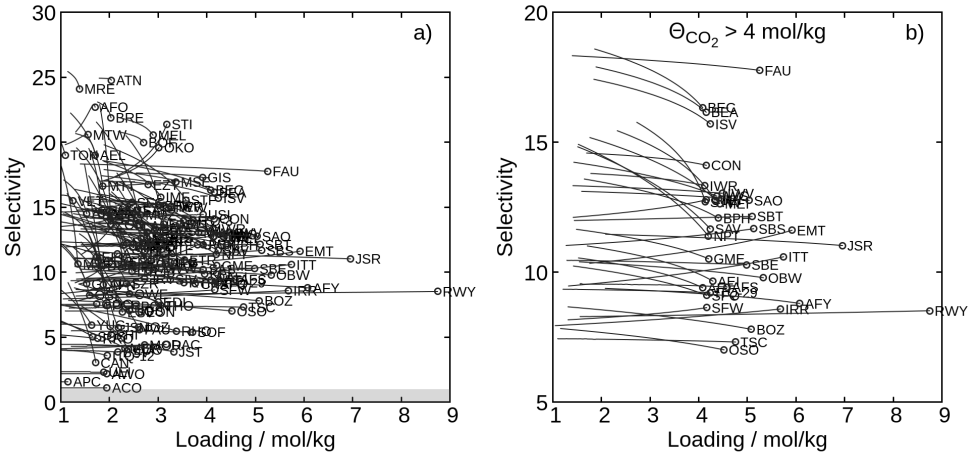

Figure B2: Adsorption selectivity towards carbon dioxide as a function of its adsorbed loading from the ternary mixture CO_2 (85%), CO (10%) and O_2 (5%) obtained by applying IAST at 298 K. Carbon dioxide uptakes correspond to those obtained in the pressure range of 10^5-10^6 Pa. a) depicts structures adsorbing at least 1 mol/kg while b) retains only structures with minimum uptakes of 4 mol/kg.

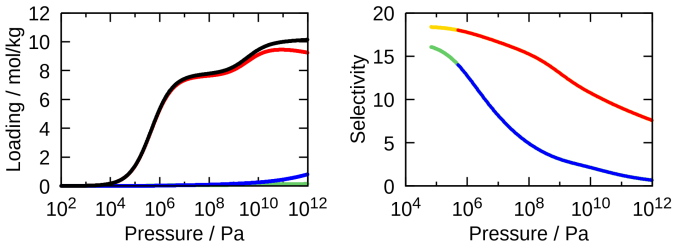

Figure B3: Left: Adsorption isotherms of the ternary mixture CO_2 (85%) (red), CO (10%) (green) and O_2 (5%) (blue) in FAU zeolite obtained by applying IAST at 298 K. Total adsorption loading is depicted in black and the saturation loading (10.24 mol/kg) is reached at 10^{12} Pa. Right: Selectivity towards carbon dioxide as a function of pressure, extracted from the adsorption isotherms. Orange and red curves are for selectivity of CO_2 over CO, and green and blue curves for selectivity of CO_2 over O_2 . While red and blue selectivity curves apply to CO_2 adsorption loadings above 4 mol/kg, orange and green selectivity curves apply to CO_2 loading between 1 and 4 mol/kg.

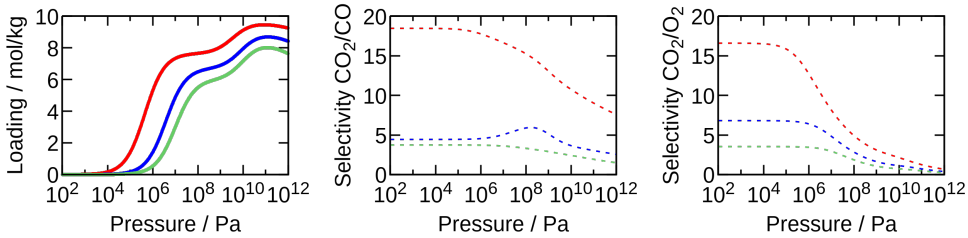

Figure B4: Adsorption isotherms of carbon dioxide in FAU (left), extracted from the adsorption isotherms of the ternary mixture CO_2 (85%), CO (10%) and O_2 (5%) obtained by applying IAST at 298K (red), 400 K (blue) and 500 K (green). Adsorption selectivity of carbon dioxide over carbon monoxide (center) and oxygen (right) in FAU at 298K (red), 400 K (blue) and 500 K (green).

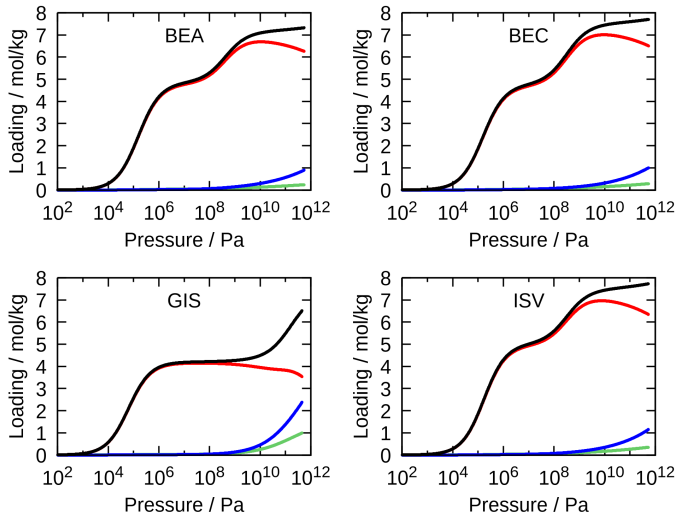

Figure B5: Adsorption isotherms of the ternary mixture CO_2 (85%) (red), CO (10%) (green) and O_2 (5%) (blue) at 298K in BEA, BEC, GIS and ISV zeolites obtained by applying IAST. Total adsorption loading is depicted in black.

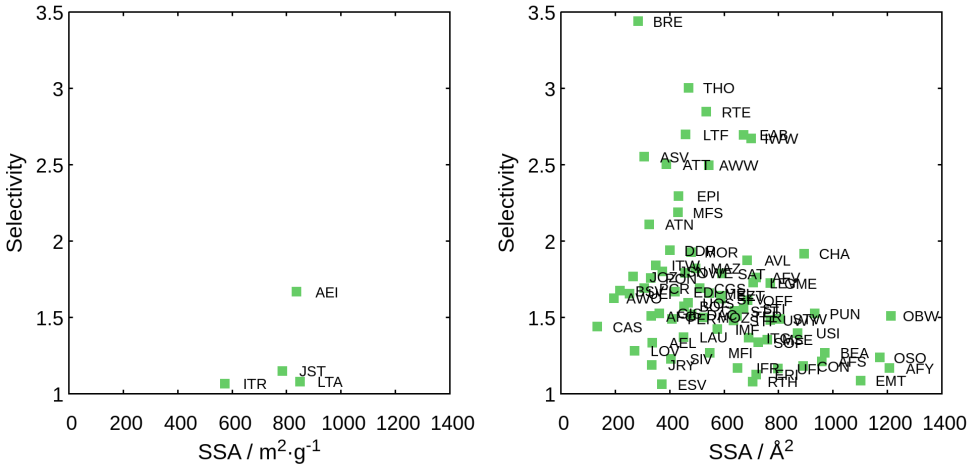

Figure B6: Maximum adsorption selectivity towards oxygen (left) and carbon monoxide (right) versus the geometrical surface area of the zeolite. The adsorption selectivity was obtained from the adsorption isotherms of the binary mixture CO (67%) and O_2 (33%) obtained by applying IAST at 300 K and 10^6-10^7 Pa.

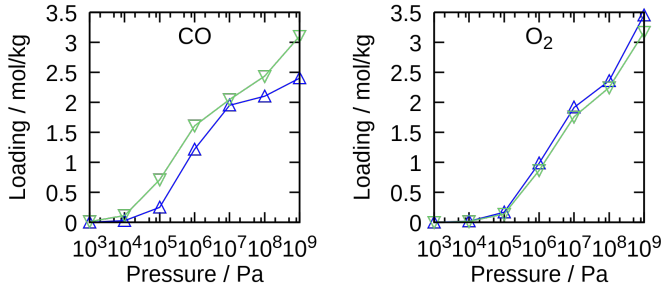

Figure B7: Carbon monoxide (left) and oxygen (right) pure component adsorption isotherms in pure silica BRE zeolite (blue up triangles) and BRE zeolite with 4 Al/uc (green down triangles) from molecular simulations.

Time Schedule of PSA I

[a] Final press., bar	2	2	1.01	1	0.1	0.1	1	2
Duration, s	60	60	60	60	60	60	60	60
Column 1	ADS	ADS	DEQ	PP	DP	RP	PEQ	PR
Column 2	PEQ	PR	ADS	ADS	DEQ	PP	DP	RP
Column 3	DP	RP	PEQ	PR	ADS	ADS	DEQ	PP
Column 4	DEQ	PP	DP	RP	PEQ	PR	ADS	ADS

[a] Pressure of Column 1 at the end of the step

Time Schedule of PSA II

[a] Final press., bar	2	2	2	0.81	0.8		0.1	0.1		0.811	2	
Duration, s	60	40	20	60	40	20	60	40	20	60	40	20
Column 1	ADS	ADS	RIN	DEQ	PP		DP	RP		PEQ	PR	
Column 2	PEQ	PR		ADS	ADS	RIN	DEQ	PP		DP	RP	
Column 3	DP	RP		PEQ	PR		ADS	ADS	RIN	DEQ	PP	
Column 4	DEQ	PP		DP	RP		PEQ	PR		ADS	ADS	RIN

[a] Pressure of Column 1 at the end of the step

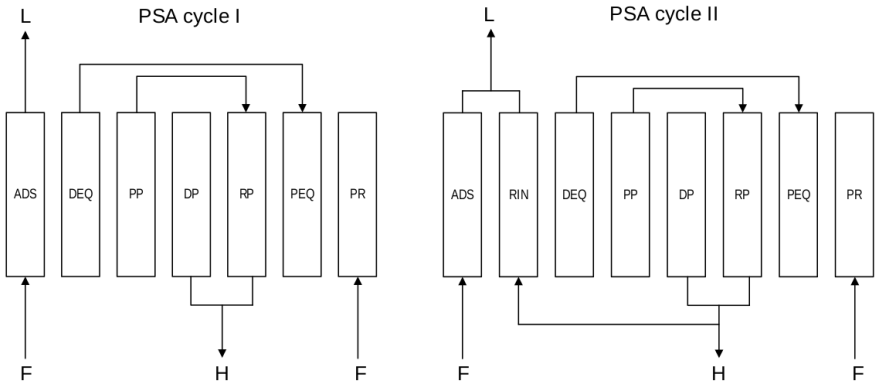

Figure B8: Scheme and time schedule of the PSA cycles I and II. F=feed mixture, L=light product, H=heavy product. ADS=adsorption step, RIN=rinse step with heavy product, DEQ=depressurizing equalization, PP=provide purge, DP=depressurization, RP=receive purge, PEQ=pressurizing equalization, PR=pressurization.

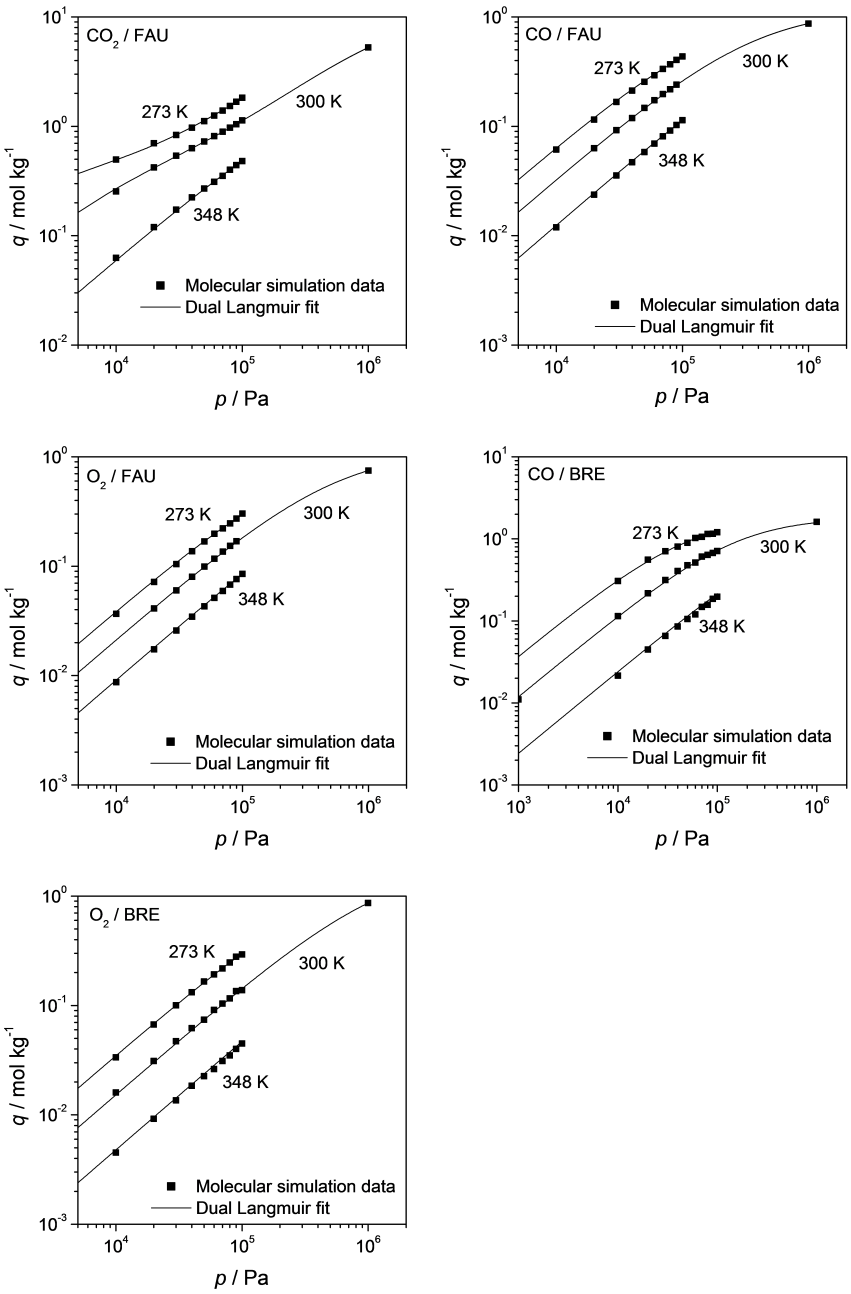

Figure B9: Comparison between pure adsorption isotherms at 300 K obtained by molecular simulation and fitted with Langmuir model.

Table B2: Langmuir parameters for CO_2 , CO and O_2 in FAU and BRE zeolites at 300K.

Adsorbent	FAU	BRE
K_{H0} CO_2 , mol kg^{-1} Pa^{-1}	$4.6846 \cdot 10^{-9}$	-
b_0 CO_2 , Pa^{-1}	$-6.9969 \cdot 10^{-10}$	-
$-\Delta H$ CO_2 , kJ mol^{-1}	17.332	-
K_{H0} CO, mol kg^{-1} Pa^{-1}	$1.6151 \cdot 10^{-8}$	$1.1583 \cdot 10^{-10}$
b_0 CO, Pa^{-1}	$2.1574 \cdot 10^{-9}$	$6.3580 \cdot 10^{-11}$
$-\Delta H$ CO, kJ mol^{-1}	9.993	28.779
K_{H0} O_2 , mol kg^{-1} Pa^{-1}	$1.8239 \cdot 10^{-8}$	$3.351 \cdot 10^{-10}$
b_0 O_2 , Pa^{-1}	$1.1861 \cdot 10^{-9}$	$1.69 \cdot 10^{-10}$
$-\Delta H$ O_2 , kJ mol^{-1}	9.308	21.012

$$q = \frac{K_{H0} exp\left(\frac{-\Delta H}{RT}\right) p}{1 + b_0 exp\left(\frac{-\Delta H}{RT}\right) p}$$

Table B3: Effect of feed gas velocity in the ADS step (u_F), high pressure of the cycle (P_{HIGH}), and final pressure of the PP step (P_{PP}) of PSA cycle I on CO_2 concentration in the light product, CO recovery in the light product and CO_2 productivity in the heavy product.

u_F m s^{-1}	P_{HIGH} bar	P_{PP} bar	CO_2 conc. in L % v/v	CO recovery in L %	CO_2 productivity in H kg kg^{-1} h^{-1}
0.015	1	0.4	47.7	93.5	0.067
0.0055	2	0.9	0.002	77.9	0.096
0.0055	2	1.0	0.012	77.2	0.097
0.0075	2	1.0	17.1	90.3	0.10
0.0064	2	1.0	0.32	87.6	0.10

Associated content of *Molecular sieves for the separation of hydrogen isotopes*

APPENDIX C

Table C1: D_2/H_2 selectivity at zero-loading. Shadowed cells correspond to zeolites that were found to be inaccessible for adsorbates in further verifications after compute their selectivity.

	25 K	30 K	35 K	40 K	45 K	50 K	60 K	70 K	80 K	90 K	100 K	120 K	140 K	160 K	180 K	200 K
ABW	2.42	2.06	1.85	1.70	1.59	1.50	1.39	1.31	1.25	1.21	1.18	1.14	1.11	1.09	1.08	1.07
ACO	1.62	1.55	1.48	1.42	1.37	1.33	1.26	1.22	1.18	1.15	1.13	1.10	1.08	1.07	1.06	1.05
AEI	2.65	2.11	1.80	1.61	1.48	1.39	1.28	1.21	1.16	1.13	1.11	1.08	1.06	1.05	1.04	1.03
AEL	1.75	1.57	1.45	1.36	1.30	1.25	1.19	1.14	1.12	1.10	1.08	1.06	1.05	1.04	1.04	1.03
AEN	2.57	2.10	1.83	1.66	1.55	1.46	1.35	1.28	1.23	1.19	1.17	1.13	1.10	1.08	1.07	1.06
AET	2.39	1.96	1.69	1.53	1.42	1.34	1.24	1.17	1.14	1.11	1.09	1.06	1.05	1.04	1.03	1.03
AFG	2.92	2.40	2.08	1.88	1.73	1.62	1.45	1.35	1.27	1.21	1.17	1.12	1.09	1.07	1.06	1.05
AFI	2.15	1.82	1.61	1.47	1.37	1.31	1.22	1.16	1.13	1.10	1.09	1.06	1.05	1.04	1.03	1.03
AFN	5.27	3.42	2.58	2.12	1.84	1.66	1.44	1.32	1.24	1.19	1.16	1.12	1.09	1.07	1.06	1.05
AFO	1.82	1.61	1.48	1.38	1.31	1.26	1.19	1.15	1.12	1.10	1.08	1.06	1.05	1.04	1.04	1.03
AFR	1.84	1.67	1.58	1.48	1.43	1.37	1.29	1.23	1.19	1.16	1.13	1.09	1.07	1.05	1.04	1.03
AFS	60.3	18.7	8.67	5.08	3.53	2.66	1.86	1.50	1.33	1.22	1.16	1.10	1.07	1.05	1.04	1.03
AFT	2.78	2.21	1.86	1.66	1.52	1.42	1.30	1.22	1.17	1.14	1.11	1.08	1.06	1.05	1.04	1.03
AFV	1.92	1.68	1.54	1.43	1.35	1.30	1.22	1.17	1.14	1.11	1.09	1.07	1.05	1.05	1.04	1.03
AFX	2.60	2.10	1.81	1.62	1.50	1.42	1.30	1.23	1.18	1.15	1.12	1.08	1.07	1.05	1.04	1.04
AFY	2.18	1.87	1.67	1.53	1.44	1.37	1.27	1.21	1.16	1.13	1.11	1.08	1.06	1.05	1.04	1.03
AHT	8.35	4.77	3.36	2.64	2.22	1.97	1.66	1.49	1.38	1.31	1.26	1.19	1.15	1.12	1.10	1.09
ANA	3.03	2.37	2.01	1.80	1.65	1.55	1.42	1.33	1.27	1.23	1.20	1.15	1.13	1.10	1.09	1.08
APC	2.59	2.10	1.82	1.64	1.52	1.44	1.33	1.26	1.22	1.18	1.16	1.12	1.10	1.08	1.07	1.06
APD	1.30	1.31	1.30	1.28	1.25	1.23	1.19	1.16	1.14	1.12	1.11	1.09	1.07	1.06	1.05	1.05
AST	1.72	1.56	1.45	1.36	1.30	1.26	1.19	1.15	1.12	1.10	1.09	1.06	1.05	1.04	1.03	1.03
ASV	1.52	1.46	1.39	1.34	1.29	1.25	1.20	1.16	1.13	1.11	1.10	1.08	1.06	1.05	1.05	1.04
ATN	2.36	2.00	1.76	1.60	1.49	1.41	1.29	1.23	1.18	1.15	1.13	1.10	1.08	1.06	1.05	1.05
ATO	1.68	1.51	1.40	1.32	1.27	1.23	1.17	1.13	1.11	1.09	1.08	1.06	1.05	1.04	1.04	1.03
ATS	3.41	2.62	2.16	1.87	1.68	1.54	1.37	1.27	1.21	1.16	1.13	1.09	1.07	1.05	1.04	1.04
ATT	2.66	2.14	1.84	1.65	1.52	1.43	1.30	1.23	1.19	1.15	1.13	1.10	1.08	1.06	1.05	1.05
ATV	1.39	1.37	1.34	1.31	1.28	1.25	1.21	1.17	1.15	1.13	1.11	1.09	1.08	1.06	1.06	1.05
AVL	190	53.4	19.6	8.77	5.00	3.24	1.86	1.45	1.28	1.19	1.14	1.10	1.07	1.05	1.04	1.04
AWO	1.53	1.46	1.39	1.34	1.30	1.26	1.21	1.17	1.15	1.13	1.11	1.09	1.07	1.06	1.05	1.05
AWW	1.88	1.66	1.52	1.42	1.34	1.29	1.22	1.17	1.14	1.11	1.10	1.07	1.06	1.05	1.04	1.03
BCT	5E4	2030	283	80.1	34.0	17.7	7.77	4.78	3.38	2.68	2.31	1.83	1.62	1.46	1.37	1.31
BEA	1.83	1.61	1.47	1.36	1.29	1.24	1.17	1.13	1.10	1.08	1.07	1.05	1.04	1.03	1.03	1.02
BEC	1.71	1.53	1.42	1.33	1.27	1.23	1.17	1.13	1.10	1.08	1.07	1.05	1.04	1.03	1.03	1.02
BIK	2.44	2.08	1.86	1.70	1.59	1.50	1.38	1.30	1.25	1.21	1.18	1.14	1.11	1.09	1.08	1.07
BOF	1.84	1.63	1.50	1.40	1.33	1.28	1.21	1.16	1.13	1.11	1.09	1.07	1.06	1.05	1.04	1.03
BOG	2.27	1.90	1.66	1.50	1.40	1.32	1.23	1.17	1.13	1.10	1.09	1.06	1.05	1.04	1.03	1.03
BOZ	2.59	2.20	1.92	1.72	1.58	1.47	1.34	1.25	1.19	1.15	1.12	1.08	1.06	1.05	1.04	1.03
BPH	61.9	19.3	8.95	5.32	3.66	2.76	1.91	1.53	1.34	1.23	1.17	1.10	1.07	1.05	1.04	1.03
BRE	2.59	2.14	1.84	1.64	1.51	1.42	1.30	1.23	1.18	1.15	1.13	1.09	1.08	1.06	1.05	1.05
BSV	2.17	1.79	1.58	1.46	1.38	1.32	1.24	1.19	1.15	1.13	1.11	1.09	1.07	1.06	1.05	1.04
CAN	2.46	2.12	1.90	1.74	1.62	1.53	1.40	1.32	1.26	1.21	1.18	1.13	1.10	1.08	1.07	1.05
CAS	1.39	1.39	1.36	1.33	1.30	1.27	1.22	1.19	1.16	1.14	1.12	1.10	1.08	1.07	1.06	1.05
CDO	2.31	2.02	1.77	1.60	1.48	1.40	1.28	1.22	1.18	1.15	1.12	1.09	1.07	1.06	1.05	1.05

	25 K	30 K	35 K	40 K	45 K	50 K	60 K	70 K	80 K	90 K	100 K	120 K	140 K	160 K	180 K	200 K
CFI	3.41	2.58	2.11	1.80	1.60	1.49	1.32	1.22	1.16	1.13	1.10	1.07	1.05	1.04	1.03	1.03
CGF	1.62	1.50	1.42	1.35	1.30	1.26	1.20	1.16	1.14	1.12	1.10	1.08	1.06	1.05	1.05	1.04
CGS	1.92	1.70	1.54	1.44	1.36	1.30	1.23	1.18	1.14	1.12	1.10	1.08	1.06	1.05	1.04	1.04
CHA	3.63	3.43	2.92	2.39	2.00	1.72	1.42	1.27	1.19	1.14	1.11	1.08	1.06	1.05	1.04	1.03
CON	1.90	1.65	1.50	1.39	1.32	1.26	1.19	1.14	1.11	1.09	1.08	1.06	1.04	1.04	1.03	1.03
CZP	1.94	1.74	1.61	1.51	1.44	1.38	1.30	1.25	1.20	1.17	1.15	1.12	1.10	1.08	1.07	1.06
DAC	1.39	1.38	1.36	1.33	1.29	1.26	1.21	1.17	1.15	1.12	1.11	1.08	1.07	1.05	1.05	1.04
DDR	1.26	1.30	1.30	1.28	1.26	1.24	1.21	1.17	1.15	1.13	1.12	1.09	1.07	1.06	1.05	1.04
DFO	1.95	1.72	1.57	1.45	1.37	1.31	1.22	1.17	1.13	1.11	1.09	1.06	1.05	1.04	1.03	1.03
DFT	1.30	1.33	1.32	1.30	1.28	1.25	1.21	1.18	1.16	1.14	1.12	1.10	1.08	1.07	1.06	1.05
DOH	1.28	1.29	1.27	1.25	1.23	1.21	1.17	1.14	1.12	1.11	1.09	1.08	1.06	1.05	1.04	1.04
DON	2.13	1.80	1.59	1.46	1.37	1.30	1.21	1.16	1.12	1.10	1.08	1.06	1.04	1.04	1.03	1.02
EAB	1.73	1.58	1.47	1.39	1.33	1.28	1.21	1.16	1.13	1.11	1.09	1.07	1.06	1.05	1.04	1.03
EDI	1.69	1.57	1.48	1.40	1.35	1.30	1.24	1.20	1.16	1.14	1.12	1.09	1.08	1.06	1.05	1.05
EEI	3.79	2.78	2.26	2.02	1.84	1.70	1.52	1.40	1.29	1.23	1.19	1.12	1.09	1.07	1.05	1.04
EMT	1.39	1.36	1.31	1.27	1.24	1.21	1.17	1.14	1.12	1.10	1.09	1.07	1.05	1.04	1.03	1.02
EON	1.77	1.70	1.60	1.51	1.44	1.38	1.29	1.23	1.19	1.15	1.13	1.10	1.08	1.06	1.05	1.04
EPI	1.92	1.71	1.56	1.45	1.37	1.32	1.24	1.19	1.15	1.13	1.11	1.08	1.07	1.06	1.05	1.04
ERI	1.77	1.63	1.53	1.45	1.38	1.32	1.24	1.18	1.14	1.11	1.10	1.07	1.05	1.04	1.04	1.03
ESV	5.02	3.38	2.64	2.21	1.95	1.77	1.52	1.39	1.30	1.23	1.19	1.13	1.09	1.07	1.06	1.05
ETR	2.36	1.94	1.70	1.54	1.43	1.36	1.26	1.20	1.16	1.13	1.11	1.08	1.06	1.05	1.04	1.03
EUO	112	31.7	12.9	7.01	4.45	3.20	2.05	1.58	1.36	1.25	1.18	1.11	1.08	1.06	1.05	1.04
EZT	1.68	1.54	1.44	1.36	1.30	1.25	1.19	1.14	1.12	1.10	1.08	1.06	1.05	1.04	1.03	1.03
FAR	4.83	3.23	2.54	2.11	1.81	1.64	1.40	1.28	1.22	1.17	1.13	1.10	1.07	1.06	1.05	1.04
FAU	1.40	1.36	1.32	1.28	1.24	1.22	1.17	1.15	1.12	1.10	1.09	1.06	1.05	1.04	1.03	1.03
FER	1.61	1.48	1.39	1.32	1.27	1.23	1.18	1.14	1.12	1.10	1.09	1.07	1.05	1.05	1.04	1.03
FRA	1.70	1.64	1.55	1.47	1.40	1.34	1.25	1.19	1.15	1.13	1.10	1.08	1.06	1.05	1.04	1.04
GIS	3.06	2.36	1.96	1.73	1.58	1.47	1.34	1.26	1.21	1.17	1.14	1.11	1.09	1.07	1.06	1.05
GIU	3.28	2.61	2.19	1.94	1.77	1.63	1.44	1.33	1.25	1.20	1.16	1.11	1.08	1.07	1.05	1.05
GME	2.59	2.10	1.81	1.63	1.51	1.43	1.31	1.24	1.19	1.15	1.13	1.09	1.07	1.06	1.05	1.04
GON	2.25	1.91	1.68	1.53	1.42	1.34	1.24	1.18	1.14	1.11	1.09	1.07	1.05	1.04	1.04	1.03
GOO	1.90	1.73	1.61	1.51	1.45	1.39	1.31	1.26	1.22	1.19	1.16	1.13	1.10	1.09	1.07	1.06
HEU	2.10	1.79	1.60	1.47	1.39	1.32	1.24	1.18	1.15	1.13	1.11	1.08	1.07	1.05	1.05	1.04
IFO	2.72	2.15	1.82	1.62	1.48	1.38	1.26	1.18	1.14	1.11	1.09	1.06	1.05	1.04	1.03	1.02
IFR	1.96	1.72	1.56	1.44	1.36	1.30	1.22	1.16	1.13	1.10	1.09	1.06	1.05	1.04	1.03	1.03
IHW	2.66	2.14	1.85	1.65	1.52	1.42	1.29	1.21	1.16	1.13	1.11	1.08	1.06	1.05	1.04	1.03
IMF	2.23	1.84	1.65	1.51	1.42	1.34	1.24	1.18	1.14	1.11	1.09	1.07	1.05	1.04	1.03	1.03
IRR	2.11	1.80	1.60	1.46	1.37	1.30	1.21	1.15	1.11	1.09	1.07	1.05	1.04	1.03	1.02	1.02
ISV	1.93	1.69	1.52	1.41	1.33	1.27	1.19	1.14	1.11	1.09	1.07	1.05	1.04	1.03	1.03	1.02
ITE	2.07	1.80	1.61	1.49	1.40	1.33	1.24	1.18	1.14	1.11	1.09	1.07	1.05	1.04	1.04	1.03
ITG	3.22	2.49	2.09	1.83	1.66	1.52	1.35	1.25	1.19	1.14	1.11	1.08	1.06	1.05	1.04	1.03
ITH	2.54	2.22	1.96	1.76	1.59	1.48	1.33	1.23	1.18	1.14	1.11	1.08	1.06	1.05	1.04	1.03
ITR	2.71	2.33	2.01	1.78	1.61	1.49	1.33	1.24	1.18	1.14	1.11	1.08	1.06	1.05	1.04	1.03
ITT	1.63	1.49	1.40	1.33	1.28	1.23	1.18	1.13	1.11	1.09	1.07	1.05	1.04	1.03	1.03	1.02
ITW	2.42	2.01	1.75	1.59	1.47	1.39	1.29	1.22	1.18	1.15	1.13	1.10	1.08	1.06	1.05	1.05
IWR	1.98	1.70	1.52	1.41	1.33	1.27	1.19	1.14	1.11	1.09	1.08	1.06	1.04	1.03	1.03	1.02
IWS	2.21	1.83	1.60	1.46	1.36	1.30	1.21	1.15	1.12	1.10	1.08	1.06	1.04	1.03	1.03	1.02
IWV	2.60	2.14	1.86	1.68	1.54	1.44	1.30	1.22	1.16	1.13	1.10	1.07	1.05	1.04	1.03	1.03
IWW	42.4	14.4	7.52	4.86	3.44	2.74	1.96	1.55	1.33	1.23	1.16	1.10	1.07	1.05	1.04	1.03
JBW	2.14	1.90	1.74	1.61	1.52	1.45	1.34	1.28	1.23	1.19	1.17	1.13	1.10	1.09	1.07	1.06
JOZ	1.79	1.64	1.54	1.45	1.39	1.35	1.28	1.23	1.19	1.17	1.15	1.11	1.09	1.08	1.07	1.06
JRY	1.93	1.68	1.52	1.42	1.35	1.29	1.22	1.18	1.15	1.12	1.11	1.08	1.07	1.06	1.05	1.04

	25 K	30 K	35 K	40 K	45 K	50 K	60 K	70 K	80 K	90 K	100 K	120 K	140 K	160 K	180 K	200 K
JSN	1.70	1.56	1.46	1.38	1.32	1.28	1.21	1.17	1.14	1.12	1.10	1.08	1.07	1.05	1.05	1.04
JSR	1.87	1.62	1.46	1.36	1.28	1.23	1.17	1.13	1.10	1.08	1.07	1.05	1.04	1.03	1.03	1.02
JST	1.45	1.39	1.34	1.30	1.26	1.23	1.18	1.15	1.13	1.11	1.09	1.07	1.06	1.05	1.04	1.04
JSW	2.37	1.98	1.74	1.58	1.47	1.39	1.29	1.22	1.17	1.15	1.12	1.09	1.07	1.06	1.05	1.04
KFI	2.79	2.22	1.90	1.70	1.56	1.46	1.33	1.25	1.19	1.15	1.13	1.09	1.07	1.05	1.04	1.04
LAU	1.81	1.61	1.48	1.38	1.32	1.27	1.20	1.16	1.13	1.10	1.09	1.07	1.05	1.04	1.04	1.03
LEV	1.88	1.67	1.53	1.42	1.35	1.29	1.22	1.17	1.13	1.11	1.09	1.07	1.06	1.04	1.04	1.03
LIO	1.65	1.62	1.55	1.48	1.42	1.36	1.29	1.23	1.19	1.16	1.13	1.10	1.08	1.06	1.05	1.05
LOS	2.73	2.31	2.05	1.86	1.71	1.60	1.43	1.32	1.24	1.19	1.15	1.11	1.08	1.06	1.05	1.04
LOV	1.31	1.34	1.34	1.32	1.29	1.27	1.22	1.19	1.16	1.14	1.12	1.10	1.08	1.07	1.06	1.05
LTA	1.43	1.39	1.33	1.29	1.25	1.22	1.18	1.15	1.12	1.10	1.09	1.06	1.05	1.04	1.03	1.03
LTF	8.47	4.73	3.24	2.54	2.11	1.83	1.52	1.36	1.26	1.20	1.16	1.11	1.08	1.07	1.05	1.05
LTJ	2.01	1.78	1.64	1.53	1.46	1.40	1.32	1.27	1.23	1.20	1.18	1.15	1.12	1.11	1.09	1.08
LTL	2.91	3.06	2.90	2.61	2.30	2.01	1.64	1.42	1.30	1.22	1.17	1.11	1.07	1.05	1.04	1.03
LTN	8.30	4.58	3.19	2.41	2.00	1.73	1.43	1.28	1.20	1.16	1.13	1.09	1.07	1.05	1.05	1.04
MAR	4.73	3.33	2.61	2.22	1.94	1.76	1.51	1.36	1.27	1.20	1.16	1.11	1.08	1.07	1.05	1.05
MAZ	2.84	2.51	2.16	1.89	1.70	1.56	1.39	1.28	1.22	1.18	1.14	1.10	1.08	1.06	1.05	1.04
MEI	2.24	1.91	1.70	1.56	1.46	1.38	1.27	1.21	1.16	1.13	1.11	1.08	1.06	1.05	1.04	1.03
MEL	1.84	1.62	1.48	1.38	1.31	1.26	1.19	1.15	1.12	1.10	1.08	1.06	1.05	1.04	1.03	1.03
MEP	1.17	1.23	1.25	1.24	1.23	1.22	1.18	1.15	1.13	1.11	1.10	1.08	1.06	1.05	1.05	1.04
MER	1.73	1.63	1.54	1.46	1.40	1.35	1.28	1.23	1.19	1.16	1.14	1.11	1.08	1.07	1.06	1.05
MFI	1.78	1.58	1.46	1.37	1.30	1.25	1.19	1.14	1.12	1.10	1.08	1.06	1.05	1.04	1.03	1.03
MFS	4.72	3.24	2.58	2.18	1.98	1.79	1.55	1.41	1.31	1.24	1.19	1.13	1.09	1.07	1.06	1.05
MON	2.13	1.91	1.76	1.64	1.55	1.48	1.38	1.31	1.25	1.21	1.18	1.14	1.11	1.09	1.08	1.07
MOR	1.40	1.41	1.38	1.35	1.31	1.28	1.22	1.18	1.16	1.13	1.11	1.09	1.07	1.06	1.05	1.04
MOZ	1.87	1.74	1.66	1.59	1.52	1.45	1.33	1.24	1.19	1.15	1.12	1.08	1.06	1.05	1.04	1.03
MRE	1.87	1.62	1.46	1.36	1.29	1.24	1.18	1.14	1.11	1.09	1.08	1.06	1.05	1.04	1.03	1.03
MSE	33.8	21.4	11.1	6.00	3.60	2.53	1.65	1.34	1.21	1.14	1.10	1.07	1.05	1.04	1.03	1.03
MSO	2.16	1.87	1.69	1.57	1.47	1.39	1.28	1.21	1.16	1.13	1.11	1.08	1.06	1.05	1.04	1.03
MTF	2.53	2.10	1.82	1.64	1.52	1.42	1.30	1.22	1.17	1.14	1.11	1.08	1.06	1.05	1.04	1.04
MTN	1.24	1.26	1.25	1.23	1.21	1.20	1.16	1.14	1.12	1.10	1.09	1.07	1.06	1.05	1.04	1.04
MTT	4.36	2.99	2.31	1.94	1.70	1.54	1.36	1.25	1.19	1.15	1.12	1.09	1.07	1.05	1.04	1.04
MTW	3.53	2.74	2.22	1.94	1.72	1.57	1.39	1.28	1.21	1.16	1.13	1.09	1.07	1.05	1.04	1.03
MVY	26.9	10.8	6.21	4.23	3.28	2.70	2.08	1.77	1.58	1.47	1.39	1.28	1.22	1.18	1.15	1.13
MWW	10.7	8.32	5.35	3.50	2.38	1.92	1.41	1.25	1.17	1.13	1.10	1.07	1.05	1.04	1.04	1.03
NAB	2.07	1.87	1.73	1.63	1.55	1.48	1.38	1.31	1.25	1.21	1.19	1.14	1.11	1.09	1.08	1.07
NAT	1.53	1.46	1.39	1.34	1.30	1.26	1.21	1.17	1.15	1.13	1.11	1.09	1.07	1.06	1.05	1.05
NES	2.64	2.15	1.84	1.66	1.51	1.41	1.28	1.20	1.15	1.12	1.10	1.07	1.05	1.04	1.03	1.03
NON	225	46.4	18.1	9.58	6.20	4.50	2.83	2.14	1.73	1.50	1.37	1.20	1.13	1.09	1.07	1.06
NPO	2.75	2.20	1.89	1.71	1.58	1.48	1.36	1.29	1.24	1.20	1.17	1.13	1.11	1.09	1.08	1.07
NPT	2.13	1.88	1.70	1.56	1.46	1.38	1.28	1.21	1.17	1.14	1.12	1.09	1.07	1.05	1.05	1.04
NSI	2.89	2.34	2.01	1.80	1.66	1.56	1.43	1.34	1.28	1.23	1.20	1.16	1.12	1.10	1.09	1.08
OBW	2.17	1.91	1.71	1.57	1.46	1.38	1.27	1.21	1.16	1.13	1.11	1.08	1.06	1.05	1.04	1.03
OFF	1.59	1.51	1.45	1.40	1.35	1.30	1.23	1.18	1.14	1.12	1.10	1.07	1.06	1.05	1.04	1.03
OKO	2.05	1.78	1.60	1.47	1.37	1.30	1.21	1.16	1.12	1.10	1.08	1.06	1.05	1.04	1.03	1.03
OSI	3.21	2.48	2.06	1.79	1.62	1.49	1.33	1.23	1.17	1.14	1.11	1.08	1.06	1.05	1.04	1.03
OSO	2.75	2.28	1.97	1.76	1.61	1.50	1.35	1.25	1.19	1.15	1.12	1.09	1.06	1.05	1.04	1.03
OWE	3.59	2.53	2.02	1.72	1.54	1.43	1.29	1.22	1.17	1.14	1.11	1.09	1.07	1.06	1.05	1.04
PAU	1.67	1.58	1.50	1.43	1.39	1.34	1.27	1.22	1.18	1.15	1.13	1.10	1.08	1.06	1.05	1.04
PCR	19.0	7.70	4.42	2.91	2.22	1.85	1.45	1.29	1.21	1.16	1.13	1.09	1.07	1.06	1.05	1.04
PHI	1.83	1.67	1.57	1.49	1.42	1.37	1.29	1.23	1.19	1.16	1.13	1.10	1.08	1.07	1.06	1.05
PON	1.53	1.45	1.38	1.33	1.29	1.25	1.20	1.16	1.14	1.12	1.10	1.08	1.07	1.06	1.05	1.04
PUN	1.97	1.71	1.55	1.43	1.35	1.30	1.22	1.17	1.14	1.12	1.10	1.08	1.06	1.05	1.04	1.04

	25 K	30 K	35 K	40 K	45 K	50 K	60 K	70 K	80 K	90 K	100 K	120 K	140 K	160 K	180 K	200 K
RHO	1.26	1.29	1.28	1.27	1.25	1.23	1.19	1.16	1.14	1.12	1.10	1.08	1.06	1.05	1.04	1.03
RRO	3.41	2.57	2.12	1.84	1.66	1.53	1.37	1.28	1.22	1.18	1.15	1.12	1.09	1.08	1.06	1.05
RSN	1.51	1.51	1.47	1.42	1.37	1.33	1.26	1.22	1.18	1.16	1.14	1.11	1.09	1.07	1.06	1.05
RTE	2.43	2.00	1.74	1.58	1.46	1.38	1.26	1.20	1.16	1.12	1.10	1.08	1.06	1.05	1.04	1.03
RTH	2.29	1.92	1.69	1.53	1.43	1.35	1.25	1.18	1.14	1.12	1.10	1.07	1.05	1.04	1.04	1.03
RUT	2.07	1.80	1.62	1.49	1.40	1.34	1.25	1.19	1.16	1.13	1.11	1.08	1.07	1.06	1.05	1.04
RWR	1.98	1.75	1.60	1.50	1.42	1.37	1.28	1.23	1.19	1.17	1.15	1.11	1.09	1.08	1.07	1.06
RWY	2.01	1.71	1.52	1.40	1.31	1.25	1.17	1.12	1.10	1.08	1.06	1.04	1.03	1.02	1.02	1.02
SAF	1.99	1.73	1.55	1.44	1.35	1.29	1.21	1.15	1.12	1.10	1.08	1.06	1.05	1.04	1.03	1.03
SAO	1.97	1.69	1.51	1.40	1.32	1.26	1.18	1.14	1.11	1.08	1.07	1.05	1.04	1.03	1.03	1.02
SAS	1.97	1.69	1.53	1.43	1.36	1.31	1.24	1.19	1.15	1.12	1.10	1.07	1.06	1.04	1.04	1.03
SAT	39.9	14.1	7.27	4.69	3.46	2.68	1.89	1.52	1.33	1.23	1.17	1.10	1.07	1.06	1.04	1.04
SAV	2.53	2.18	1.97	1.81	1.67	1.55	1.38	1.27	1.20	1.16	1.12	1.09	1.06	1.05	1.04	1.03
SBE	1.34	1.35	1.35	1.32	1.30	1.27	1.24	1.20	1.17	1.14	1.12	1.09	1.06	1.05	1.04	1.03
SBN	1.30	1.32	1.31	1.28	1.26	1.23	1.19	1.16	1.14	1.12	1.10	1.08	1.07	1.06	1.05	1.04
SBS	10.7	5.85	3.84	2.99	2.46	2.18	1.80	1.56	1.41	1.30	1.22	1.12	1.08	1.05	1.04	1.03
SBT	11.2	6.03	4.09	3.07	2.54	2.18	1.80	1.57	1.40	1.30	1.22	1.12	1.08	1.05	1.04	1.03
SEW	1.98	1.77	1.60	1.49	1.40	1.34	1.24	1.18	1.14	1.12	1.09	1.07	1.05	1.04	1.03	1.03
SFE	3.43	2.63	2.16	1.86	1.67	1.53	1.36	1.26	1.20	1.15	1.12	1.09	1.06	1.05	1.04	1.03
SFF	4.48	3.10	2.46	2.01	1.75	1.56	1.36	1.25	1.18	1.14	1.11	1.08	1.06	1.05	1.04	1.03
SFG	1.72	1.56	1.45	1.36	1.30	1.25	1.18	1.14	1.11	1.10	1.08	1.06	1.05	1.04	1.03	1.03
SFH	3.34	2.55	2.12	1.84	1.65	1.51	1.34	1.24	1.18	1.14	1.11	1.08	1.06	1.04	1.03	1.03
SFN	3.53	2.64	2.16	1.85	1.64	1.50	1.34	1.24	1.18	1.14	1.11	1.08	1.06	1.04	1.03	1.03
SFO	1.98	1.75	1.61	1.52	1.45	1.39	1.30	1.24	1.19	1.16	1.13	1.09	1.07	1.05	1.04	1.04
SFS	1.99	1.74	1.56	1.44	1.36	1.30	1.21	1.16	1.13	1.10	1.09	1.06	1.05	1.04	1.03	1.03
SFV	1.79	1.60	1.46	1.37	1.30	1.26	1.19	1.15	1.12	1.10	1.08	1.06	1.05	1.04	1.03	1.03
SFW	2.71	2.18	1.87	1.67	1.54	1.44	1.32	1.24	1.19	1.15	1.13	1.09	1.07	1.05	1.04	1.04
SGT	851	157	43.4	18.0	9.53	5.89	3.11	2.07	1.61	1.39	1.26	1.14	1.09	1.07	1.05	1.04
SIV	1.82	1.69	1.59	1.51	1.45	1.38	1.30	1.24	1.19	1.16	1.14	1.10	1.08	1.07	1.06	1.05
SOD	1.64	1.52	1.42	1.35	1.30	1.26	1.20	1.16	1.13	1.11	1.09	1.07	1.06	1.05	1.04	1.04
SOF	2.04	1.79	1.61	1.48	1.40	1.33	1.25	1.19	1.15	1.13	1.11	1.08	1.06	1.05	1.04	1.04
SOS	3.69	2.64	2.13	1.83	1.65	1.52	1.37	1.27	1.22	1.17	1.15	1.11	1.08	1.07	1.06	1.05
SSF	14.6	9.39	6.13	4.20	3.27	2.63	1.99	1.65	1.47	1.32	1.24	1.14	1.09	1.06	1.04	1.04
SSY	3.64	2.72	2.20	1.89	1.69	1.54	1.37	1.26	1.20	1.15	1.12	1.08	1.06	1.05	1.04	1.03
STF	2.76	2.21	1.88	1.67	1.52	1.42	1.29	1.21	1.16	1.13	1.10	1.07	1.06	1.04	1.04	1.03
STI	2.71	2.09	1.76	1.56	1.43	1.35	1.24	1.18	1.14	1.11	1.09	1.07	1.05	1.04	1.04	1.03
STO	1.95	1.71	1.55	1.45	1.36	1.31	1.23	1.17	1.13	1.11	1.09	1.06	1.05	1.04	1.03	1.03
STT	2.11	1.82	1.63	1.50	1.41	1.34	1.24	1.18	1.14	1.12	1.10	1.07	1.05	1.04	1.04	1.03
STW	2.15	1.83	1.63	1.50	1.41	1.34	1.24	1.19	1.15	1.12	1.10	1.08	1.06	1.05	1.04	1.03
SVV	1.98	1.74	1.58	1.47	1.39	1.33	1.24	1.19	1.15	1.13	1.11	1.08	1.06	1.05	1.04	1.04
SZR	20.5	8.87	5.24	3.69	2.88	2.38	1.84	1.56	1.40	1.30	1.23	1.15	1.11	1.08	1.07	1.05
TER	1.94	1.70	1.53	1.42	1.34	1.28	1.20	1.16	1.12	1.10	1.09	1.06	1.05	1.04	1.03	1.03
THO	1.65	1.54	1.46	1.39	1.34	1.29	1.23	1.19	1.16	1.13	1.11	1.09	1.07	1.06	1.05	1.05
TOL	3.03	2.42	2.10	1.86	1.71	1.58	1.42	1.32	1.25	1.20	1.16	1.11	1.08	1.07	1.06	1.05
TON	2.73	2.21	1.89	1.68	1.54	1.43	1.30	1.22	1.17	1.14	1.11	1.08	1.06	1.05	1.04	1.04
TSC	2.13	1.82	1.62	1.50	1.42	1.36	1.27	1.21	1.17	1.14	1.12	1.09	1.06	1.05	1.04	1.03
TUN	1.92	1.67	1.51	1.41	1.33	1.28	1.20	1.16	1.13	1.10	1.09	1.06	1.05	1.04	1.03	1.03
UEI	1.45	1.40	1.36	1.32	1.28	1.25	1.21	1.17	1.15	1.13	1.12	1.09	1.08	1.07	1.06	1.05
UFI	1.58	1.49	1.41	1.34	1.29	1.25	1.20	1.16	1.13	1.11	1.09	1.07	1.05	1.04	1.04	1.03
UOS	1.65	1.53	1.43	1.36	1.30	1.26	1.20	1.16	1.13	1.11	1.10	1.07	1.06	1.05	1.04	1.04
UOZ	1.96	1.73	1.58	1.46	1.38	1.32	1.24	1.19	1.15	1.13	1.11	1.09	1.07	1.06	1.05	1.04
USI	1.72	1.57	1.47	1.39	1.33	1.28	1.21	1.16	1.13	1.11	1.09	1.06	1.05	1.04	1.03	1.03

	25 K	30 K	35 K	40 K	45 K	50 K	60 K	70 K	80 K	90 K	100 K	120 K	140 K	160 K	180 K	200 K
UTL	1.98	1.76	1.59	1.47	1.39	1.32	1.23	1.17	1.13	1.10	1.08	1.06	1.04	1.03	1.03	1.02
UWY	1.21	1.24	1.24	1.22	1.20	1.19	1.15	1.12	1.10	1.09	1.07	1.06	1.04	1.04	1.03	1.03
VET	3.13	2.37	1.94	1.69	1.52	1.41	1.28	1.20	1.15	1.12	1.10	1.07	1.05	1.04	1.04	1.03
VFI	2.79	2.21	1.87	1.65	1.52	1.40	1.27	1.19	1.14	1.11	1.09	1.06	1.04	1.03	1.03	1.02
VNI	6.83	3.97	2.85	2.28	1.95	1.74	1.49	1.36	1.28	1.23	1.19	1.14	1.11	1.09	1.08	1.07
VSV	2.68	2.15	1.86	1.67	1.55	1.46	1.34	1.27	1.22	1.18	1.16	1.12	1.10	1.08	1.07	1.06
WEI	3.30	2.48	2.06	1.81	1.65	1.53	1.38	1.30	1.24	1.20	1.17	1.13	1.10	1.09	1.07	1.06
YUG	9.26	4.98	3.32	2.53	2.09	1.83	1.54	1.38	1.29	1.23	1.19	1.14	1.11	1.09	1.08	1.07
ZON	1.87	1.68	1.54	1.44	1.37	1.31	1.23	1.19	1.15	1.13	1.11	1.08	1.07	1.06	1.05	1.04

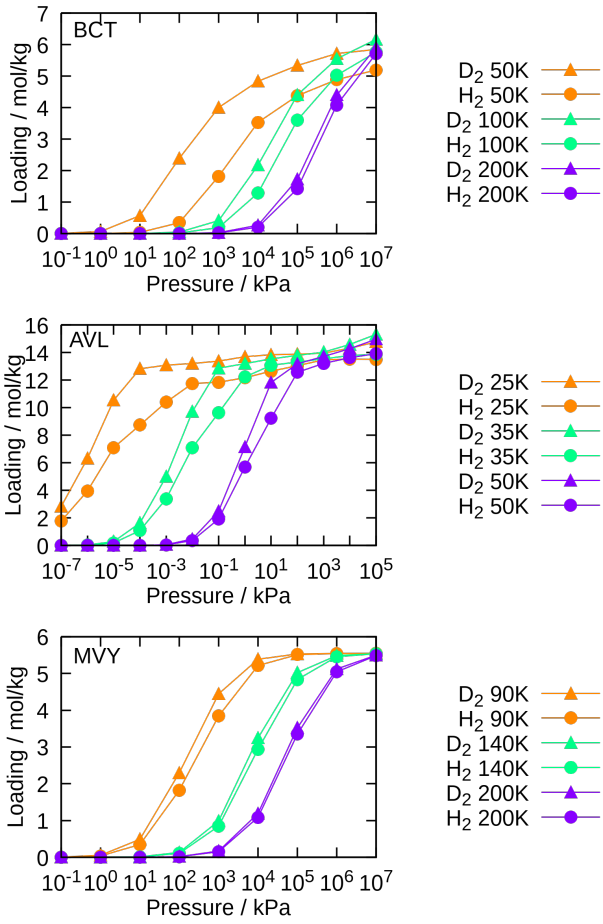

Figure C1: Pure component D_2 (triangles) and H_2 (circles) adsorption isotherms in BCT (top), AVL (center), and MVY (bottom) zeolites.

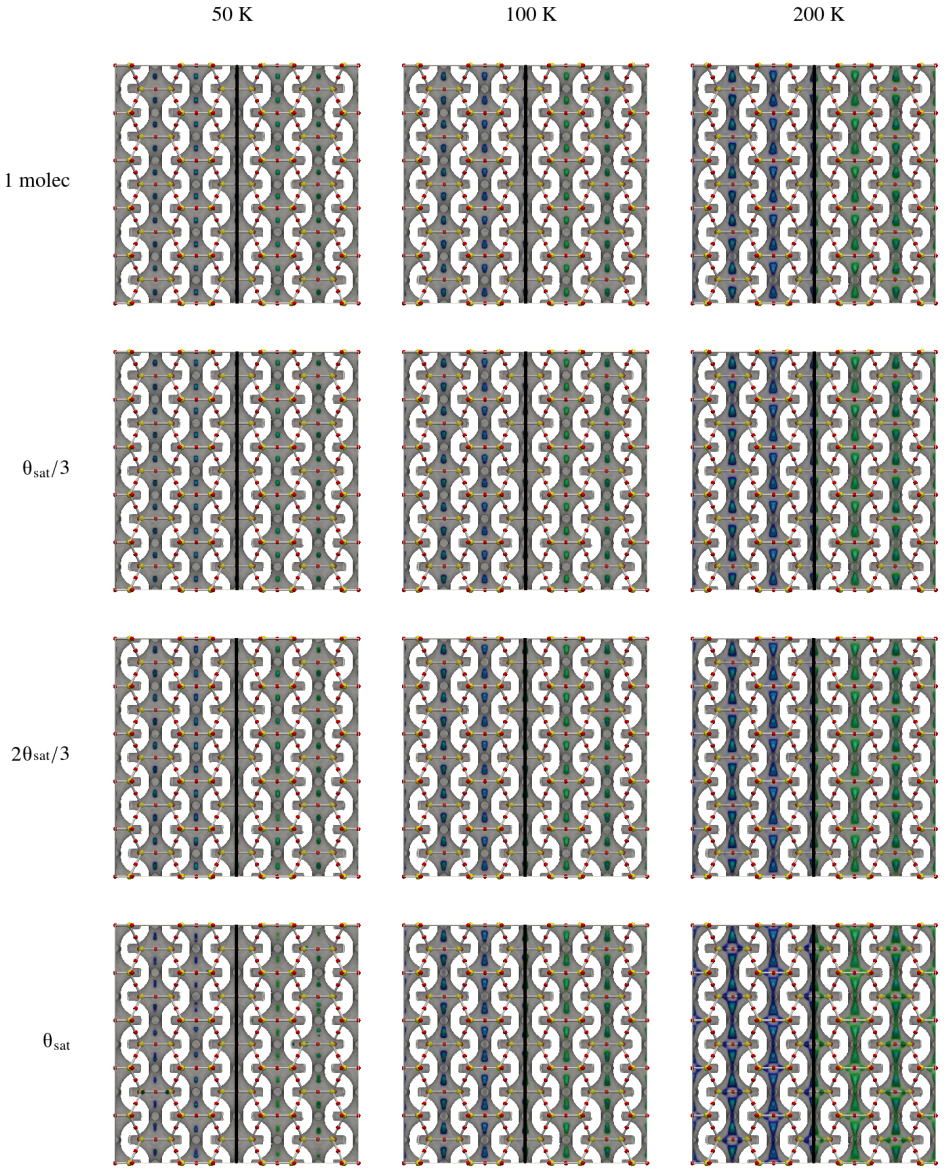

Figure C2: Probability density (adsorption sites) of adsorbates in BCT zeolite as a function of temperature and loading (θ_{sat} is the saturation loading). xz-plane projection of BCT is split in half to ease the comparison: D_2 (blue, left) and H_2 (green, right)

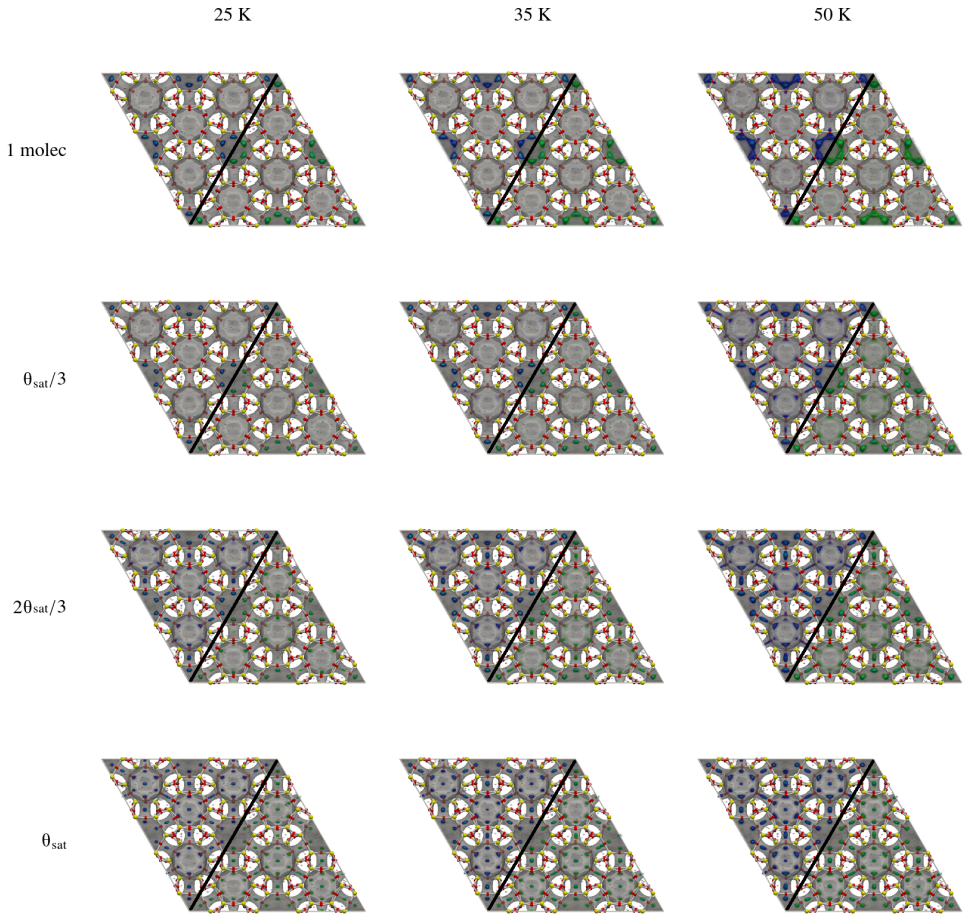

Figure C3: Probability density (adsorption sites) of adsorbates in AVL zeolite as a function of temperature and loading (θ_{sat} is the saturation loading). *xy*-plane projection of AVL is split in half to ease the comparison: D_2 (blue, left) and H_2 (green, right)

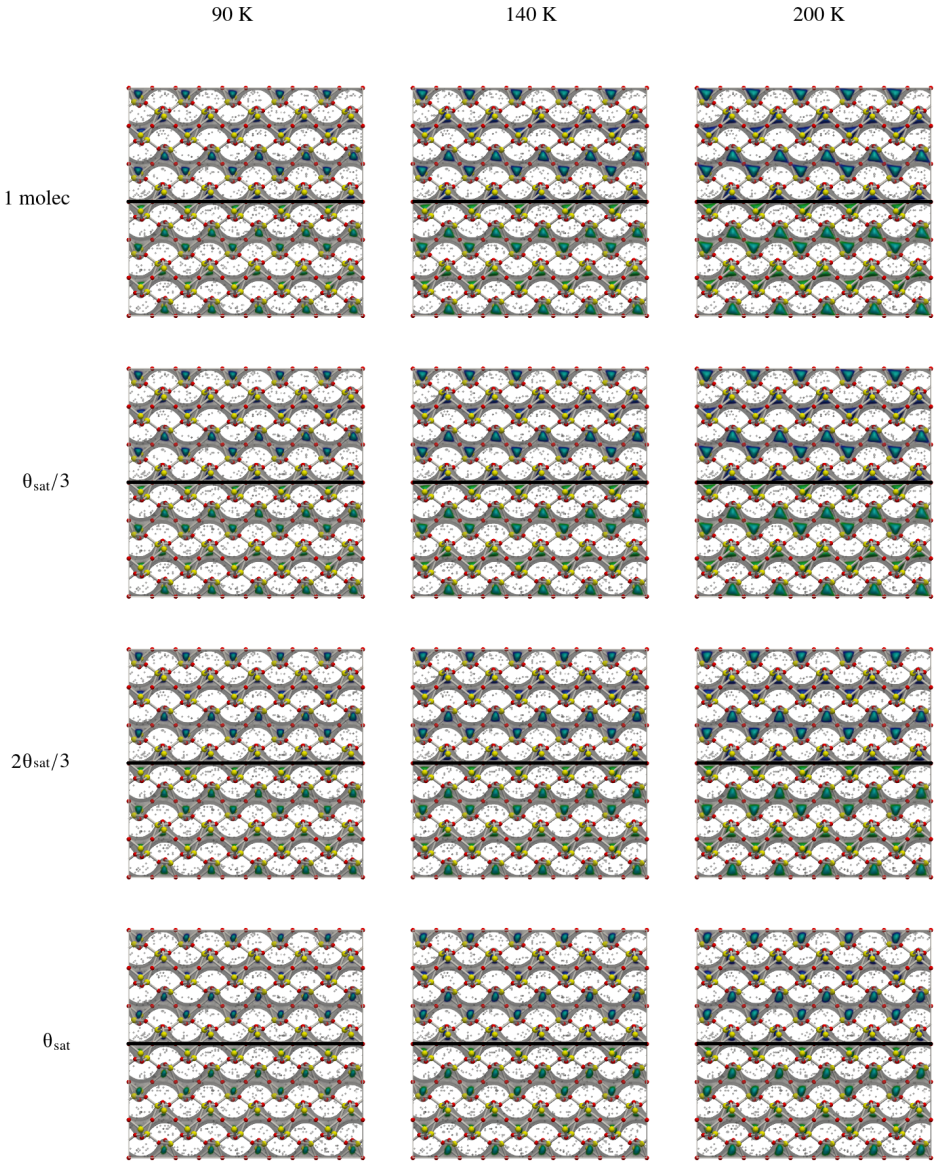

Figure C4: Probability density (adsorption sites) of adsorbates in MVY zeolite as a function of temperature and loading (θ_{sat} is the saturation loading). *xy*-plane projection of MVY is split in half to ease the comparison: D_2 (blue, up) and H_2 (green, down)

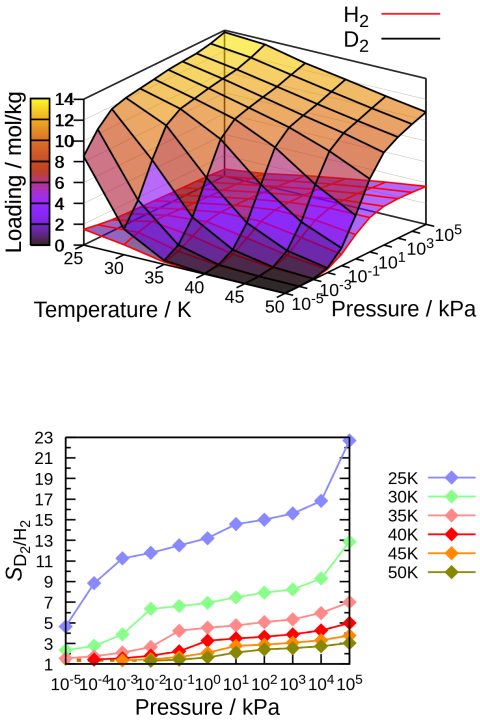

Figure C5: Adsorption loading (top) of deuterium (black lines grid) and hydrogen (red lines grid) in AVL zeolite from a 1:1 mixture as a function of pressure and temperature; grid cell colors match loading color-box. Adsorption selectivity (bottom) of deuterium over hydrogen as a function of pressure and temperature (color code assigned univocally for each temperature). Dashed lines and little symbols for selectivity whose associated loading of D_2 is less than 0.1 mol/kg.

Figure C6: Adsorption loading (top) of deuterium (black lines grid) and hydrogen (red lines grid) in MVY zeolite from a 1:1 mixture as a function of pressure and temperature; grid cell colors match loading color-box. Adsorption selectivity (bottom) of deuterium over hydrogen as a function of pressure and temperature (color code assigned univocally for each temperature). Dashed lines and little symbols for selectivity whose associated loading of D_2 is less than 0.1 mol/kg.

Table C2: T_2/H_2 selectivity at zero-loading. Shadowed cells correspond to zeolites that were found to be inaccessible for adsorbates in further verifications after compute their selectivity.

	25 K	30 K	35 K	40 K	45 K	50 K	60 K	70 K	80 K	90 K	100 K	120 K	140 K	160 K	180 K	200 K
ABW	3.49	2.77	2.36	2.08	1.89	1.75	1.58	1.44	1.36	1.30	1.26	1.20	1.16	1.13	1.11	1.09
ACO	2.02	1.87	1.74	1.64	1.55	1.48	1.38	1.30	1.25	1.22	1.19	1.14	1.12	1.10	1.08	1.07
AEI	4.17	2.99	2.38	2.02	1.79	1.63	1.43	1.31	1.23	1.19	1.15	1.11	1.08	1.06	1.05	1.05
AEL	2.31	1.94	1.71	1.55	1.44	1.37	1.27	1.20	1.16	1.14	1.12	1.09	1.07	1.06	1.05	1.04
AEN	3.69	2.79	2.30	2.01	1.83	1.69	1.50	1.39	1.32	1.27	1.23	1.18	1.14	1.12	1.10	1.08
AET	3.59	2.64	2.13	1.83	1.64	1.51	1.35	1.25	1.19	1.15	1.13	1.09	1.07	1.05	1.04	1.04
AFG	4.45	3.35	2.76	2.38	2.13	1.93	1.67	1.50	1.39	1.31	1.25	1.17	1.13	1.10	1.08	1.07
AFI	3.07	2.37	1.97	1.73	1.57	1.46	1.32	1.24	1.18	1.15	1.12	1.09	1.07	1.05	1.04	1.04
AFN	10.2	5.51	3.69	2.82	2.32	2.01	1.65	1.46	1.35	1.27	1.22	1.16	1.12	1.10	1.08	1.07
AFO	2.44	2.01	1.76	1.59	1.47	1.39	1.27	1.21	1.17	1.14	1.12	1.09	1.07	1.06	1.05	1.04
AFR	2.35	2.05	1.88	1.73	1.62	1.54	1.41	1.33	1.27	1.22	1.18	1.13	1.09	1.07	1.06	1.05
AFS	275	54.5	18.9	9.49	5.74	3.90	2.35	1.75	1.47	1.32	1.23	1.14	1.10	1.07	1.06	1.05
AFT	4.48	3.14	2.44	2.05	1.81	1.64	1.44	1.32	1.25	1.20	1.16	1.11	1.09	1.07	1.06	1.05
AFV	2.63	2.14	1.86	1.67	1.54	1.44	1.32	1.24	1.19	1.16	1.13	1.10	1.08	1.06	1.05	1.04
AFX	4.06	2.92	2.35	2.01	1.79	1.64	1.45	1.34	1.26	1.21	1.17	1.12	1.09	1.07	1.06	1.05
AFY	3.08	2.44	2.06	1.82	1.66	1.54	1.39	1.29	1.23	1.19	1.15	1.11	1.08	1.07	1.05	1.04
AHT	17.8	8.33	5.16	3.74	2.96	2.50	1.98	1.71	1.54	1.44	1.36	1.26	1.21	1.17	1.14	1.12
ANA	4.55	3.25	2.61	2.23	1.99	1.81	1.60	1.47	1.38	1.32	1.28	1.21	1.17	1.14	1.12	1.11
APC	3.81	2.79	2.29	1.99	1.78	1.65	1.48	1.37	1.31	1.26	1.22	1.17	1.14	1.12	1.10	1.09
APD	1.52	1.51	1.47	1.42	1.38	1.34	1.28	1.23	1.20	1.17	1.15	1.12	1.10	1.08	1.07	1.06
AST	2.23	1.91	1.70	1.56	1.45	1.38	1.28	1.21	1.17	1.14	1.12	1.09	1.07	1.06	1.05	1.04
ASV	1.93	1.77	1.63	1.53	1.44	1.38	1.29	1.23	1.19	1.16	1.14	1.11	1.09	1.07	1.06	1.05
ATN	3.62	2.77	2.28	1.97	1.76	1.62	1.43	1.33	1.26	1.21	1.18	1.13	1.10	1.09	1.07	1.06
ATO	2.18	1.83	1.63	1.49	1.40	1.33	1.24	1.19	1.15	1.13	1.11	1.08	1.07	1.06	1.05	1.04
ATS	5.98	3.99	3.00	2.43	2.08	1.85	1.56	1.40	1.30	1.23	1.19	1.13	1.09	1.07	1.06	1.05
ATT	3.83	2.83	2.30	1.99	1.78	1.63	1.44	1.33	1.26	1.21	1.17	1.13	1.10	1.09	1.07	1.06
ATV	1.65	1.59	1.53	1.47	1.41	1.37	1.30	1.25	1.21	1.18	1.16	1.13	1.11	1.09	1.08	1.07
AVL	1.89	1.10	1.00	1.00	1.00	1.00	1.00	1.03	1.05	1.07	1.07	1.06	1.05	1.04	1.04	1.03
AWO	1.92	1.76	1.62	1.52	1.44	1.39	1.30	1.25	1.21	1.18	1.16	1.12	1.10	1.09	1.07	1.07
AWW	2.53	2.09	1.82	1.64	1.52	1.43	1.31	1.24	1.19	1.16	1.13	1.10	1.08	1.06	1.05	1.05
BCT	1.85E6	25900	1880	354	109	46.4	15.1	8.07	5.06	3.71	3.03	2.26	1.89	1.67	1.53	1.43
BEA	2.44	2.00	1.73	1.56	1.44	1.36	1.25	1.18	1.14	1.11	1.10	1.07	1.05	1.04	1.04	1.03
BEC	2.20	1.87	1.65	1.51	1.41	1.33	1.24	1.18	1.14	1.11	1.09	1.07	1.05	1.04	1.04	1.03
BIK	3.56	2.83	2.38	2.09	1.89	1.75	1.55	1.43	1.35	1.30	1.25	1.19	1.15	1.13	1.11	1.09
BOF	2.47	2.06	1.79	1.61	1.50	1.41	1.30	1.23	1.18	1.15	1.13	1.10	1.08	1.06	1.05	1.05
BOG	3.32	2.53	2.06	1.79	1.61	1.48	1.33	1.24	1.18	1.14	1.12	1.09	1.07	1.05	1.04	1.04
BOZ	4.52	3.28	2.58	2.18	1.92	1.73	1.50	1.36	1.27	1.21	1.17	1.12	1.09	1.07	1.05	1.05
BPH	282	55.5	19.6	9.94	5.87	4.06	2.45	1.80	1.49	1.33	1.24	1.14	1.10	1.07	1.06	1.04
BRE	4.12	3.03	2.39	2.03	1.78	1.63	1.44	1.33	1.26	1.21	1.18	1.13	1.10	1.08	1.07	1.06
BSV	2.97	2.26	1.90	1.69	1.55	1.46	1.34	1.26	1.22	1.18	1.16	1.12	1.10	1.08	1.07	1.06
CAN	3.60	2.89	2.45	2.16	1.95	1.80	1.59	1.46	1.37	1.30	1.25	1.18	1.14	1.11	1.09	1.07
CAS	1.70	1.65	1.58	1.51	1.45	1.40	1.32	1.27	1.22	1.19	1.17	1.13	1.11	1.09	1.08	1.07
CDO	4.23	3.05	2.38	2.01	1.77	1.61	1.42	1.32	1.25	1.21	1.17	1.13	1.10	1.08	1.07	1.06
CFI	5.96	3.91	2.92	2.32	2.01	1.74	1.46	1.32	1.23	1.18	1.14	1.10	1.07	1.05	1.04	1.04
CGF	2.09	1.82	1.66	1.53	1.45	1.38	1.29	1.23	1.19	1.16	1.14	1.11	1.09	1.07	1.06	1.06
CGS	2.63	2.16	1.87	1.68	1.55	1.45	1.33	1.25	1.20	1.17	1.14	1.11	1.09	1.07	1.06	1.05
CHA	3.47	2.51	2.01	1.72	1.53	1.41	1.27	1.19	1.15	1.12	1.10	1.07	1.05	1.04	1.04	1.03
CON	2.60	2.09	1.79	1.60	1.47	1.39	1.27	1.20	1.16	1.13	1.11	1.08	1.06	1.05	1.04	1.03
CZP	2.58	2.19	1.95	1.77	1.65	1.56	1.43	1.35	1.29	1.25	1.21	1.16	1.13	1.11	1.09	1.08
DAC	1.69	1.64	1.57	1.50	1.44	1.39	1.31	1.25	1.21	1.17	1.15	1.11	1.09	1.07	1.06	1.06
DDR	1.47	1.50	1.48	1.43	1.40	1.36	1.30	1.25	1.21	1.18	1.16	1.12	1.10	1.08	1.07	1.06
DFO	2.69	2.21	1.92	1.71	1.56	1.46	1.32	1.24	1.18	1.15	1.12	1.09	1.07	1.05	1.04	1.04
DFT	1.54	1.55	1.51	1.46	1.42	1.38	1.31	1.26	1.22	1.19	1.17	1.14	1.11	1.10	1.08	1.07
DOH	1.49	1.48	1.43	1.39	1.34	1.31	1.25	1.20	1.17	1.15	1.13	1.10	1.08	1.07	1.06	1.05
DON	3.04	2.34	1.96	1.72	1.56	1.45	1.31	1.23	1.18	1.14	1.12	1.08	1.06	1.05	1.04	1.03
EAB	2.27	1.95	1.74	1.60	1.49	1.41	1.30	1.23	1.19	1.16	1.13	1.10	1.08	1.06	1.05	1.05

	25 K	30 K	35 K	40 K	45 K	50 K	60 K	70 K	80 K	90 K	100 K	120 K	140 K	160 K	180 K	200 K
EDI	2.27	1.98	1.78	1.64	1.54	1.46	1.35	1.28	1.23	1.20	1.17	1.13	1.10	1.09	1.07	1.06
EEI	6.27	4.10	3.19	2.67	2.31	2.09	1.79	1.58	1.43	1.33	1.26	1.17	1.12	1.09	1.07	1.06
EMT	1.68	1.58	1.49	1.42	1.36	1.32	1.25	1.20	1.17	1.14	1.12	1.09	1.07	1.05	1.04	1.03
EON	2.49	2.21	1.99	1.82	1.69	1.59	1.44	1.34	1.27	1.22	1.18	1.13	1.10	1.08	1.07	1.06
EPI	2.67	2.21	1.90	1.70	1.57	1.48	1.35	1.27	1.22	1.18	1.15	1.12	1.09	1.08	1.06	1.06
ERI	2.63	2.34	2.05	1.83	1.65	1.53	1.36	1.26	1.20	1.16	1.13	1.10	1.07	1.06	1.05	1.04
ESV	9.09	5.28	3.77	2.97	2.50	2.17	1.79	1.57	1.43	1.33	1.27	1.18	1.13	1.10	1.08	1.07
ETR	3.57	2.63	2.13	1.85	1.66	1.54	1.37	1.28	1.22	1.18	1.15	1.11	1.08	1.07	1.05	1.05
EUO	674	113	32.8	14.4	7.76	5.07	2.77	1.90	1.54	1.36	1.26	1.15	1.11	1.08	1.06	1.05
EZT	2.16	1.88	1.68	1.55	1.45	1.37	1.27	1.21	1.16	1.13	1.11	1.08	1.06	1.05	1.04	1.04
FAR	8.49	4.99	3.56	2.77	2.26	1.98	1.60	1.41	1.30	1.24	1.19	1.13	1.10	1.08	1.07	1.06
FAU	1.70	1.59	1.50	1.42	1.37	1.32	1.25	1.21	1.17	1.14	1.12	1.09	1.07	1.05	1.04	1.03
FER	2.06	1.79	1.62	1.49	1.41	1.35	1.26	1.21	1.17	1.14	1.12	1.09	1.08	1.06	1.05	1.05
FRA	2.30	2.08	1.89	1.73	1.61	1.50	1.36	1.27	1.22	1.17	1.15	1.11	1.08	1.07	1.06	1.05
GIS	5.13	3.43	2.61	2.17	1.89	1.71	1.49	1.37	1.29	1.24	1.20	1.15	1.12	1.10	1.08	1.07
GIU	5.20	3.74	2.94	2.50	2.19	1.94	1.66	1.48	1.36	1.28	1.23	1.16	1.12	1.09	1.07	1.06
GME	4.03	2.92	2.35	2.01	1.80	1.66	1.46	1.35	1.28	1.22	1.18	1.13	1.10	1.08	1.06	1.05
GON	3.26	2.54	2.10	1.83	1.65	1.51	1.35	1.26	1.20	1.16	1.13	1.09	1.07	1.06	1.05	1.04
GOO	2.59	2.23	1.98	1.81	1.69	1.59	1.46	1.37	1.31	1.26	1.23	1.18	1.14	1.12	1.10	1.09
HEU	3.04	2.36	1.98	1.74	1.59	1.48	1.35	1.27	1.21	1.18	1.15	1.11	1.09	1.07	1.06	1.06
IFO	4.22	2.99	2.34	1.96	1.73	1.57	1.38	1.26	1.20	1.15	1.12	1.09	1.06	1.05	1.04	1.03
IFR	2.69	2.19	1.88	1.68	1.54	1.44	1.31	1.23	1.18	1.15	1.12	1.09	1.07	1.05	1.04	1.04
IHW	4.00	2.92	2.37	2.01	1.79	1.62	1.41	1.30	1.23	1.18	1.15	1.11	1.08	1.07	1.05	1.05
IMF	3.60	2.82	2.36	2.03	1.77	1.59	1.38	1.26	1.20	1.16	1.13	1.09	1.07	1.06	1.05	1.04
IRR	3.00	2.34	1.96	1.72	1.56	1.44	1.30	1.22	1.16	1.13	1.10	1.07	1.05	1.04	1.03	1.03
ISV	2.63	2.13	1.83	1.63	1.49	1.40	1.27	1.20	1.16	1.12	1.10	1.07	1.06	1.05	1.04	1.03
ITE	2.91	2.33	1.98	1.75	1.60	1.49	1.34	1.25	1.20	1.16	1.13	1.10	1.07	1.06	1.05	1.04
ITG	5.05	3.52	2.75	2.31	2.00	1.79	1.52	1.36	1.26	1.20	1.16	1.11	1.08	1.06	1.05	1.04
ITH	4.06	3.21	2.64	2.23	1.94	1.73	1.48	1.34	1.25	1.20	1.16	1.11	1.08	1.07	1.05	1.05
ITR	4.48	3.43	2.71	2.26	1.94	1.74	1.48	1.34	1.25	1.19	1.16	1.11	1.08	1.07	1.05	1.05
ITT	2.09	1.81	1.63	1.50	1.41	1.34	1.25	1.19	1.15	1.12	1.10	1.07	1.05	1.04	1.03	1.03
ITW	3.52	2.67	2.20	1.91	1.72	1.59	1.42	1.32	1.26	1.21	1.18	1.13	1.11	1.09	1.07	1.06
IWR	2.75	2.16	1.84	1.63	1.49	1.40	1.28	1.21	1.16	1.13	1.11	1.08	1.06	1.05	1.04	1.03
IWS	3.23	2.41	2.00	1.75	1.58	1.46	1.32	1.23	1.17	1.14	1.11	1.08	1.06	1.04	1.04	1.03
IWV	4.02	3.00	2.41	2.07	1.83	1.66	1.45	1.31	1.23	1.18	1.14	1.09	1.07	1.05	1.04	1.03
JBW	3.01	2.51	2.18	1.95	1.79	1.67	1.50	1.40	1.32	1.27	1.23	1.18	1.14	1.12	1.10	1.09
JOZ	2.39	2.08	1.87	1.71	1.60	1.52	1.41	1.33	1.27	1.24	1.20	1.16	1.13	1.11	1.09	1.08
JRY	2.65	2.14	1.83	1.65	1.52	1.43	1.32	1.25	1.21	1.17	1.15	1.11	1.09	1.08	1.06	1.06
JSN	2.22	1.93	1.73	1.59	1.49	1.41	1.31	1.24	1.20	1.17	1.15	1.11	1.09	1.07	1.06	1.05
JSR	2.51	2.02	1.73	1.55	1.43	1.34	1.24	1.18	1.14	1.11	1.09	1.07	1.05	1.04	1.04	1.03
JST	1.73	1.61	1.52	1.44	1.38	1.33	1.26	1.21	1.18	1.15	1.13	1.10	1.08	1.07	1.06	1.05
JSW	3.45	2.65	2.20	1.91	1.72	1.58	1.42	1.31	1.25	1.20	1.17	1.13	1.10	1.08	1.07	1.06
KFI	4.47	3.18	2.54	2.15	1.90	1.72	1.50	1.36	1.28	1.22	1.18	1.12	1.09	1.07	1.06	1.05
LAU	2.42	2.01	1.76	1.59	1.48	1.39	1.29	1.22	1.18	1.15	1.13	1.09	1.07	1.06	1.05	1.04
LEV	2.56	2.11	1.84	1.65	1.53	1.44	1.31	1.24	1.19	1.15	1.13	1.10	1.08	1.06	1.05	1.04
LIO	2.25	2.07	1.89	1.75	1.63	1.55	1.41	1.33	1.27	1.22	1.19	1.14	1.11	1.09	1.07	1.06
LOS	4.15	3.24	2.73	2.37	2.10	1.92	1.63	1.46	1.35	1.26	1.22	1.15	1.11	1.09	1.07	1.06
LOV	1.53	1.55	1.52	1.48	1.43	1.39	1.32	1.26	1.22	1.19	1.17	1.13	1.11	1.09	1.08	1.07
LTA	7.95	5.76	4.52	3.72	3.21	2.84	2.36	2.07	1.87	1.73	1.63	1.49	1.39	1.33	1.28	1.25
LTF	18.3	8.29	5.06	3.58	2.78	2.30	1.78	1.52	1.38	1.29	1.23	1.16	1.12	1.09	1.07	1.06
LTJ	2.66	2.24	1.98	1.80	1.68	1.59	1.47	1.39	1.33	1.29	1.26	1.21	1.17	1.15	1.13	1.11
LTL	15.9	12.1	7.93	5.57	4.05	3.16	2.15	1.69	1.46	1.32	1.24	1.15	1.10	1.07	1.06	1.05

	25 K	30 K	35 K	40 K	45 K	50 K	60 K	70 K	80 K	90 K	100 K	120 K	140 K	160 K	180 K	200 K
LTN	17.1	8.04	4.76	3.36	2.58	2.14	1.64	1.41	1.29	1.22	1.18	1.12	1.09	1.07	1.06	1.05
MAR	8.54	5.18	3.77	2.98	2.50	2.18	1.77	1.53	1.38	1.29	1.23	1.15	1.11	1.09	1.07	1.06
MAZ	6.13	4.34	3.23	2.56	2.16	1.89	1.58	1.42	1.32	1.25	1.20	1.14	1.11	1.09	1.07	1.06
MEI	3.23	2.55	2.13	1.88	1.69	1.57	1.40	1.30	1.23	1.18	1.15	1.11	1.08	1.06	1.05	1.04
MEL	2.51	2.05	1.77	1.59	1.47	1.38	1.27	1.21	1.16	1.13	1.11	1.08	1.06	1.05	1.04	1.04
MEP	1.33	1.39	1.40	1.38	1.35	1.32	1.27	1.22	1.19	1.16	1.14	1.11	1.09	1.07	1.06	1.05
MER	2.27	2.03	1.85	1.71	1.60	1.52	1.41	1.32	1.27	1.23	1.19	1.15	1.12	1.09	1.08	1.07
MFI	2.38	1.98	1.73	1.57	1.45	1.37	1.27	1.21	1.16	1.14	1.11	1.08	1.07	1.05	1.05	1.04
MFS	8.20	5.01	3.63	2.91	2.50	2.21	1.83	1.60	1.45	1.34	1.27	1.18	1.13	1.10	1.08	1.06
MON	2.93	2.50	2.21	2.00	1.84	1.72	1.55	1.44	1.36	1.30	1.26	1.20	1.16	1.13	1.11	1.09
MOR	1.74	1.70	1.62	1.54	1.47	1.41	1.33	1.26	1.22	1.19	1.16	1.12	1.09	1.08	1.06	1.05
MOZ	3.12	2.92	2.62	2.31	2.03	1.82	1.54	1.38	1.28	1.21	1.17	1.12	1.09	1.07	1.06	1.05
MRE	2.55	2.03	1.74	1.56	1.44	1.36	1.26	1.20	1.16	1.13	1.11	1.08	1.06	1.05	1.04	1.04
MSE	363	115	36.8	14.5	7.19	4.12	2.12	1.53	1.31	1.20	1.15	1.10	1.07	1.05	1.04	1.04
MSO	3.39	2.81	2.37	2.06	1.82	1.64	1.43	1.31	1.23	1.18	1.15	1.11	1.08	1.06	1.05	1.04
MTF	3.87	2.92	2.35	2.02	1.79	1.63	1.43	1.32	1.24	1.20	1.16	1.11	1.09	1.07	1.06	1.05
MTN	1.44	1.44	1.40	1.36	1.32	1.29	1.24	1.20	1.17	1.15	1.13	1.10	1.08	1.07	1.06	1.05
MTT	8.70	4.82	3.32	2.55	2.11	1.84	1.53	1.37	1.28	1.21	1.17	1.12	1.09	1.07	1.06	1.05
MTW	6.16	4.15	3.10	2.51	2.14	1.88	1.58	1.41	1.30	1.23	1.18	1.12	1.09	1.07	1.06	1.05
MWW	146	47.2	19.3	8.46	4.35	2.82	1.73	1.40	1.26	1.18	1.14	1.10	1.08	1.06	1.05	1.04
MVY	83.7	24.7	11.7	6.96	4.96	3.80	2.69	2.16	1.86	1.68	1.56	1.40	1.31	1.25	1.20	1.17
NAB	2.77	2.39	2.14	1.96	1.82	1.71	1.55	1.44	1.36	1.30	1.26	1.20	1.16	1.13	1.11	1.09
NAT	1.91	1.74	1.61	1.52	1.44	1.39	1.30	1.25	1.21	1.18	1.16	1.12	1.10	1.09	1.07	1.06
NES	4.10	3.00	2.41	2.03	1.79	1.62	1.41	1.29	1.22	1.17	1.14	1.09	1.07	1.06	1.05	1.04
NON	1400	172	47.8	20.9	11.4	7.47	4.13	2.82	2.12	1.73	1.52	1.29	1.18	1.13	1.10	1.08
NPO	3.99	2.94	2.39	2.07	1.86	1.71	1.52	1.41	1.33	1.28	1.24	1.18	1.15	1.12	1.11	1.09
NPT	3.19	2.56	2.16	1.89	1.70	1.58	1.41	1.31	1.24	1.20	1.16	1.12	1.09	1.07	1.06	1.05
NSI	4.41	3.25	2.63	2.26	2.02	1.84	1.62	1.49	1.39	1.33	1.28	1.22	1.17	1.14	1.12	1.10
OBW	3.31	2.62	2.19	1.90	1.71	1.57	1.40	1.30	1.23	1.18	1.15	1.11	1.08	1.06	1.05	1.04
OFF	2.27	2.12	1.94	1.75	1.61	1.50	1.36	1.27	1.21	1.17	1.14	1.10	1.08	1.06	1.05	1.04
OKO	2.87	2.30	1.94	1.72	1.57	1.45	1.31	1.23	1.17	1.14	1.11	1.08	1.06	1.05	1.04	1.04
OSI	354	66.9	24.1	12.2	7.51	5.38	3.39	2.50	1.99	1.73	1.53	1.30	1.19	1.12	1.09	1.07
OSO	4.66	3.44	2.74	2.30	2.00	1.79	1.52	1.37	1.28	1.21	1.17	1.12	1.09	1.07	1.06	1.05
OWE	6.32	3.77	2.69	2.14	1.84	1.65	1.43	1.31	1.24	1.19	1.16	1.12	1.09	1.07	1.06	1.05
PAU	2.11	1.93	1.77	1.66	1.57	1.50	1.39	1.31	1.26	1.21	1.18	1.13	1.10	1.09	1.07	1.06
PCR	57.6	16.9	7.70	4.47	3.09	2.34	1.69	1.43	1.30	1.22	1.18	1.13	1.10	1.08	1.07	1.06
PHI	2.36	2.07	1.87	1.74	1.63	1.54	1.42	1.33	1.27	1.22	1.19	1.14	1.11	1.09	1.08	1.07
PON	1.91	1.74	1.60	1.51	1.43	1.37	1.29	1.24	1.20	1.17	1.15	1.11	1.09	1.08	1.07	1.06
PUN	2.73	2.19	1.87	1.67	1.54	1.44	1.32	1.25	1.20	1.16	1.14	1.10	1.08	1.07	1.06	1.05
RHO	1.46	1.48	1.45	1.41	1.37	1.33	1.27	1.22	1.19	1.16	1.14	1.11	1.08	1.07	1.05	1.05
RRO	5.71	3.79	2.88	2.34	2.02	1.81	1.55	1.41	1.32	1.26	1.22	1.16	1.13	1.10	1.09	1.07
RSN	1.88	1.83	1.73	1.64	1.56	1.49	1.38	1.31	1.26	1.22	1.19	1.15	1.12	1.10	1.08	1.07
RTE	3.64	2.72	2.21	1.91	1.70	1.56	1.39	1.28	1.22	1.18	1.15	1.11	1.08	1.07	1.05	1.05
RTH	3.34	2.56	2.11	1.83	1.65	1.52	1.36	1.26	1.20	1.16	1.13	1.10	1.07	1.06	1.05	1.04
RUT	2.95	2.35	2.00	1.77	1.61	1.50	1.36	1.28	1.22	1.18	1.15	1.11	1.09	1.08	1.06	1.06
RWR	2.67	2.22	1.94	1.76	1.63	1.54	1.41	1.33	1.27	1.23	1.20	1.16	1.13	1.11	1.09	1.08
RWY	2.78	2.17	1.82	1.61	1.47	1.37	1.25	1.18	1.13	1.11	1.08	1.06	1.04	1.03	1.03	1.02
SAF	2.76	2.21	1.89	1.67	1.53	1.43	1.30	1.22	1.17	1.14	1.11	1.08	1.06	1.05	1.04	1.03
SAO	629	179	55.2	20.2	9.31	5.03	2.33	1.61	1.34	1.22	1.15	1.09	1.06	1.05	1.04	1.03
SAS	2.68	2.18	1.91	1.74	1.62	1.52	1.38	1.29	1.22	1.18	1.14	1.10	1.08	1.06	1.05	1.04
SAT	141	34.4	14.5	8.14	5.27	3.81	2.40	1.79	1.49	1.33	1.24	1.14	1.10	1.07	1.06	1.05
SAV	4.66	4.01	3.38	2.79	2.33	2.01	1.63	1.42	1.30	1.23	1.18	1.12	1.09	1.07	1.06	1.05

	25 K	30 K	35 K	40 K	45 K	50 K	60 K	70 K	80 K	90 K	100 K	120 K	140 K	160 K	180 K	200 K
SBE	1.56	1.58	1.54	1.48	1.47	1.41	1.35	1.29	1.24	1.21	1.17	1.12	1.09	1.07	1.05	1.04
SBN	1.52	1.52	1.48	1.43	1.38	1.34	1.27	1.23	1.19	1.17	1.15	1.12	1.09	1.08	1.07	1.06
SBS	24.2	10.6	6.30	4.37	3.40	2.82	2.18	1.81	1.60	1.43	1.31	1.17	1.11	1.07	1.05	1.04
SBT	26.7	11.2	6.65	4.58	3.54	2.84	2.21	1.85	1.59	1.43	1.32	1.17	1.11	1.07	1.05	1.04
SEW	2.77	2.29	1.97	1.77	1.62	1.51	1.36	1.26	1.20	1.16	1.13	1.09	1.07	1.06	1.05	1.04
SFE	6.07	4.01	2.99	2.41	2.06	1.82	1.53	1.38	1.28	1.21	1.17	1.12	1.09	1.07	1.05	1.05
SFF	8.68	5.09	3.56	2.73	2.19	1.87	1.53	1.36	1.26	1.20	1.16	1.11	1.08	1.06	1.05	1.04
SFG	2.27	1.93	1.71	1.56	1.45	1.37	1.27	1.20	1.16	1.13	1.11	1.08	1.07	1.05	1.04	1.04
SFH	5.84	3.88	2.92	2.35	2.01	1.79	1.50	1.35	1.26	1.20	1.16	1.11	1.08	1.06	1.05	1.04
SFN	6.26	4.08	2.97	2.38	2.02	1.78	1.50	1.35	1.25	1.20	1.16	1.11	1.08	1.06	1.05	1.04
SFO	2.62	2.18	1.94	1.78	1.66	1.56	1.43	1.34	1.27	1.22	1.18	1.13	1.09	1.07	1.06	1.05
SFS	2.82	2.25	1.90	1.69	1.54	1.44	1.31	1.23	1.18	1.15	1.12	1.09	1.07	1.05	1.04	1.04
SFV	2.43	1.99	1.74	1.58	1.46	1.38	1.27	1.21	1.16	1.13	1.11	1.08	1.07	1.05	1.04	1.04
SFW	4.36	3.13	2.46	2.08	1.85	1.67	1.47	1.35	1.27	1.21	1.17	1.12	1.09	1.07	1.06	1.05
SGT	1120	963	171	51.1	22.1	11.7	4.84	2.79	1.97	1.59	1.38	1.20	1.13	1.09	1.07	1.06
SIV	2.33	2.11	1.91	1.78	1.67	1.57	1.43	1.34	1.27	1.22	1.19	1.14	1.11	1.09	1.08	1.07
SOD	2.13	1.85	1.67	1.54	1.45	1.38	1.29	1.22	1.18	1.15	1.13	1.10	1.08	1.07	1.06	1.05
SOF	3.08	2.41	2.01	1.77	1.61	1.50	1.36	1.28	1.22	1.18	1.15	1.11	1.09	1.07	1.06	1.05
SOS	6.18	3.86	2.86	2.31	2.00	1.79	1.53	1.39	1.30	1.25	1.20	1.15	1.12	1.09	1.08	1.07
SSF	68.5	27.9	13.6	8.01	5.22	3.86	2.53	1.97	1.69	1.49	1.35	1.19	1.13	1.08	1.06	1.05
SSY	6.48	4.15	3.05	2.48	2.10	1.83	1.55	1.38	1.28	1.22	1.17	1.12	1.09	1.07	1.05	1.05
STF	4.41	3.13	2.46	2.07	1.81	1.64	1.43	1.31	1.23	1.18	1.15	1.10	1.08	1.06	1.05	1.04
STI	4.33	2.94	2.27	1.89	1.67	1.52	1.35	1.25	1.20	1.16	1.13	1.10	1.07	1.06	1.05	1.04
STO	2.70	2.23	1.94	1.76	1.61	1.49	1.34	1.25	1.19	1.15	1.13	1.09	1.07	1.05	1.04	1.04
STT	2.98	2.39	2.02	1.78	1.62	1.50	1.35	1.26	1.20	1.16	1.14	1.10	1.07	1.06	1.05	1.04
STW	3.07	2.41	2.03	1.78	1.62	1.51	1.36	1.27	1.21	1.17	1.14	1.10	1.08	1.07	1.05	1.05
SVV	2.75	2.25	1.93	1.73	1.59	1.49	1.35	1.27	1.21	1.18	1.15	1.11	1.09	1.07	1.06	1.05
SZR	60.9	19.9	9.89	6.16	4.36	3.38	2.34	1.85	1.59	1.43	1.33	1.21	1.15	1.11	1.09	1.07
TER	2.70	2.17	1.85	1.65	1.51	1.42	1.29	1.22	1.18	1.14	1.12	1.09	1.07	1.06	1.05	1.04
THO	2.18	1.92	1.74	1.61	1.52	1.44	1.34	1.27	1.22	1.19	1.16	1.12	1.10	1.08	1.07	1.06
TOL	4.95	3.53	2.84	2.39	2.09	1.89	1.62	1.46	1.35	1.28	1.23	1.16	1.12	1.09	1.07	1.06
TON	4.42	3.18	2.51	2.11	1.84	1.67	1.45	1.32	1.24	1.19	1.16	1.11	1.09	1.07	1.06	1.05
TSC	2.92	2.32	1.99	1.77	1.63	1.53	1.39	1.30	1.25	1.21	1.17	1.12	1.09	1.07	1.05	1.04
TUN	2.63	2.12	1.83	1.65	1.52	1.42	1.30	1.23	1.18	1.15	1.12	1.09	1.07	1.06	1.05	1.04
UEI	1.80	1.67	1.57	1.48	1.43	1.37	1.30	1.25	1.21	1.19	1.16	1.13	1.11	1.09	1.08	1.07
UFI	2.02	1.80	1.64	1.53	1.44	1.37	1.29	1.22	1.18	1.15	1.13	1.09	1.07	1.06	1.05	1.04
UOS	2.12	1.86	1.68	1.55	1.45	1.38	1.29	1.23	1.19	1.15	1.13	1.10	1.08	1.07	1.06	1.05
UOZ	2.68	2.21	1.92	1.71	1.58	1.49	1.36	1.27	1.22	1.18	1.15	1.12	1.09	1.08	1.07	1.06
USI	2.20	1.92	1.73	1.59	1.49	1.41	1.30	1.23	1.18	1.15	1.12	1.09	1.07	1.06	1.05	1.04
UTL	2.74	2.26	1.95	1.74	1.59	1.48	1.33	1.24	1.18	1.14	1.12	1.08	1.06	1.05	1.04	1.03
UWY	1.37	1.39	1.37	1.34	1.30	1.27	1.22	1.17	1.14	1.12	1.10	1.08	1.06	1.05	1.04	1.04
VET	5.25	3.46	2.58	2.10	1.81	1.62	1.41	1.29	1.21	1.17	1.14	1.10	1.07	1.06	1.05	1.04
VFI	4.40	3.11	2.50	2.08	1.78	1.60	1.39	1.28	1.21	1.16	1.12	1.08	1.06	1.05	1.04	1.03
VNI	13.6	6.56	4.16	3.08	2.49	2.12	1.72	1.52	1.40	1.32	1.27	1.19	1.15	1.12	1.11	1.09
VSV	3.95	2.89	2.35	2.03	1.82	1.68	1.49	1.39	1.31	1.26	1.22	1.17	1.14	1.11	1.10	1.08
WEI	5.36	3.58	2.74	2.26	1.98	1.79	1.56	1.43	1.34	1.28	1.24	1.18	1.14	1.12	1.10	1.08
YUG	23.6	9.58	5.35	3.64	2.79	2.30	1.80	1.56	1.42	1.33	1.27	1.20	1.15	1.12	1.10	1.09
ZON	2.56	2.13	1.86	1.69	1.56	1.47	1.34	1.27	1.22	1.18	1.15	1.12	1.09	1.07	1.06	1.06

Associated content of *Diffusion patterns in zeolite MFI: the cation effect*

APPENDIX D

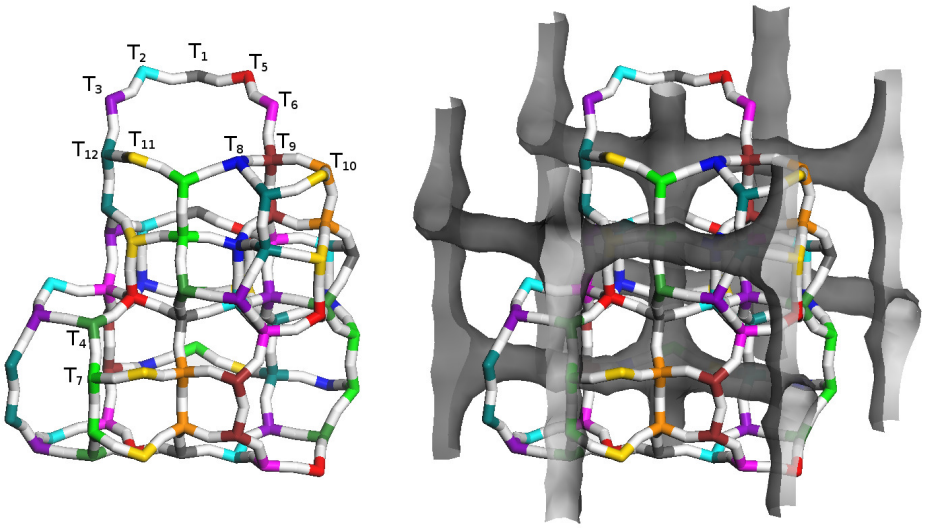

Figure D1: Distribution of T atoms in 10-membered rings defining straight and zigzag channels. T atoms color is in accordance with rest of figures: T_1 grey, T_2 cyan, T_3 purple, T_4 green; T_5 red, T_6 pink, T_7 light green, T_8 dark blue, T_9 brown, T_{10} orange, T_{11} yellow, and T_{12} teal. Oxygen atoms are colored in white. For clarity, some TO links are not depicted. Energy surface areas are also shown on the right.

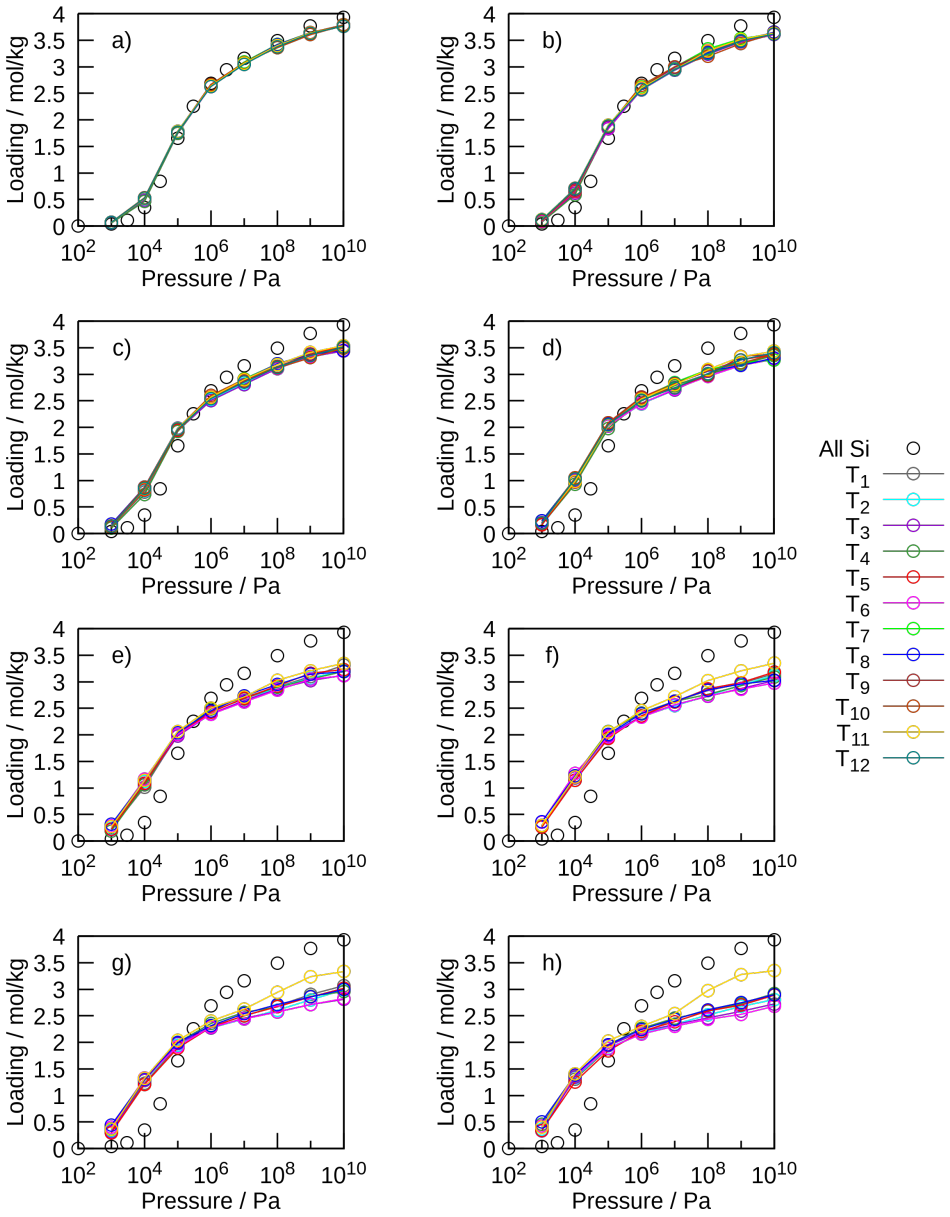

Figure D2: Adsorption isotherms of CO_2 in MFI structures with increasing Al substitutions and Na^+ cations: a) 1 Al/uc, b) 2 Al/uc, c) 3 Al/uc, d) 4 Al/uc, e) 5 Al/uc, f) 6 Al/uc, g) 7 Al/uc, and h) 8 Al/uc. Each color line and symbol indicates the T crystallographical position where the substitutions are done. Black symbols without line stand for pure silica MFI.

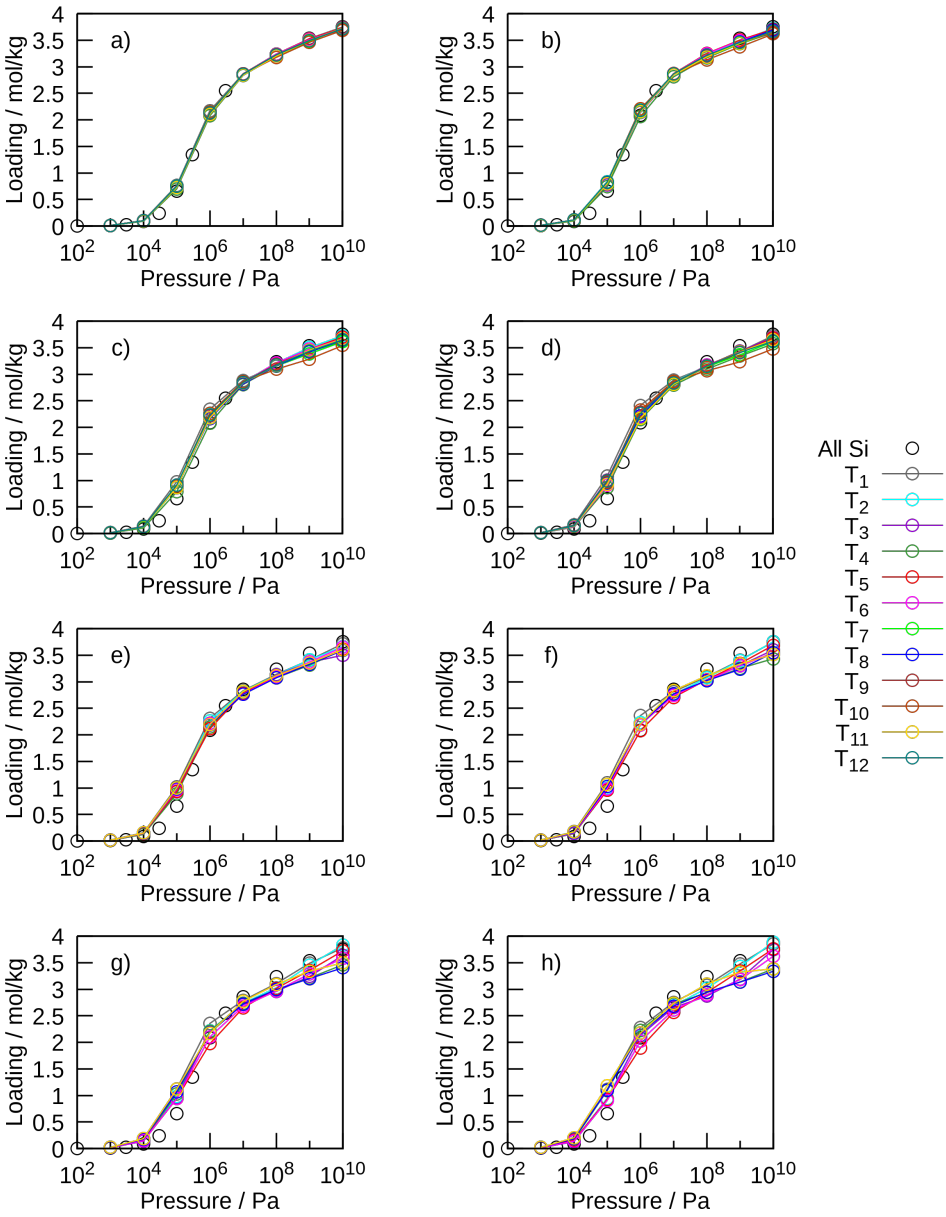

Figure D3: Adsorption isotherms of CH_4 in MFI structures with increasing Al substitutions and Na^+ cations: a) 1 Al/uc, b) 2 Al/uc, c) 3 Al/uc, d) 4 Al/uc, e) 5 Al/uc, f) 6 Al/uc, g) 7 Al/uc, and h) 8 Al/uc. Each color line and symbol indicates the T crystallographical position where the substitutions are done. Black symbols without line stand for pure silica MFI.

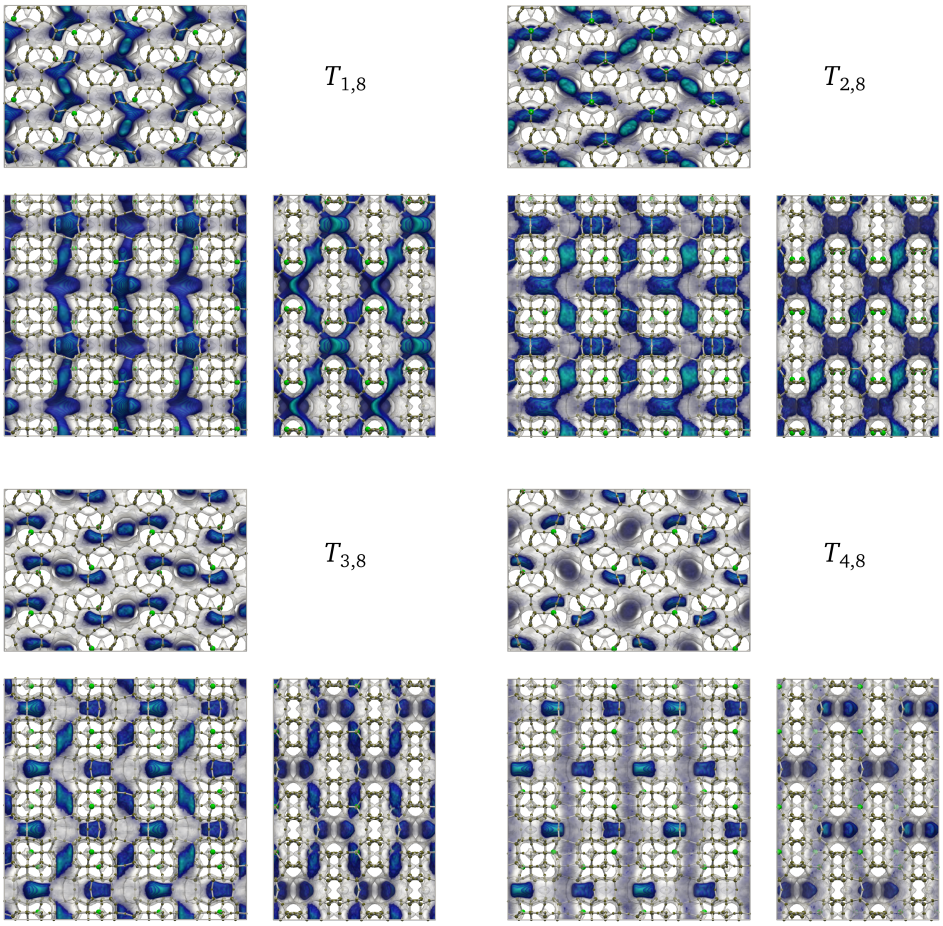

Figure D4: Probability density of Na^+ cations in $T_{n,8}$ ($n \in [1-4]$) MFI channels projected on xy plane (bottom-left), zy plane (bottom-right), and xz plane (top). For easier identification, Al atoms are oversized and colored in green.

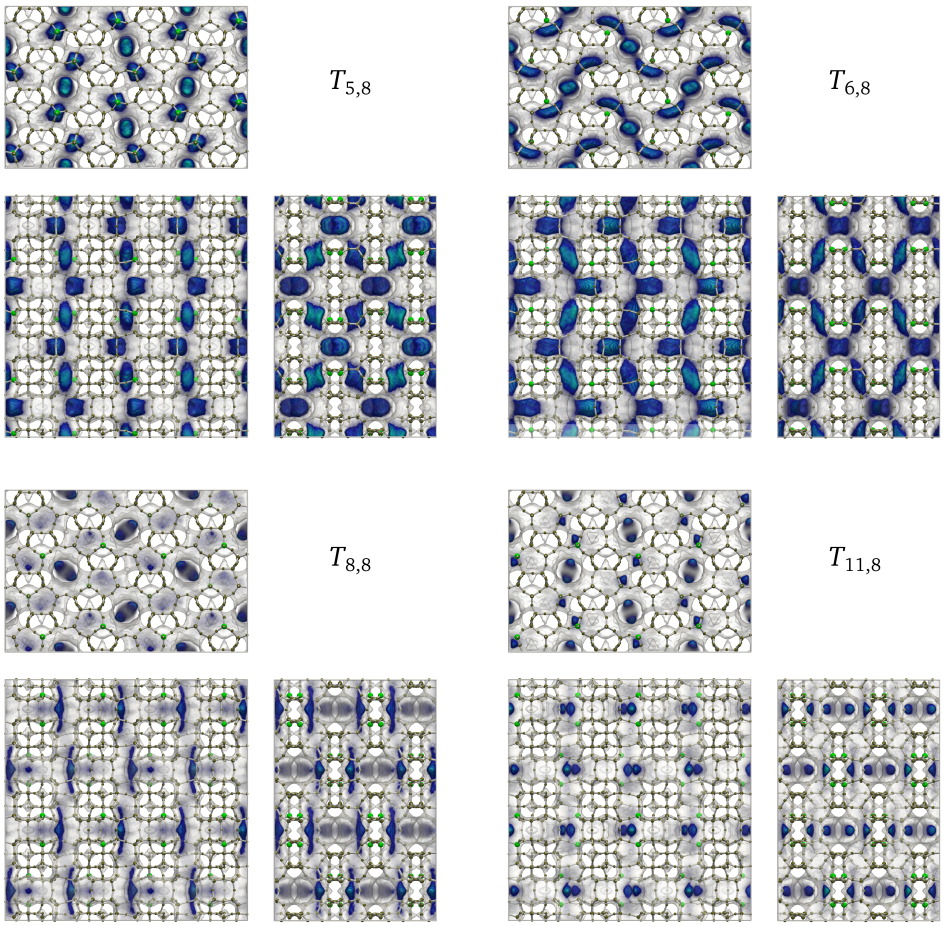

Figure D5: Probability density of Na^+ cations in $T_{n,8}$ ($n \in [5,6,8,11]$) MFI channels projected on xy plane (bottom-left), zy plane (bottom-right), and xz plane (top). For easier identification, Al atoms are oversized and colored in green.

Table D1: Diffusion coefficients (overall and directional components) in pure silica and $T_{n,8}$ MFI structures of CO_2, CH_4, and Na^+ in presence of any of the adsorbates at low loading. All the diffusion coefficients units are $10^{-8} m^2 s^{-1}$.

$T_{n,8}$	D coeff.	CO_2	Na^+ (CO_2)	CH_4	Na^+ (CH_4)
$AllSi$	D	1.058	-	2.612	-
	D^x	1.126	-	2.846	-
	D^y	1.780	-	4.425	-
	D^z	0.267	-	0.564	-
$T_{1,8}$	D	0.348	0.420	0.704	0.508
	D^x	0.232	0.441	0.649	0.543
	D^y	0.740	0.687	1.341	0.815
	D^z	0.067	0.133	0.197	0.166
$T_{2,8}$	D	0.356	0.367	0.535	0.418
	D^x	0.413	0.494	0.632	0.568
	D^y	0.547	0.476	0.773	0.538
	D^z	0.104	0.129	0.144	0.148
$T_{3,8}$	D	0.283	0.271	0.386	0.293
	D^x	0.254	0.226	0.368	0.244
	D^y	0.523	0.504	0.676	0.544
	D^z	0.072	0.083	0.109	0.089
$T_{4,8}$	D	0.390	0.472	0.766	0.626
	D^x	0.084	0.161	0.094	0.209
	D^y	1.051	1.194	2.206	1.588
	D^z	0.034	0.062	0.038	0.082
$T_{5,8}$	D	0.078	0.070	0.119	0.077
	D^x	0.049	0.059	0.096	0.065
	D^y	0.167	0.132	0.228	0.143
	D^z	0.017	0.020	0.032	0.022
$T_{6,8}$	D	0.314	0.328	0.425	0.333
	D^x	0.325	0.333	0.413	0.340
	D^y	0.560	0.540	0.727	0.548
	D^z	0.081	0.112	0.116	0.110
$T_{8,8}$	D	0.319	0.348	0.870	0.398
	D^x	0.451	0.351	1.133	0.401
	D^y	0.417	0.614	1.235	0.701
	D^z	0.088	0.079	0.248	0.091
$T_{11,8}$	D	0.178	0.137	0.672	0.141
	D^x	0.183	0.094	0.444	0.098
	D^y	0.305	0.293	1.427	0.296
	D^z	0.046	0.025	0.144	0.027

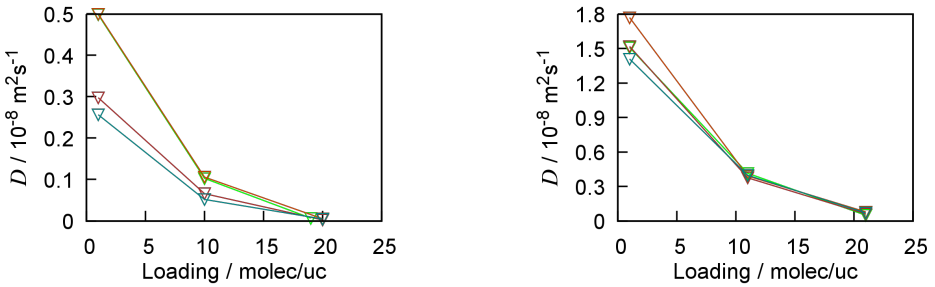

Figure D6: Diffusion coefficients of CO_2 (left) and CH_4 (right) as a function of loading in $T_{7,4}$, $T_{9,4}$, $T_{10,4}$, and $T_{12,4}$ MFI structures with Na^+ cations.

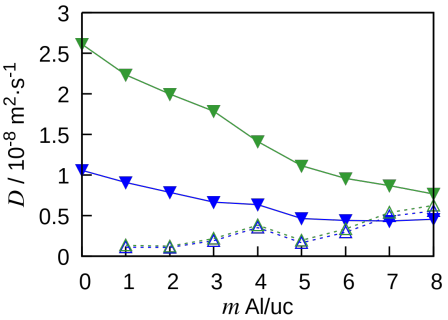

Figure D7: Diffusion coefficients at infinite dilution of CO_2 (blue filled symbols, solid line), Na^+ (blue open symbols, dashed line) in presence of 1 CO_2 guest per simulation supercell, CH_4 (green filled symbols, solid line) and Na^+ (green open symbols, dashed line) in presence of 1 CH_4 guest per simulation supercell, as a function of the number of aluminum (and sodium cation) substitutions per unit cell in the position $T_{4,m}$.

Roughly midway through the Al substitution scheme of site 4, a noticeable diffusion loss of a single probe molecule is observed (Figure D7). This loss is seen clearly with methane going from 3 to 4 Al/uc. For CO_2, this loss of diffusivity is observed between $T_{4,4}$ and $T_{4,5}$ and extends even to loadings up to half maximum guest molecule loading. This can be related to a decrease of roughly a quarter in $D^{y}_{CO_2}$ and $D^{x}_{CO_2}$ due to cations populating all the zigzag channels and increasing the transition energy barriers along straight channels (Figure D8). However, these results should not be overinterpreted: although structures generated for $T_{4,2}$-$T_{4,6}$ have an Al distribution that is favorable, other nonequivalent distributions with similarly favorable Al distributions are possible and may lead to slightly different results.

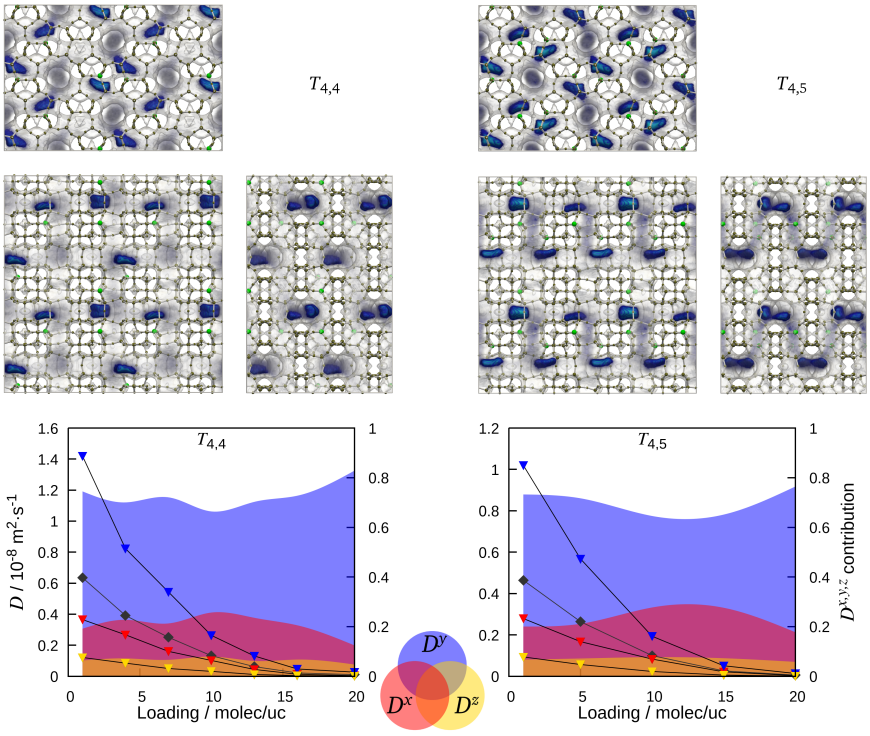

Figure D8: Top: Probability density of Na^+ cations in $T_{4,4}$ (right) and $T_{4,5}$ (left) MFI channels projected on xy plane (bottom-left), zy plane (bottom-right), and xz plane (top). For easier identification, Al atoms are oversized and colored in green. Bottom: Diffusion coefficients (symbols and left vertical axis) of CO_2 and normalised contributions to total diffusion (colored areas and right vertical axis) of the directional components D^x (red), D^y (blue), and D^z (yellow) as a function of loading in $T_{4,4}$ (left) and $T_{4,5}$ (right) MFI structures with Na^+ cations. Total diffusion coefficient, D, is depicted in dark grey diamond symbols.

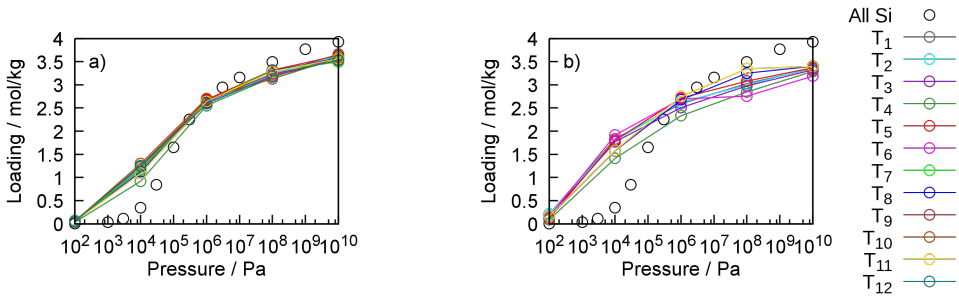

Figure D9: Adsorption isotherms of CO_2 in MFI structures with 4 and 8 Al substitutions and Ca^{2+} cations, a) and b) respectively. Each color line and symbol indicates the T crystallographical position where the substitutions are done. Black symbols without line is for pure silica MFI in order to compare.

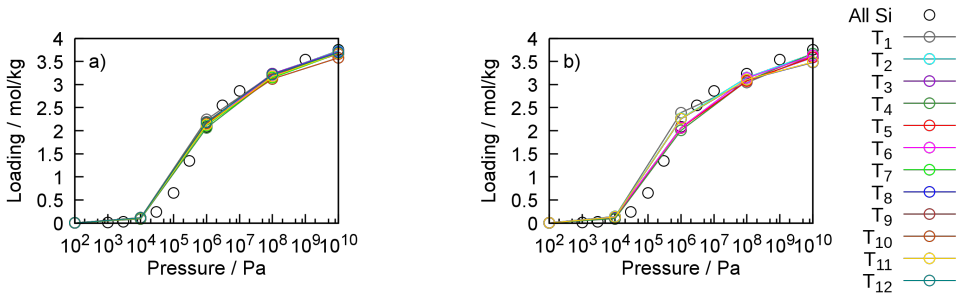

Figure D10: Adsorption isotherms of CH_4 in MFI structures with 4 and 8 Al substitutions and Ca^{2+} cations, a) and b) respectively. Each color line and symbol indicates the T crystallographical position where the substitutions are done. Black symbols without line is for pure silica MFI in order to compare.

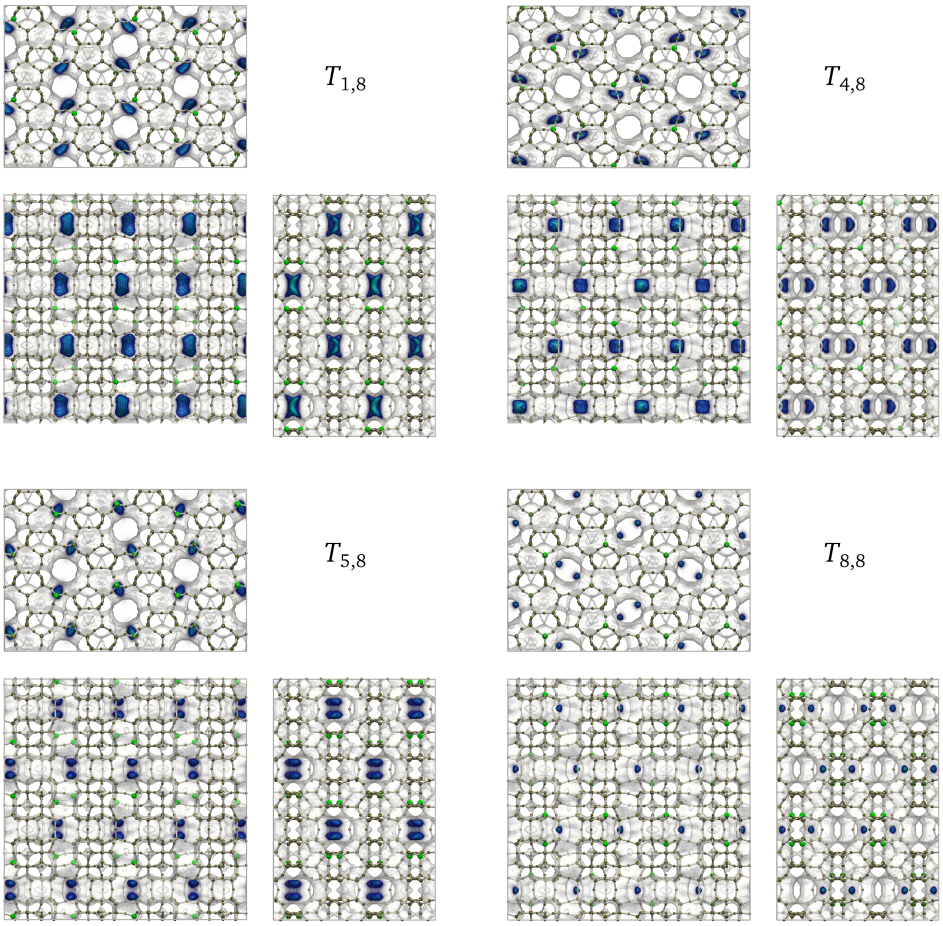

Figure D11: Probability density of Ca^{2+} cations in $T_{n,8}$ ($n \in [1,4,5,8]$) MFI channels projected on xy plane (bottom-left), zy plane (bottom-right), and xz plane (top). For easier identification, Al atoms are oversized and colored in green.

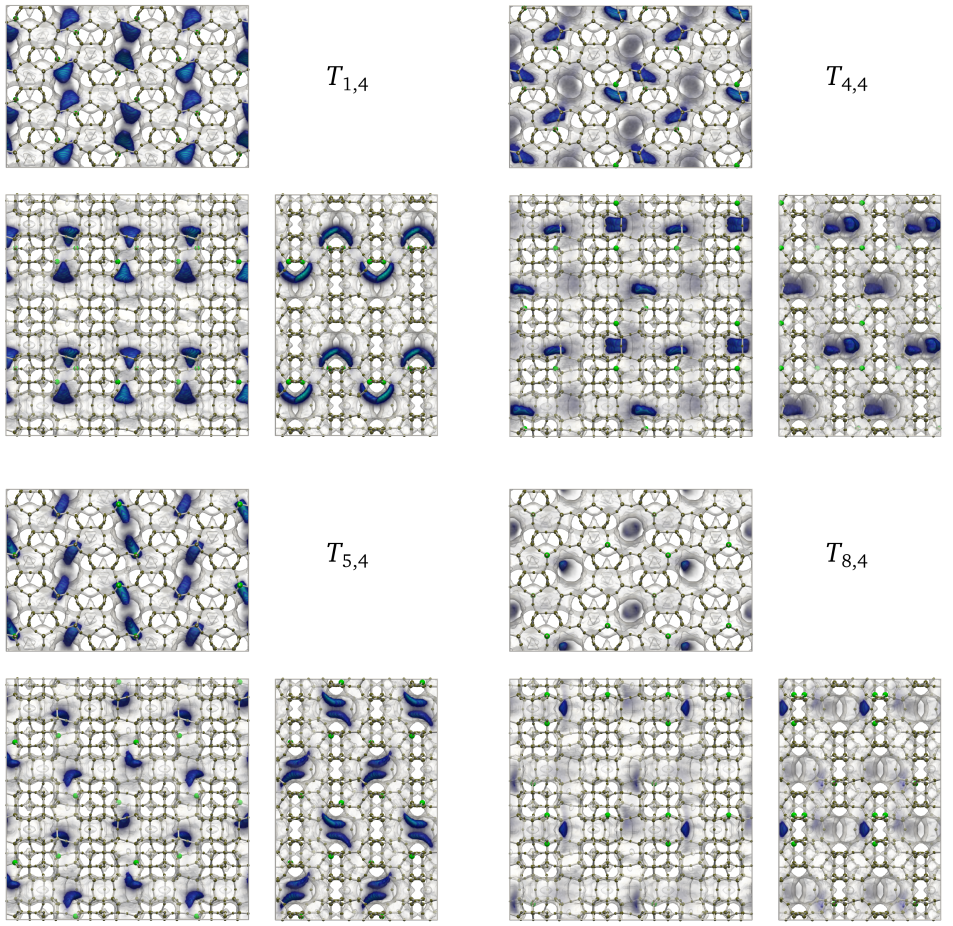

Figure D12: Probability density of Na^+ cations in $T_{n,4}$ ($n \in [1,4,5,8]$) MFI channels projected on xy plane (bottom-left), zy plane (bottom-right), and xz plane (top). For easier identification, Al atoms are oversized and colored in green.

Publications included in this thesis

- **Chapter 2**

  Perez-Carbajo, J.; Gómez-Álvarez, P.; Bueno-Perez, R.; Merkling, P. J.; Calero, S. "Optimisation of the Fischer–Tropsch Process Using Zeolites for Tail Gas Separation" *Phys. Chem. Chem. Phys.*, 16, 5678-5688, **2014**.

- **Chapter 3**

  Perez-Carbajo, J.; Matito-Martos, I.; Balestra, S. R. G.; Tsampas, M. N.; Van De Sanden, M. C. M.; Delgado, J. A.; Águeda, V. I.; Merkling, P. J.; Calero, S. "Zeolites for CO_2-CO-O_2 Separation to Obtain CO_2-neutral Fuels" *ACS Appl. Mater. Interfaces*, 10 (24), 20512-20520, **2018**.

- **Chapter 4**

  Perez-Carbajo, J.; Parra, J. B.; Ania, C. O.; Merkling, P. J.; Calero, S. "Molecular Sieves for the Separation of Hydrogen Isotopes" *ACS Appl. Mater. Interfaces*, Just Accepted Manuscript, DOI: 10.1021/acsami.9b02736, **2019**.

- **Chapter 5**

  Perez-Carbajo, J.; Dubbeldam, D.; Merkling, P. J.; Calero, S. "Diffusion Patterns in MFI: the Cation Effect" *J. Phys. Chem. C*, 122 (51), 29274-29284, **2018**.

- **Chapter 6**

  Perez-Carbajo, J.; Balestra, S. R. G.; Merkling, P. J.; Calero, S. "Effect of Lattice Shrinking on the Migration of Water Within Zeolite LTA" Submitted to *Micropor. Mesopor. Mat.*, **2019**. Pre-print currently available in arXiv:1904.08185.

Publications not included in this thesis

- Gómez-Álvarez, P.; Perez-Carbajo, J.; Balestra, S. R. G.; Calero, S. "Impact of the Nature of Exchangeable Cations on LTA-Type Zeolite Hydration" *J. Phys. Chem. C*, 20 (40), 23254-23261, **2016**.

Non-peer reviewed journals

- Perez-Carbajo, J. "Zeolitas para Mejorar la Síntesis de Hidrocarburos a Partir de Syngas" *MoleQla: Revista de Química*, ISSN 2173-0903, 9, 107-108, **2013**.
- Perez-Carbajo, J. "Comment on: In Silico Screening of Carbon-Capture Materials" *Revista Materiales en Adsorción y Catálisis*, ISSN 2173-0253,4, 32-33, **2012**.